Decoupling Mechanical and Ion Transport Properties in Polymer Electrolyte Membranes

A DISSERTATION

SUBMITTED TO THE FACULTY OF THE GRADUATE SCHOOL

OF THE UNIVERSITY OF MINNESOTA

BY

Lucas D. McIntosh

IN PARTIAL FULFILLMENT OF THE REQUIREMENTS

FOR THE DEGREE OF

Doctor of Philosophy

Timothy P. Lodge

August 2014

Acknowledgements

In writing this section, I find myself genuinely concerned that I'll forget to thank someone who deserves my gratitude. I'll do my best.

It has been a privilege to learn from Tim Lodge. I've discovered over the past five years that even in the scientific community, Tim's approach to science is unique. It's easy to come up with a complex answer to a complex question, but Tim's forte is distilling complex problems down to the basic scientific concepts, and more often than not down to a simple equation in "the book". I hope that I've gleaned some fraction of what it means to be a scientist from him.

I owe my present and future happiness to my wife, Dani, who single-handedly guaranteed that we would end up together.

My family—Mom, Dad, and Stu—and my new family—Judy, Dee, Emily, and Graham—have always given me their unfailing support. It means the world to me that they're proud of what I do and play such an active role in my life.

Two thirds of the research in this thesis was done in close collaboration with Marc Hillmyer and Morgan Schulze, and I'm immensely grateful that they were willing to work with me. Morgan, in particular, has been an excellent collaborator. I look forward to reading future papers from her, and eventually from what will undoubtedly be her successful research group.

The Lodge group is full of competent, intelligent people who also happen to be incredible friends. Just being surrounded by a culture of excellence is critically important to success, and the Lodge group consistently provides an atmosphere where I

feel at home striving to be a better scientist. Unfortunately, this is where this section gets tricky, because so many people have helped me along the way. I was a first-year, once, and Brad Jones and Adam Moughton displayed saintlike patience with me, teaching me without hesitation. Sipei Zhang taught me impedance spectroscopy. Yuanyan Gu, too, helped me learn my way around the lab. John McAllister et al. have become great friends to my family. I've had many helpful discussions with Matt Irwin.

The lines between research groups are blurred in the Minnesota Polymer Group. I don't think I can contribute anything novel in favor of this situation, but I want to point out how helpful this is from a student's perspective. I've received help from every corner of the Polymer Group, and I thank all the students and PIs.

Finally, the friends. Bike rides and brewing beer with Tim Gillard. Dinners with Ben and Cara Bangasser. Christmas with RyRy Henning and Dan Schwent. Settlers of Catan with Clark, Momo, and Kelpie. Thank you for the memories.

Dedication

For my wife.

Abstract

Polymer electrolytes are mixtures of a polar polymer and salt, in which the polymer replaces small molecule solvents and provides a dielectric medium so that ions can dissociate and migrate under the influence of an external electric field. Beginning in the 1970s, research in polymer electrolytes has been primarily motivated by their promise to advance electrochemical energy storage and conversion devices, such as lithium ion batteries, flexible organic solar cells, and anhydrous fuel cells. In particular, polymer electrolyte membranes (PEMs) can improve both safety and energy density by eliminating small molecule, volatile solvents and enabling an all-solid-state design of electrochemical cells.

The outstanding challenge in the field of polymer electrolytes is to maximize ionic conductivity while simultaneously addressing orthogonal mechanical properties, such as modulus, fracture toughness, or high temperature creep resistance. The crux of the challenge is that flexible, polar polymers best-suited for polymer electrolytes (*e.g.*, poly(ethylene oxide)) offer little in the way of mechanical robustness. Similarly, polymers typically associated with superior mechanical performance (*e.g.*, poly(methyl methacrylate)) slow ion transport due to their glassy polymer matrix. The design strategy is therefore to employ structured electrolytes that exhibit distinct conducting and mechanically robust phases on length scales of tens of nanometers.

This thesis reports a remarkably simple, yet versatile synthetic strategy—termed polymerization-induced phase separation, or PIPS—to prepare PEMs exhibiting an unprecedented combination of both high conductivity and high modulus. This performance is enabled by co-continuous, isotropic networks of poly(ethylene oxide)/ionic liquid and highly crosslinked polystyrene. A suite of *in situ*, time-resolved experiments were performed to investigate the mechanism by which this network morphology forms, and it appears to be tied to the disordered structure observed in diblock

polymer melts near the order-disorder transition. In the resulting solid PEMs, the conductivity and modulus are both high, exceeding the 1 mS/cm and approaching the 1 GPa metrics, respectively, often cited for lithium-metal batteries. In the final chapter, an alternative synthetic route to generate nanostructured PEMs is presented. This strategy relies on the formation of a thermodynamically stable network morphology exhibited by a triblock terpolymer prepared with crosslinking moieties along the backbone. Although the mechanical properties of the resulting PEM are excellent, the conductivity is found to be somewhat limited by network defects that result from the solvent-casting procedure.

Table of Contents

List of Tables

List of Figures

xii

Chapter 1

Introduction

The polyethers-alkali metal salt complexes appear as a new class of ion-conducting solids, and deserve special attention.

— M. Armand, in *Fast Ion Transport in Solids*, 1979

1.1 Opportunity and Challenge of Polymer Electrolytes

Polymer electrolytes are mixtures of a polar polymer and salt, in which the salt can (at least partially) dissociate into free ions that migrate under the influence of an external electric field.[1–6] In many cases, polymer electrolytes can simply be thought of by analogy to more traditional aqueous electrolytes (*e.g.*, $LiClO_4$ in water), where the polymer takes the place of the small molecule solvent and provides the medium in which salts can dissolve. For example, a well-studied, prototypical polymer electrolyte is poly(ethylene oxide) (PEO) and $LiClO_4$. The role of polymer electrolytes is identical to liquid-based electrolytes, namely to electrically insulate electrodes while allowing internal ionic current in electrochemical energy storage and conversion devices, such as batteries, fuel cells, and photovoltaics (Figure 1.1).
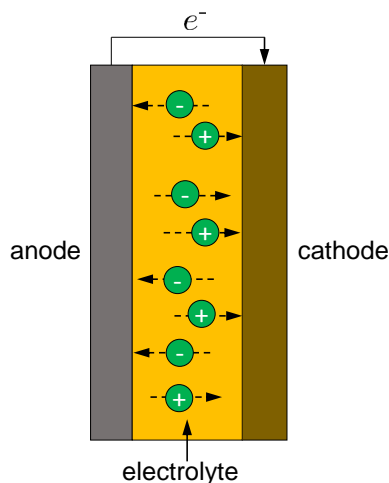
Figure 1.1: Schematic of a generic electrochemical device during discharge. External current (e^-) is driven by a gradient in electochemical potential of electrons in dissimilar metals (denoted by different colored electrodes). Electrons are liberated at the anode (on the left) via an oxidation reaction. The electrolyte is ion conducting but electrically insulating, forcing electrons through an external circuit where they can be used to do work. Finally, ions are reduced at the cathode (on the right).

Compared to liquid-based electrolytes, polymer electrolytes offer several key advantages that have motivated almost four decades of research. (i) Polymer electrolytes eliminate the need for small molecule, volatile solvents, thus avoiding issues of electrolyte leakage and the associated safety concerns of combustible vapors. For example, a common commercial lithium ion (Li-ion) battery electrolyte is $LiPF_6$ dissolved in organic solvents such as ethylene and propylene carbonate, which pose a fire hazard due to their volatility and combustibility.

(ii) Polymer electrolytes can exhibit intrinsic mechanical integrity, enabling an all-solid-state design. At a minimum, a solid electrolyte layer can physically separate the electrodes without the need for additional support.[7] Current batteries rely on a microporous polyolefin (typically polyethylene and/or polypropylene) layer to prevent electrode contact, and the liquid electrolyte resides in the pores. However, the polyolefin separator fills *ca.* 40% of the volume between the electrodes,[7] effectively wasting volume that could be used by the electrolyte. Furthermore, solid electrolytes

can be processed into thin films (on the order of a few microns or less, as compared to tens of microns for current separators), thus reducing internal resistance (which is proportional to thickness). From a processing perspective, a solid-state design simplifies manufacturing because electrolyte leakage is not a concern.

(iii) Finally, certain electrochemical devices pose application-specific challenges that mechanically or thermally robust electrolytes could address. For example, anhydrous fuel cells could hypothetically operate well above 100 °C to minimize poisoning of the platinum catalyst, but would require a polymer electrolyte with long-term creep resistance.[8] Similarly, the energy density of Li-ion batteries could be increased by a factor of 10 if a lithium metal anode were used in lieu of a graphite-based intercalation host anode. However, lithium metal anodes are not compatible with liquid electrolytes,[9,10] and requires a glassy (modulus $G \approx 1$ GPa) electrolyte to prevent growth of lithium metal dendrites,[5,11–14] one of the main causes of battery failure.[15] The modulus cannot be increased at the expense of conductivity, however, as Li-ion batteries must exhibit conductivity $\geq 10^{-3}$ S/cm to be commercially viable.[16] Motivated by these reasons, among others, the polymer electrolyte community has pursued a wide range of applications,[17] including electrochemical energy storage and conversion devices, such as batteries,[16,18–20] fuel cells,[8,21] and photovoltaics,[22] as well as organic gate dielectrics for flexible, thin-film transistors.[23–26]

Independent of the specific application, however, the universal goal is to develop a high conductivity polymer electrolyte that simultaneously satisfies an orthogonal mechanical or thermal property (*e.g.*, high modulus, elasticity, toughness, long-term creep resistance, or high temperature stability). The crux of the challenge is that flexible, low glass transition temperature (T_g) polymers such as poly(ethylene oxide) (PEO, $T_g \approx -60$ °C) are best-suited to exhibit high conductivity, but offer little in the way of inherent mechanical robustness. Similarly, high T_g polar thermoplastics such as poly(methyl methacrylate) (PMMA, $T_g \approx 120$ °C) readily mix with some

salts and offer superior mechanical robustness, but the glassy polymer matrix cripples ionic conductivity for most relevant operational temperatures. Attention has therefore been focused on composite materials that can simultaneously exhibit both high conductivity and excellent mechanical properties.

Before proceeding, however, the next section will provide a primer on ionic conductivity, which is a central theme of this thesis but is less common than many of the polymer characterization techniques discussed. Following that, the remainder of this chapter will provide a literature overview of polymer electrolyte research.

1.2   Ionic Conductivity

This section will provide some detail on how conductivity is defined and how it fits into the larger scheme of mass transport, as well as some context on which parameters and equations are most relevant in the design of polymer electrolytes. Newman[27] has an excellent discussion of electrochemical systems in general, and the reader is referred to his text for a more thorough treatment of the ideas presented here.

1.2.1   Derivation of Conductivity

The conductivity, σ, of an electrolyte solution is a simple, intuitive parameter characterizing the key property of interest: the transport rate of ions. However, conductivity is only rigorously defined under a particular set of conditions, and this section will develop the ideas around which experiments that measure conductivity (*e.g.*, impedance spectroscopy) are designed. Ions in solution are subject to the same forces that drive the overall flux of neutral species (*e.g.*, convective flow or gradients in concentration), but with the additional consideration that they migrate under the influence of an external electric field. In general, the flux, $\mathcal{J}$, of species j is proportional to spatial

gradients in electrochemical potential, $\bar{\mu}_j$.[i]

$$\boldsymbol{\mathcal{J}_j} \sim -\nabla\bar{\mu}_j \tag{1.1}$$

The electrochemical potential includes both the influence of an electric potential, Φ,[ii] on the Gibbs free energy of ions, in addition to the chemical potential for neutral species, μ_j.

$$\bar{\mu}_j = \mu_j + z_j\mathfrak{F}\Phi \tag{1.2}$$

In eq 1.2, z_j is the integer charge of an ion. $\mathfrak{F}$ ($= eN_A$) is Faraday's constant, and gives the total charge of a mole of unit charges, where e is the charge of one electron and N_A is Avogadro's number. $z_j\mathfrak{F}$ is therefore the molar charge of ion j.

In the limit of infinite dilution, the chemical potential reduces to a gradient in concentration, ∇c_j. In practice, of course, dilute solutions are not often used in electrochemical devices, which seek to maximize conductivity with concentrated electrolyte solutions. However, the equations for dilute solutions are useful because they provide a framework to understand the factors that influence conductivity. The total flux of species j in solution (charged or neutral) can therefore be written

$$\boldsymbol{\mathcal{J}_j} = -\underbrace{D_j\nabla c_j}_{\text{diffusion}} - \underbrace{u_jz_j\mathfrak{F}n_j\nabla\Phi}_{\text{migration}} + \underbrace{c_j\mathbf{v}}_{\text{convection}} \tag{1.3}$$

The diffusion term applies to both charged and neutral species, and defines an important transport property, the diffusivity D_j, which gives the proportionality between a concentration gradient driving force and the flux. The migration term in eq 1.3 is unique to charged species, as they experience a force when acted on by an external electric field, $\nabla\Phi$. The electric field, in turn, is simply the gradient of the electric

---

[i]The subscript j is used to denote individual species to avoid confusion with the symbol used for flux of current, $\mathbf{i}$, as well as the imaginary number $\sqrt{-1}$.

[ii]Electric potential is a scalar quantity defined as the electric potential energy of a unit charge, with units of volts, V. The term "voltage" refers to the electric potential difference between two points in space.

potential. The variable n_j is used to represent the concentration of dissociated ions, which is almost always less than the concentration of salt added to the solution, c_j. At equilibrium, some fraction of the salt exists as dissociated, free ions, and the remainder exist as neutral ion pairs (or larger aggregates), which do not experience an electric force. Only dissociated ions contribute to the measured current. Eq 1.3 defines another transport property, the ion mobility, u_j, which gives the proportionality between the electric force and ion flux when the accelerating force of the electric field is balanced by the viscous drag of the medium. Finally, the convection term represents flux by bulk motion of the fluid.

In electrolyte solutions, the pertinent measure of flux is the ionic current, $\mathbf{i}$, which is simply the sum of the flux of all charged species.

$$\mathbf{i} = \mathfrak{F} \sum_j z_j \boldsymbol{\mathcal{J}_j} \tag{1.4}$$

Combining the general flux equation (eq 1.3) with the definition of current (eq 1.4) gives the expression for the total ionic current in an electrolyte solution.

$$\mathbf{i} = -\mathfrak{F}^2 \nabla \Phi \sum_j u_j z_j^2 n_j - \mathfrak{F} \sum_j D_j z_j \nabla c_j + \mathfrak{F} \mathbf{v} \sum_j z_j c_j \tag{1.5}$$

In the bulk solution (far from the electrodes), the solution is electrically neutral, which demands that the summation in the convection term equal zero. That is, even if bulk fluid motion is present, no current can be carried because the fluid does not carry a net charge. If the diffusion term can be eliminated (for example, by experimental design, as will be discussed below), then the ionic current is due entirely to the migration term. The non-driving force terms can then be combined to define the conductivity, σ, as

$$\sigma = \mathfrak{F}^2 \sum_j u_j z_j^2 n_j \tag{1.6}$$

Conductivity is therefore a single parameter that conveniently summarizes the proportionality between the applied electric field and the measured current.

$$\mathbf{i} = -\sigma \nabla \Phi \tag{1.7}$$

Eq 1.7 is an expression of Ohm's law and predicts that for a given applied electric field (in the limit of a dilute solution and in the absence of concentration gradients), the magnitude of the measured current increases with increasing conductivity.

It is sometimes more intuitive to think of conductivity in terms of the diffusion coefficient, rather than mobility. The Nernst-Einstein equation provides the relationship between these two transport properties.[28]

$$u_j = \frac{D_j}{RT} \tag{1.8}$$

Here, R is the gas constant and T is absolute temperature. Substituting the rhs of eq 1.8 for u_j in eq 1.6 gives

$$\sigma = \frac{\mathfrak{F}^2}{RT} \sum_j D_j z_j^2 n_j \tag{1.9}$$

Eq 1.9 is arguably one of the most important equations to consider when designing polymer electrolytes. It must be emphasized, though, that it will not likely be quantitatively correct, as most real-world systems comprise concentrated electrolyte solutions. Nonetheless, the following scaling relationship remains useful:

$$\sigma \sim (\text{mobility or diffusivity}) \times (\text{net charge})^2 \times (\text{number of ions}) \tag{1.10}$$

Conductivity increases with higher diffusion coefficient or mobility, higher net ion charge (whether positive or negative), and an increasing number of dissociated ions. These parameters must be tuned and optimized to meet the needs of a particular application, as most devices require some minimum value of conductivity to be commercially viable.

Returning briefly to the general expression for σ (eq 1.9), the summation over all species j leads to an important concept in polymer electrolytes: the transference number, t_j,[iii] which is the fraction of total current carried by each species.

$$t_j = \frac{u_j z_j^2 n_j}{\sum_k u_k z_k^2 n_k} \tag{1.11}$$

Eq 1.11 predicts that ions with higher mobility or net charge contribute more to the measured current. Returning to the example of Li-ion batteries, one seeks to maximize the transference number of the pertinent electroactive species, Li^+, to maximize the external electrical current. This is one of the key challenges posed by polymer electrolyte-based Li-ion batteries, because anions in Li-based salts often migrate 3–10 times faster than Li^+, so t_{Li^+} can be as low as 0.1–0.3.[29,30] For commercial viability, Li-ion batteries should exhibit conductivity of Li^+, σ_{Li^+}, of at least 10^{-4} S/cm.[16] Taking the lower limit of $t_{Li^+} = 0.1$, the total measured conductivity (which includes current due to anions) should be $\geq 10^{-3}$ S/cm, which is the metric often cited by the Li-ion battery community.[16]

1.2.2   Temperature Dependence of Conductivity

Temperature is one of the most important parameters to consider when designing polymer electrolytes because it has a profound impact on the conductivity and is relatively easy to modulate. The general definition of conductivity (eq 1.9) is reproduced below, explicitly showing the parameters that exhibit temperature dependence.

$$\sigma(T) = \frac{\mathfrak{F}^2}{RT} \sum_j D_j(T) z_j^2 n_j(T) \tag{1.12}$$

The parameters n_j and D_j are both functions of T, so the net temperature dependence of σ will depend on the balance between (i) RT, (ii) $n_j(T)$, and (iii) $D_j(T)$.

[iii]The variables t_+ and t_- are also used when only one type of cation and anion are present.

(i) Thermal energy (RT) reduces conductivity because the corresponding increase in thermal fluctuations of the solvating medium lowers mobility of the ions.

(ii) Electrochemical devices typically use strong electrolytes, which are fully (or almost fully) ionized. However, because the salt concentration used is almost always higher than the dilute limit, some fraction of ions associate to form solvated pairs that are effectively net neutral.[31,32] This is related to the problem of calculating the activity of a strong electrolyte solution, as formalized by Debye, Hückel, and Onsager.[33] At a given T, equilibrium exists between dissociated cations, M^+, and anions, X^- (both of which contribute to current), and neutral ion pairs,[iv] MX (which do not contribute to current).

$$MX \xrightleftharpoons{K_d} M^+ + X^- \tag{1.13}$$

The equilibrium dissociation constant, K_d, is most generally defined by the Boltzmann probability distribution, in terms of the change in Gibbs free energy, ΔG_d, when the ions in a neutral pair are moved infinitely far apart.[31]

$$K_d = \exp\left(\frac{-\Delta G_d}{RT}\right) \tag{1.14}$$

In practice, the ions need only be far enough apart that the dielectric medium effectively screens the Coulombic interactions, and the attractive potential between oppositely-charged species is of comparable magnitude to RT (*i.e.*, the Bjerrum length).[34] The potential of the neutral ion pair is proportional to the lattice energy of the ionic solid. As a result, high lattice energy (high T_m) salts have a lower thermodynamic drive to dissociate, and equilibrium lies on the side of neutral ion pairs. If the lattice energy is too high, the ionic solid will not dissolve at all. The identity of the dielectric medium factors into eq 1.14 through the relative permittivity, ϵ_r.[v]

[iv]Larger aggregates also exist, but will be ignored for this qualitative treatment.
[v]The frequency-independent plateau (typically somewhere in the frequency range from 1 kHz–1 GHz) in the real part of relative permittivity is also known as the dielectric constant, but in general ϵ_r is not a constant.

Salts in high ϵ_r media such as water tend to dissociate, as the Coulombic potential is screened over relatively short length scales, relative to nonpolar (often organic) media of low ϵ_r. The resulting temperature dependence of the number density of dissociated ions, n_j, takes an Arrhenius form, where E_{eff} is related to the free energy barrier to ion dissociation.

$$n_j(T) = n_0 \exp\left(\frac{-E_{\text{eff}}}{RT}\right) \tag{1.15}$$

Eq 1.15 predicts that n_j approaches the number density of the fully dissociated salt, n_0, in the limit that the Coulombic interaction between oppositely-charged ions goes to zero, or as T approaches infinity. The slope, E_{eff}/R, of $\ln(n_j)$ plotted versus $1/T$ contains information about the Coulombic potential between ions in a given medium.[28,35]

Electrolyte solutions are typically modeled as discrete charged species in a dielectric continuum. Ionic liquids—salts that melt at low temperature and are often liquid at ambient conditions—appear to violate this assumption, as all species are charged. Interestingly, Gebbie et al.[35] recently used force-distance measurements and found that the equilibrium fraction of dissociated ions in the ionic liquid 1-butyl-3-methylimidazolium bis(trifluoromethylsulfonyl)imide (BMITFSI) is lower than 0.1%. Hunt et al.[36] had previously used electronic structure calculations to show that the attractive potential between BMI$^+$ and TFSI$^-$ is *ca.* $130kT$, yielding an anticipated K_{d} within 10% of the experimental value measured by Gebbie et al. A physical interpretation of this result is that ionic liquids behave in some sense simply like low ϵ_r media, in that they do not screen charges over short length scales. In contrast, a number of reports—for example, by Sangoro et al.[37,38] and Tokuda et al.[39]—have measured the fraction of charge-carrying ions during transport experiments, which is more pertinent for electrochemical device applications. In these studies, the authors compared the ion diffusion coefficient measured with impedance spectroscopy (which only probes free ions) to measurements of diffusion in pulsed-field gradient
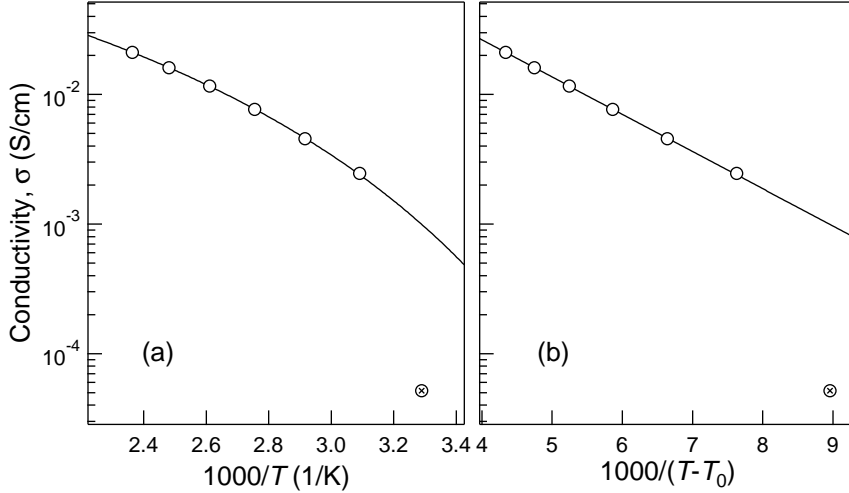
Figure 1.2: Comparison of (a) Arrhenius and (b) Vogel-Fulcher-Tammann (VFT) plots of ionic conductivity of a poly(ethylene oxide)/ionic liquid blend. Crossed circles were at temperatures below $T_{m,PEO}$ and were not included in the fits. In (b), $T_0 = 193$ K. The data are linear when the temperature axis is scaled by the Vogel temperature, T_0, corroborating that conductivity is limited by the available free volume in the conducting matrix.

NMR spectroscopy experiments (which probes all diffusing species with the appropriate nucleus), and found the charge-carrying ion fraction to be as high as 50–85%. The authors also experimentally determined that $n_j(T)$ of the ionic liquids followed the expected effective Arrhenius dependence. The large discrepancy between the results of the transport experiments and that of Gebbie et al. is interesting, although the two experiments should not necessarily yield the same result. The difference likely stems from the fact that the force-distance experiment measured the equilibrium value of n_j. In contrast, the transport experiments measured a system *en route* to equilibrium, as ions were migrating under an external potential.

(iii) For glass-forming liquids such as polymers, the dominant T-dependent term in the vicinity of the glass transition temperature is $D_j(T)$. In particular, ion transport is limited by the available free volume in the polymer/salt matrix, which in turn limits segmental relaxation of polymer chains. It is this local chain relaxation that is strongly dependent on the temperature interval above the T_g.[3,40] As the T_g is

approached from high T, the timescale of chain relaxation appears to diverge to infinity. As a result, polymer electrolyte conductivity data asymptotically approach zero as T_0 is approached, and exhibit curvature on an Arrhenius plot (see Figure 1.2). The data are therefore modeled by the Vogel-Fulcher-Tammann (VFT) equation:[41]

$$\sigma(T) = \sigma_0 \exp\left(\frac{-B}{T - T_0}\right) \tag{1.16}$$

In eq 1.16, σ_0 is related to the concentration of mobile charges and can be thought of as the asymptotic conductivity at very high T. B is a pseudo-activation energy related to the local, primarily entropic barrier to motion. T_0 is the temperature at which conductivity asymptotically approaches zero. The physical origin of T_0 is related to T_g, and T_0 is sometimes found to be *ca.* 50 °C below T_g,[42] although the exact interval varies. In any case, T_0 is always lower than T_g because the polymer is not completely immobile at the T_g, and T_0 represents the extrapolated temperature at which ion motion is frozen in a glassy polymer matrix.

The VFT behavior of polymer electrolyte conductivity is one of the key factors determining the choice of polymer. Flexible polymers with T_gs well below the practical operating temperatures of polymer electrolytes (typically room temperature and above) substantially increase conductivity relative to high T_g, glassy polymers. For example, PEO ($T_g \approx -60$ °C) and PMMA ($T_g \approx 120$ °C) are both polar polymers capable of mixing with salts such as ionic liquids, but PEO-rich electrolytes exhibit higher conductivity than an analogous PMMA-based system of equal polymer concentration. The trade-off in the design of polymer electrolytes is that flexible polymers offer little in the way of mechanical robustness, whereas high T_g polymers exhibit conductivity too low for practical applications.

Combining the T-dependence of RT, n_j, and D_j, eq 1.17 and Figure 1.3 summarize the net functional form experimental polymer electrolyte conductivity should take.

$$\sigma(T) \sim \frac{1}{T} \exp\left(\frac{-B}{T - T_0} - \frac{E_{\text{eff}}}{RT}\right) \tag{1.17}$$
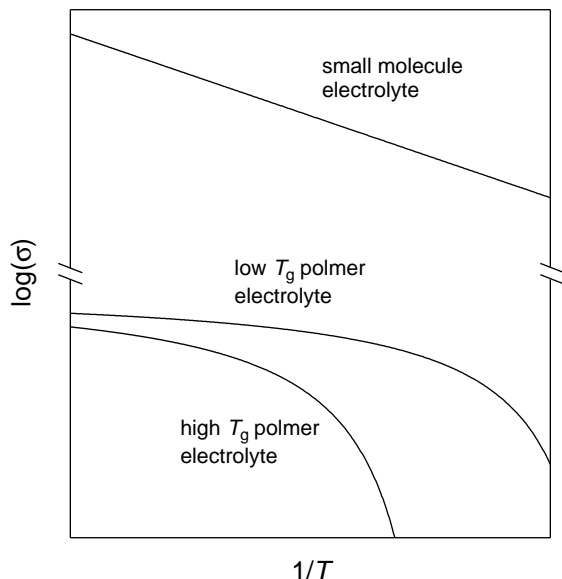
Figure 1.3: Comparison of the T-dependence and magnitude of conductivity for electrolytes based on small molecule solvents versus polymers. Note the break in the vertical axis, as the conductivity of small molecule solvent electrolytes is several orders of magnitude higher than polymer electrolytes at a given T.

In the vicinity of the T_g, the VFT term in eq 1.17 dominates, but at temperatures far above the T_g (the exact value depends on the relative magnitudes of the prefactors), the data will be approximately linear on an Arrhenius plot. In this case, the effect of free volume limitations plateaus, and the Arrhenius dependence of n_j takes over.

To put the temperature scaling of polymer electrolyte conductivity into context, conductivity data for small-molecule electrolyte solutions (*e.g.*, $LiClO_4$ in water) follow a straight line on an Arrhenius plot. In this case, the dominant T-dependent term is $n_j(T)$. In contrast to polymers, the diffusivity of ions in water is not a strong function of T, and typically obeys the Stokes-Einstein equation.[28]

$$D(T) = \frac{kT}{a\pi\eta R_\text{h}} \tag{1.18}$$

Here, a is a constant ($= 6$ for the no-slip boundary condition), η is the viscosity of water, and R_h is the hydrodynamic radius of the diffusing species (*e.g.*, dissociated

Table 1.1: Comparison of the conductivity of various electrolytes at 25 °C

system	conductivity (mS/cm)	ref
1 M NaCl in water	86	43
EMITFSI	9	44
LiClO$_4$ in PPO	0.01	3

ions or neutral ion pairs, which would each diffuse according to a characteristic R_{h}). The slope of $D(T)$ is actually steeper than eq 1.18 would suggest, as η decreases with increasing T. However, the viscosity of water only decreases by *ca.* 80% (from 1.8 to 0.3 mPa·s) over the liquid temperature range,[45] so the T-dependence of D is negligible compared to $n_j(T)$. As a final comment to highlight a key difference between polymer and aqueous electrolytes, the conductivity of aqueous electrolytes is orders of magnitude higher than in polymer electrolytes (see Table 1.1). This, of course, is a reflection of the orders of magnitude difference in viscosity.

1.2.3 Experimental Considerations

The conductivity of dielectrics is not directly measured, but rather is calculated from measurements of resistance. As alluded to earlier, one of the primary experiments used to determine conductivity of polymer electrolytes is impedance spectroscopy.[vi] In general, direct current (DC) experiments are not used, as the response to a step change in voltage would be current that quickly decays to zero. Although the same information can be extracted from this hypothetical experiment, as will be shown, it is more useful to apply periodic oscillations of voltage (*i.e.*, an alternating current, or AC, experiment) to probe a wide range of frequency-dependent behavior. Impedance spectroscopy can be thought of by analogy to a more common polymer characterization experiment: measurements of linear viscoelasticity by oscillatory rheology.

[vi]Impedance spectroscopy falls under the broader scope of dielectric spectroscopy, for which the book by Kremer and Schönhals[41] is an excellent reference.
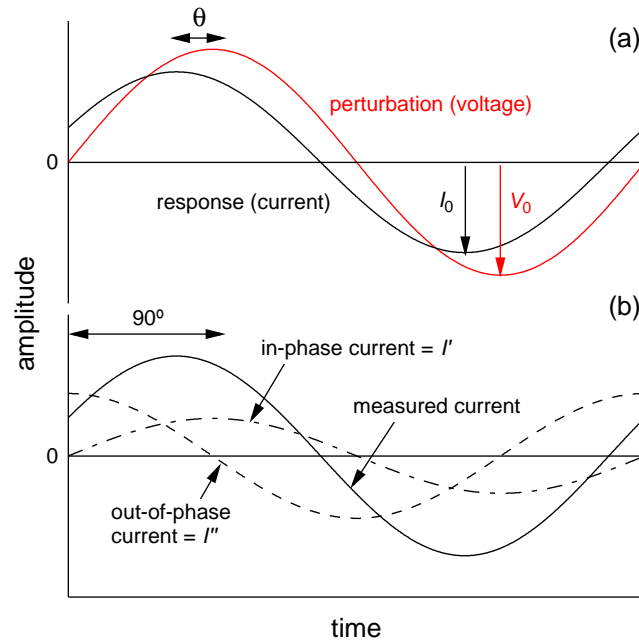
Figure 1.4: (a) Impedance spectroscopy experiments measure the phase shift between a sinusoidally varying input (voltage) and output (current). The impedance analyzer sweeps over a range of frequency, f_{AC}, with voltage amplitude V_0, and the resulting current has amplitude I_0 and is shifted in phase by angle θ. (b) The measured current is resolved into in-phase and out-of-phase components. Per eq 1.21, the two dashed lines sum to give the total measured current (solid line).

In rheology, the input is a sinusoidally varying deformation, and the output is the measured stress induced in the material. As shown in Figure 1.4(a), the input in an impedance spectroscopy experiment is a sinusoidally varying voltage,

$$V(t) = V_0 \sin(\omega t) \tag{1.19}$$

If the experiment is performed within the linear response regime,[vii] the output is the total measured current, which is simply shifted in phase (by angle θ) and

[vii]Linearity of the response should be verified by performing voltage amplitude sweeps at several values of frequency.

amplitude from the voltage.

$$I(t) = I_0 \sin(\omega t + \theta) \tag{1.20}$$

Here, V_0 and I_0 are the amplitude of voltage and current, respectively, t is time, and ω is the angular frequency, given as $\omega = 2\pi f_{AC}$, where f_{AC} is the electric field oscillation frequency in Hz. As shown in Figure 1.4(b), the measured current can then be resolved into components that are in-phase and 90° out-of-phase with the applied voltage,

$$I(t) = I_0' \sin(\omega t) + I_0'' \sin\left(\omega t + \frac{\pi}{2}\right) \tag{1.21}$$

I_0' and I_0'' are the amplitudes of the in-phase and out-of-phase dashed lines shown in Figure 1.4. Per Ohm's law, the frequency-dependent resistance, or impedance, can be calculated at any t as

$$Z^*(\omega) = \frac{V^*(\omega)}{I^*(\omega)} \tag{1.22}$$

Z^* is a complex number given by $Z' + iZ''$, where $i = \sqrt{-1}$.[viii] The magnitude of Z^* is given by

$$|Z^*| = \left[(Z')^2 + (Z'')^2\right]^{\frac{1}{2}} = \frac{V_0}{I_0} \tag{1.23}$$

The in-phase and out-of-phase current can therefore be represented in terms of the applied voltage and the impedance.

$$I(t) = \frac{V_0}{Z'} \sin(\omega t) + \frac{V_0}{Z''} \sin\left(\omega t + \frac{\pi}{2}\right) \tag{1.24}$$

Physically, $Z'(= V_0/I_0')$ is proportional to the resistive, energy-dissipating response of the material, and $Z''(= V_0/I_0'')$ is a measure of the capacitive, energy-storing reponse. In this respect, the physical interpretation of Z' and Z'' is opposite that of the dynamic mechanical moduli, G' and G'', but similar to that of the real and imaginary

---

[viii]The complex notation used in eq 1.22 is equivalent to the trigonometric notation per Euler's formula: $e^{ix} = \cos(x) + i\sin(x)$.
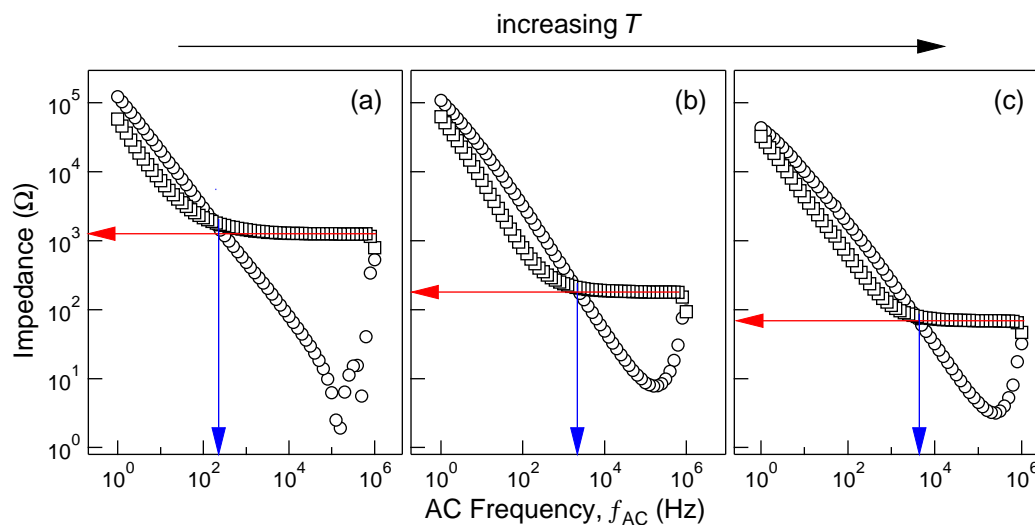
Figure 1.5: Representative raw impedance data collected at various temperatures. Squares ($\square$) are Z', circles ($\bigcirc$) are Z''. The red line denotes the bulk resistance, R, used to calculate conductivity per eq 1.31. The blue line denotes the timescale for the formation of an electrical double layer (EDL), $\tau_{EDL} = 1/f_{AC}$, at the electrode/electrolyte interface, which corresponds to the crossover of Z' and Z''.

components, η' and η'', of the complex viscosity.

Figure 1.5 is an example of raw impedance data for an electrolyte comprising a mixture of ionic liquid (a low T_m salt) and poly(ethylene oxide). The applied voltage oscillates over a wide AC frequency range, f_{AC} (*e.g.*, sweeping f_{AC} from 1 MHz to 1 Hz is typical). As shown schematically in Figure 1.6, ions respond to the electric field by migrating toward the oppositely-charge electrode. In the limit of a DC field ($f_{AC} \rightarrow 0$), ions form an electric double layer (EDL) at the oppositely-charged electrode to neutralize the electric field, leaving the bulk electrolyte charge neutral. Note that the schematic in Figure 1.6 over-simplifies the physical picture of the EDL, but in general, the competition between charge neutralization and the entropic drive for ions to explore space results in a diffuse layer over which the applied potential is neutralized.
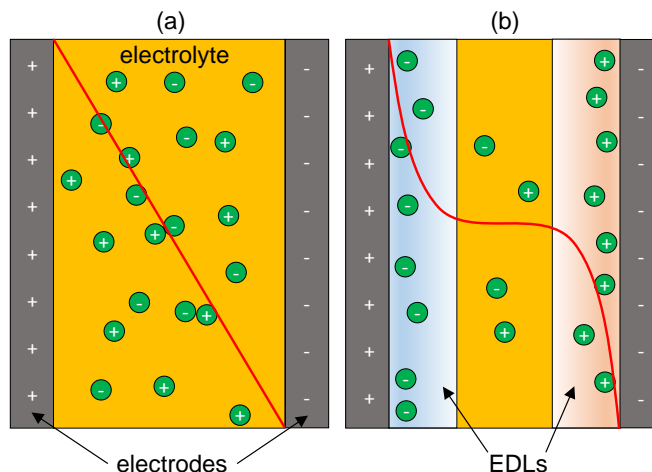
Figure 1.6: Schematic of the electrical double layer. (a) When a DC electric field (denoted by the red line) is first applied, cations and anions are distributed throughout the electrolyte. (b) After some time (or in the case of an impedance spectroscopy experiment, $f_{AC} < f_{EDL}$), ions have migrated to the oppositely-charged electrode. The resulting electrical double layers (denoted by the blue and red regions) neutralize the electric field over some length scale.

During the course of the frequency sweep, ions continue to form an EDL at frequencies lower than some characteristic frequency, f_{EDL}, or equivalently, some characteristic timescale, $\tau_{EDL} = 1/f_{EDL}$. The exact value of f_{EDL} is a reflection of the rate at which ions migrate in solution, that is, the conductivity. At frequencies higher than f_{EDL}, ions do not have sufficient time to form an EDL before the polarity switches, so concentration gradients do not develop at the electrodes. Therefore, for $f_{AC} > f_{EDL}$, the diffusion term in eq 1.5 can be ignored. Physically, the plateau in Z' at $f_{AC} > f_{EDL}$ corresponds to the bulk resistance, R, of the electrolyte. In the mathematical framework described above, $Z' \to R$ in the limit that $\theta \to 0$; that is, all of the measured current is in phase with the applied voltage. Physically, ions exhibit higher mobility as T increases, so higher frequencies are required to prevent buildup of ions at the electrodes (hence the shift of the blue line to the right from (a) to (c) in Figure 1.5).

In practice, however, concentration gradients play a major role in electrochemical devices. In Li-ion batteries, for example, anions typically to migrate 3–10 times faster than Li$^+$. The resulting EDL at the positive electrode reduces the magnitude of the

electric field between the electrodes, thus reducing the driving force for Li^+ migration. This problem, known as electrode polarization, drives the study of single-ion conductors, in which the anion is fixed to a polymer backbone, such that only Li^+ is free to migrate.[29,46,47] On the other hand, the formation of EDLs can be beneficial. Referring again to Figure 1.6, the two EDLs can be employed as two energy-storing capacitors in series. In the field of printable electronics (*e.g.*, for flexible e-ink displays), ions gels—crosslinked polymer networks swollen with ionic liquid—have shown outstanding performance as gate insulators in organic thin-film transistors.[23–25,48] Here, the advantage of an ion gel is that it requires lower voltage ($\mathcal{O}(1)$ V) than the more traditional silicon dioxide-based gate dielectric ($\mathcal{O}(10)$ V), although the switching speeds can be substantially slower.

Once the bulk resistance of a polymer electrolyte is known from an impedance spectroscopy experiment, the conductivity can be calculated using the sample geometry (Figure 1.7). The following derivation treats the experiment as if a DC voltage of magnitude V_0 is applied, so it is important to remember that it only applies in the high-frequency limit, where $Z' \to R$. The sample cell is designed such that the electrodes are planar and parallel to one another, so the electric field lines are linear and orthogonal to the electrodes (ignoring minor edge effects). The gradient operator in eq 1.7 can be therefore evaluated in one dimension, say the x direction.

$$i_x = \sigma \frac{d\Phi}{dx} \tag{1.25}$$

Note that it is the magnitude of current that is of interest, so the negative sign has been dropped. Furthermore, i_x is, strictly speaking, the current density (*i.e.*, current per unit area). This detail was not mentioned in the earlier derivation, but will be used shortly. Integration proceeds as follows.

$$\int_0^l i_x dx = \int_0^{V_0} \sigma d\Phi \tag{1.26}$$
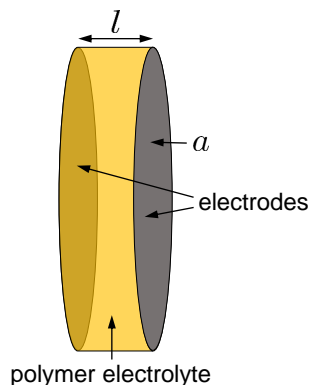
Figure 1.7: Schematic of the geometry commonly used to measure the conductivity of polymer electrolytes. Once the bulk resistance, R, is known from impedance experiments, the sample thickness, l, and superficial area, a, are used to calculate conductivity per eq 1.31.

$$i_x l = \sigma V_0 \tag{1.27}$$

The measured variable is actually the total current, I_x, which equals the current density times the total sample area, $i_x a$. Both sides of the equation are thus multiplied by the area, a, of the sample.

$$i_x l a = \sigma V_0 a \tag{1.28}$$

$$I_x l = \sigma V_0 a \tag{1.29}$$

Collecting terms,

$$\frac{I_x}{V_0} = \frac{\sigma a}{l} \tag{1.30}$$

The lhs is simply $1/R$, per Ohm's law, where R is the bulk resistance extracted from the high frequency plateau in the real part of impedance, Z' (see Figure 1.5). Conductivity can therefore be calculated as

$$\sigma = \frac{l}{Ra} \tag{1.31}$$

Eq 1.31 is the expression for conductivity commonly cited in the literature, but it is important to remember the assumptions under which it is derived, namely the

absence of concentration gradients. The units of eq 1.31 are $1/(\Omega \times \text{length})$, although conductivity is more commonly reported as S/cm, where the unit of siemens (S) is defined as $1/\Omega$. If the geometry is not planar or is otherwise difficult to characterize, the sample cell can be calibrated using a standard of known conductivity, and the measured resistance used to calculate a cell constant, κ. Rearranging terms, conductivity is then calculated as

$$\sigma = \frac{\kappa}{R} \tag{1.32}$$

Eqs 1.31 and 1.32 both serve the same purpose, namely to transform an extensive property (resistance) into an intensive property (conductivity) that can easily be compared between systems.

1.3   Polymer Electrolytes

The field of polymer electrolytes began in the mid-1970s with the observations by Fenton et al.[49] and Wright et al.[50] that certain polar polymers are capable of dissolving high melting temperature (T_m) salts. Several years after polymer electrolytes were first reported, Armand et al.[51,52] first characterized the conductivity of several polymer/salt mixtures, primarily comprising high T_m salts based on Li and Na (*e.g.*, $LiCF_3CO_2$ and $NaBF_4$) dissolved in PEO or PPO. Perhaps the most important result of that pioneering work was the realization that polymer electrolytes could potentially be used in Li-ion batteries. Interestingly, the authors concluded with the suggestion that a key feature of entangled linear chain polymer electrolytes would be their ability to flow and conform to the surface of electrodes. The authors perhaps did not envision the need for solid-state (especially high modulus) polymer electrolytes. This point also necessitates a clarification of jargon used in the polymer electrolyte literature. One often encounters reports on "solid" polymer electrolytes, especially in the early literature from the 1980s. However, "solid" is sometimes simply used to mean "solvent-free". Such systems simply comprise highly entangled linear chain polymers,
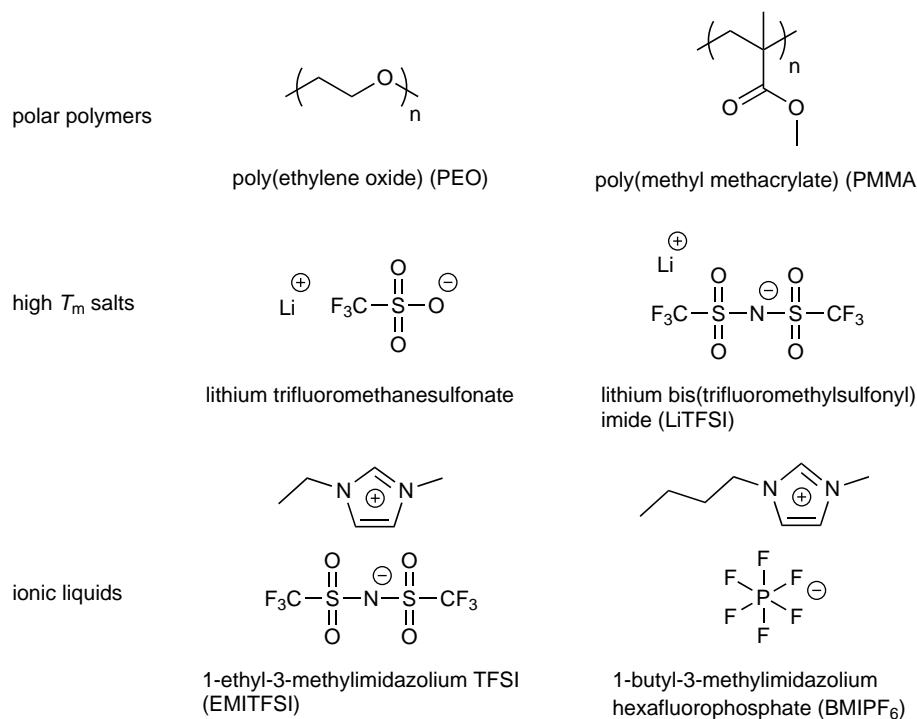
Figure 1.8: Examples of polymer electrolyte constituent species.

and as such do not flow on the experimental timescale of interest. The focus in this thesis is true solid-state polymer electrolytes, which exhibit both a persistent solid structure and an elastic response (in the sense that $G' > G''$) over all frequencies.

The first three decades of polymer electrolyte research focused primarily on high T_m salts. More recently, there has been considerable interest in mixing polymers with ionic liquids (ILs),[53–56] which are defined as salts that melt below 100 °C, although many are liquid at room temperature.[44,57–59] Broadly speaking, the two classes of polymer electrolytes (*i.e.*, high T_m salt- versus IL-based) are similar in many respects, although there are key differences, which will be highlighted when necessary.

Figure 1.8 shows examples of two common ILs. A common feature among many ILs is bulky, asymmetric ions, which frustrate the ordered packing required for crystallization. However, strong Coulombic interactions between oppositely-charged species

are still present, so ILs exhibit negligible vapor pressure and, as such, are not combustible. In the context of electrochemical devices, ILs exhibit a wide window of electrochemical stability (often > 4 V),[60] which means they are typically not electroactive. Instead, they are candidates as non-volatile solvents in electrochemical devices, for example, replacing the volatile organic solvent ethylene carbonate in Li-ion batteries.[61–64] Alternatively, the wide electrochemical stability window of ionic liquids can be utilized for applications such as gate dielectrics for thin film transistors, where electron transfer should not take place at the electrolyte/electrode interface.[23–25,48]

Even outside the scope of the conductive behavior of ILs (which polymer electrolytes rely on) mixtures of polymers and ILs exhibit fascinating and potentially market-disruptive properties. For example, certain ILs preferentially solvate CO_2, and solid-state polymer/IL thin films can passively separate CO_2 from mixed gas streams,[26,65,66] which are produced when burning coal and oil in municipal power plants. These alternative applications will not be discussed further in this thesis, of course, but they nonetheless help to put the electrolyte applications of ILs into a broader context.

1.3.1 Dissolution and Transport of Ions

Mixing polymers and salt (high T_m or ILs) is a thermodynamically downhill process, that is, $\Delta G_{\text{mixing}} = \Delta H_{\text{mixing}} - T\Delta S_{\text{mixing}} < 0$. In the case of high T_m salts, the resulting mixtures display interesting composition- and temperature-dependent crystalline phase behavior,[1,2,67] although for most practical applications, a low T_g, fully amorphous phase of polymer and salt is desired.[ix] Similarly, polymer/IL mixtures can exhibit traditional liquid-liquid phase behavior, such as upper and lower critical solution temperatures,[54] so the potential operating conditions must be considered when designing polymer electrolytes based on ILs. To contrast polymer electrolytes

---

[ix]It has been demonstrated that Li^+ can rapidly shuttle within channels defined by crystalline PEO,[68] but this class of polymer electrolytes will not be further considered here.

with traditional aqueous systems, water is a virtually universal solvent for ionic solids because it exhibits high relative permittivity ($\epsilon_r \approx 80$) and shields Coulombic interactions between dissociated ions that would induce aggregation. The entropic drive for ions to explore space then dominates the change in free energy upon mixing. Polar polymers, on the other hand, typically exhibit $\epsilon_r = \mathcal{O}(10)$, and the enthalpic drive for salts to dissociate quite often relies on specific, favorable interactions between the cation and oxygen atoms in the backbone.[69] Additional factors to consider include the lattice energy of the salt, which can overwhelm any entropic contribution to the free energy if it is too high, and the loss of entropy associated with the polymer chain wrapping around the cation.[69]

Given these considerations, it is evident why systems like PEO/LiClO$_4$ are among the most thoroughly-studied polymer electrolytes: (i) Li$^+$ strongly coordinates with the lone electron pairs on oxygen, (ii) the relatively large, monovalent ClO$_4^-$ anion reduces the lattice energy of the salt, and (iii) the low T_g of PEO provides chains the flexibility to wrap around the cation without excessive strain. The specific nature of the interaction between the cation and the polymer ultimately limits the polymer/salt combinations that make effective electrolytes. For example, it was recognized in one of the first polymer electrolyte studies by Armand et al.[51] that the spacing between oxygen atoms in polyethers is crucial: neither $-(\text{CH}_2-\text{O})_n-$ nor $-(\text{CH}_2-\text{CH}_2-\text{CH}_2-\text{O})_n-$ complex with salts, but $-(\text{CH}_2-\text{CH}_2-\text{O})_n-$ does. Similarly, poly(propylene oxide) (PPO) has the appropriate spacing of oxygen atoms, but the methyl side group lowers the maximum salt loading relative to PEO.[1,3]

In contrast to high T_m salts, mixing polymers and ILs can be generally be thought of as mixing miscible liquids. In general, polar polymers such as PEO and PMMA readily mix with many ILs, such as those shown in Figure 1.8, while nonpolar polymers, such as polystyrene and polyolefins, do not mix with ILs. Above the T_m (which, to reiterate, is often below room temperature and can be depressed far lower when
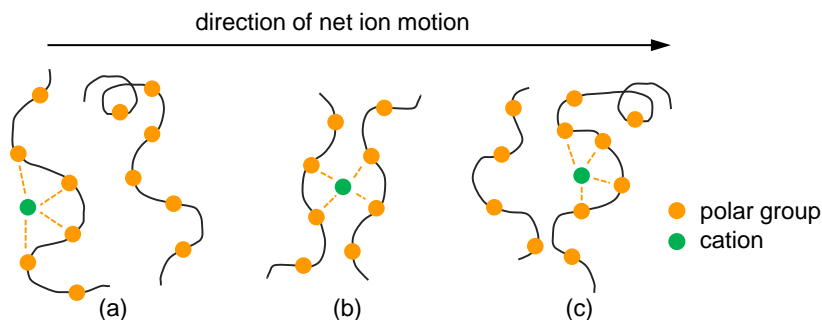
Figure 1.9: Illustration of ion transport of high T_m salts in a polymer matrix. (a) Ions dissolve by virtue of specific interactions between the cation and polar groups in the polymer backbone. (b) Ion migration occurs when random segmental relaxation brings two polymer chains close together, allowing inter-chain coordination with the cation. Long-range ion translation is therefore limited by the segmental relaxation of polymer chains. (c) The cation has been transferred to a new polymer chain. Counter ions are not shown.

mixed with polymers) ILs self-dissociate and thus do not require strong coordination with polar groups in the polymer backbone to dissociate into free ions.[37,39,70] An important result of the lack of strong coordination between ILs and polymers— and a key distinction from polymer electrolyte comprising high T_m salts—is that ion transport is much less coupled to segmental relaxation of the polymer chais. However, it is important to remember that there still exists the relatively strong and long-range[x] ion-dipole attractive potential between the cation and the lone electron pairs of the ether oxygens. Seki et al.[70] clearly demonstrated decoupled ion motion in IL-based electrolytes by comparing conductivity of PEO-*co*-PPO random copolymer/LiTFSI to PMMA/EMITFSI electrolytes of equal salt concentration. PPO was incorporated randomly in the PEO chain at a concentration of 16 mol% to suppress PEO crystallinity and ensure the resulting electrolyte was fully amorphous. Even after correcting for differences in T_g between the two systems, the conductivity of the IL-containing electrolyte was orders of magnitude higher than the Li-containing system.

---

[x]The ion-dipole attractive potential falls off as $1/r^2$, the inverse square of the center-to-center distance between the ion and dipole.

Figure 1.9 demonstrates the mechanism of long-range translation of high T_{m} salts dissolved in a polymer matrix. Net translation requires that the ion be passed from one chain to another and, as such, is governed by segmental relaxation of the polymer chains. Under the influence of an external electric field, there is a preferred direction of net motion, but the kinetics are ultimately limited by the free volume available to the polymer chains, which is proportional to the temperature interval above the T_{g}. Coupling ion motion to polymer local chain dynamics has two practical implications: (i) the magnitude of conductivity is often too low for low T applications, and (ii) conductivity exhibits a maximum as salt concentration is increased.[3,71,72]

Figure 1.10 illustrates the local maximum in conductivity for a PEO/LiClO$_4$ electrolyte reported by Gray.[71] The sharp reduction in molar conductivity, Λ,[xi] at low salt concentration is typical of many strong electrolyte systems, and is a result of increased ion pairing with increasing salt concentration. Gray plotted Λ versus $c^{1/2}$ because the decrease in Λ for small c is modeled by Kohlrausch's law,

$$\Lambda = \Lambda_0 - \mathscr{K} c^{1/2} \tag{1.33}$$

where Λ_0 is the zero concentration limit of molar conductivity and $\mathscr{K}$ is the slope.[xii] The next feature—the local maximum in conductivity—is unique to polymer electrolytes using high T_{m} salts. The physical origin of the local maximum in conductivity is illustrated in Figure 1.9(b), where the ion is complexed with two different polymer chains. The ion acts as a transient crosslink that slows down local chain dynamics, increasing the effective T_{g} of the polymer electrolyte.[3,70] Therefore, at a given experimental T, the temperature interval above the T_{g} decreases with increasing salt concentration, offsetting the increase in conductivity that should accompany an

---

[xi]Molar conductivity is the measured conductivity normalized by the salt concentration.

[xii]Kohlrausch's law is, in turn, a limiting case of the Debye-Hückel-Onsager (DHO) equation, which models the activity of strong electrolyte solutions as a function of ionic strength. The DHO equation provides physical insight—and an analytical prediction—for the slope, $\mathscr{K}$, in Kohlrausch's law.
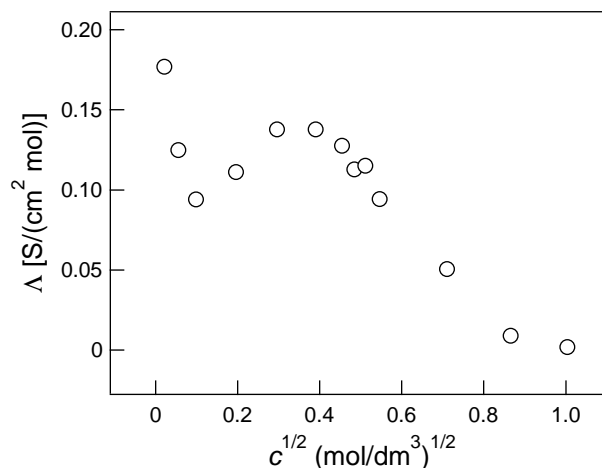
Figure 1.10: Example of the maximum in conductivity observed in polymer electrolytes using high T_{m} salts. The electrolyte comprises PEO ($M = 10^5$ g/mol) and LiClO$_4$ at 25 °C. Λ is molar conductivity, which is the measured conductivity normalized to the concentration of salt added, c. The data were reproduced from ref 71.

increase in the number of ions.

Before proceeding, several practical comments on how salt concentration is reported are in order. In this thesis, salt concentration is typically reported in terms of volume fraction. Samples are prepared gravimetrically, and volume is calculated using reported densities at 140 °C. This choice of temperature is somewhat arbitrary, although one important feature is that all of the polymers of interest, including poly(ethylene oxide) and polystyrene, are amorphous melts at 140 °C. Furthermore, the coefficients of thermal expansion, α, are *ca.* 6×10^{-4} 1/K for all species (including the ionic liquids), so the volume fractions should be approximately constant in the vicinity of 140 °C. Table 1.2 summarizes the pertinent values used to calculate salt concentration in this thesis. Alternatively, salt concentration is often reported in terms of r, which is defined as the molar ratio of either ethylene oxide repeat units to cations, or cations to ethylene oxide repeat units (care should be taken to note how authors define r). The parameter r has the advantage that it is independent of temperature, whereas volume fraction provides a more direct measure of the amount of salt added. Eq 1.34 shows how to calculate r given the volume fraction, v_{salt}, of

Table 1.2: Parameters used to calculate salt concentration

species	M (g/mol)	ρ at 140 °C (g/cm^3)	$\alpha \times 10^4$ (1/K)	refs
poly(ethylene oxide)	44	1.064	5.9	73, 74
polystyrene	104	0.969	5.6	73, 74
BMITFSI	419	1.329	6.6	44, 75
EMITFSI	391	1.406	6.6	44, 75

a 1:1 (cation:anion) salt in the mixture. ρ is density and M is molar mass (of the repeat unit, in the case of polymers).

$$r = \frac{[\text{EO}]}{[+]} = \frac{(1 - v_{\text{salt}}) \times \rho_{\text{EO}} \times (1/M_{\text{EO}})}{v_{\text{salt}} \times \rho_{\text{salt}} \times (1/M_{\text{salt}})} \tag{1.34}$$

1.3.2 Solid Polymer Electrolyte Design Considerations

As mentioned at the beginning of this chapter, the focus of this thesis is overcoming the trade-off between mechanical properties and conductivity. Put another way, the goal is to develop a framework to maximize ionic conductivity while independently modulating an orthogonal property to address a particular application. It is relatively straightforward to design a high conductivity *or* a mechanically robust polymer electrolyte, but integrating both properties into one material has proven difficult. Figure 1.11 summarizes the interplay between mechanical and ion transport properties in polymer electrolytes, and will be revisited throughout this thesis. First, several comments about Figure 1.11 are in order.

On the ordinate, the linear mechanical modulus, G (*i.e.*, the low strain limiting slope of stress-strain response) is used as a simple, quantitative metric to summarize mechanical robustness. In general, of course, modulus is only one measure of mechanical response, and for a given application, properties such as fracture toughness, strain-to-break, or creep resistance might be more relevant. On the abscissa,

the measured ionic conductivity is plotted. The dotted horizontal and vertical lines provide a reference point to discuss "low" versus "high" modulus and conductivity. The metrics of 1 GPa and 1 mS/cm are not universal, but rather are those commonly cited for Li-ion battery electrolytes.[16,76] Nonetheless, the region in the upper right corner of Figure 1.11 represents a reasonable target for electrolyte performance, in which mechanical and ion transport properties have been effectively decoupled and optimized. As a final note, plotting the measured conductivity can be misleading, as different salts exhibit different intrinsic conductivity (*e.g.*, polymer electrolytes using ILs are expected to exhibit higher conductivity than electrolytes with equal concentration of high T_m salt). It is sometimes useful to normalize conductivity by various parameters—for example, the intrinsic salt conductivity or the conductivity of the polymer/salt conducting phase—to directly compare different systems. That being said, it is not the normalized conductivity that ultimately matters in an electrochemical device, but rather the ionic current of the electroactive species (*e.g.*, Li^+), as that will determine the external electrical current that can be used to do work. In the following discussion, Figure 1.11 will be used to compare the performance of a variety of solid-state polymer electrolytes reported in the literature. The list of polymer electrolyte examples used is not meant to be exhaustive, but rather serves as a representative sampling of various classes of electrolytes, based primarily on the solidification method and type of salt used.

One of the simplest methods to prepare solid-state polymer electrolytes is chemical or physical crosslinking of a homogeneous polymer matrix. One of the earliest reports of this strategy was by Watanabe et al.[77] in 1984. The authors used toluene diisocyanate to lightly crosslink 3 kg/mol linear poly(propylene oxide) (PPO) chains. Although the mechanical properties were not reported, it is likely that the resulting films were soft solids with a modulus of order 10^3 to 10^4 Pa. Furthermore, these electrolytes were *homogeneous*, meaning the solidification mechanism (crosslinks between chains) and conducting phase co-exist in the same volume. In homogeneous
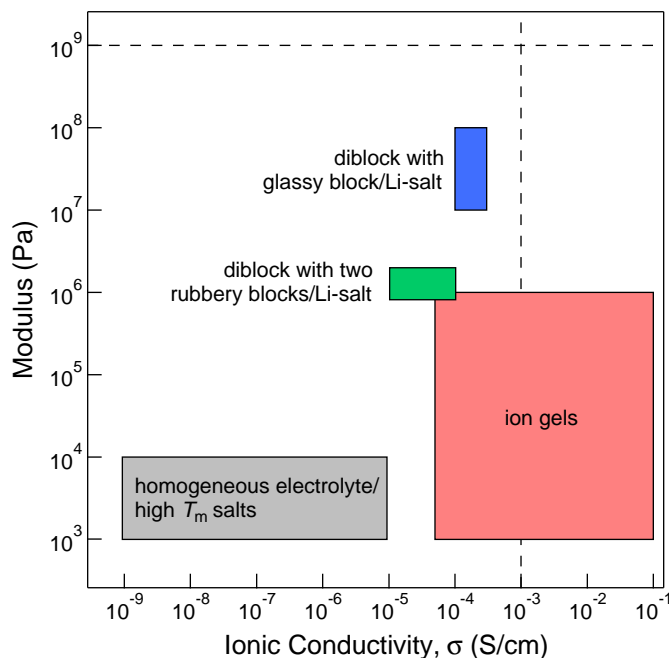
Figure 1.11: Interplay between mechanical and ion transport properties in solid-state polymer electrolytes. To put polymer electrolyte performance into context, the dashed lines indicate the threshold metrics (modulus $\geq 10^9$ Pa, $\sigma \geq 10^{-3}$ S/cm) often cited for Li-ion battery electrolytes.[16,76] The systems are taken from the following references: gray, ref 77; red, refs 53, 78, and 79; green, ref 80; blue, ref 76.

electrolytes, higher crosslink density can be used to increase the modulus, but the conductivity inevitably suffers as local chain dynamics slow with decreasing molar mass between crosslinks, M_x. On the other hand, if the crosslink density is commensurate with that required to gel ($\sim 1/N$, where N is the chemical degree of polymerization), local chain dynamics are predominantly uninhibited, but macroscopically, the sample does not flow. (It should be mentioned that for some applications, simply preventing flow is a sufficient mechanical response.) The conductivity of three lithium salts— LiBF$_4$, LiClO$_4$, and LiSCN—ranged from 10^{-9} to 10^{-5} S/cm over the temperature range from -10 to 110 °C. The low magnitude of conductivity in that report is an example of the coupled motion of ions to polymer chain dynamics when high T_m salts are used. The gray region in Figure 1.11 broadly summarizes the performance of this class of lightly crosslinked, homogeneous polymer electrolytes using high T_m salts.

In 1985, Watanabe et al.[81] also demonstrated a physical gelation approach for crosslinking polymer electrolytes. The authors used an ABA-type triblock copolymer with poly(urethane urea) (PUU) endblocks and a PPO midblock. Although the morphology was not rigorously characterized, it is plausible—based on the conductivity of the samples and on previous work with PUU elastomers[82]—that the electrolyte microphase separated into discrete hard domains of PUU within a continuous matrix of PPO/Li-salt. Electrolytes in this class are termed *structured*, as the mechanically robust and ion transport domains are microphase separated. Many of the structured polymer electrolytes discussed in this thesis could be more precisely defined as *nanostructured*, as the length scale of compositional heterogeneity is typically tens of nanometers. In this report, Watanabe et al. directly measured the modulus of the elastomeric electrolytes to be of order 10^7 Pa over a wide temperature range (0 to 200 °C). Not surprisingly, the conductivity of $LiClO_4$ spanned roughly the same range as the previously reported crosslinked PPO electrolyte (10^{-9} to 10^{-5} S/cm), because the mechanism of ion transport was identical to the homogeneous PPO electrolytes. However, an important lesson from this early work is that structured electrolytes can increase the modulus without impacting conductivity in the transport domain, in this case by confining the solidifying mechanism to discrete domains.

As discussed earlier, decoupling ion motion from polymer chain relaxation—as observed in IL-based electrolytes—has a profound impact on conductivity. In the early 2000s, Noda et al.[78] and Susan et al.[79] first demonstrated ion gel electrolytes, in which a lightly crosslinked PMMA polymer network was swollen with a high fraction of ionic liquid, for example EMITFSI (see Figure 1.8 for the structure). In this class of ion gels, the IL serves as the reaction medium in which vinyl monomers and an appropriate crosslinker undergo a free radical polymerization, resulting in free-standing, flexible, and transparent films. Consistent with the intrinsically high conductivity of EMITFSI, these ions gels exhibit high conductivity ($> 10^{-3}$ S/cm over the temperature range from −10 to 110 °C), only slightly reduced from neat IL for

lightly crosslinked samples. These ion gels were homogeneous, and the conductivity dropped off sharply as the crosslink density was increased. It is therefore reasonable that samples with the lowest crosslink density (*i.e.*, those that exhibited the highest conductivity) exhibited moduli of order 10^3 Pa, placing homogeneous ion gels in the red region in Figure 1.11. Conversely, samples comprising a majority of polymer were glassy for part of the temperature range studied, resulting in immeasurably low conductivity. These samples would fall in the upper left corner of Figure 1.11, as the low conductivity is a direct result of the stiff, glassy polymer matrix. This result directly demonstrates the guaranteed trade-off between mechanical and ion transport properties for homogeneous polymer electrolytes.

In 2007, He et al.[53] first demonstrated nanostructured ion gels, in which the triblock copolymer poly(styrene-*b*-ethylene oxide-*b*-styrene) provided the gelation mechanism. By virtue of incompatibility of the PS endblocks in the ionic liquid $BMIPF_6$ (see Figure 1.8 for the structure), the block polymer self-assembled into discrete glassy cores of PS bridged by solvated PEO midblocks. Relative to homogeneous ion gels, one of the advantages of nanostructured ion gels is that gelation is achieved at much lower polymer concentration (*ca.* 5 wt%), while maintaining a modulus of order 10^3 Pa. It was later shown by Zhang et al.[23] that the PS cores simply act as insulating obstructions to ion transport occurring in the continuous PEO/IL matrix. As a result, ion gels exhibit high conductivity, only slightly reduced relative to neat IL (*e.g.*, an ion gel with 10 wt% polymer saw only a factor of two reduction relative to, in this case, EMITFSI). Ultimately, however, the outstanding performance of ion gels (whether homogeneous or nanostructured) is best suited for low- to rubbery-modulus (10^3 to 10^6 Pa) applications, as illustrated by the red region in Figure 1.11. To increase the modulus with minimal decrease in conductivity, *both* the mechanically robust and conductive domains must exhibit long-range continuity, which is the subject of the following discussion.

To design polymer electrolytes exhibiting both high conductivity and mechanical
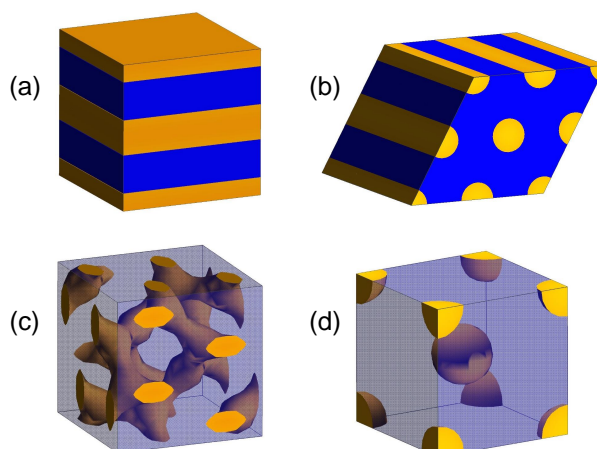
Figure 1.12: Diblock copolymer equilibrium morphologies: (a) lamellae, (b) hexagonally close-packed (HCP) cylinders, (c) gyroid, (d) body-centered cubic (BCC) spheres. The characteristic domain size is of order 10 nm. These figures were created using a level set model developed by Eric Cochran.[95,96]

robustness, the polymer electrolyte community has turned to polymer-rich, structured electrolytes.[56,83–91] The general design rationale for this class of polymer electrolytes is that one phase dominates the macroscopic mechanical response of the material, while the other phase provides a low T_g domain in which ions migrate. In this field, block polymers have emerged as the most promising candidates, as they self-assemble into well-defined nanostructures in which each phase exhibits precise, desired functionality.[55,92–94] For example, Figure 1.12 shows the four equilibrium morphologies observed in linear AB diblock copolymers. The system can be designed such that the blue phase is a mechanically robust (*e.g.*, high T_g, T_m, or highly crosslinked) insulating block, and the yellow phase is a low T_g polar ion conductor.

The preceding discussion and Figure 1.12 are not meant to suggest that long-range *periodic* domain order is required for polymer electrolytes. Rather, as will be shown in this thesis, long-range domain *continuity* is the necessary condition for both high conductivity and modulus.[97] In this respect, of the four morphologies shown, lamellae, HCP cylinders, and gyroid are all potentially viable candidates, although

one quickly encounters challenges with ensuring macroscopic domain continuity between electrodes.[6,84,86,90] As mentioned previously, ion gels—in which one phase is discrete and which can exhibit BCC symmetry[24]—typically do not exhibit moduli higher than 10–100 kPa because the glassy domain is not continuous. Similarly, if the yellow spheres in Figure 1.12(d) were conductive, and the blue phase were insulating, one expects that the conductivity would be exceedingly low. Although much of the literature on block polymer-based electrolytes focuses on diblock copolymers, the number of blocks can be increased to access an even wider array of thermodynamically stable network morphologies,[96,98–105] in which domains are isotropically continuous in space. This is the subject of Chapter 4.

There are many excellent examples in the literature of block polymer-based electrolytes. Some of the early work on this class of polymer electrolytes was reported by the groups of Sadoway and Mayes.[80,106–108] In these studies, the conducting block was typically poly[(oxy-ethylene)$_x$ methacrylate] (POEM, $T_g \approx -60$ °C), where x is the number of ethylene oxide repeat units in the methacrylate side group. The oligo(ethylene oxide) side chains complex with salts such as lithium trifluoromethyl-sulfonate (see Figure 1.8 for the structure), but are short enough to inhibit crystallinity. The identity of the second block varied, but in general, it was another low T_g block, for example poly(lauryl methacrylate) (PLMA, $T_g \approx -35$ °C). The design strategy was that the neat diblock was disordered and could be processed as a liquid, and microphase-separation could be induced by salt doping. The elastic modulus of the ordered diblock—which was typically on the order of 10^6 Pa—was a product of the combination of microphase separation and entanglements in each phase. The conductivity of $LiCF_3SO_3$ in the POEM block spanned the range from 10^{-5} to 10^{-4} S/cm from room temperature up to 90 °C,[80] placing these systems in the green region in Figure 1.11. Finally, it is worth highlighting one interesting result by Soo et al.[80] that can be extended to any block polymer-based electrolyte: the importance of confining ions to a low T_g environment to achieve high conductivity. The authors

prepared a POEM-*b*-PMMA diblock and an analogous POEM-*co*-PMMA random copolymer. At equal block volume fractions and salt loading, the conductivity of the random copolymer was *ca.* three orders of magnitude lower than the block polymer, a direct result of the increased T_g of the conducting phase upon mixing POEM with the high T_g PMMA block.

Relative to the rubbery electrolytes described above, replacing one of the rubbery blocks with a high T_g block has a profound impact on the macroscopic modulus, an idea pioneered by Balsara and coworkers.[5,14,76,109–114] In this body of work, the prototypical electrolyte is a symmetric (*i.e.*, lamellae-forming) poly(styrene-*b*-ethylene oxide) (PS-*b*-PEO) diblock copolymer doped with lithium bis(trifluoromethylsulfonyl)-imide (LiTFSI). Singh et al.,[76] who first characterized the mechanical and conductive properties of PS-*b*-PEO/LiTFSI, reported conductivity of LiTFSI in the PEO domains to be slightly higher than 10^{-4} S/cm over the temperature range from 90 to 120 °C. In this system, PEO exhibited a high degree of crystallinity, so the temperature was kept well above $T_\mathrm{m,PEO}$. The modulus was directly measured at 90 °C, and was found to increase from 10^7 to 10^8 Pa with increasing overall molar mass, M, of the diblock. The performance of PS-*b*-PEO/LiTFSI electrolytes is summarized by the blue region in Figure 1.11. One potential drawback of relying on glassy PS to provide mechanical integrity is that the electrolyte is only solid at temperatures below $T_\mathrm{g,PS}$. For the PS-*b*-PEO diblock, heating above *ca.* 100 °C results in a precipitous drop in the elastic modulus. For batteries intended to operate at 80 °C (which is the target application for PS-*b*-PEO/LiTFSI), glassy PS is a viable solidification mechanism, but the T_g perhaps limits the operational temperature window for non-battery, high T applications. Furthermore, although diblocks can be designed to exhibit high modulus, they generally exhibit poor nonlinear properties, such as fracture toughness and elasticity.[115,116] For these reason, *inter alia*, chemical crosslinking is explored in this thesis as a temperature-independent solidification mechanism.

In addition to high T_m, Li-based salts, there have been a number of papers investigating blends of diblock copolymers and ionic liquids.[56,89,117] For example, Simone et al.[56] studied the conductivity and phase behavior of blends of PS-b-PEO and EMITFSI across a wide concentration range. Virgili et al.[91] studied a similar system comprising poly[styrene-b-(2-vinylpyridine)] (P2VP) and the ionic liquid imidazolium bis(trifluoromethylsulfonyl)imide (ImTFSI), which is a protic IL and is considered a good candidate for anhydrous fuel cells.[118] Although the motivation for including a high T_g insulating block (*e.g.*, PS) is to impart high modulus to the electrolyte, the mechanical properties were typically not explicitly reported in these studies. However, there are other important common lessons to be learned: (i) block polymer/IL blends typically exhibit high ionic conductivity if the conductive phase is the majority phase,[117] consistent with the intrinsically high IL conductivity, and (ii) ILs act as highly selective solvents for the polar block, driving interesting and potentially useful lyotropic phase transitions. Alternatively, the conducting block can be a polymerized ionic liquid, or poly(IL), in which one of the ions is covalently bound to the polymer backbone.[84,86,119–121] The reasons for using a poly(IL) block in lieu of a simple polar block like PEO are (i) they eliminate the possibility of IL leaching out of a membrane during long-term application, due to the strong Coulombic forces between the bound and free ions, and (ii) they are single-ion conductors, thus guaranteeing a free ion transference number of unity. In general, though, the same caveats apply to poly(IL)-based electrolytes as polymer/IL blends, namely the importance of morphology and block identity (*i.e.*, low T_g conducting block, high T_g insulating block) on the measured conductivity and mechanical properties.

When designing structured electrolytes, it must be recognized that—independent of the details of how the structured electrolyte is made or the exact chemical identity of each phase—there will be an increase in the resistance relative to a bulk electrolyte of equivalent geometry. Conductivity is then calculated using the macroscopic geometry (via l/Ra or κ/R), so the increase in resistance translates into lower measured

$$\sigma = \sigma_{\rm c} \qquad\qquad \sigma = \sigma_{\rm c} f_{\rm c} \qquad\qquad \sigma = \sigma_{\rm c}\frac{f_{\rm c}}{\tau} \qquad\qquad \sigma < \sigma_{\rm c}\frac{f_{\rm c}}{\tau}$$
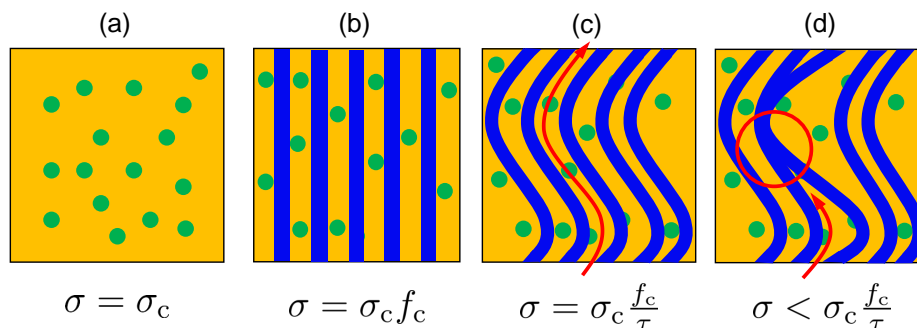
Figure 1.13: Factors that lower the conductivity of a structured electrolyte relative to a bulk electrolyte. (a) A bulk electrolyte comprising homopolymer and salt exhibits conductivity $\sigma_{\rm c}$. Green dots are ions, the yellow matrix is polymer. (b) A blue insulating phase is introduced, lowering the conductivity because the volume fraction of conducting phase, $f_{\rm c}$, is < 1. The local salt concentration in the conducting phase is equal to the bulk electrolyte. (c) If the conducting channels are not straight paths between electrodes, conductivity is further reduced because the tortuosity, τ, is > 1. (d) Network defects, such as dead ends in the conducting pathway, reduce conductivity more than volume fraction and geometric arguments predict.

conductivity, even if the intrinsic conductivity of the conducting phase is identical to the bulk electrolyte. Figure 1.13 illustrates the factors that increase the resistance of a structured electrolyte. In Figure 1.13(a), a bulk electrolyte (*e.g.*, $LiClO_4$ in PEO, or EMITFSI in PMMA) exhibits intrinsic conductivity $\sigma_{\rm c}$. Introducing an insulating phase lowers the measured conductivity, σ, because the volume fraction of conducting phase, $f_{\rm c}$, is necessarily < 1. That is, because the salt concentration in the conducting phase of the structured electrolyte is equivalent to the bulk electrolyte, the total number of ions decreases from Figure 1.13(a) to (b).

$$\sigma = \sigma_{\rm c} f_{\rm c} \tag{1.35}$$

However, the picture in Figure 1.13(b) is unrealistic, in that the conducting domains typically exhibit some degree of tortuosity, τ. Long-range domain alignment (in this case, orthogonal to the plane of the electrodes) is difficult to achieve in block polymers without, for example, applying an external magnetic[122] or stress[123] field. As a result,

ions must travel further between electrodes in (c) relative to (b), and the measured conductivity is reduced by an additional factor, $\tau > 1$.

$$\sigma = \sigma_{\text{c}} \frac{f_{\text{c}}}{\tau} \tag{1.36}$$

In practice, the measured conductivity is often found to be lower than eq 1.36 predicts, for two primary reasons: (i) the conducting phase does not exhibit long-range connectivity, *and/or* (ii) the properties of the conducting phase in the structured electrolyte deviate from that of the bulk electrolyte. For example, the conducting phase might not exhibit long-range connectivity due to "network defects", a term used to describe, *inter alia*, dead ends in the conducting pathway, as shown in Figure 1.13(d). In regards to condition (ii), the conducting phase might deviate from bulk behavior because the characteristic size is too small or because of a diffuse interface between domains. If the diameter of the conducting domain is smaller than a few nanometers, the mechanism of ion conduction might break down, chain relaxation will be inhibited by confinement, *etc.* This effectively sets a practical lower limit on the characteristic domain size in polymer electrolytes. The natural length scale of periodicity in block polymers is $\mathcal{O}(10)$ nm, and it appears that overall, this size scale is appropriate for many electrochemical device applications.

Alternatively, the interface between domains in block polymers can also induce departures from the bulk response. For example, Yuan et al.[114] studied the conductivity of LiTFSI in a series of symmetric PS-*b*-PEO diblocks of increasing overall molar mass, M. The authors found that at low M, the interface comprised a non-trivial fraction of the volume of each phase. As a result, the stiff PS chains slowed PEO chain relaxation, lowering the conductivity. Only at very high M did the domains become pure enough to behave like the respective bulk homopolymer. As a final comment on domain size, the upper limit is less well-defined than the lower limit, and is likely to be governed more by the intended application, rather than physics. For example, in Li-metal batteries, the periodicity of low and high modulus domains

should be smaller than the characteristic size of lithium dendrites ($\mathcal{O}(1)$ μm),[15] so the dendrites "see" an electrolyte with high effective modulus.

1.4   Thesis Overview

This thesis is divided into three primary research chapters. Chapter 2 presents work that represents an important advancement in the design of mechanically robust polymer electrolyte membranes. A remarkably simple, yet versatile synthetic strategy—termed polymerization-induced phase separation, or PIPS—is used to prepare PEMs that exhibit an unprecedented combination of high conductivity and high modulus. This performance is enabled by the long-range co-continuity of poly(ethylene oxide)/ionic liquid and crosslinked polystyrene domains. Chapter 2 focuses primarily on the bulk properties of PIPS PEMs, while Chapter 3 investigates the mechanistic details by which the PIPS strategy generates the optimal co-continuous network structure. A suite of *in situ*, time-resolved experiments are used to build a molecular picture of how the sample transitions from a liquid precursor to a high modulus solid. Finally, Chapter 4 details a different strategy to prepare PEMs. Whereas the PIPS reaction represents kinetic control over the PEM microstructure, the system discussed in Chapter 4 relies on a thermodynamically stable network morphology to precisely tune the microstructure. The objective remains the same, however, namely to decouple the mechanical and ion transport properties of the PEM. In particular, in Chapter 4, a high modulus electrolyte is prepared from a triblock terpolymer known to exhibit three distinct thermodynamically stable network morphologies, in which each domain is continuous in space.

Chapter 2

High Modulus, High Conductivity Nanostructured Polymer Electrolyte Membranes via Polymerization-Induced Phase Separation[i],[ii]

2.1 Introduction

Seo and Hillmyer[124] recently reported a simple, yet versatile strategy to generate mechanically robust, nanoporous polymer membranes. The authors dissolved poly-lactide macro chain-transfer agent (PLA-CTA) in a monomer mixture of styrene (S) and divinylbenzene (DVB). Heating the homogeneous liquid reaction precursor

---

[i]Aadapted with permission from Schulze, M. W.; McIntosh, L. D.; Hillmyer, M. A.; Lodge, T. P. *Nano Lett.* **2014**, *14*, 122-126. Copyright 2014 American Chemical Society.
[ii]This work was done in collaboration with Morgan W. Schulze and Marc A. Hillmyer.

to 120 °C effected controlled growth of S and DVB from PLA-CTA via reversible-addition fragmentation chain-transfer (RAFT) polymerization. Simultaneous chemical crosslinking of the growing polystyrene chains by DVB arrested the system in a bicontinuous network morphology that was reminiscent of transient structures observed during phase separation via spinodal decomposition[125–128] and equilibrium structures observed in disordered block polymers in the vicinity of the order-disorder transition.[129–131] The samples were easily rendered nanoporous by hydrolyzing PLA with a mild base.

Previously, co-continuous materials had primarily been prepared by kinetically trapping the non-equilibrium bicontinuous structure encountered during macrophase separation via spinodal decomposition. For example, porous Vycor glass is made from a borosilicate melt that phase separates upon cooling into co-continuous silica- and borosilicate-rich phases.[132] The increase in viscosity accompanying the cooling process prevents macrophase separation, and the borosilicate-rich phase can be acid etched to achieve a porous structure. In the context of organic materials, Yamanaka et al.[133,134] prepared co-continuous rubber/epoxy composites by dissolving poly(acrylonitrile-*co*-butadiene) random copolymers in an epoxy resin. Phase separation was induced as the molar mass of the epoxy increased during the reaction, and a co-continuous structure could be trapped if the rates of crosslinking and phase separation were commensurate.[135] Finally, Trifkovic et al.[136] demonstrated that large-scale melt processing is a viable route to co-continuous blends of polyethylene and poly(ethylene oxide) (PE/PEO). Coarsening of the network structure was prevented by thermally quenching the extruded melt, thus crystallizing the PE, and the samples were rendered porous by etching PEO with water.

The common theme among the examples above is that the co-continuous structure is a product of spinodal decomposition and, as such, the characteristic length scale of heterogeneity is $\mathcal{O}(1)$ μm. Alternatively, Yamamoto et al.[137] reported a system similar in some respects to that of Seo and Hillmyer. Yamamoto et al. dissolved

poly(dimethylsiloxane) (PDMS) that was functionalized on both ends with an acrylate group in the monomer N,N-dimethylacrylamide (DMA). The homogeneous mixture was heated in the presence of a radical initiator to effect free radical polymerization of the DMA off both ends of the PDMS. The resulting structure exhibited heterogeneity on length scales of approximately 15 nm, per SAXS and TEM. Unfortunately, the authors did not corroborate claims of long-range continuity with macroscopic mass transport experiments. Furthermore, the authors labeled the structure as a bicontinuous microemulsion (BμE) on the basis of fitting SAXS data to the Teubner-Stray model. However, the final structure appeared to be kinetically trapped by virtue of the high T_g of the poly(DMA) block, whereas the BμE is generally considered to be an equilibrium morphology.[138–143]

Returning to the work of Seo and Hillmyer, some of the key results were (i) the size scale of domains was $\mathcal{O}(10)$ nm, several orders of magnitude smaller than the systems described above which undergo spinodal decomposition, (ii) macroscopic samples (in particular, predominantly defect-free membranes) could be readily prepared in a facile, one-pot synthetic scheme, and (iii) the nanoporous films retained a high modulus, preventing pore collapse that can result from high Laplace pressure. The authors envisioned that the resulting high surface area to volume ratio of the etched samples would enable, *inter alia*, selective gas adsorption. Importantly, they were able to prepare nanoporous membranes 100s of μm thick with long-range connectivity of pores, as confirmed by macroscopic mass tranport (water and CO_2) experiments.

The key features of the nanoporous PIPS membranes highlighted above (mechanical robustness, well-defined microphase separation, *etc.*) are also desirable features in polymer electrolytes membranes (PEMs). Therefore, the focus of this chapter is to extend the PIPS strategy reported by Seo and Hillmyer to prepare PEMs that are particularly attractive as highly conductive, thermally stable, and mechanically

robust composites. The PIPS strategy exploits simultaneous *in situ* block copolymer linear growth and chemical crosslinking, such that local segregation of a growing poly(styrene-*co*-divinylbenzene) segment from an ionic liquid-swollen poly(ethylene oxide) domain is preserved. The unprecedented performance of the bulk PEMs is then due to the long-range, isotropic continuity of the high modulus (crosslinked polystyrene) and ion-conducting (PEO/ionic liquid) domains. PEMs with (i) room temperature moduli near 1 GPa, (ii) significantly improved mechanical stability over previously reported systems at high temperature ($E' > 0.1$ GPa for $T < 125$ °C), and (iii) ionic conductivity in excess of 1 mS/cm can be produced by this facile and scalable process. To the best of our knowledge, no other polymer electrolyte reported achieves such combination of modulus ($\geq 10^8$ Pa) and ionic conductivity ($\geq 10^{-3}$ S/cm), nor the high temperature robustness.

2.2   Experimental Section

Synthesis and Characterization

Asymmetrically end-capped poly(ethylene oxide) ($M_n = 28$ kg/mol, $Đ = 1.03$) was synthesized by anionic polymerization from a potassium *tert*-butoxide initiator (1.0 M in THF, Sigma Aldrich) using standard Schlenck techniques.[144,145] Poly(ethylene glycol) methyl ether ($M_n = 5$ kg/mol, $Đ = 1.11$) was purchased from Sigma Aldrich. The chain transfer agent (CTA), (S)-1-dodecyl-(S')-(α,α'-dimethyl-α''-acetic acid) trithiocarbonate, was prepared as previously reported,[146] and coupled to the hydroxyl-terminus of each polymer via an acid chloride intermediate to produce a macromolecular PEO-CTA. SEC traces of linear PS-*b*-PEO block copolymers prepared and initiated from PEO-CTA in the bulk polymerization of styrene monomer had narrow molecular weight distributions. This result supported complete end-functionalization of PEO and agreed with the quantitative end-group analysis performed using ^{1}H-NMR spectroscopy.

The room temperature ionic liquid (IL) 1-butyl-3-methylimidazolium bis(trifluoro-methylsulfonyl)imide (BMITFSI) was prepared following established procedures.[44,58,59] A 10% molar excess of 4-chlorobutane was mixed with 1-methylimidazole in a 250–500 mL round bottom flask (depending on reaction scale), and cyclohexane was added ($\approx$ 100 mL cyclohexane/20 g chlorobutane) to dilute the reagents. The mixture was heated to reflux conditions and stirred vigorously for 48 h. Cyclohexane was removed via rotovap and the product, 1-butyl-3-methylimidazolium chloride (BMICl), was dried at 100 °C under dynamic vacuum overnight. Lithium bis(trifluoromethyl-sulfonyl)imide was added to BMICl at 10% molar excess, assuming complete conversion in the first step. DI water was added at a volumetric ratio of 10/1, and the mixture was heated to 70 °C and stirred vigorously for 48 h. The resulting solution phase separated into BMITFSI and an aqueous phase containing LiCl. BMITFSI was dissolved in chloroform ($\geq 4\times$ dilution) and washed with distilled water three times and purified by passing through a silica column. ^{1}H-NMR spectroscopy was used to confirm purity of the final product (> 99 mol%). A representative ^{1}H-NMR spectrum of BMITFSI is shown in Appendix B.2. The ionic liquid was dried at elevated temperature under dynamic vacuum for 2 d before use and was subsequently stored in an argon-filled glovebox.

Typical reactions to produce polymer electrolyte membranes were performed in a glass vial without degassing. Styrene (99%, Sigma Aldrich) and divinylbenzene (technical grade: 24% para, 56% meta, 20% isomeric mixture of ethyl styrene, Sigma Aldrich) were passed through activated alumina columns prior to use. Solutions were typically prepared gravimetrically at 32 wt% ($= 30$ vol%) PEO-CTA by the sequential addition of macro-CTA, styrene, and divinylbenzene. The monomer molar ratio of sytrene/divinylbenzene was maintained at 4/1. BMITFSI was added at a predetermined concentration, and the entire solution was well-mixed prior to heating to 120 °C to auto-initiate the polymerization of styrene. The use of azobisisobutyronitrile

(AIBN) as an external initiator (0.05 *eq* to PEO-CTA) was necessary for the uniform generation of radicals to prevent density inhomogeneities that would otherwise induce cracks during polymerization. The resulting transparent, solid monolith could be sanded to a flat surface of *ca.* 500 μm thickness for additional analysis.

Differential scanning calorimetry (DSC) experiments were performed on a TA Instruments Discovery DSC. Samples for measurement were prepared using standard aluminum T-zero pans with standard or hermetic lids. Each sample was annealed at 200 °C for 5 min. Subsequent cooling and heating ramps were applied at 5 °C/min. Heats of fusion were estimated from the endotherm of the second heating and the weight fraction of PEO incorporated into the crosslinked block polymer. Percent crystallinity was calculated in reference to the enthalpy of fusion of 200 J/g for pure crystalline PEO.[147,148]

Morphological Characterization

Bulk samples were microtomed at room temperature on a Leica UC6 Ultramicrotome to obtain sections with a nominal thickness of 70 nm. Sample sections were collected on a 300 mesh copper grid and were stained with the vapor of a 0.5 wt% RuO_4 aqueous solution for 5 min. On this time-scale, RuO_4 preferentially stains poly(ethylene oxide), which appears dark in TEM images. Sections were imaged at room temperature on an FEI Tecnai G2 Spirit Bio-TWIN using an accelerating voltage of 120 kV. Images were collected by a 2048 × 2048 pixel CCD. ImageJ software was used to generate Fourier transforms (FTs) of TEM images and then azimuthally integrate pixel intensity to generate 1D plots of intensity versus the magnitude of the wave vector, q.

Small-angle X-ray scattering (SAXS) experiments were performed at the Argonne National Laboratory Advanced Photon Source beamline 5-ID-D, which is maintained by the DuPont-Northwestern-Dow Collaborative Access Team. Samples were exposed at room temperature to synchrotron-source X-rays with a nominal wavelength of 0.729

Å. Scattered X-rays were collected on a 2D MAR CCD detector located at a sample-to-detector distance of 5680 mm. The sample-to-detector distance was calibrated using a silver behenate standard. Intensity was not reduced to an absolute scale. Corrected 2D SAXS intensity was reduced to a function of the magnitude of the wave vector, q, by azimuthally integrating the 2D data. q is given by

$$q = |\mathbf{q}| = \frac{4\pi}{\lambda} \sin\left(\frac{\theta}{2}\right) \tag{2.1}$$

where λ is the X-ray wavelength and θ is the scattering angle.

Ionic Conductivity

Ionic conductivity was measured using 2-point probe impedance spectroscopy on a Solartron 1255B frequency response analyzer connected to a Solartron SI 1287 electrochemical interface. Bulk polymer electrolyte membrane samples were sanded to uniform thickness (*ca.* 0.5 mm) and sandwiched between stainless steel electrodes. Impedance was measured over the frequency range from 1 MHz to 1 Hz using a voltage amplitude of 100 mV. Voltage amplitude sweeps were performed at several values of frequency to check for linearity. Bulk resistance, R, was determined from the frequency-independent plateau of the real part, Z', of the impedance. Ionic conductivity, σ, was calculated as

$$\sigma = \frac{l}{Ra} \tag{2.2}$$

where l is the sample thickness and a is the superficial area. Thickness was measured with a Mitutoyo micrometer (1 μm resolution). Area was calculated by photographing the sample placed next to a ruler, which was used to calibrate the length/pixel ratio, and area was measured using ImageJ software.

Samples were stored in either an argon-filled glovebox or under dynamic vacuum. Each sample was heated ($\geq$ 100 °C) under dynamic vacuum ($\leq$ 100 mTorr) for at least 1 d prior to running impedance experiments. Impedance measurements were

performed in an open atmosphere at temperatures from 30 to 150 °C in 10 °C increments. Each temperature was maintained for 1 h prior to measurement to allow thermal equilibrium. To test the effect of water absorption at temperatures below 100 °C, the conductivity of a rigorously dry sample was measured, the sample was allowed to sit in open atmosphere for 1 d, and the impedance experiment was re-run. Samples that contained only ionic liquid were generally reproducible over the entire temperature range studied, suggesting they did not exhibit strong affinity for water. It is possible that water slightly increased the error of repeated measurements below 100 °C. In contrast, the conductivity of samples containing LiTFSI was not reproducible after the sample sat in open atmosphere for 1 d, indicating that these samples were highly absorptive. For this reason, samples containing LiTFSI were heated to 100 °C for 3 h prior to measurement and temperatures were restricted to 100–150 °C.

Mechanical Response

Mechanical response was measured in the linear viscoelastic regime using an RSA-G2 Solids Analyzer (TA Instruments). Samples prepared for mechanical response measurements were polymerized in Teflon molds to produce samples with the appropriate geometry (approximately $50 \times 10 \times 1$ mm). To generate time-temperature superposition (tTS) master curves, samples were heated to a series of increasing temperatures and thermally equilibrated at a given temperature for at least 10 min. Strain sweeps were performed at a radial frequency of 10 rad/s to determine the limit of linear viscoelastic response, followed by a frequency sweep performed at fixed strain over the frequency range from 100–0.1 rad/s. Raw data were shifted horizontally by visual alignment of the elastic modulus, E'.
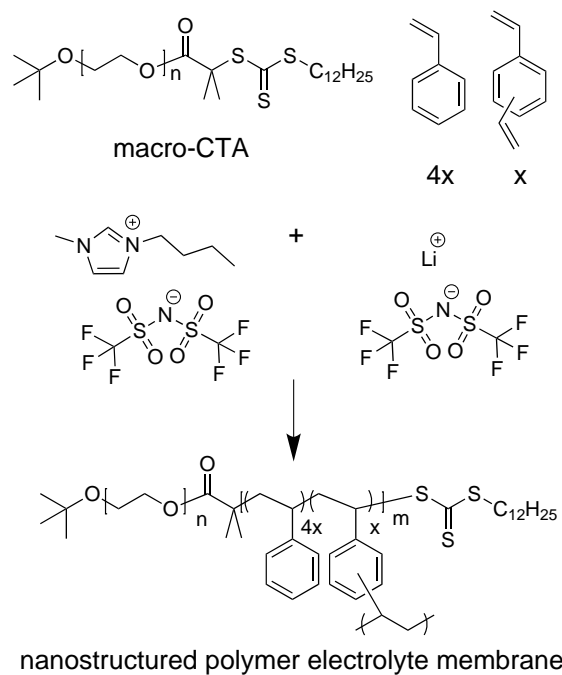
Figure 2.1: Reaction scheme used to prepare polymerization-induced phase separation polymer electrolyte membranes.

2.3   Results and Discussion

In the work presented in this thesis, one of the most important results is that the polymerization-induced phase separation (PIPS) strategy reported by Seo and Hillmyer[124] can be readily extended to prepare high modulus, high conductivity polymer electrolyte membranes (PEMs). Figure 2.1 summarizes the reaction scheme used to prepare PEMs via PIPS. In lieu of PLA-CTA, a poly(ethylene oxide) macro-CTA (PEO-CTA) was dissolved in a mixture of S/DVB, because PEO is the prototypical polymer used for polymer electrolytes and is miscible with a wide variety of salts. The principal salt used in this study was the room temperature ionic liquid (IL) 1-butyl-3-methylimidazolium bis(trifluoromethylsulfonyl)imide (BMITFSI). BMITFSI was added directly to the stock solution of PEO-CTA + S/DVB, and the homogeneous mixture was heated to 120 °C to generate radicals and initiate linear RAFT
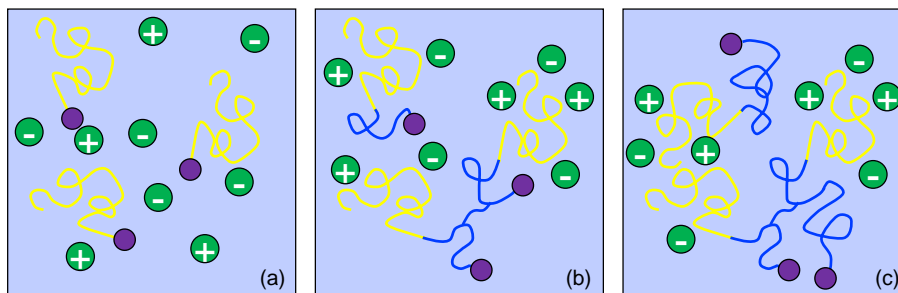
Figure 2.2: Schematic of chain growth and ionic liquid partitioning during polymerization-induced phase separation. (a) Poly(ethylene oxide) (PEO) macro chain-transfer agent (CTA) (PEO is denoted by yellow lines, purple circles are the CTA) is dissolved in a mixture of styrene and the di-functional crosslinker divinylbenzene (denoted by the blue background), with ionic liquid (green pluses and minuses). (b) Heating the reaction mixture effects linear chain growth of styrene and simultaneous crosslinking of chains by divinylbenzene (dark blue lines). (c) At some point during the reaction, the ionic liquid becomes immiscible in the polystyrene matrix and partitions to PEO-rich regions.

polymerization of S and simultaneous chemical crosslinking by DVB off the PEO-CTA. Samples were typically allowed to react overnight, and the resulting glassy solids were transparent with a yellow tint (a result of the $-C=S-$ double bond in the CTA). As shown schematically in Figure 2.2, one of the important hypotheses when first designing this system was that the ionic liquid would initially be miscible in the reaction mixture, but would ultimately reside in the PEO domains, where the ions can rapidly migrate.

Table 2.1 summarizes the composition of samples reported in this chapter. The concentration of salt is given as the volume percent of the total PEM. For example, one of the samples was prepared with an impressive 40 vol% BMITFSI (a liquid at room temperature), but macroscopically, the sample remained solid. The "PEO + salt" column gives the volume fraction of the conducting phase; the remainder of the sample is crosslinked PS. Finally, the concentration of salt in the conducting phase is reported in the "salt in PEO + salt domain". This measure of concentration is important because it governs the intrinsic conductivity, σ_c, of the conducting phase. σ_c is the conductivity of a bulk, homopolymer-based electrolyte of equivalent composition as

Table 2.1: Composition of PIPS PEM samples

$M_{\text{PEO-CTA}}$ (kg/mol)	$w_{\text{PEO-CTA}}$ (wt%)	type of salt[i]	salt[ii]	PEO + salt[iii]	salt in PEO + salt domain[iv]
				concentration (vol%)	
5	32	no salt	0	32	0
5	32	BMITFSI	5	35	15
5	32	BMI/LiTFSI	7	36	18
5	32	BMITFSI	21	47	45
5	32	BMI/LiTFSI	21	47	45
5	32	BMITFSI	30	52	57
5	32	BMITFSI	40	59	67
5	32	BMITFSI	50	66	75
5	42	no salt	0	42	0
5	42	BMITFSI	12	50	25
5	42	BMITFSI	21	54	38
5	42	BMITFSI	30	60	50
28	32	no salt	0	32	0
28	32	BMITFSI	4	32	12
28	32	BMITFSI	21	47	46
28	32	BMITFSI	30	52	59
28	32	BMITFSI	50	66	75

[i] "Salt" refers to either pure BMITFSI or mixtures of LiTFSI in BMITFSI
[ii] Overall volume fraction of salt
[iii] Volume fraction of the conducting phase
[iv] Volume fraction of salt in the conducting phase

the conducting phase in nanostructured electrolytes like PIPS PEMs. This idea will be revisited when PIPS PEM conductivity data are discussed.

Several control experiments were performed to demonstrate the conditions necessary to generate macroscopically homogeneous, bicontinuous PEMs, and can be summarized as follows. (i) The liquid reaction precursor must be homogeneous at $T_{\text{rxn}} = 120$ °C (at the earliest stages of the reaction) to ensure isotropic, homogeneous controlled growth of the P(S-*co*-DVB) block off the PEO-CTA throughout the sample volume. (ii) Domain connectivity between the PEO-CTA and the growing
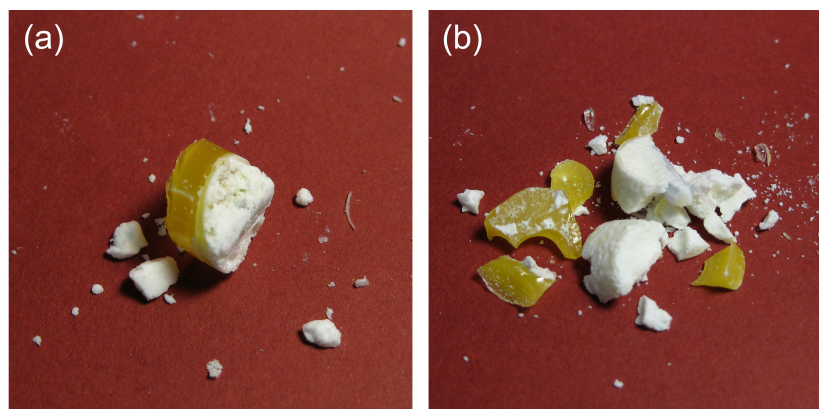
Figure 2.3: Photographs of samples prepared to test the reaction conditions necessary to produce macroscopically homogeneous, bicontinuous PEMs. (a) Polymerization of styrene and divinylbenzene in the presence of free CTA and no PEO-CTA. The yellow portion is likely P(S-*co*-DVB)-CTA, and it is plausible that the white material is P(S-*co*-DVB) that grew via free radical polymerization. (b) Polymerization of styrene and divinylbenzene in the presence of free CTA and 5 kg/mol PEO-OH. The yellow portion likely comprises P(S-*co*-DVB)-CTA, and the white portion includes both PEO-OH and P(S-*co*-DVB). The macrophase separation observed in these samples indicates that domain connectivity achieved in the *in situ* synthesis of a diblock copolymer is necessary to produce a homogeneous structure. Sample sizes are of order 1 cm.

P(S-*co*-DVB) block is required. As shown in Figure 2.3, samples prepared with (a) PEO-OH in lieu of PEO-CTA and (b) with free CTA and no PEO both exhibit macrophase separation. These control samples were not tested further.

Figure 2.4 qualitatively demonstrates the miscibility of the constituent components of the PIPS PEM reaction mixture. In panel (a), mixtures of S/DVB + BMITFSI macrophase separate into an IL-rich phase (on the bottom, based on its higher density) and an S/DVB-rich phase. Evidently, some of the S/DVB partitions into the IL-rich phase, because the meniscus would be closer to the bottom (only 28 vol% IL was added) if the IL phase were pure. Styrene monomer is known to exhibit some degree of solubility in ionic liquids. Susan et al.[79] attempted to prepare a homogeneous ion gel via radical polymerization and chemical crosslinking of styrene in the ionic liquid EMITFSI. However, the growing polystyrene network precipitated out of solution at some threshold molar mass. Similarly, Zhang et al.[23]
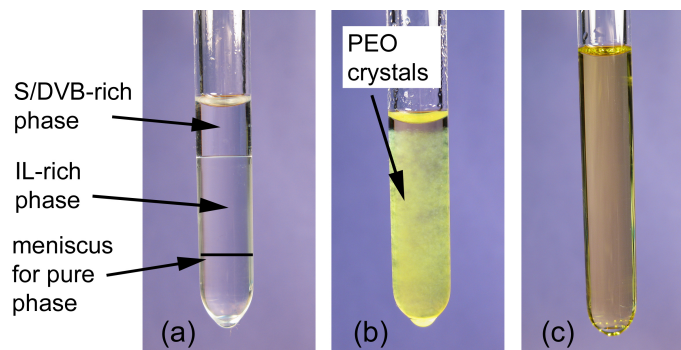
Figure 2.4: Photographs of PIPS PEM liquid reaction mixtures demonstrating the conditions under which homogeneity is achieved. The photographs were taken several hours after preparing the samples. (a) S/DVB + BMITFSI (28 vol%). (b) S/DVB + PEO-CTA (32 vol%). (c) S/DVB + PEO-CTA (26 vol%) + BMITFSI (21 vol%). In all samples, the molar ratio of S/DVB = 4/1 and $M_{\text{PEO-CTA}}$ = 5 kg/mol. In (a) and (b), the concentration was chosen to equal the concentration in the full reaction mixture (*i.e.*, taking into account dilution by the absent species).

studied the triblock copolymer-based nanostructured ion gel poly(styrene-*b*-ethylene oxide-*b*-styrene)/EMITFSI and found that M_{PS} needed to be at least 3 kg/mol to induce the PS endblocks to aggregate and form the physical crosslinks of the gel. Moving to Figure 2.4(b), when PEO-CTA is mixed with S/DVB, the solution is initially homogeneous, but after several hours at room temperature, PEO begins to crystallize out of solution. In practice, this is not a problem, because the PEO crystals melt upon heating the mixture to $T_{\text{rxn}} = 120\ ^{\circ}\text{C}$. Nevertheless, it demonstrates that the S/DVB mixture is not a good solvent for PEO-CTA at room temperature. Figure 2.4(c) shows that the ternary blend (PEO-CTA + S/DVB + BMITFSI) is homogeneous up to several hours after the reaction mixture was prepared. The suppression of PEO-CTA crystallinity is consistent with differential scanning calorimetry data of the solid PEMs (DSC data will be presented and discussed shortly), suggesting close association of the PEO-CTA and BMITFSI in the ternary blend. Interestingly, it appears that the ternary blend (S/DVB + PEO-CTA + BMITFSI) necessary to generate the desired bicontinuous structure of PEO/IL and crosslinked PS also ensures the long-term homogeneity of the liquid precursor.

The PIPS parameter space is large, as one can vary, *inter alia*, $M_{PEO\text{-}CTA}$, the concentration of PEO-CTA, the molar ratio of styrene/divinylbenzene, the identity of the salt, and the concentration of salt. The following discussion will provide some justification for why particular values were used. In general, for this preliminary work using PIPS to produce PEMs, values known to generate the desired bicontinuous morphology were used, but each could likely be tuned to optimize performance for a specific application.

For most samples presented here, the concentration of PEO-CTA was held at 32 wt% (= 30 vol%) in the S/DVB monomer mixture. A series of samples was also prepared with 42 wt% (= 40 vol%) PEO-CTA. The series of PEMs with higher PEO-CTA concentration was not analyzed as thoroughly as samples prepared with 32 wt% PEO-CTA, but as will be shown, the scattering data are qualitatively similar to samples prepared with 32 wt% PEO-CTA. The concentration of PEO-CTA likely has a lower limit roughly predicted by the percolation threshold ($\approx$ 15 vol%),[149] below which there would not be enough PEO to form a sample-spanning network. In the case of PEMs, increasing the volume fraction of PEO above 32 wt% could be done to increase conductivity, as more salt could be loaded into the conductive phase. However, increasing the volume fraction of the conducting phase results in a commensurate decrease in volume fraction of the high modulus phase. At high PEO volume fraction, the concern is that the volume fraction of the mechanically robust phase will drop below the percolation threshold. The upper limit of PEO-CTA concentration would therefore be defined by the point at which mechanical properties drop below some metric (*e.g.*, modulus or fracture toughness) set by a specific application.

Two PEO-CTA molar masses, $M_{PEO\text{-}CTA}$ = 5 and 28 kg/mol, were studied. The primary motivation for varying $M_{PEO\text{-}CTA}$ was the observation by Singh et al.[76] that conductivity of LiTFSI increases with increasing M_{PEO} in symmetric PS-*b*-PEO-based

electrolytes. This interesting result will be discussed in more detail when the conductivity data are presented. In practice, low molar mass PEO-CTA dissolves more readily in the S/DVB monomer mixture than high $M_{\text{PEO-CTA}}$, even at the reaction T of 120 °C. This observation suggests that very high molar mass PEO would not be amenable to the PIPS synthetic strategy because it would not form a homogeneous liquid reaction mixture. On the other hand, the microstructure of samples prepared with high molar mass PEO-CTA is easier to image in real space (*e.g.*, TEM and SEM) because the characteristic domain size is larger than 10 nm. In general, the effect of varying $M_{\text{PEO-CTA}}$ will be highlighted when applicable.

The molar ratio of S/DVB was fixed at 4/1 for most of the samples discussed in this chapter. Other ratios of S/DVB also generate the desired bicontinuous morphology, but tuning this parameter was not the focus of this particular study. In any case, one of the advantages of using a bicontinuous morphology is that modulating the crosslink density in the high modulus, crosslinked PS phase should not impact ion transport in the PEO phase. Tuning the crosslink density could, however, be used to increase the bulk modulus, or reduce brittleness, as a specific application requires. In the limit of no DVB, the PIPS reaction simply produces a diblock that self-assembles into either cylinders of PEO in a matrix of PS, or a lamellar microstructure, depending on the concentration of both the PEO-CTA and ionic liquid.

As mentioned previously, one of the key advancements of this work was to use the PIPS strategy for direct incorporation of salt into the liquid reaction precursor. For context, most diblock copolymer-based electrolytes are prepared by first synthesizing the block polymer, then mixing the polymer and salt in a good, volatile solvent, and finally solvent-casting the mixture to obtain a thin membrane. Direct incorporation of the salt into a relatively low viscosity liquid reaction mixture should enable ease of processing in the liquid state, followed by *in situ* solidification. As mentioned earlier, the principal salt used in this study was the room temperature ionic liquid BMITFSI.

Other common ILs exhibit slightly higher conductivity than BMITFSI (*e.g.*, the conductivity of EMITFSI is approximately three times higher than BMITFSI), but it was originally hypothesized that the hydrophobic character of the aliphatic chain in BMITFSI would lead to enhanced solubility in the liquid reaction mixture. As the reaction proceeds, BMITFSI becomes less soluble in the medium of the growing P(S-*co*-DVB) block and partitions to the PEO phase when the effective M of the growing P(S-*co*-DVB) block is on the order of several kg/mol.[23,56] In spite of the preliminary concerns regarding ionic liquid solubility, it will be shown that the PIPS PEM strategy appears to also work with EMITFSI.

For Li-ion battery applications, lithium-based salts are required, so samples were also prepared with mixtures of lithium bis(trifluoromethylsulfonyl)imide (LiTFSI) in BMITFSI. LiTFSI is a crystalline solid at low temperature ($T_m \approx 234\,°C$), and it was found that neat LiTFSI did not fully dissolve in mixtures of S/DVB + PEO-CTA, even at the reaction temperature ($120\,°C$). It is possible that LiTFSI exhibits some degree of solubility under these conditions, and that a measurable concentration of salt would ultimately reside in the PEO phase, but samples containing only LiTFSI were not tested further. Instead, it was found that mixtures of up to 2 M LiTFSI in BMITFSI were readily soluble in the reaction mixture, and these samples were used as a proof-of-concept for Li-ion battery applications.

Morphological Characterization

The morphology of PIPS PEM samples was characterized with a combination of SAXS, TEM, and SEM. Figure 2.5 shows SAXS data for samples prepared with 5 and 28 kg/mol PEO-CTA ($w_{\text{PEO-CTA}} = 32$ wt% ≈ 30 vol%) and a range of BMITFSI concentrations. In general, the SAXS data exhibit a relatively broad peak at low q and few, if any, higher order peaks, which is consistent with microphase separated domains lacking periodic long-range order. Assuming all of the BMITFSI partitions to the PEO domain (this assumption will be explored shortly), the equivalent linear
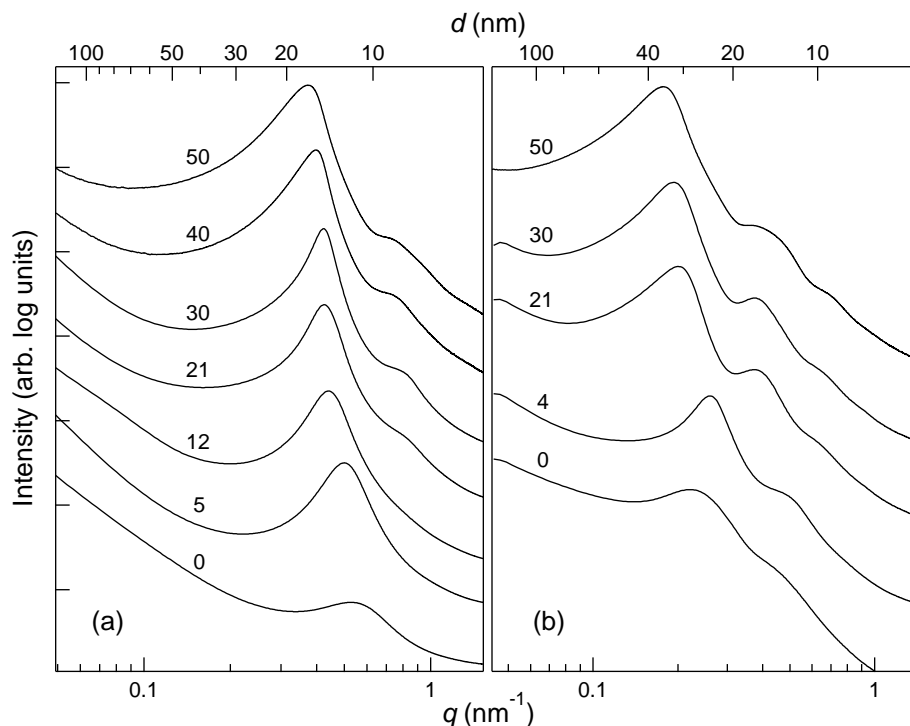
Figure 2.5: Small angle X-ray scattering data of PIPS PEM samples prepared with (a) 5 and (b) 28 kg/mol PEO-CTA (32 wt%) and various concentrations of the ionic liquid BMITFSI. All samples were exposed at room temperature. The top axis shows the d-spacing, which is given by $d = 2\pi/q$. BMITFSI concentration is reported by the numbers in the graph as overall vol%. Refer to Table 2.1 for a complete description of sample composition.

diblock volume fractions would place PIPS PEMs inside either the hexagonally close-packed cylinder or lamellar phase window, depending on the amount of ionic liquid added. The possible existence of long-range domain order was investigated by referencing the observed peaks to allowed reflections for four common diblock copolymer equilibrium morphologies: lamellae, gyroid, hexagonally close-packed (HCP) cylinders, and body-centered cubic (BCC) spheres. Figure 2.6 shows referenced peaks for one representative sample prepared with 28 kg/mol PEO-CTA ($w_{\text{PEO-CTA}} = 32$ wt%) and 30 vol% BMITFSI. The observed peaks are clearly inconsistent with the gyroid, HCP, and BCC Bragg conditions. For this particular sample, the second peak is close to the $2q^*$ peak for the lamellar structure factor, suggesting some degree of lamellar
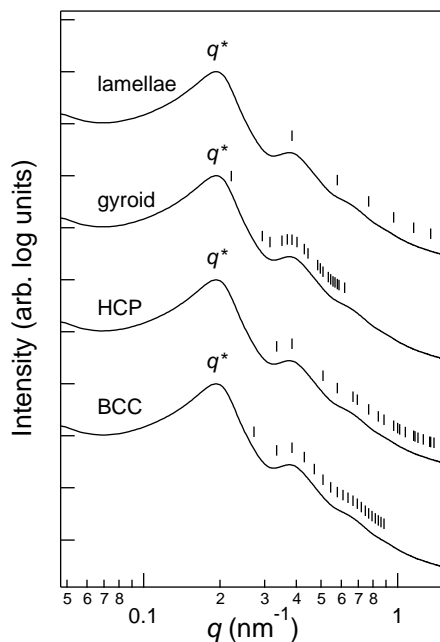
Figure 2.6: Small angle X-ray scattering data of a PIPS PEM sample prepared with 28 kg/mol PEO-CTA (32 wt%) and 30 overall vol% BMITFSI. The tick marks point to locations of allowed reflections for common diblock copolymer equilibrium morphologies (identified next to each trace). Allowed reflections are given as ratios of q/q^*. Lamellar: $1:2:3:4\ldots$; gyroid (Ia$\bar{3}$d): $\sqrt{6}:\sqrt{8}:\sqrt{14}:\sqrt{16}:\sqrt{20}\ldots$ HCP: $1:\sqrt{3}:\sqrt{4}:\sqrt{7}:\sqrt{9}:\sqrt{12}\ldots$; BCC: $1:\sqrt{2}:\sqrt{3}:\sqrt{4}:\sqrt{5}:\sqrt{6}\cdots$

character. However, there appears to be a broad, higher order peak at $q \approx 0.67$ nm^{-1} which cannot be accounted for by the lamellar structure factor. It is likely that the higher order peaks in PIPS PEMs scattering data simply reflect long-range domain correlations, such as those observed in the structure factor of liquid argon.[150]

The position of the primary scattering peak indicates that preferred spacing of compositional heterogeneity exists on length scales between 10 and 30 nm. This characteristic domain size can be tuned by modulating several easily accessible experimental parameters: (i) $M_{\text{PEO-CTA}}$, (ii) the concentration of PEO-CTA in the reaction mixture, $w_{\text{PEO-CTA}}$, and (iii) the concentration of ionic liquid. Referring back to Figure 2.5, samples prepared with 5 kg/mol PEO-CTA have a characteristic length scale between 10–15 nm, and increasing $M_{\text{PEO-CTA}}$ to 28 kg/mol at a fixed concentration

in the reaction mixture (in this case, 32 wt%) increases the average center-to-center distance to 25–35 nm.

The addition of ionic liquid has several effects on the scattering, all of which are consistent with the ionic liquid acting as a selective "solvent" for PEO.[56,151] Increasing the concentration of BMITFSI increases the average domain size both by simple volume addition to the PEO domain and increasing chain stretching at the PEO/P(S-co-DVB) interface. The latter effect is a result of increasing the effective interaction parameter, χ^{eff}, between P(S-co-DVB) and PEO/BMITFSI, relative to P(S-co-DVB) and pure PEO.[152] The increase in χ^{eff} upon salt doping can be approximated as follows. Zhu et al.[153] fit experimental X-ray scattering data of a disordered PS-b-PEO diblock to Leibler's random phase approximation (RPA) structure factor[154] to determine the temperature dependence of $\chi^{\text{eff}}_{\text{SO}}$ (SO refers to PS-b-PEO). The authors found that well above the order-disorder transition temperature, T_{ODT}, the inverse intensity is linear in $1/T$, and the temperature dependence of χ^{eff} is

$$\chi^{\text{eff}}_{\text{SO}}(T) = \frac{21.3}{T} - 7.05 \times 10^{-3} \tag{2.3}$$

using a reference volume of 100 Å^3. Per eq 2.3, at the reaction temperature typically used for PIPS PEMs (120 °C), $\chi^{\text{eff}}_{\text{SO}} = 0.047$. A number of studies have directly investigated the effect of doping block polymers with high T_{m} salt on χ^{eff}.[85,155–159] For example, Young et al.[159] calculated χ^{eff} for PS-b-PEO diblocks doped with the Li-based salts LiClO$_4$, LiCF$_3$SO$_3$, and LiAsF$_6$. The authors used the observed increase in domain spacing with increasing salt concentration to calculate the change in $\chi^{\text{eff}}_{\text{salt}}$, relative to the neat diblock, $\chi^{\text{eff}}_{\text{neat}}$. In the limit of strong segregation (defined as $\chi N \gg 10$), Semenov[160] had previously shown that $d^* \sim \chi^{1/6}$, from which Young et al. calculated the increase in the effective interaction parameter (relative to the neat diblock) as $\chi^{\text{eff}}_{\text{salt}} = \chi^{\text{eff}}_{\text{neat}}(d^*_{\text{salt}}/d^*_{\text{neat}})^6$. In a complementary example, Wanakule et al.[85] also studied PS-b-PEO, but doped with LiTFSI. In this case, the authors measured the T_{ODT} and calculated χ^{eff} within the framework of both mean field and

fluctuation-corrected theories. Both of the studies above found a steep linear increase in the interaction parameter relative to the neat diblock. More recently, Teran et al.[157] calculated χ^{eff} for PS-b-PEO/LiTFSI blends by fitting SAXS data to Leibler's full RPA expression for the structure factor of disordered diblocks. However, one possible source of quantitative discrepancy in this study is the close proximity of the experimental temperatures to the T_{ODT}. Scattering was typically measured within 50 °C of the T_{ODT}, and it has been shown that fluctuation-induced departures from the mean field prediction for scattered intensity can extend well above the T_{ODT}.[129,161]

Despite quantitative differences between all these studies (most likely due to the different methods used to calculate χ^{eff},[162] even after factoring in slightly different reference volumes), the common lesson is that doping one phase of a block polymer with salt results in a drastic increase in the interaction parameter relative to the neat diblock. Furthermore, the effect of salt doping often overwhelms the standard temperature dependence of χ, pushing the T_{ODT} outside the experimentally accessible window. It is therefore not surprising that adding a strongly selective salt to the PIPS reaction mixture increase domains spacing by increasing chain stretching at the interface, as the addition of salt substantially increases χ^{eff}.

The addition of ionic liquid increases the relative scattered intensity: compare, for example, the height of the structure factor peaks relative to the respective baselines as ionic liquid concentration increases for samples in Figure 2.5. In SAXS, the contrast required for scattering originates from differences in the electron density—typically reported in terms of the scattering length density, ρ—between domains.

Figure 2.7 is a schematic of scattering contrast for an ideal two-phase model, which approximates a microphase separated block polymer. In the limit that the two domains of a microphase separated block polymer exhibit identical scattering length densities, the sample scatters like a homogeneous material: scattered radiation will always destructively interfere with radiation of equal amplitude originating an integer of a half wavelength away, resulting in zero net scattered intensity. The X-ray
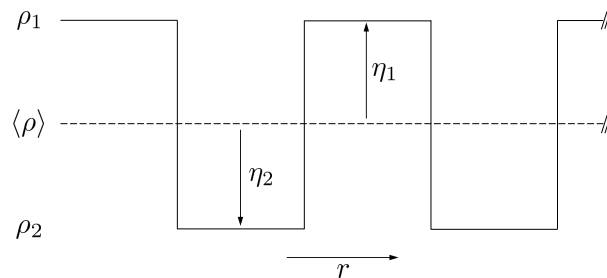
Figure 2.7: Schematic of the ideal two-phase model. ρ_i is the scattering length density (SLD) of phase i. $\langle\rho\rangle$ is the average SLD, calculated as $\langle\rho\rangle = \phi_1\rho_1 + \phi_2\rho_2$, where ϕ_i is the volume fraction of phase i. η_i is the difference between the SLD of phase i and the average SLD, calculated as $\eta_i = \rho_i - \langle\rho\rangle$. The scattered intensity is proportional to the mean square fluctuation of SLD about the average, calculated as $\langle\eta^2\rangle = \phi_1\eta_1^2 + \phi_2\eta_2^2$.

scattering length density of PEO is 9.8×10^{-10} cm^{-2}, which is only slightly higher than PS (8.8×10^{-10} cm^{-2}), providing little inherent contrast between the PS and PEO domains and, thus, weak scattering intensity from samples prepared without ionic liquid. Addition of BMITFSI ($\rho = 11.5 \times 10^{-10}$ cm^{-2}) to the PEO phase increases the contrast between domains, thus increasing the intensity of the scattering peaks. Finally, as mentioned above, samples prepared with ionic liquid exhibit higher order peaks that grow in number and intensity as the concentration of BMITFSI increases. This result indicates that BMITFSI increases the domain correlation length from less than one wavelength of compositional periodicity to more than several domains.

DSC data for PIPS PEMs (Table 2.2 and Figure 2.8) are consistent with BMITFSI partitioning to the PEO phase. In general, the DSC thermograms exhibit an endothermic peak corresponding to melting PEO crystals, and some DSC traces exhibit a glass transition at temperatures consistent with PEO/BMITFSI mixtures (*ca.* -60 °C). Furthermore, the thermal response of the PEO/IL phase in PIPS PEMs mirrors that of bulk electrolytes prepared with PEO homopolymer ($M = 8$ kg/mol) and BMITFSI.

As shown in Figure 2.8, increasing the concentration of ionic liquid reduces both the temperature at which the PEO melting peak exhibits a maximum and the overall weight fraction of PEO that crystallizes. Table 2.2 summarizes these parameters for

Table 2.2: Thermal transitions of PIPS PEM and PEO homopolymer/BMITFSI electrolyte samples shown in Figure 2.8

$M_{\text{PEO-CTA}}$ (kg/mol)	BMITFSI concentration[i] (vol%)	T_{g} (°C)	$T_{\text{m,max}}$ (°C)	crystallinity[ii] (wt%)
5	0	–52	26	25
5	12	–58	29	28
5	21	–58	-	-
5	30	–61	-	-
28	0	-	49	42
28	4	-	46	43
28	21	–66	35	32
28	30	–64	25	25
M_{PEO}[iii]				
8	5	-	61	80
8	10	-	60	68
8	20	-	58	52
8	30	-	54	43

[i] Overall volume fraction of BMITFSI
[ii] Calculated using 200 J/g, per ref 148
[iii] M_{PEO} refers to PEO homopolymer

most samples shown in Figure 2.8. In addition, PIPS PEM samples prepared with 5 kg/mol PEO-CTA exhibit a lower crystalline fraction than the analogous samples prepared with 28 kg/mol PEO-CTA. This is consistent with the higher concentration of chain ends, which act as defects in crystal formation,[40] in the shorter PEO. One notable difference between the homopolymer-based samples and PIPS PEMs is in the scale: the crystalline fraction in the bulk electrolyte is *ca.* 2–3 times greater than in the nanostructured PIPS PEMs. The most likely explanation for the reduction in crystallinity is confinement of PEO to nanoscopic domains and tethering of one end of the PEO chains to the glassy P(S-*co*-DVB) wall, both of which kinetically inhibit crystallization.[163–169] The morphology of PIPS PEMs therefore inherently reduces PEO crystallinity, which should enhance room temperature conductivity, an idea
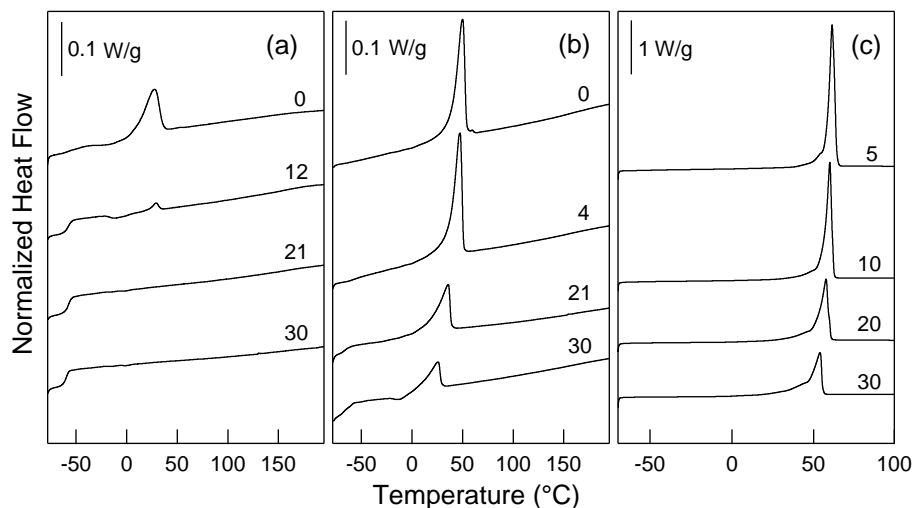
Figure 2.8: Differential scanning calorimetry thermograms (exo down) for PIPS PEMs prepared with (a) 5 and (b) 28 kg/mol PEO-CTA (32 wt%) and various concentrations of the ionic liquid BMITFSI. (c) Mixture of homopolymer PEO (M_n = 8 kg/mol) and BMITFSI. The numbers next to the traces give the concentration of BMITFSI in vol% of the PEO/IL phase. Note that the vertical scale in (c) is 10 times larger than in (a) and (b).

which will be revisited when conductivity data are discussed.

As mentioned previously, the majority of the samples discussed in this chapter were prepared with a PEO-CTA conentration, $w_{\text{PEO-CTA}}$, of 32 wt% in the reaction mixture. However, one advantage of the PIPS strategy is the versatility it offers in terms of the compositional window. To demonstrate this versatility, PEMs were also prepared with a nominal PEO-CTA concentration of 42 wt%. Figure 2.9 compares SAXS data for samples prepared with 32 wt% PEO-CTA to those prepared with 42 wt% PEO-CTA, over a range of concentration of the ionic liquid BMITFSI. The scattering data for samples prepared with 42 wt% PEO-CTA show similar trends to those discussed earlier for samples prepared with 32 wt% PEO-CTA, suggesting that the PIPS strategy can be successfully extended to higher concentrations of PEO-CTA. Specifically, the structure factor is characterized by a broad peak corresponding to length scales between 10 and 15 nm. In addition, the peak shifts to lower q as the concentration of ionic liquid is increased, consistent with the ionic liquid preferentially
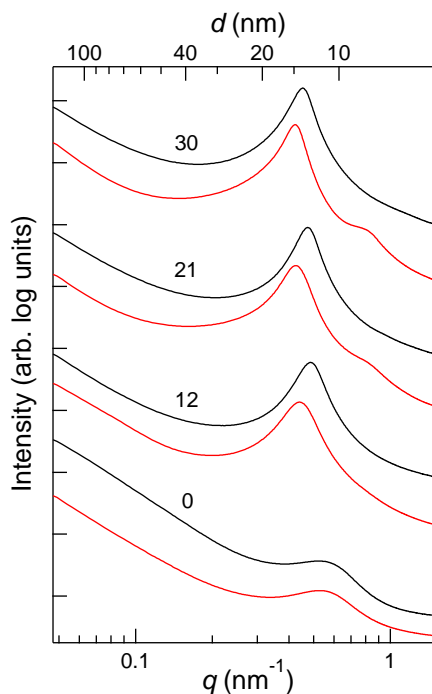
Figure 2.9: SAXS data of PIPS PEMs prepared with 5 kg/mol PEO-CTA at (red traces) 32 and (black traces) 42 wt%, a 4/1 molar ratio of styrene/divinylbenzene, and the ionic liquid BMITFSI. The number next to each pair of traces gives the overall concentration of BMITFSI in vol%.

swelling the PEO domain. Finally, the primary scattering peak for samples prepared with 42 wt% is shifted to higher q relative to the corresponding sample prepared with 32 wt% PEO-CTA, across the entire range of ionic liquid concentrations studied. That is, the average center-to-center domain spacing decreases slightly with increasing $w_{\text{PEO-CTA}}$.

As a proof-of-concept for Li-ion battery applications, PIPS PEMs were prepared with mixtures of LiTFSI in BMITFSI. Figure 2.10 shows scattering data for samples prepared with 5 and 28 kg/mol PEO-CTA (32 wt%) and mixtures of LiTFSI in BMITFSI at an overall concentration of 21 vol%. At this fixed overall salt concentration, the concentration of LiTFSI was increased from 0 (pure BMITFSI) to 2 M LiTFSI. The motivation for increasing the concentration of LiTFSI will be discussed in more detail when conductivity data are presented, although briefly, higher
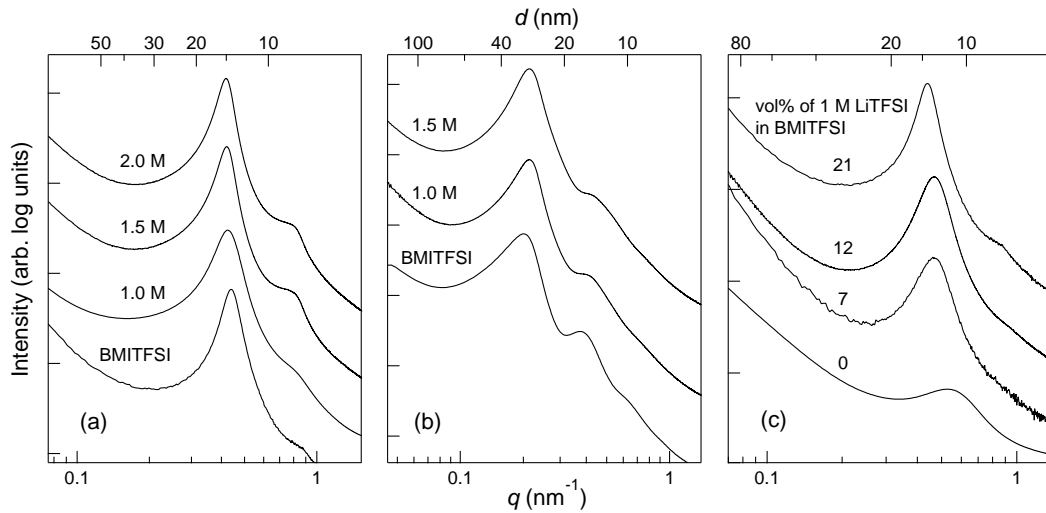
Figure 2.10: SAXS data of PIPS PEMs prepared with (a) 5 and (b) 28 kg/mol PEO-CTA (32 wt%) and increasing concentration of LiTFSI in BMITFSI. The overall salt concentration for all samples is 21 vol%. (c) SAXS data of PIPS PEMs prepared with 5 kg/mol PEO-CTA (32 wt%) and a mixture of 1 M LiTFSI in BMITFSI. The numbers next to each trace are the overall salt mixture concentration in vol%.

concentrations of LiTFSI should increase the transference number of Li ions, t_{Li^+}, an important parameter in electrochemical device design. In terms of morphology, Figure 2.10 shows that for a given $M_{PEO\text{-}CTA}$, the characteristic length scale of heterogeneity does not change. This is not surprising, as the overall volume fraction of salt is fixed at 21 vol% for all samples.

The predominant effect of increasing the molarity of Li^+ appears to be an increase in the correlation length, as evidenced by the emergence and subsequent sharpening of a higher order peak in samples prepared with 5 kg/mol PEO-CTA (Figure 2.10(a)). The increase in structural coherence is likely a result of an increase in segregation strength with increasing molarity of Li^+, which is consistent with previous reports of the increase in χ^{eff} between PEO/LiTFSI and polystyrene, relative to the neat diblock.[85,170] It is not clear why samples prepared with 28 kg/mol PEO-CTA do not appear to follow the trend observed in samples prepared with 5 kg/mol PEO-CTA. Figure 2.10(c) shows the effect of increasing the overall salt concentration of a mixture
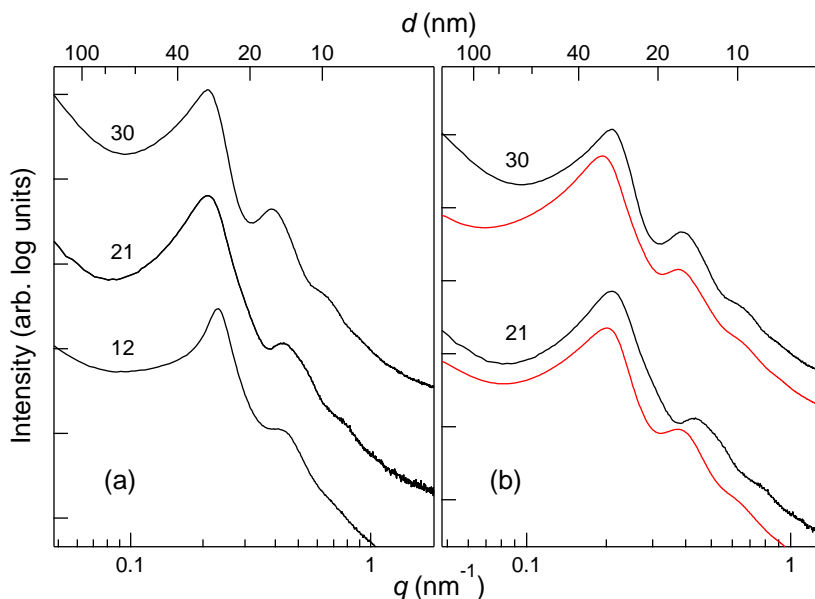
Figure 2.11: (a) SAXS data of PIPS PEMs prepared with 28 kg/mol PEO-CTA (32 wt%) and the ionic liquid EMITFSI. (b) Comparison of SAXS data for samples prepared with (black traces) EMITFSI or (red traces) BMITFSI at the same ionic liquid concentration. The numbers next to each trace are the overall ionic liquid concentration in vol%.

of 1 M LiTFSI in BMITFSI. In general, the trend is similar to that observed in samples prepared with pure BMITFSI, namely the overall shift of the primary peak to lower q with increasing salt concentration. It is not clear why the peak shift between 7 and 12 vol% is negligible.

As another test of the versatility of the PIPS framework, PEMs were prepared with the ionic liquid 1-ethyl-3-methylimidazolium bis(trifluoromethylsulfonyl)imide (EMITFSI) in lieu of BMITFSI. The motivation for using EMITFSI is that the conductivity of neat EMITFSI is approximately three times higher than that of BMITFSI. The conductivity of nanostructured electrolytes such as PIPS PEMs is guaranteed to be lower than the neat polymer/salt mixture, and starting with a higher conductivity salt helps to offset the inherent reduction.

Figure 2.11 shows scattering data for samples prepared with 28 kg/mol PEO-CTA (32 wt%) and various concentrations of EMITFSI. Although there are subtle difference between samples containing EMITFSI versus BMITFSI (Figure 2.11(b)), the data in
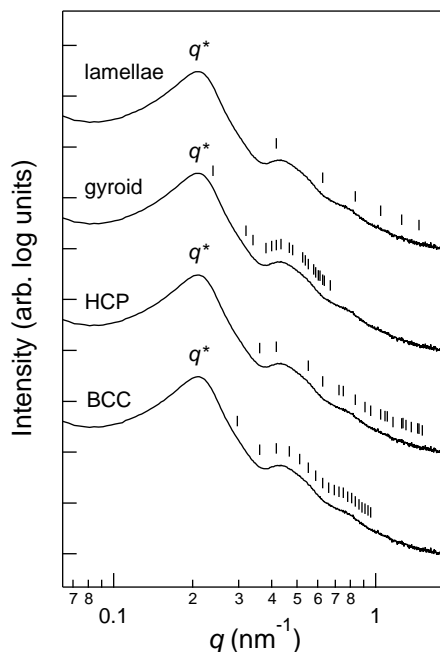
Figure 2.12: Small angle X-ray scattering data of a PIPS PEM sample prepared with 28 kg/mol PEO-CTA (32 wt%) and 30 overall vol% EMITFSI. The tick marks point to locations of allowed reflections for common diblock copolymer equilibrium morphologies (identified next to each trace). Allowed reflections are given as ratios of q/q^*. Lamellar: $1 : 2 : 3 : 4 \ldots$; gyroid (Ia$\bar{3}$d): $\sqrt{6} : \sqrt{8} : \sqrt{14} : \sqrt{16} : \sqrt{20} \ldots$; HCP: $1 : \sqrt{3} : \sqrt{4} : \sqrt{7} : \sqrt{9} : \sqrt{12} \ldots$; BCC: $1 : \sqrt{2} : \sqrt{3} : \sqrt{4} : \sqrt{5} : \sqrt{6} \ldots$

general are consistent with previously discussed samples containing BMITFSI. In particular, the traces exhibit a broad peak at low q and higher order peaks that quickly fall off in intensity. Furthermore, the primary peak shifts to lower q with increasing concentration of EMITFSI. Finally, as shown in Figure 2.12, the observed peak ratios do not reduce to those allowed for four common diblock polymer morphologies (lamellae, gyroid, HCP cylinders, and BCC spheres). One notable difference appears to be the relative increase in intensity of the higher order peaks. For example, the EMITFSI-containing samples exhibit a clear third peak at high q (≈ 0.66 nm^{-1}), whereas the higher order peak BMITFSI-containing samples is less pronounced. The fact that higher order peaks are observed in EMITFSI-containing samples indicates
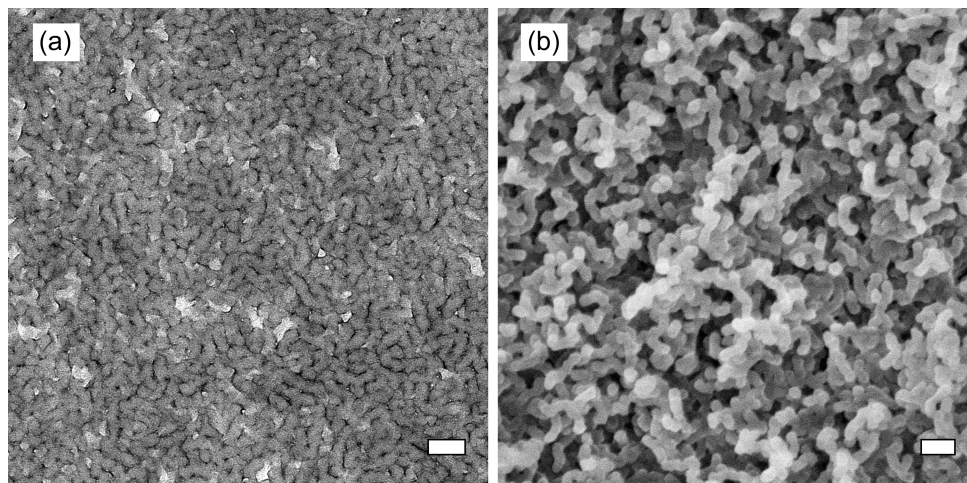
Figure 2.13: Morphology of PIPS PEM samples prepared with 28 kg/mol PEO-CTA and 21 vol% BMITFSI. (a) Transmission electron micrograph of the sample prior to etching. The PEO/ionic liquid domain appears dark after staining with RuO_4. Bright regions are crosslinked polystyrene (b) Scanning electron micrograph of the sample after etching PEO and BMITFSI with 57 wt% aqueous hydroiodic acid. The pores/voids are regions that were PEO/BMITFSI prior to etching. The remaining bright structure is crosslinked polystyrene. The sample was coated with 1–2 nm of Pt prior to imaging. Both scale bars represent 100 nm.

that, as in the case with BMITFSI, the domain correlation length extends well beyond the size of one domain. One plausible explanation for the increased intensity is that EMITFSI is less hydrophobic than BMITFSI. The corresponding increase in χ^{eff} between PEO/EMITFSI and P(S-*co*-DVB) should increase domain purity and, thus, scattered intensity, possibly helping to resolve the weak higher order correlation peaks.

Real space images of PIPS PEMs corroborate the scattering data discussed above. Figure 2.13 shows TEM and SEM micrographs of PIPS PEM samples prepared with 28 kg/mol PEO-CTA and 21 vol% BMITFSI. In general, both micrographs reveal spatial heterogeneity on length scales consistent with the SAXS primary scattering peak (25–35 nm). In addition, the domains lack long-range periodic order, in agreement with lack of higher order SAXS peaks.

The SEM image was collected after etching the PEO/IL phase with hydroiodic
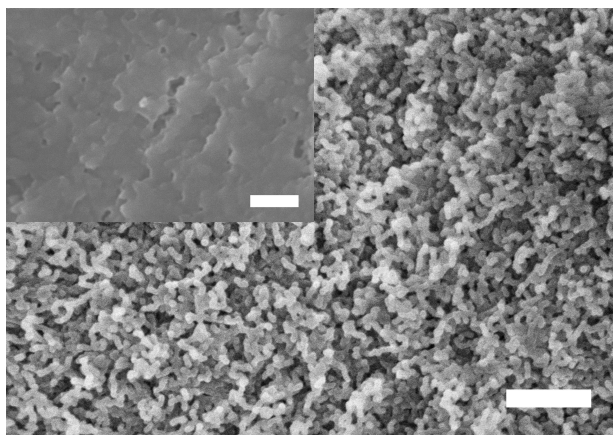
Figure 2.14: Scanning electron micrographs comparing a PIPS PEM sample prepared with 28 kg/mol PEO-CTA and 21 vol% BMITFSI, before (inset) and after (main panel) etching out PEO/IL with 57 wt% hydroiodic acid. Both samples were freeze-fractured to expose a fresh surface and were coated with 1–2 nm of Pt prior to imaging. Both scale bars represent 500 nm.

acid, so the dark regions in the TEM image (a result of staining PEO with RuO_4) are pores in the SEM image. Figure 2.14 compares the topography of unetched and etched samples, confirming that the porous network results from etching PEO/IL. The SEM image mirrors the TEM image in size scale and spatial arrangement of domains and provides a "3D" perspective of the "2D" TEM slice. Note that although both images appear to reveal a "bicontinuous" morphology, true macroscopic bicontinuity (which is critical for maximizing conductivity) must be confirmed with macroscopic mass transport experiments. For example, an auxiliary result of SEM sample preparation was that the mass loss upon etching PEO/BMITFSI was found to be in quantitative agreement (within measurement error) with the expected mass loss, suggesting long-range connectivity of the PEO domains.

Figure 2.15 compares TEM images prepared with 28 kg/mol PEO-CTA, with and without BMITFSI (21 vol%). As shown in Table 2.1, the addition of BMITFSI to PIPS PEMs swells the PEO domain and increases the volume fraction of the conductive phase from 32 to 47 vol%. Since PEO was stained with RuO_4 and appears dark in TEM images, the increase in volume should appear as an increase in the total
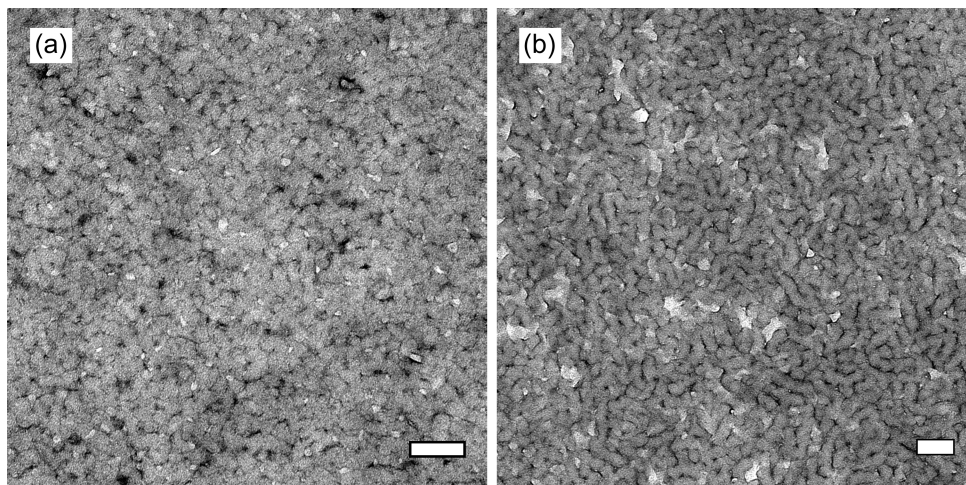
Figure 2.15: Morphology of PIPS PEMs prepared with 28 kg/mol PEO-CTA (a) without ionic liquid and (b) with 21 vol% BMITFSI. The PEO/ionic liquid domain appears dark after staining with RuO_4. Bright regions are crosslinked polystyrene. Both scale bars represent 100 nm.

number of dark pixels (assuming the sections are approximately the same thickness). Although the relative fraction of light and dark pixels was not quantified, visual inspection of the TEM images with and without ionic liquid suggests an increase in the number of dark pixels upon addition of ionic liquid. Furthermore, the sample prepared without ionic liquid appears to have a wider distribution of domain size and arrangement, as compared to the sample prepared with ionic liquid. For example, Figure 2.15(a) reveals seemingly randomly-placed PEO-rich dark regions within a matrix of more uniform domains, whereas the morphology in Figure 2.15(b) is a more consistent "mesh" across the whole image. This distribution of feature sizes might explain why the primary SAXS peak is broader for samples prepared without ionic liquid, and becomes more narrow as ionic liquid concentration increases.

One shortcoming of microscopy is that analysis of morphology is based on regions that are only hundreds of square nanometers (*e.g.*, the images in Figures 2.13 and 2.15), which are not necessarily representative of the average morphology. Therefore, as shown in Figure 2.16, Fourier transform (FT) analysis of TEM images was used to investigate whether the morphology observed in microscopy accurately represents
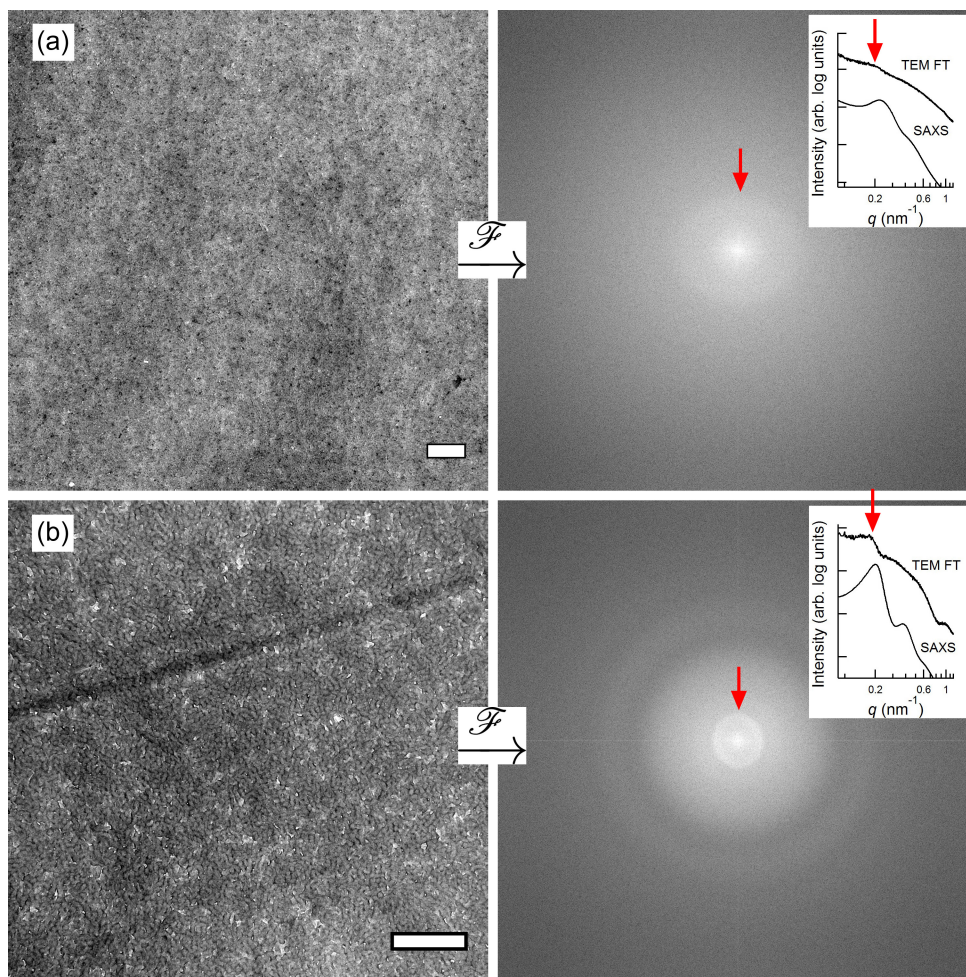
Figure 2.16: Fourier transform (FT) analysis of TEM images of PIPS PEMs. (a) TEM image of a sample prepared with 28 kg/mol PEO-CTA and no ionic liquid, and the corresponding FT. (b) TEM image of a sample prepared with 28 kg/mol PEO-CTA and 21 vol% BMITFSI, and the corresponding FT. The dark streak in the TEM image in (b) is likely an artifact of microtoming. Pixel intensity in the FTs was azimuthally integrated and plotted versus wave vector q. The inset graphs compare FT integration to SAXS data collected from bulk samples. Scale bars in (a) and (b) represent 500 nm.

the average, bulk morphology. In contrast, scattering experiments such as SAXS inherently probe the average structure within the illuminated sample volume. In the case of FT analysis, as in scattering experiments, if there exists a preferred frequency of spatial heterogeneity in the real space distribution, $\rho(r)$, of scattering centers (which is proportional to pixel intensity in TEM images), then $\mathscr{F}(\rho)$ returns a peak in the structure factor. Strictly speaking, $\mathscr{F}(\rho)$ gives the structure factor in terms of the scattering amplitude, the square of which is scattered intensity, but the results of FT analysis here can still be correlated with SAXS data in terms of q. The graphs in Figure 2.16 show good agreement between TEM FTs and SAXS data, confirming that the TEM images are representative of the bulk morphology. In practice, FT analysis requires images at low magnification relative to the sample feature size to average over many domains. For example, the scale bars in Figure 2.16 represent 500 nm, while the characteristic sample feature size is only 25–35 nm. Furthermore, if the wavelength of the average domain size is large relative to the image, the FT ring appears too close to the bright center of the 2D FT (*i.e.*, at too low a frequency) to clearly resolve a peak.

Collectively, the scattering and real space morphological characterization data are consistent with a microphase separated structure lacking periodic long-range order, shown schematically in Figure 2.17. Compositional heterogeneity exists on length scales between 10 and 30 nm, in which the domains comprise poly(ethylene oxide)/salt (yellow) and highly crosslinked polystyrene (blue). This nanoscale heterogeneity should effectively decouple the key macroscopic properties, modulus and conductivity.
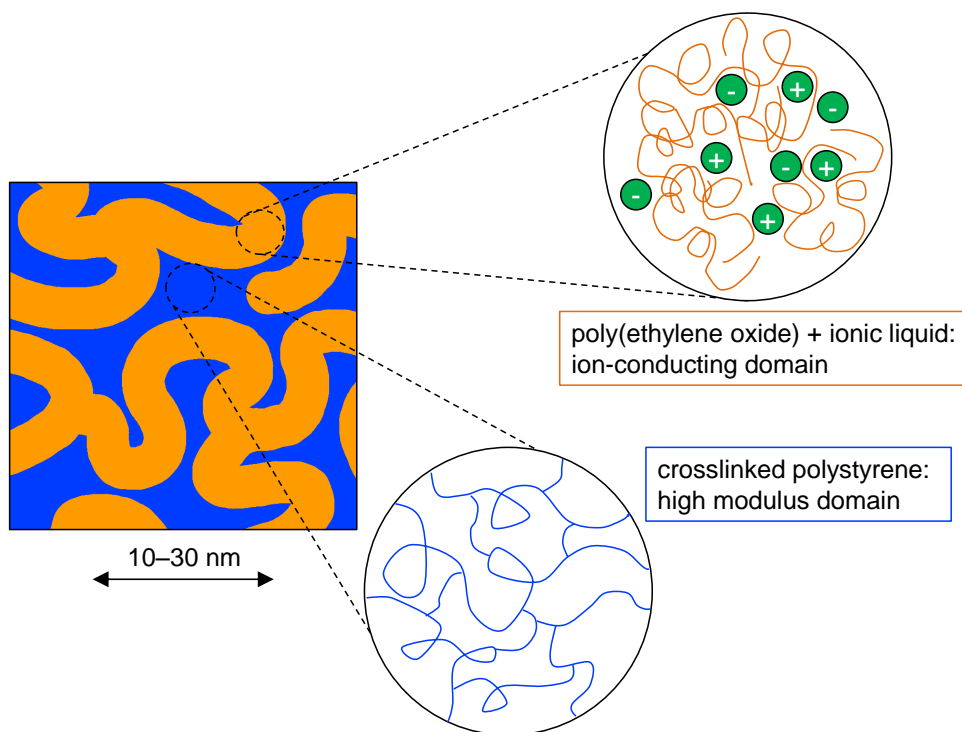
Figure 2.17: Schematic representation of the morphology in PIPS PEMs, as supported by a suite of experimental techniques, including SAXS, DSC, TEM, and SEM. PIPS PEMs are microphase separated on length scales of 10–30 nm, but the domains lack long-range periodic order. The yellow domains are poly(ethylene oxide)/salt, and blue domains are crosslinked polystyrene.

Mechanical Response

The linear mechanical response of PIPS PEM samples was measured with isothermal frequency sweeps from room temperature up to *ca.* 200 °C (Figure 2.18). Samples were also prepared without ionic liquid to quantify the effect of adding mobile charges to the PEO domain on macroscopic mechanical properties. In general, PIPS PEMs are high modulus solids ($\tan(\delta) = E''/E' < 0.1$) across the entire temperature range studied. The elastic modulus, E', approaches 1 GPa at room temperature, nearly satisfying the 1 GPa modulus metric often cited in the Li-ion battery community.[5,11–13,76] Furthermore, the samples soften only moderately to *ca.* 10 MPa in the vicinity of 200 °C. The mechanically robust, crosslinked P(S-*co*-DVB) network enables PIPS PEMs to operate as solid electrolytes at temperature well above the glass transition of linear PS ($T_g \approx 100$ °C). In contrast, polymer electrolytes that rely on a glassy block for mechanical integrity (*e.g.*, PS-*b*-PEO/LiTFSI) experience a drastic decrease in elastic modulus above $T_{g,PS}$ and eventually flow.[5,76,111,113,171]

To generate Figure 2.18, the raw frequency sweep data were shifted horizontally according to time-temperature superposition (tTS) to generate viscoelastic master curves extending over an impressive 18–25 decades of reduced frequency. The fact that tTS works for a composite material like PIPS PEMs suggests that the macroscopic mechanical response is dominated by one phase (*i.e.*, one monomeric friction factor). This is reasonable, as the high modulus, crosslinked PS phase is isotropically continuous and the PEO/IL phase contributes effectively nothing to the bulk modulus over most of the temperature range studied. Figure 2.19 shows the shift factors, a_T, used for tTS in Figure 2.18. For all samples studied, the temperature dependence of the shift factors is roughly linear on a log scale and thus cannot be modeled by the Williams-Landel-Ferry (WLF) equation.[172] However, WLF behavior requires a linear dependence of free volume with temperature,[40] which is only expected to occur above the T_g. The PIPS PEM samples were measured in part below the T_g of linear PS, and crosslinking PS increases the effective T_g well above 100 °C, so the observed
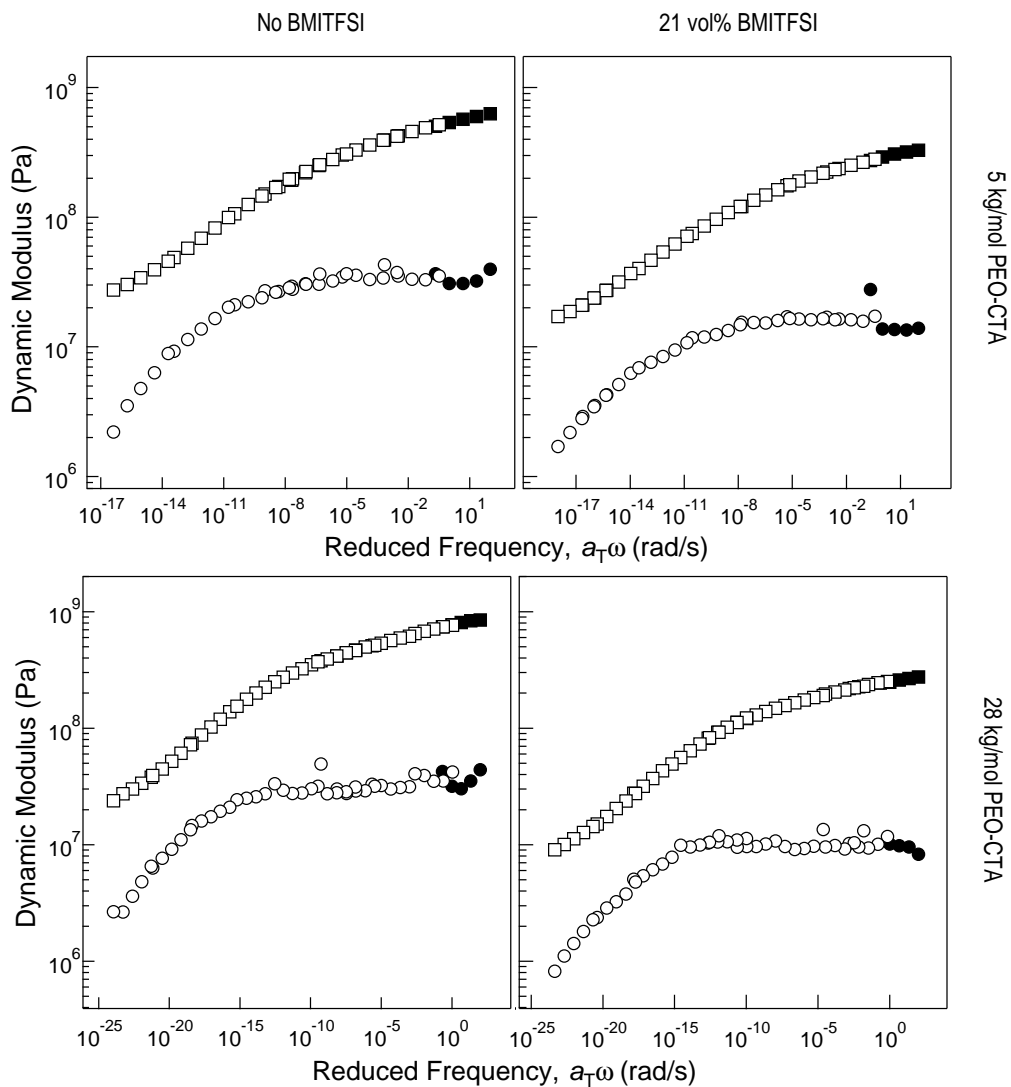
Figure 2.18: Time-temperature superposition master curves for PIPS PEM samples prepared with 5 and 28 kg/mol PEO-CTA and 21 vol% BMITFSI. Samples were also measured without ionic liquid. The subplots are arranged in a grid, and the samples are identified by labels on the top and right. The elastic (E', □) and viscous (E'', ○) moduli were measured as a function of angular frequency from room temperature up to *ca.* 200 °C. The reference temperature data sets ($T_{ref} = 25$ °C for all data sets) are denoted by filled symbols. Some of the filled data points are hidden by open symbols.
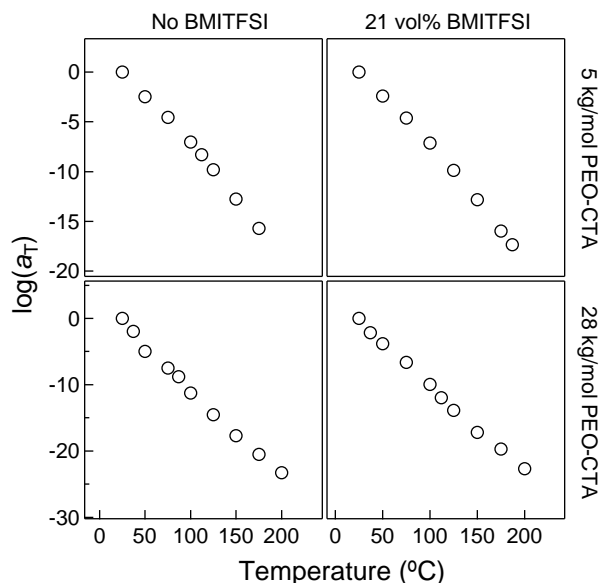
Figure 2.19: Shift factors, a_T, for time-temperature superposition master curves shown in Figure 2.18. The subplots are arranged in a grid, and the samples are identified by labels on the top and right.

non-WLF behavior is not surprising.

Interestingly, there does not appear to be a distinct glass transition in the frequency sweeps in Figure 2.18. Instead, the samples gradually soften with progressive increases in T. This observation is consistent with DSC experiments (Figure 2.8), which did not exhibit a clear change in slope of the heat traces up to 200 °C. The lack of a distinct T_g is likely a result of the high crosslink density. On average, one in five repeat units in the P(S-co-DVB) block are crosslinked. However, due to the presumed random incorporation of DVB into the growing P(S-co-DVB) block, there are likely runs of higher crosslink density, as well as regions of essentially linear PS. It is plausible that the non-uniform crosslink density effectively traps dynamic heterogeneities, which are local regions of the polymer matrix that exhibit widely disparate relaxation dynamics.[173–175] The result is the wide T range of softening of the P(S-co-DVB) matrix seen in the master curves.
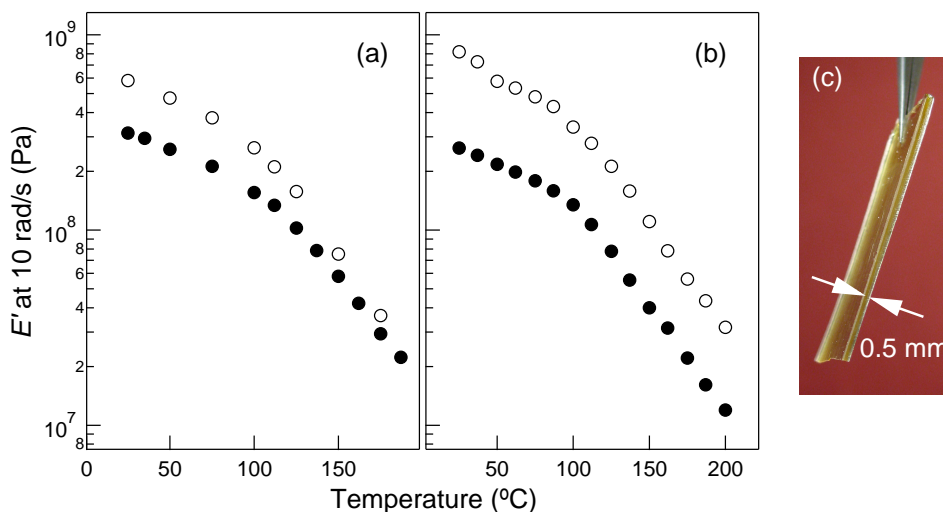
Figure 2.20: Linear elastic modulus at 10 rad/s for PIPS PEMs prepared with (a) 5 and (b) 28 kg/mol PEO-CTA and 21 vol% BMITFSI (●). For comparison, samples were prepared without ionic liquid (○). The data points are the elastic modulus, E', at 10 rad/s and were extracted from isothermal frequency sweeps shown in Figure 2.18. (c) Photograph of a typical tensile bar used.

Figure 2.20 shows the elastic modulus versus temperature at a fixed angular frequency (10 rad/s) to clearly illustrate that addition of ionic liquid to the PEO phase has minimal impact on the macroscopic mechanical properties. Adding 21 vol% BMITFSI reduces the bulk elastic modulus by a factor of 2–3 for both values of $M_{\text{PEO-CTA}}$ studied (5 and 28 kg/mol). For co-continuous composites in which the two phases exhibit orthogonal properties, the effective macroscopic properties are a (potentially complex) function of volume fraction and morphology.[97,176–178] However, to a first approximation, a simple volume-weighted average roughly predicts the drop in modulus observed in PIPS PEMs. As shown schematically in Figure 2.21, the volume fraction of crosslinked PS decreases by a factor of 1.5, from 68 to 53 vol% (see Table 2.1), consistent with the factor of 2 decrease in modulus. The most striking result of this experiment is that approximately half of the ionic liquid-containing sample is effectively liquid (PEO/salt), yet the macroscopic sample is a high modulus solid. This performance is enabled by the bicontinuous network morphology and, in particular,
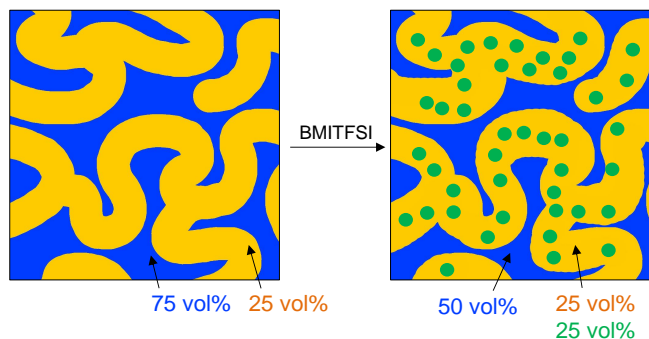
Figure 2.21: Schematic showing the decrease in volume fraction of high modulus crosslinked polystyrene (blue) upon addition of ionic liquid (green dots) to the poly(ethylene oxide) (yellow) domain. This example roughly corresponds to the samples shown in Figure 2.20, although the volume fractions listed are approximated for clarity.

the long-range continuity of the crosslinked polystyrene domain.

The effect of $M_{\text{PEO-CTA}}$ on the linear mechanical response of PIPS PEMs is minimal, at most. There are minor quantitative differences in elastic modulus between samples prepared with 5 and 28 kg/mol PEO-CTA, but the overall trends in the data are similar. The dominant factor here is the crosslink density and continuity of the crosslinked P(S-*co*-DVB) phase, which is identical in both samples. There could potentially exist higher order effects due to differences in domain "mesh" size or purity (*i.e.*, interfacial thickness), although further studies would be required to explore this. It is more likely that the presence of the compliant PEO phase would influence the nonlinear mechanical response. Ultimately, though, if the mechanical response of PIPS PEMs is to be optimized for a particular application, focus should be placed on the PS phase. As mentioned previously, increasing the crosslink density (*i.e.*, the concentration of DVB) would increase the modulus, although the resulting materials would likely be extremely brittle. Alternatively, the addition of a small amount of higher T_{g} comonomer (*e.g.*, 4-*tert*-butylstyrene or maleic anhydride) could push the elastic modulus above 1 GPa and simultaneously enhance nonlinear properties such as fracture toughness.
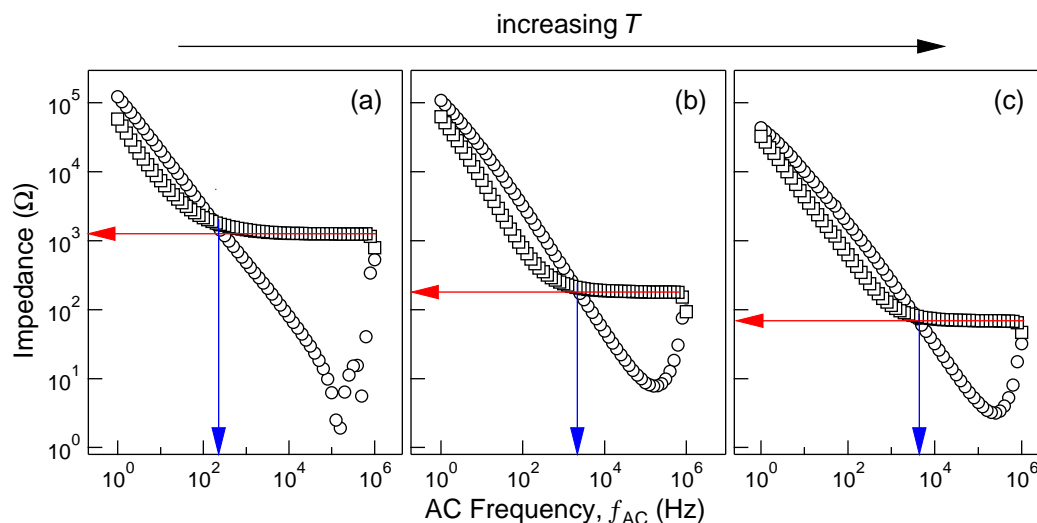
Figure 2.22: Representative raw impedance data (squares are Z', circles are Z'') collected at $T =$ (a) 31.5, (b) 90, and (c) 130 °C. The sample was prepared with 5 kg/mol PEO-CTA (32 wt%) and 21 vol% BMITFSI. The red line denotes the bulk resistance, R, used to calculate conductivity per eq 2.2. The blue line denotes the time scale for the formation of an electrical double layer (EDL), τ_{EDL}, at the electrode/electrolyte interface, which corresponds to the crossover of Z' and Z''. Note that $\tau_{\text{EDL}} = 1/f$, where f is the AC frequency of the applied electric field. As T is increased, both R and τ_{EDL} decrease. Physically, bulk resistance, R, is observed when the field switches polarity more quickly than ions can undergo long-range translation to form an EDL. Futhermore, ions exhibit higher mobility as T increases, so higher frequencies are required to prevent buildup of ions at the electrode (hence the shift of the blue line to the right from (a) to (c)).

Ionic Conductivity

Impedance spectroscopy was used to characterize the bulk conductivity of PIPS PEMs. Figure 2.22 shows an example of representative raw impedance data for a sample prepared with 5 kg/mol PEO-CTA (32 wt%) and 21 vol% BMITFSI. Figure 2.23 shows photographs of typical samples used for impedance experiments. Figure 2.24 shows the corresponding conductivity data (calculated per eq 2.2) from room temperature up to 150 °C for PIPS PEM samples prepared with 5 and 28 kg/mol PEO-CTA and the ionic liquid BMITFSI. Samples can be prepared over a wide ionic liquid composition window (5–40 overall vol%), which will allow substantial flexibility when optimizing the performance of the electrolyte membrane.
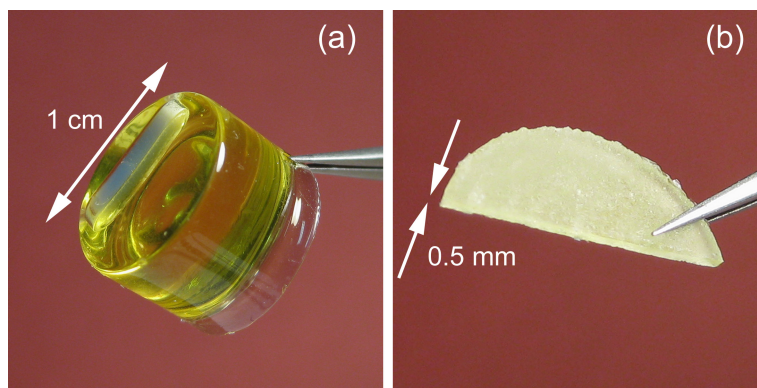
Figure 2.23: (a) Photograph of a PIPS PEM sample after removal from the reaction vial. (b) The sample in (a) is sanded down to uniform thickness for impedance experiments. The sample is opaque due to surface roughness from the sanding procedure.

In general, PIPS PEM conductivity data exhibit the expected curvature on an Arrhenius plot and were fit to the Vogel-Fulcher-Tammann (VFT) equation:[3]

$$\sigma = \sigma_0 \exp\left(\frac{-B}{T - T_0}\right) \tag{2.4}$$

In eq 2.4, σ_0 is the asymptotic conductivity in the absence of free volume limitations, B is pseudo-activation energy related to the local, primarily entropic barrier to motion, and T_0 is the extrapolated temperature at which molecular motion is frozen and conductivity asymptotically approaches zero. The VFT behavior of polymer electrolytes was discussed in more detail in Chapter 1.2.2. VFT parameters for the data in Figure 2.24 are given in Table 2.3.

Eq 2.4 is an exponential function and is highly sensitive to measurement error when fitting the data. It is therefore worth commenting on the experimental error observed when measuring conductivity of PIPS PEMs. For a given sample (*e.g.*, the sample shown in Figure 2.23(b)) loaded in the stainless steel electrodes and heating block, replicate measurements were reproducible well within 10%. However, for replicate membranes from the same monolith (*e.g.*, the sample shown in Figure 2.23(a)), the error increases up to a factor of 2–3. It is possible that the increase in error is due to
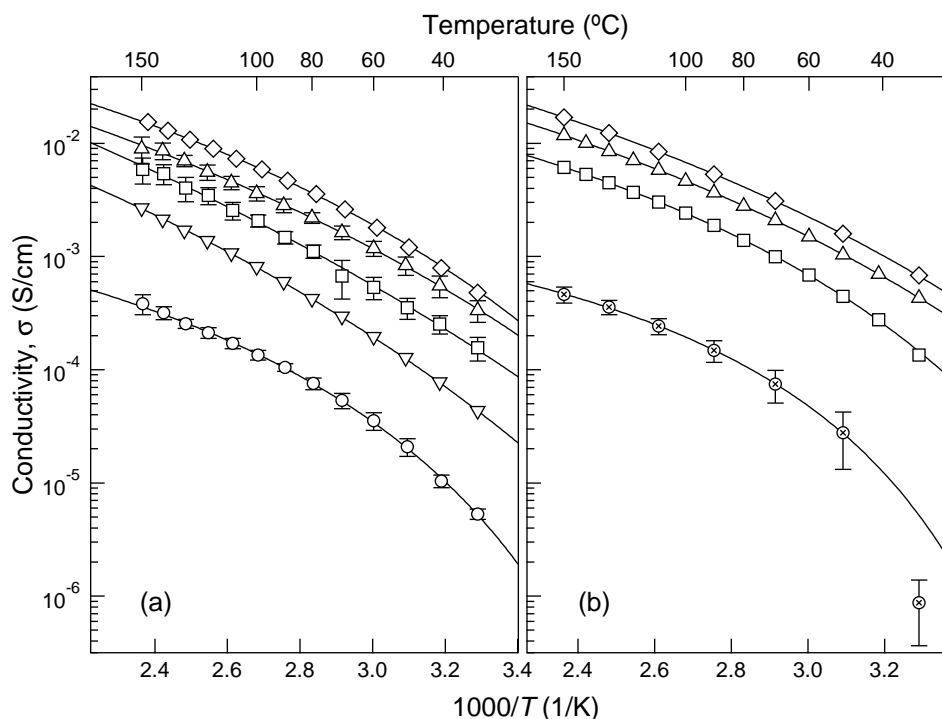
Figure 2.24: Ionic conductivity of PIPS PEMs prepared with (a) 5 and (b) 28 kg/mol PEO-CTA and the ionic liquid BMITFSI at concentrations of 4 ($\otimes$), 5 ($\bigcirc$), 12 ($\triangledown$), 21 ($\square$), 30 ($\triangle$), and 40 ($\diamond$) overall vol%. Error bars (in some cases under the data points) are one standard deviation based on at least three samples. Parameters of the VFT fits are provided in Table 2.3.

the sanding procedure used to create uniform membranes, which results in variable effective contact area between the electrodes and the sample. When calculating the conductivity as $\sigma = l/Ra$ (eq 2.2), the superficial area of the sample is used, but the measured conductivity depends on the actual contact area between the electrolyte and the electrodes. This issue is unique to high modulus, crosslinked PEMs. For context, when measuring samples that flow at high T, the samples are often annealed above the T_{ODT} so they can conform to the electrode surface, and conductivity data are collected upon cooling. In this work, the error in impedance spectroscopy experiments could potentially be reduced by polymerizing the liquid precursor between electrodes, since the liquid would conform to roughness on the electrode surface. A potential difficulty with this approach would be the volume decrease during polymerization, which might

Table 2.3: VFT parameters for PIPS PEM conductivity data in
Figure 2.24

$M_{\text{PEO-CTA}}$	composition (vol%)[i]			σ_0	B	T_0
	IL[ii]	PEO + IL[iii]	IL in PEO + IL Domain[iv]			
(kg/mol)				(S/cm)	(K)	(K)
5	40	59	67	0.59	884	178
5	30	52	57	0.67	1148	152
5	21	47	45	2.0	1730	122
5	12	41	30	0.56	1467	149
5	5	35	15	0.0064	575	223
28	40	59	67	0.81	1012	161
28	30	52	59	0.55	991	165
28	21	47	46	0.15	697	203
28	4	35	12	0.0045	404	244

[i] All samples in this table contain only BMITFSI
[ii] Overall volume fraction of ionic liquid
[iii] Volume fraction of the conducting phase
[iv] Volume fraction of ionic liquid in the conducting phase

cause the sample to pull away from the electrodes.

As shown in Figures 2.24 and 2.25, increasing the concentration of BMITFSI (which is proportional to the effective number density of ions, n) increases the conductivity, as predicted by the Nernst-Einstein equation (eq 1.8). However, the concentration increases by a factor 8 from the lowest to highest IL-content samples measured, while conductivity increases by a factor of 40. The right vertical axis of Figure 2.25 shows the raw conductivity data normalized to the conductivity at 5 vol% IL (*ca.* 4×10^{-4} S/cm) to more clearly illustrate the increase. Most of the factor of 40 increase occurs at low BMITFSI concentration. In particular, increasing from 5 to 21 vol% IL increases the conductivity by a factor of 15–20.

There are a number of possible explanations for this result, and the net observed increase in conductivity is likely some combination of several factors. (i) Plasticization of PEO with increasing concentration of BMITFSI lowers the T_{g} of the conducting phase and increases the value of $(T - T_0)$ for a given experimental temperature.
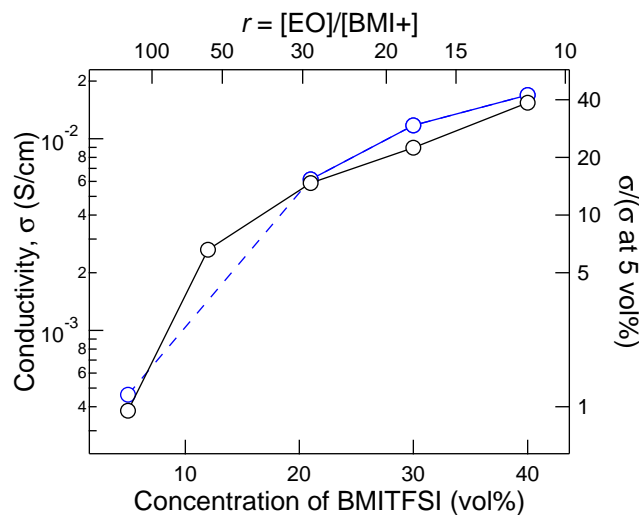
Figure 2.25: Conductivity at 150 °C versus BMITFSI concentration for PIPS PEMs prepared with 5 (○) and 28 (○) kg/mol PEO-CTA. The right vertical axis shows the conductivity scale on the left normalized to a value of 4×10^{-4} S/cm, the approximate conductivity for both samples at 5 vol% BMITFSI. The top horizontal axis gives the concentration of BMITFSI in terms of r, which is the molar ratio of ethylene oxide repeat units to BMI$^+$ cations. Lines are drawn to guide the eye. The dashed line indicates that a 28 kg/mol PEO-CTA sample with 12 vol% BMITFSI was not prepared.

However, most of the experimental temperatures are well above the T_g, where the effect of the $(T - T_0)$ term begins to plateau. Furthermore, as shown in Table 2.2, the T_g of the conducting phase decreases by only 10 °C over the entire composition range of IL, so this decrease cannot solely account for the increase in σ, per eq 2.4. Nonetheless, if plasticization does play a role, it would likely have the greatest impact in the low IL concentration regime. (ii) Another possibility that would more directly account for the order of magnitude increase in conductivity from 5 to 12 vol% BMITFSI is the degree of connectivity of the conducting pathways. That is, the PEO/salt domain might not exhibit long-range connectivity until some threshold concentration of ionic liquid is passed. (iii) Incorporation of BMITFSI increases the segregation strength between the PEO/IL and crosslinked PS domains, increasing domain purity. At low BMITFSI concentration, a diffuse interface between the glassy PS domain and the low T_g conducting domain might impede ion transport by driving
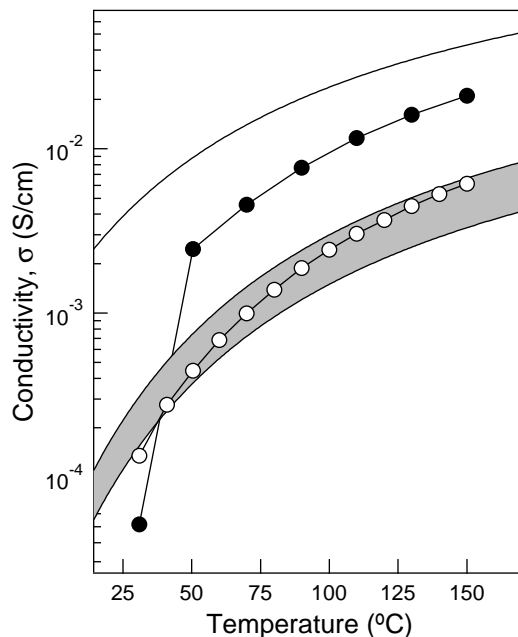
Figure 2.26: Comparison of PIPS PEM conductivity data ($\bigcirc$) to the tortuosity model (eq 2.5) to demonstrate long-range continuity of the conducting phase. The conductivity of pure BMITFSI (solid black line) is also shown for reference, and was calculated using VFT parameters from ref 44. The homogeneous electrolyte ($\bullet$) was prepared from an 8 kg/mol PEO homopolymer/BMITFSI mixture (50 vol%), and the nanostructured PEM sample was prepared with 28 kg/mol PEO-CTA and BMITFSI at 21 overall vol%. In the conducting phase of the nanostructured electrolyte, the resulting concentration of ionic liquid is 46 vol% (see Table 2.1). The gray region is defined according to eq 2.5 with $f_c = 0.47$ and $1.5 \leq \tau \leq 3$. Lines between data points are drawn to guide the eye. The large reduction in conductivity at low T for the homopolymer-based electrolyte is discussed in the text.

up the effective T_g of the conducting phase. Increasing the concentration of BMITFSI from 21 to 40 vol% increases the conductivity by a more moderate factor of 1.5–2. In this concentration regime, the conductivity scales closely with the number density of ions, as the effect of plasticization has plateaued.

Irrespective of minor morphological details (*e.g.*, long-range periodic order versus microphase separated but disordered), long-range connectivity of ion transport domains is required to maximize conductivity in nanostructured polymer electrolytes. To demonstrate defect-free continuity of conductive domains in PIPS PEMs, Figure 2.26 compares experimental conductivity data for a sample prepared with 28 kg/mol
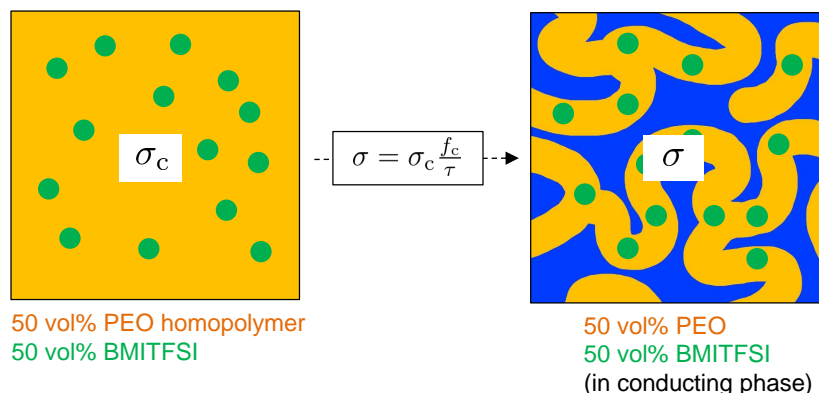
Figure 2.27: Conductivity in a nanostructured electrolyte (on the right) is reduced relative to a hompolymer-based, homogeneous electrolyte by the volume fraction of conducting phase ($f_c \leq 1$) and the tortuous pathway ions must traverse ($\tau \geq 1$). In this example, the homogeneous electrolyte comprises PEO homopoolymer and the ionic liquid BMITFSI. This example roughly corresponds to the samples shown in Figure 2.26, although volume fractions are approximated for clarity.

PEO-CTA and 21 vol% BMITFSI to the tortuosity model for co-continuous composites.[179] The conductivity of pure BMITFSI is included for context and was calculated using best-fit VFT parameters in the literature.[44] Blending BMITFSI with PEO homopolymer at 50 vol% (filled circles in Figure 2.26) results in a bulk, homogeneous electrolyte with conductivity *ca.* 2 times lower than the neat IL. The experimental temperatures measured are well above the T_g of the blend, so the importance of the $(T - T_0)$ term in the VFT equation is negligible. Instead, the reduction in conductivity can simply be attributed to decreasing the number of ions by 50% in the PEO/IL blend, relative to pure BMITFSI. As shown schematically in Figure 2.27 and discussed in detail in Chapter 1.3.2, a further reduction in conductivity is expected in nanostructured electrolytes such as PIPS PEMs, and is given by

$$\sigma = \sigma_c \frac{f_c}{\tau} \tag{2.5}$$

In eq 2.5, σ_c is the intrinsic conductivity of the conductive phase. Recall that σ_c is the conductivity of a bulk, homogeneous electrolyte of the same PEO/ionic liquid

composition as the conducting phase of the PIPS PEM. f_c is the volume fraction of the conducting phase, and τ is the tortuosity, which quantifies the longer path ions must travel relative to a straight line between electrodes. Physically, eq 2.5 assumes the conductive domain behaves exactly like the bulk electrolyte (*e.g.*, the mechanism of ion transport does not change), and the conductivity is simply reduced by the volume fraction and geometric effects. It ignores, for example, the fact that chains are tethered to the domain wall, and the fact that the interfacial thickness between domains of moderately segregated block polymers can be a relatively large fraction of the domain size.

Eq 2.5 can be used in one of two ways, assuming the value of f_c is known. If transport domains are known to be continuous, experimental data can be compared to eq 2.5 to calculate the value of τ. Alternatively, one can assume a value for τ to predict flux through connected domains. Here, the latter strategy was employed, and a range of values for τ ($1.5 \leq \tau \leq 3$) was estimated based on experiments measuring transport of small molecules in one phase of co-continuous composite membranes,[179–182] to generate a region of anticipated conductivity. As shown in Figure 2.26, the conductivity measured in the PIPS PEM is in excellent agreement with the prediction of eq 2.5, confirming that the conductive domains predominately exhibit long-range, defect-free continuity.

A relatively minor observation from Figure 2.26 is that the conductivity of the PIPS PEM falls off more quickly at low temperature (from room temperature up to *ca.* 100 °C) than the analogous bulk electrolyte. At high enough temperature (>100 °C), however, the conductivity of the nanostructured electrolyte scales equivalently to the the bulk electrolyte. This discrepancy in the temperature scaling of conductivity is likely a result of a "fuzzy", or diffuse, interface between PEO and the crosslinked PS domains. At low temperature, the proximity of stiff PS chains slows chain relaxation in the conductive domain. PS chains exhibit faster relaxation dynamics at $T > 100$ °C, so the PEO chains recover their intrinsic mobility and effectively behave like the

bulk electrolyte.

As a final comment about Figure 2.26, the data demonstrate a point alluded to during the discussion of DSC data, namely that the morphology of PIPS PEMs inhibits crystallization of PEO. PEO crystallization lowers ionic conductivity because (i) crystals are an insulating barrier that physically impede ion transport, and (ii) crystals reduce mobility of tethered PEO chains in the vicinity of the crystal. A great deal of research has focused on maximizing the fraction of amorphous PEO at ambient conditions, typically by introducing side groups that disrupt the long-range order necessary for crystallization (an early example was poly(propylene oxide), or PPO).[3] Researchers in the battery community have continued to use PEO despite its inherently high crystalline fraction because it is capable of solubilizing the highest concentration of Li^+ (compared to, for example, PPO). However, recent work by Barteau et al.[183] has shown that allyl glycidyl ether-based polymers can effectively suppress crystallinity while retaining the excellent Li^+ solubilization properties of PEO.

Returning to Figure 2.26, the conductivity data for the homogeneous electrolyte exhibit a precipitous drop below $T = 50$ °C, which correlates well with the melting peak in the DSC data (Figure 2.8). Moreover, the crystalline fraction is *ca.* 50 wt%. In contrast, the conductivity data for the PIPS PEM sample smoothly decrease to the lowest temperature measured because the crystalline fraction is only 30 wt% and because T_m is close to room temperature. That is, at most of the temperatures measured, PEO in the PIPS PEM sample is an amorphous melt. If the small residual crystalline fraction in PIPS PEMs is found to limit their viability, or if sub-room temperature operation is required, one could envision replacing PEO-CTA with a macro-CTA based on allyl glycidyl ethers. The result would be a high modulus PEM in which the conducting phase is amorphous over a much wider temperature range than is possible in the current PEO-based system.
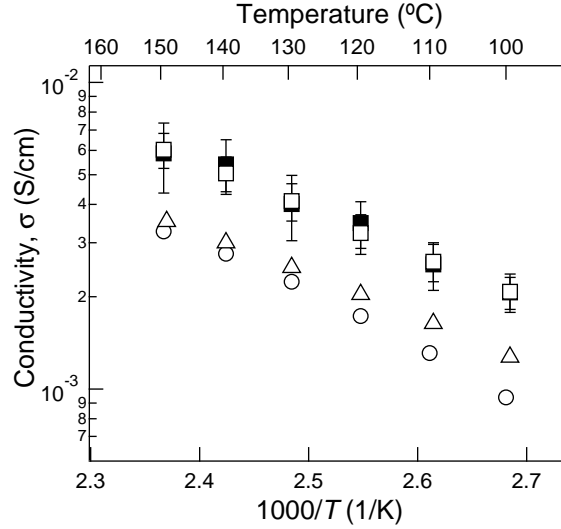
Figure 2.28: Conductivity of mixtures of LiTFSI/BMITFSI in PIPS PEMs prepared with 5 kg/mol PEO-CTA. Mixtures were prepared at concentration of 1 ($\square$), 1.5 ($\triangle$), and 2 ($\bigcirc$) M LiTFSI in BMITFSI. For comparison, a sample prepared with pure BMITFSI ($\blacksquare$) and 5 kg/mol PEO-CTA is included. Error bars are one standard deviation based on at least three samples.

The majority of the PEMs studied in this work contain only BMITFSI, but samples containing Li-based salt were also prepared as a proof-of-concept for Li-ion battery applications. Figure 2.28 shows conductivity data for PIPS PEM samples prepared with 5 kg/mol PEO-CTA and mixtures of LiTFSI in BMITFSI. As discussed previously, mixtures of LiTFSI and BMITFSI were necessary to ensure homogeneity of the liquid reaction mixture. Furthermore, the temperature range for conductivity experiments was limited to > 100 °C, as LiTFSI is hygroscopic, and replicate measurements performed in open atmosphere below 100 °C were not reproducible.

As discussed in Chapter 1, for mixtures of different types of ions (in this case, BMI^+, Li^+, and $TFSI^-$), the total measured conductivity is proportional to the sum of the conductivity of each species j.

$$\sigma \sim \sum_j u_j z_j^2 n_j \sim \sum_j D_j z_j^2 n_j \tag{2.6}$$

Eq 2.6 predicts that the measured conductivity will decrease if the diffusivity or, equivalently, the mobility of one of the ion species decreases, all other things being equal. As shown in Figure 2.28, increasing the concentration of LiTFSI from 1 to 2 M in BMTIFSI decreases the measured conductivity by approximately a factor of 2. The total number of ions is constant (21 vol%) across the samples, which means that increasing the concentration of Li^+ decreases the fraction of highly mobile BMI^+. The mobility of Li^+ is lower than that of BMI^+ because Li^+ strongly coordinates with oxygen atoms in the PEO chains due to the relatively long-range ion-dipole attractive interaction potential.[3] As a result, the translational diffusion of Li^+ is coupled to local relaxation of polymer chains, which is slower than diffusion of a liquid like BMITFSI. The reduction in conductivity is consistent with a report by Seki et al.,[63] who also showed that mixing LiTFSI with the room-temperature ionic liquid 1,2-dimethyl-3-propylimidazolium bis(trifluoromethylsulfonyl)imide reduced the total conductivity with increasing LiTFSI content.

As shown in Figure 2.28, the total conductivity of the PIPS PEM samples exceeds 1 mS/cm, even with up to 2 M LiTFSI. However, for battery applications, the most important component of the total current is that due to Li^+. As discussed in Section 1.2, the fraction of current carried by each species j is quantified by the transference number, t_j. Diluting LiTFSI in BMITFSI reduces t_{Li^+} while the total conductivity increases, because there are fewer Li^+ ions. However, $\sigma \sim$ (number of ions) $\times$ (ion mobility), so enhancing the mobility of Li^+ by mixing it with BMITFSI could potentially offset the effect of dilution. Ultimately, experiments would have to be performed to directly measure t_{Li^+}, and it may be possible to maximize t_{Li^+} by optimizing the balance between n_{Li^+} and u_{Li^+}.

As mentioned in Section 2.3, one of the motivations for varying $M_{PEO\text{-}CTA}$ in PIPS PEMs was the observation that conductivity of LiTFSI in symmetric poly(styrene-b-ethylene oxide) electrolytes increases with increasing M_{PEO}.[76,111,114] In contrast, in homogeneous, PEO homopolymer-based electrolytes, conductivity decreases as M_{PEO}
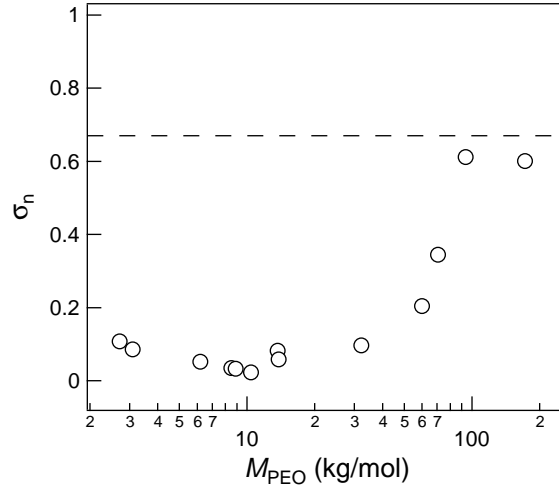
Figure 2.29: Normalized conductivity of LiTFSI as a function of M_{PEO} in symmetric poly(styrene-b-ethylene oxide) electrolytes. All samples were measured at $T = 90$ °C with a LiTFSI concentration of $r = [\mathrm{EO}]/[\mathrm{Li^+}] \approx 12$. The data were normalized according to eq 2.7. The dashed line denotes the Sax and Ottino model prediction for the theoretical maximum σ_{n} for isotropically-oriented lamellae, for which $\mathfrak{f} = 2/3$. The data in this figure were reported by Yuan et al. in ref 114.

increases from oligomeric ethylene oxide and plateaus at $M_{\mathrm{PEO}} \approx 1$ kg/mol.[3] The decrease in conductivity at low M_{PEO} in the homopolymer electrolyte is due to the increase in local viscosity as chain length increases. Above $M \approx 1$ kg/mol, the segmental chain relaxation responsible for transport of high-T_{m} salts such as LiTFSI does not depend on the overall chain length, hence the plateau in conductivity.

Figure 2.29 summarizes the effect of increasing M_{PEO} on conductivity in symmetric PS-b-PEO/LiTFSI electrolytes. The data were reported by Yuan et al.[114] as normalized conductivity, σ_{n}, which are plotted here according to

$$\sigma_{\mathrm{n}} = \frac{\sigma}{\sigma_{\mathrm{c}} f_{\mathrm{c}}} \qquad (2.7)$$

In eq 2.7, σ is the measured conductivity of the nanostructured electrolyte, f_{c} is the volume fraction of the conducting phase (PEO/LiTFSI, in the case of PS-b-PEO/LiTFSI), and σ_{c} is the intrinsic conductivity of the conducting phase. A value

of $\sigma_n = 1$ is therefore the theoretical maximum conductivity achievable in nanostructured electrolytes. Note that in the literature, ϕ_c is sometimes used to denote the volume fraction of the conducting phase. Here, f_c is used to be consistent with eq 2.5.

As written, eq 2.7 does not account for geometric constraints on ion transport. In lieu of tortuosity, Yuan et al. and a number of other reports [76,84,111,112] in the literature invoke a "morphology factor", $\mathfrak{f}$, which is based on the work of Sax and Ottino. [184] The morphology factor is a separate entity from τ, although it attempts to quantity the same idea of geometric constraints on translational diffusion. With $\mathfrak{f}$, eq 2.7 becomes

$$\sigma_n = \frac{1}{\mathfrak{f}} \left(\frac{\sigma}{\sigma_c f_c} \right) \tag{2.8}$$

The Sax and Ottino model predicts that for isotropically-oriented grains of lamellae, $\mathfrak{f} = 2/3$. Note that this is mathematically equivalent to setting $\tau = 1.5$ in the tortuosity model (eq 2.5). In practice, σ_n is sometimes found to be less than the value eq 2.8 predicts, which is often attributed to "network defects", a general term used to describe dead ends in the conducting pathway, diffusion resistance at grain boundaries, *etc.*[86,90] Alternatively, a number of reports attribute the low σ_n to M_{PEO}, as will be discussed shortly. [76,111,114] Before proceeding, it is important to note that in this work, the morphology factor was not employed to analyze the conductivity data. The Sax and Ottino model appears to break down in the limit that the transport phase exhibits long-range continuity, as is achieved in PIPS PEMs. In particular, the model predicts that $\mathfrak{f} = 1$ for bicontinuous structures such as gyroid, which means the model ignores the effect of the tortuous pathways ions must traverse. However, the tortuosity of the gyroid morphology has been experimentally measured and was found to be greater than unity. [180]

Returning to Figure 2.29, Yuan et al. [114] argue that the change in conductivity is primarily due to the increase in segregation strength between PS and PEO, which increases domain purity. To reiterate, all the polymers represented in Figure 2.29 are
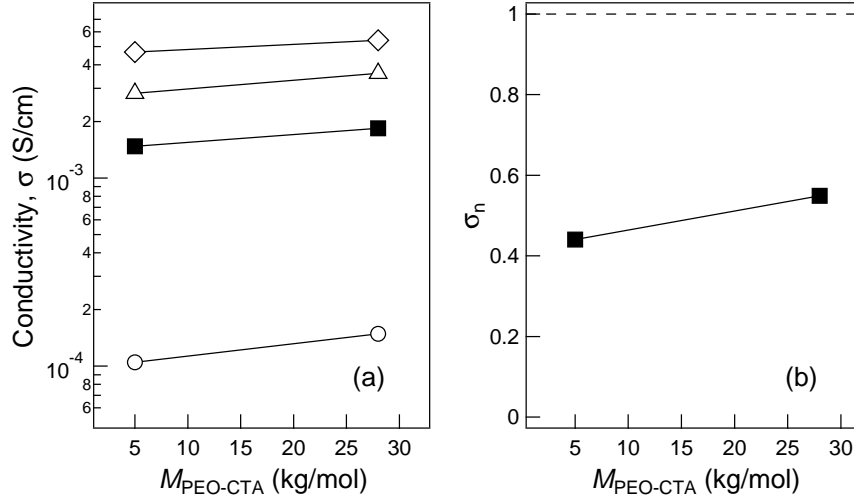
Figure 2.30: (a) Conductivity of BMITFSI as a function of $M_{\text{PEO-CTA}}$ in PIPS PEMs prepared with ionic liquid concentrations of 5 ($\bigcirc$), 21 ($\blacksquare$), 30 ($\triangle$), and 40 ($\diamondsuit$) vol%. $T = 90\ °\text{C}$ for all samples. (b) Normalized conductivity data for the samples in (a) prepared with 21 vol% BMITFSI. The data were normalized according to eq 2.7 with $f_c = 0.47$. The dashed line denotes the Sax and Ottino prediction for the theoretical maximum σ_n for network morphologies, for which $\mathfrak{f} = 1$. Lines are drawn to guide the eye.

symmetric, lamellar-forming diblocks. At low M_{PEO}, the chains are oligomeric, which enhances conductivity because (i) the viscosity is relatively low and (ii) the chains are not entangled and undergo relatively rapid translational diffusion. Furthermore, M_{PS} is low enough that $T_{\text{g,PS}}$ is well below the experimental temperature (90 °C). Increasing M_{PEO} up to *ca.* 10 kg/mol decreases the conductivity because the PS and PEO domains are mixed, and the increasing $T_{\text{g,PS}}$ drives up the overall T_{g} of the conducting phase. Between 10 and 100 kg/mol, the purity of the PEO domain increases (equivalently, the interfacial thickness decreases), providing the ions a low-T_{g} environment in which to migrate. Above 100 kg/mol, the PS/PEO interface is a negligible fraction of the PEO phase, and ions migrate in an environment effectively identical to the bulk electrolyte. In this case, ion are only limited by the volume fraction and geometric factors discussed in the context of eq 2.7, as well as network defects.

In Figure 2.30, PIPS PEM conductivity data are cast in the framework of the Sax and Ottino model for direct comparison to Figure 2.29 and the work of Yuan et al.[114] As shown in Figure 2.30(a), the conductivity increases by *ca.* 50% when $M_{\text{PEO-CTA}}$ increases from 5 to 28 kg/mol, for each concentration of BMITFSI studied. This fractional increase is qualitatively consistent with the normalized conductivity data reported by Yuan et al. (Figure 2.29).[114] However, as shown in Figure 2.30(b), the magnitude of normalized conductivity in PIPS PEMs is 2–3 times larger than in PS-*b*-PEO/LiTFSI for similar M_{PEO}. Looking at Figure 2.30(b), it must be re-emphasized that the Sax and Ottino model used to calculate σ_{n} does not account for tortuosity. If this effect were included, σ_{n} in Figure 2.30(b) would be close to unity. This analysis corroborates our earlier assertion that the conducting phase in PIPS PEMs is largely devoid of network defects. In addition, it appears that if the segregation strength argument is correct, the PEO domain in PIPS PEMs is effectively pure even at low $M_{\text{PEO-CTA}}$, which is reasonable since the presence of ionic liquid in the PEO phase and crosslinking in the P(S-*co*-DVB) phase both serve to increase χN.

Ultimately, PIPS PEMs would have to be prepared with higher $M_{\text{PEO-CTA}}$ to fully explore the molar mass dependence of conductivity. In practice, though, this may not be possible, as high molar mass PEO-CTA might not dissolve in the liquid reaction mixture. For example, PEO-CTA at 28 kg/mol is more difficult to dissolve in S/DVB than at 5 kg/mol. From a purely practical viewpoint, since the conductivity in PIPS PEMs already appears to be close to the maximum theoretical value, examining the molar mass dependence of conductivity may not be a priority.

2.4   Conclusions

To put the results of this work into context, Figure 2.31 compares the bulk modulus and conductivity for several polymer electrolyte membranes that are prototypical examples of distinct classes of PEMs. Because each system uses a different salt (see
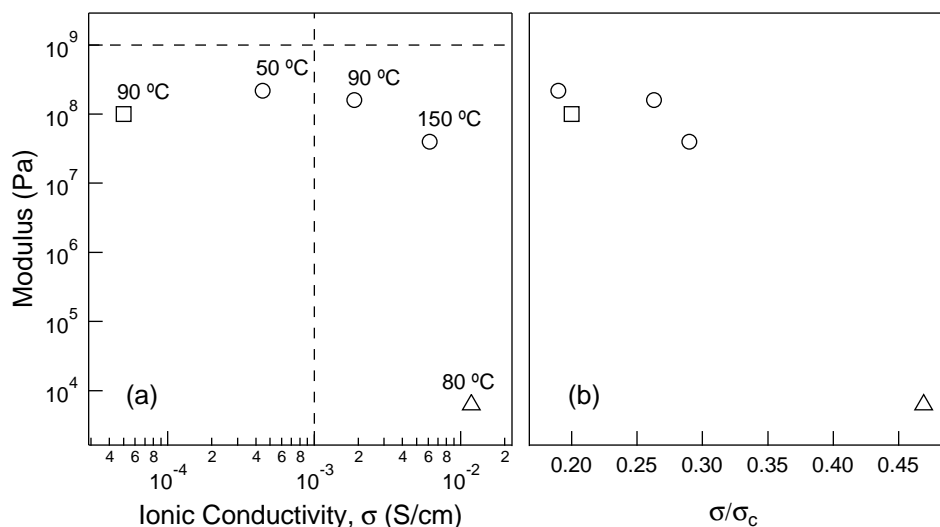
Figure 2.31: Comparison of the modulus and conductivity in a variety of solid polymer electrolyte membranes. (a) Modulus versus measured conductivity. The experimental temperature is noted next to each data point. Data are from refs 23 ($\triangle$), 76 ($\square$), and this work ($\bigcirc$). Details of each system are given in Table 2.4. (b) Modulus versus normalized conductivity (σ/σ_c) for each system in (a). Conductivity data were normalized to the intrinsic conductivity of the conducting phase because different salts were used in each system.

Table 2.4), Figure 2.31 also reports conductivity normalized to the intrinsic conductivity of the conducting phase, σ_c. This normalization scheme effectively factors out the identity of the salt.

Ion gels ($\triangle$) are physically or chemically crosslinked polymer networks swollen with a high fraction of ionic liquid. Because they comprise a majority of ionic liquid with minimal insulating phase, ion gels exhibit outstanding conductivity, only slightly reduced from neat ionic liquid. In terms of mechanical response, they are best-suited for soft solid (modulus $\approx$ 1 kPa) applications such as organic gate dielectrics for flexible thin-film transistors.[25] A number of ion gel solidification mechanisms have been reported, but two common examples are (i) self-assembly of block polymers (*e.g.*, ABA or ABC) by virtue of incompatibility of the endblocks in the ionic liquid,[23,24,26,53] and (ii) direct polymerization of vinyl monomers and crosslinkers in an ionic liquid.[70,79] An advantage of these gelation mechanisms is that ion gels can be processed in the

Table 2.4: Description of polymer electrolyte membrane systems in Figure 2.31

symbol	ref	description	polymer	salt
△	23	ion gel with 20 wt% polymer	poly(styrene-*b*-ethylene oxide-*b*-styrene)	EMITFSI
□	76	lamellar-forming diblock	poly(styrene-*b*-ethylene oxide)	LiTFSI

liquid state, then solidified *in situ*. The system shown in Figure 2.31 is an example of a physically crosslinked gel, comprising the triblock copolymer poly(styrene-*b*-ethylene oxide-*b*-styrene) and the room temperature IL EMITFSI.[23] Ultimately, ion gels are not suited—nor are they intended—for high modulus applications. Increasing the modulus of an ion gel requires increasing the polymer concentration and/or crosslink density, which inevitably reduces conductivity as the T_g of the transport medium and volume fraction of insulating phase both increase. However, ion gels are included in Figure 2.31 because they illustrate that to increase the modulus of a PEM without a commensurate decrease in conductivity, *both* the mechanically robust and conductive phases must exhibit independent, long-range continuity.

Electrolytes comprising a majority volume fraction of block polymer are ideally suited to exhibit both high conductivity and superior mechanical properties because they self-assemble into well-defined nanostructures. Ions can then be confined to a low-T_g conducting phase, in which conductivity is decoupled from an independently continuous high modulus phase. One of the primary goals of the block polymer electrolyte community has been to exploit the well-understood phase behavior of block polymers to maximize orthogonal macroscopic properties like modulus and conductivity. For example, an appealingly simple, yet effective PEM might comprise cylinders of PEO/salt within a glassy matrix. The key to success, however, is alignment of the cylinders perpendicular to the electrode surface, which requires large external fields (*e.g.*, magnetic or stress),[122,123] and will not likely scale easily beyond the benchtop.

Alternatively, the isotropic, bicontinuous gyroid morphology would not require domain alignment. The challenges here are that the gyroid phase window is narrow at best,[94] and perhaps more importantly, doping the block polymer with salt tends to shift thermodynamic equilibrium away from network morphologies.[103,104,159]

Despite these challenges, the potential of block polymer-based electrolytes has fueled a wide variety of studies, many of them based on diblock copolymers. The most thoroughly-studied block polymer-based electrolytes are lamellae-forming diblock copolymers, which are represented in Figure 2.31 by symmetric PS-b-PEO doped with LiTFSI ($\square$).[76] PS-b-(PEO/LiTFSI) self-assembles into isotropically oriented grains of lamellae, with alternating domains of glassy PS and PEO/LiTFSI. Somewhat surprisingly, even when no processing is done to macroscopically align the structure, the domains achieve sufficient continuity to exhibit both high modulus and reasonably high conductivity. As mentioned previously, however, the conductivity is ultimately limited by network defects and the inherent geometric constraints of the lamellar morphology. Furthermore, the electrolyte is solid only below $T_{\mathrm{g,PS}}$, and suffers a precipitous drop in modulus above 100 °C.

This last point warrants comment, as it has implications for electrochemical device applications. In certain applications, a solid electrolyte that melts at high T can be considered advantageous. For example, in Li-ion batteries, the traditional liquid electrolyte formulation of $LiPF_6$ in ethylene and propylene carbonate can undergo thermal runaway, so a thin layer of microporous polyethylene (PE) is included between the electrodes to melt and fill in transport domains if the temperature exceeds $T_{\mathrm{m,PE}}$.[20] However, next-generation solid-state Li-ion batteries will likely replace volatile organic solvents in favor of non-volatile ionic liquids, reducing the possibility for thermal runaway. Furthermore, electrolytes that melt at high T, such as PS-b-PEO, cannot be used where mechanically robust membranes are required to operate at high T (*e.g.*, non-aqueous fuel cells).

In this work, the key contribution to the polymer electrolyte field is a process

that marries the processibility and synthetic simplicity of a liquid precursor with the independent tunability of mechanical and ion transport properties offered by a nanostructured block polymer. The result is a material that achieves record combinations of modulus and conductivity owing to the bicontinuous morphology, in which both high modulus and conductive domains exhibit long-range continuity. Furthermore, as shown in Figure 2.31(a), there is minimal trade-off between modulus and conductivity as temperature is increased, allowing significant flexibility when designing PEMs for specific applications. This approach is promising for the scalable production of PEMs for critical energy applications such as solid-state lithium ion batteries and high temperature fuel cells.

Chapter 3

Evolution of Morphology, Modulus, and Conductivity in Polymer Electrolytes Prepared via Polymerization-Induced Phase Separation[i]

3.1 Introduction

Chapter 2 presented work that represents an important advancement in the design of mechanically robust, high conductivity polymer electrolyte membranes (PEMs) for possible use in electrochemical energy storage and conversion devices. It was shown that PEMs could be prepared in a simple, yet versatile one-pot synthetic scheme— termed polymerization-induced phase separation, or PIPS—by direct incorporation of salt into an easily processible liquid reaction mixture. The resulting PEMs exhibit an unprecedented combination of high conductivity and high modulus owing to

---

[i]This work was done in collaboration with Morgan W. Schulze and Marc A. Hillmyer.
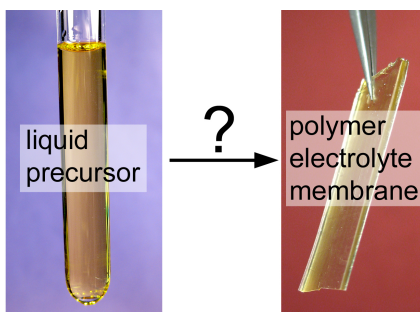
Figure 3.1: Photographs of the polymerization-induced phase separation polymer electrolyte membrane liquid precursor (left) and the resulting high modulus solid membrane after the reaction (right). The focus of this chapter is understanding the mechanistic details of polymerization-induced phase separation.

the long-range, co-continuity of poly(ethylene oxide)/ionic liquid domains and highly crosslinked polystyrene domains. Figure 3.1 shows examples of the liquid precursor and a sample prepared for linear mechanical response experiments. The liquid precursor is solidified *in situ* by simply heating to 120 °C, allowing substantial flexibility in tailoring the sample geometry to the needs of a particular experiment or application. Furthermore, Chapter 2 explored the parameter space that produces PEMs with the desired bicontinuous nanostructure. It was shown that the PIPS strategy allows substantial flexibility when choosing, *inter alia*, the identity and concentration of the salt, the identity of the high modulus component, and the concentration of the macro chain-transfer agent. However, to continue to advance the PIPS strategy, the goal of the work in this chapter is to understand the mechanism by which the bicontinuous morphology is formed. The general strategy is to correlate the results of *in situ*, time-resolved characterization experiments—reaction kinetics, rheology, conductivity, and small-angle scattering—to build a molecular picture of the electrolyte as it transitions from a liquid to a high modulus solid.

Table 3.1: Composition (vol%) of PIPS PEM samples

BMITFSI	PEO-CTA	S/DVB
0	30	68
21	25	54
30	22	48

3.2   Experimental Section

Sample Preparation

In general, sample preparation for *in situ* experiments followed the same protocol as that described in Chapter 2. As shown in Figure 3.2, samples were prepared with 32 wt% (= 30 vol%) of a 5 kg/mol poly(ethylene oxide) macro chain-transfer agent (PEO-CTA) dissolved in a monomer mixture of styrene (S) and divinylbenzene (DVB) (4/1 molar ratio S/DVB). Unless otherwise noted, samples presented in this chapter included the radical initiator azobisisobutyronitrile (AIBN) at a concentration of 0.05 *eq* to PEO-CTA. Samples prepared without ionic liquid are referred to as "neat". To prepared electrolytes, the ionic liquid 1-butyl-3-methylimidazolium bis(trifluoromethylsulfonyl)imide (BMITFSI) was added to the PEO-CTA + S/DVB stock solution at two concentrations, 21 and 30 overall vol%. Table 3.1 summarizes the resulting concentration of all species in the reaction mixture. Heating the macroscopically homogeneous liquid reaction mixture to 120 °C effects controlled linear growth of S and simultaneous chemical crosslinking by DVB off the PEO-CTA via a reversible addition-fragmentation chain-transfer (RAFT) polymerization. In addition to P(S-*co*-DVB)-based PEMs, samples were prepared with methyl methacrylate and a methacrylate-based di-functional crosslinking agent, triethylene glycol dimethacrylate (see Figure 3.3).
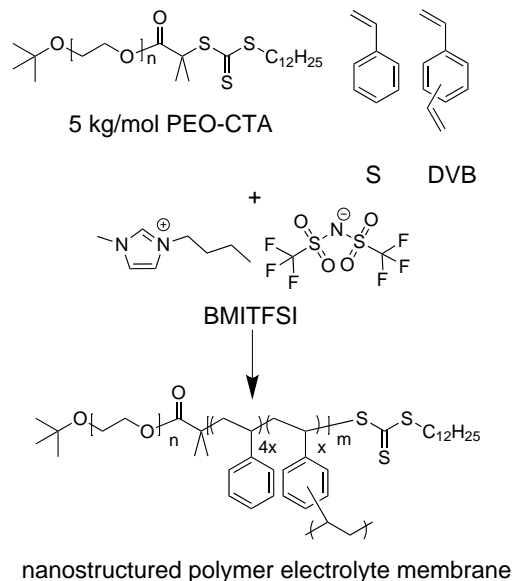
Figure 3.2: Reaction scheme used for *in situ* experiments of polymerization-induced phase separation polymer electrolyte membranes.
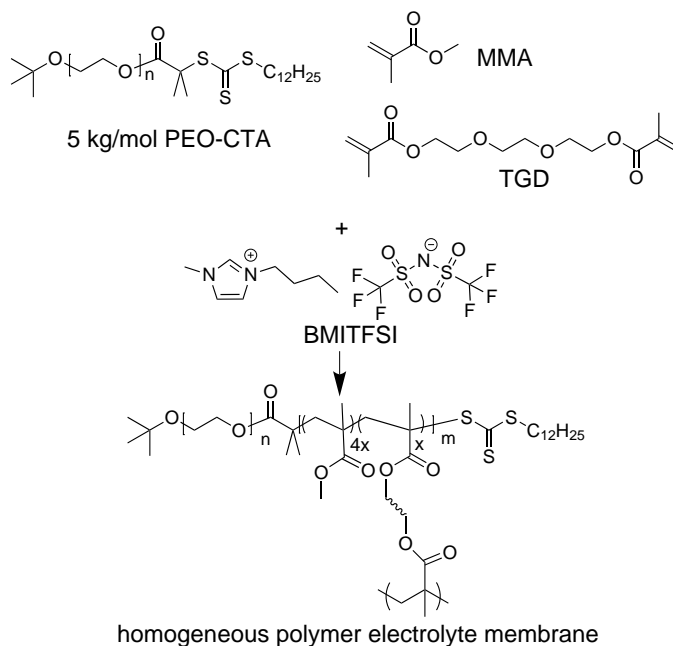
Figure 3.3: Reaction scheme used to prepare PMMA-based homogeneous PEMs. MMA is methyl methacrylate, TGD is the di-functional crosslinking agent triethylene glycol dimethacrylate.

Reaction Kinetics[ii]

Polymerization kinetics of styrene and divinylbenzene were investigated under the conditions utilized in the preparation of PIPS PEMS. A stock solution of S/DVB monomer, 5 kg/mol PEO-CTA, 21 overall vol% BMITFSI, and AIBN was distributed into a series of vials that were simultaneously heated to 120 °C to initiate the polymerization. At various time points, the reaction was stopped by immersing a vial in liquid nitrogen. Each vial was then allowed to warm to room temperature, and *ca.* 1.5 mL of chloroform with *tert*-butyl catechol inhibitor was added to the reaction mixture to prevent further reaction and to ensure all of the reaction mixture was transferred for precipitation. The dissolved solids were precipitated in hexanes and recovered by gravity filtration, then rigorously dried under dynamic vacuum for several days. Mass yield was calculated from the mass of dried solids relative to the known mass of the prepared solution. The recovered mass was further characterized by size exclusion chromatography (SEC), which was performed using THF as the mobile phase at room temperature and a flow rate of 1 mL/min. Eluents were monitored by a Wyatt Optilab T-rEX refractive index detector. Molar mass and distribution was determined based on a 12-point calibration curve using polystyrene standards (Agilent Technologies).

Morphological Characterization

Small angle X-ray scattering experiments were performed at the Argonne National Laboratory Advanced Photon Source. Samples of the liquid reaction precursor were flame-sealed in boron-rich capillary tubes (Charles Supper Company). The capillaries were maintained at –10 °C to suppress radical formation and were warmed to room temperature shortly before the start of the experiment. Samples were loaded in a Linkham heating stage, and the temperature was set to 120 °C for the duration

---

[ii]These experiments were performed by Morgan W. Schulze. The procedure is included here for completeness.
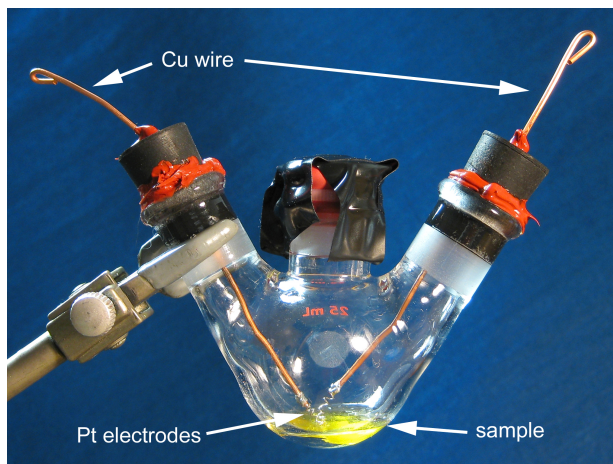
Figure 3.4: Photograph of a conductivity cell used for *in situ* conductivity experiments.

of the experiment. A thermocouple placed in the sample holder indicated that the temperature was within ± 1 °C of the set point. Scattering data were collected at discrete time points during the reaction; typical exposure times were 1–2 s. Scattered intensity was recorded on a Pilatus 2M area detector. The sample-to-detector distance was calibrated with a silver behenate standard. Intensity was not reduced to absolute unit; however, the sample thickness was approximately the same for all samples, and the intensity was normalized by the exposure time, so the intensity can be interpreted in relative units between samples. 2D scattering data, which were isotropic in all cases, were reduced to intensity as a function of the magnitude of the scattering wave vector

$$q = |\mathbf{q}| = \frac{4\pi}{\lambda} \sin\left(\frac{\theta}{2}\right) \tag{3.1}$$

where λ is the nominal X-ray wavelength and θ is the angle of scattered intensity.

Ionic Conductivity

Impedance spectroscopy (Solartron 1255B frequency response analyzer connected to a Solartron SI 1287 electrochemical interface) was used to measure the bulk resistance of samples during polymerization. The conductivity cell was custom-built using a

three-neck, 25 mL round bottom flask (see Figure 3.4). The two outer ports were plugged with rubber stoppers, through which copper wires were inserted to connect the electrical leads. The sample electrodes were platinum wires soldered to the copper wire. The conductivity cell constant, κ, was calibrated with 1 mL of a 0.01 M KCl standard (Fluka, 1.413 mS/cm at 25 °C). The position of the electrodes in the cell was identical for calibration and the corresponding experiment. After calibration, the cell was washed 3–5 times with distilled water to ensure removal of all KCl, then rigorously dried at elevated temperature (> 80 °C) under dynamic vacuum (< 100 mTorr). 1 mL of sample was loaded through the middle port, after which the port was sealed with a rubber septum. The headspace was purged with argon for 20 min, after which the vessel was pressurized with argon to a gauge pressure of 5 psi to perform the impedance spectroscopy experiment under an inert atmosphere. The conductivity cell held positive argon pressure throughout the course of the conductivity experiment.

Ionic conductivity, σ, was calculated as

$$\sigma = \frac{\kappa}{R} \tag{3.2}$$

where R is the bulk resistance as determined from the high-frequency plateau of the real part of impedance, Z'. Impedance spectroscopy data collection consisted of back-to-back AC frequency sweeps (1 MHz to 1 Hz) for the first 6 h, followed by a frequency sweep every 10 min for the remainder of the experiment. Frequency sweeps were started when the sample was at room temperature, after which the sample cell was quickly immersed in an oil bath thermally equilibrated at the reaction temperature (120 °C). The measured conductivity typically reached a maximum by the second frequency sweep, which started *ca.* 3 min after immersing the sample, indicating that the sample thermally equilibrated in 1–2 min. Conductivity was also measured for solid PEMs polymerized in standard glass vials. These monolithic samples were sanded down to uniform thickness (typically 0.5 mm), and were rigorously dried at elevated temperature (> 80 °C) under dynamic vacuum (< 100 mTorr). The
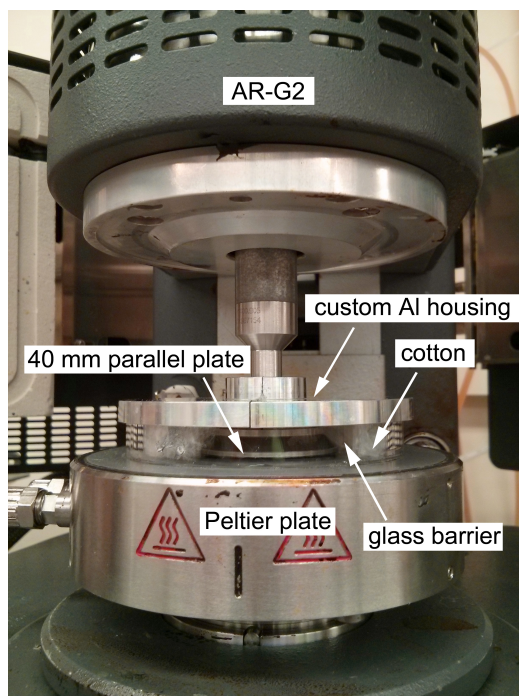
Figure 3.5: Photograph of the AR-G2 rheometer set up for *in situ* rheology experiments.

solid membranes were sandwiched between stainless steel electrodes, and impedance was measured as a function of temperature from 30 to 150 °C. These samples were measured in open atmosphere, although it has been previously determined that water uptake does not significantly impact the results for electrolytes using the ionic liquid BMITFSI. For membrane samples, σ was calculated as

$$\sigma = \frac{l}{Ra} \tag{3.3}$$

where l is the sample thickness and a is the superficial area.

Mechanical Response

The linear viscoelastic response of PIPS PEMs was measured during the course of the polymerization using small-amplitude oscillatory shear rheology with a 40 mm diameter parallel plate geometry (TA Instruments AR-G2). Approximately 1 mL of

liquid reaction precursor was loaded at room temperature on a Peltier plate, which provided temperature control with a resolution of 0.5 °C. Evaporation of styrene and divinylbenzene monomer was suppressed by enclosing the sample in a custom-built housing (see Figure 3.5), which consisted of a glass cylindrical barrier capped by two aluminum plates. All adjoining surfaces (*e.g.*, the surfaces between the glass barrier and the Peltier plate and where the two aluminum plates are joined) were coated with a thin layer of silicon grease as a sealant. The 40 mm parallel plate features a shallow well, which was filled with light silicon oil to provide a liquid barrier to monomer evaporation with minimal impact on the experimental results. The aluminum plates were designed with a protrusion that is immersed in the silicon oil to complete the barrier to evaporation. The inside of the glass housing was lined with styrene monomer-soaked cotton to saturate the environment and further reduce the driving force for monomer evaporation from the sample. Data collection was started at room temperature, and the sample was then heated to the reaction temperature of 120 °C, where it was held for the duration of the experiment. The elastic, G', and viscous, G'', moduli were measured at an angular frequency of 10 rad/s, and as the sample stiffened, the strain amplitude was reduced to remain inside the linear response regime.

3.3   Results and Discussion

The focus of this chapter is understanding the mechanistic details of polymerization-induced phase separation (PIPS), to build a molecular picture of how the polymer electrolyte membranes (PEMs) transition from a homogeneous liquid reaction mixture to a high modulus solid with a bicontinuous network of ion-conducting poly(ethylene oxide)/ionic liquid channels and crosslinked polystyrene. To this end, a series of *in situ*, time-resolved experiments were performed to measure reaction kinetics, ionic conductivity, modulus, and morphological development during the polymerization.

Before proceeding, however, it is worthwhile to summarize the state of understanding of the reaction precursor and the solid PEM. Any molecular picture intended to describe the PIPS reaction must also describe the reaction precursor and the solid PEM. The liquid reaction precursor is a ternary mixture of monomer (styrene and divinylbenzene, or S and DVB), poly(ethylene oxide) macro chain-transfer agent (PEO-CTA), and the ionic liquid (IL) 1-butyl-3-methylimidazolium bis(trifluoromethylsulfonyl)imide (BMITFSI). This liquid precursor exhibits relatively low viscosity and is macroscopically homogeneous at the reaction temperature of 120 °C. The P(S-*co*-DVB) block grows off the PEO-CTA via reversible addition-fragmentation chain-transfer polymerization (RAFT), in which S adds linearly and chemical crosslinking occurs by incorporation of DVB.

Ultimately, the sample exhibits a microphase separated morphology that lacks long-range, periodic order, as confirmed by a combination of small-angle scattering and real space imaging (TEM and SEM). In particular, the morphology consists of co-continuous networks of glassy, highly crosslinked polystyrene (P(S-*co*-DVB)) and an ion-conducting domain of poly(ethylene oxide)/ionic liquid (PEO/IL). This interpretation is supported by analysis of conductivity and calorimetry data, which indicate that during the course of the polymerization, essentially all of the BMITFSI segregates to the PEO-rich domains. In addition, the PEO conducting domains are predominantly continuous, enabling high conductivity. Similarly, the macroscopic mechanical response is dominated by the highly crosslinked P(S-*co*-DVB) phase, which imparts a glassy response at room temperature with only a moderate reduction in modulus at temperatures as high as 200 °C.

Figures 3.6 and 3.7 summarize the key results of the *in situ*, time-resolved experiments for neat samples and samples prepared with 21 overall vol% BMITFSI. Small angle X-ray scattering (SAXS) and rheology experiments were performed for both neat and IL-containing samples, while mass yield and conductivity experiments were
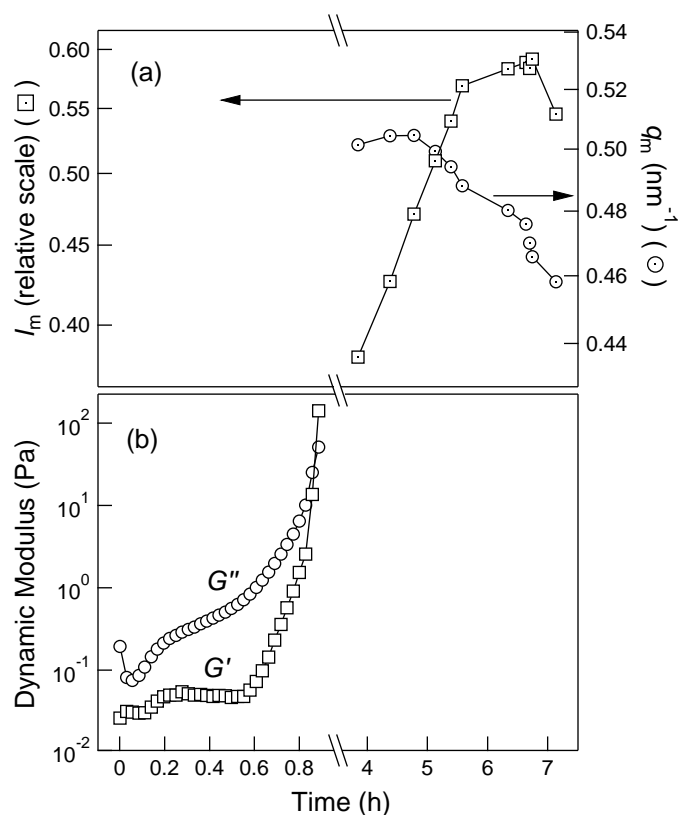
Figure 3.6: Comparison of (a) SAXS and (b) rheology *in situ* experiments for a sample prepared without ionic liquid. I_m is the maximum scattered intensity of the structure factor peak at wave vector q_m.
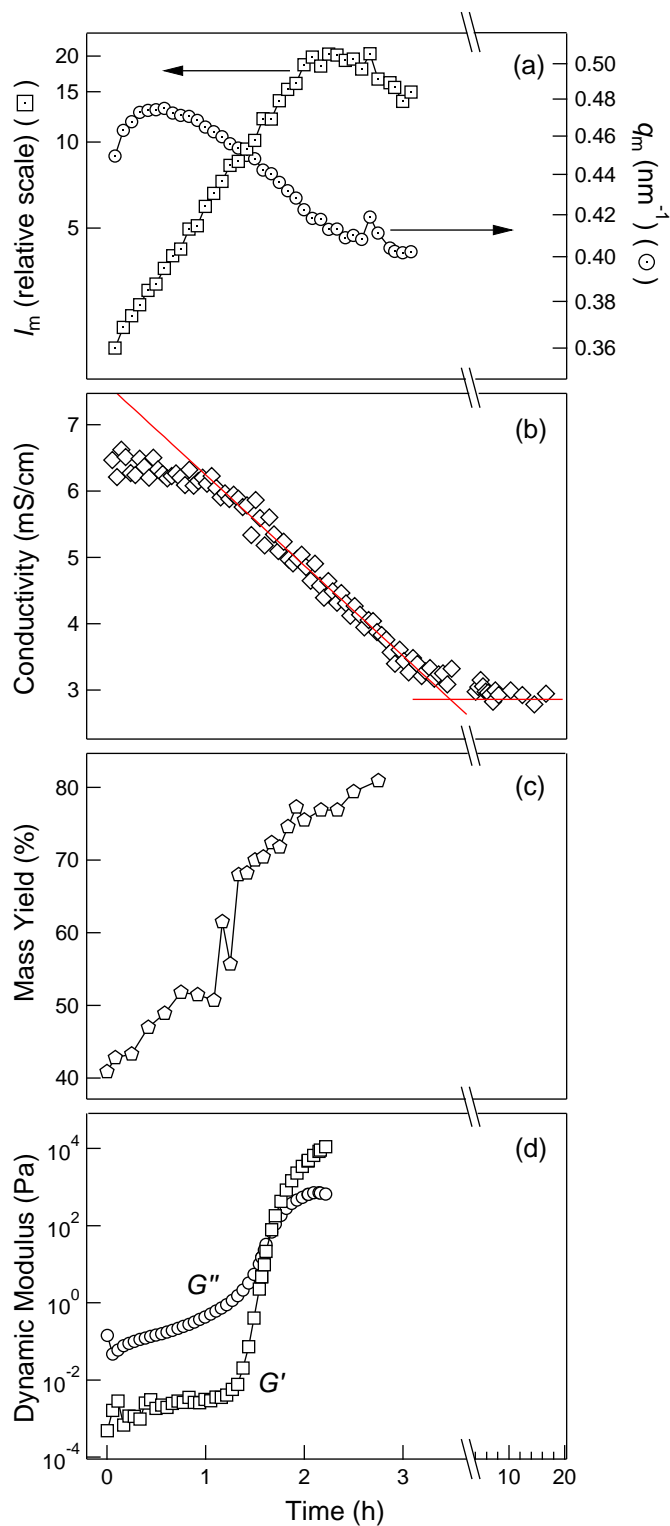
Figure 3.7: Comparison of (a) SAXS, (b) conductivity, (c) mass yield, and (d) rheology *in situ* experiments for a sample prepared with 21 vol% BMITFSI. I_m is the maximum scattered intensity of the structure factor peak at wave vector q_m.

Table 3.2: Comparison of the characteristic timescales of *in situ* experiments

	characteristic time, t_x (h)			
sample	SAXS	conductivity	mass yield	rheology
neat	3.8	na	na	0.87
21 vol% IL	0.08	3.5	1.08	1.65

conducted exclusively on IL-containing samples. Table 3.2 compares the characteristic timescales from the *in situ* experiments for both neat and IL-containing samples. The characteristic timescale, t_x, for each experiment is defined as follows. For SAXS experiments, t_x is the time at which scattering peaks first emerge. In Figures 3.6 and 3.7, the SAXS data are summarized by plotting the position, q_m, and intensity, I_m, of the primary structure factor peak, obtained by fitting the peak to a Lorentzian function (see Figures A.1 and A.2 in Appendix A.1). In the rheology experiments, the dynamic moduli, G' and G'', were measured as the sample solidified, and t_x is the time to reach the apparent gel point, where $G' = G''$. For the mass yield experiment, t_x corresponds to the sharp upturn in recovered mass. In the conductivity experiment, t_x is the time at which the measured conductivity plateaus, and was obtained from the crossover of linear fits of the conductivity data before and after the plateau.

One of the most interesting differences between the neat and IL-containing samples is the inversion of the time to gel versus emergence of scattering peaks. The neat samples reach the apparent rheological gel point at 0.87 h, and scattering peaks do not appear until 3.8 h. In contrast, for samples with ionic liquid, the scattering peaks appear much earlier than the apparent gel point (0.08 versus 1.65 h, respectively). For samples with ionic liquid, the values of t_x for the mass yield and rheology experiments correlate fairly well with one another. In fact, the upturn in mass yield appears to coincide more closely with the upturn in G', which occurs *ca.* 30 min before the apparent gel point. Finally, the conductivity of the IL-containing samples does not plateau until 3.5 h, well after both the emergence of scattering peaks and the apparent

gel point. The results of the individual experiments will now be analyzed in more detail, before concluding by revisiting the aggregated data.

Kinetics

Figure 3.8 shows the mass of solids recovered at various points during the PIPS reaction for a sample prepared with 21 overall vol% BMITFSI. The data point at $t = 0$ min was collected before the polymerization was started, and should simply reflect the mass of PEO-CTA added to the reaction mixture. Interestingly, the recovered mass at $t = 0$ min is approximately 40% of the mass of the initial reaction mixture, or 15 percentage points higher than expected from PEO-CTA alone. This discrepancy could indicate the error associated with this measurement, although it is more likely that some ionic liquid closely associates with the PEO-CTA, contributing to the measured mass yield. The precipitated solids were isolated via simple gravity filtration, and it is plausible that not all of the ionic liquid passed through the filter paper with the S/DVB monomer mixture, as there exists a relatively strong ion-dipole attractive interaction between PEO and the BMI^+ cation.

In general, the mass yield increases with time, indicating growth of the P(S-*co*-DVB) block. Prior to $t = 45$ min, the dry solids recovered by precipitation could be readily re-dissolved in, for example, THF for size exclusion chromatography. At $t \geq 55$ min, small insoluble particulates were observed when the recovered solids were re-dissolved in THF. This observation most likely corresponds to the formation of discrete regions of crosslinked polymer and correlates well with the rapid increase in the mass yield between 65 and 80 min.

Figure 3.9 shows size exclusion chromatograms for reaction aliquots for $t \leq 45$ min. As in the mass yield results, the SEC trace at $t = 0$ min was collected before the reaction began, and should simply correspond to PEO-CTA. In agreement with this anticipated result, the narrow, monomodal trace at $t = 0$ is nearly identical to a previously collected SEC trace for PEO-CTA. For context, an SEC trace of a linear
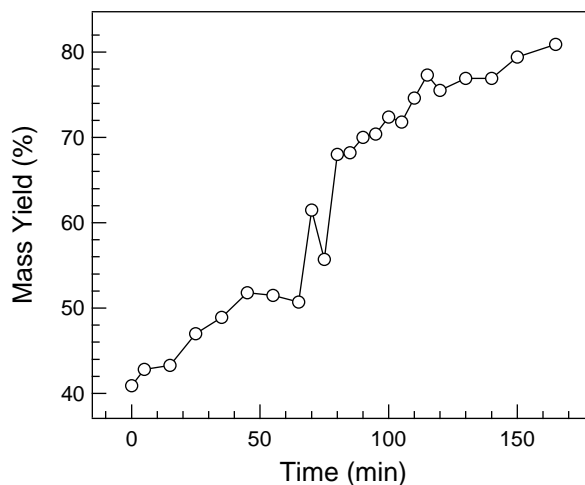
Figure 3.8: Mass yield at various time points during a reaction kinetics experiment.

PS-*b*-PEO diblock prepared from the PEO-CTA is also shown. This neat diblock was prepared with equivalent composition as the PIPS reactions—but without ionic liquid or the crosslinking agent DVB—to verify the controlled nature of the polymerization. One difference in preparation between the linear diblock and the *in situ* samples is that the linear diblock was de-gassed (via freeze-pump-thaw cycles) prior to the reaction. In the PIPS reaction mixtures, the presence of oxygen might have an effect on the kinetics data. In general, though, PIPS PEMs are prepared without de-gassing, so the kinetics data are representative of the typical procedure used for PIPS reactions.

The molar mass and dispersity from all the traces in Figure 3.9 are summarized in Table 3.3. As early as $t = 5$ min, a peak begins to emerge at lower elution volume than the PEO-CTA, indicating growth of the P(S-*co*-DVB) block. This peak grows in intensity and breadth relative to the PEO-CTA peak, until at $t = 45$ min, a broad peak at much lower elution volume appears. Note that the intensity was normalized to the maximum value, rather than the concentration of sample injected, so the fact that the height of the PEO-CTA peak remains constant is not physically meaningful. Presumably, if the intensity were normalized to the concentration, the intensity of
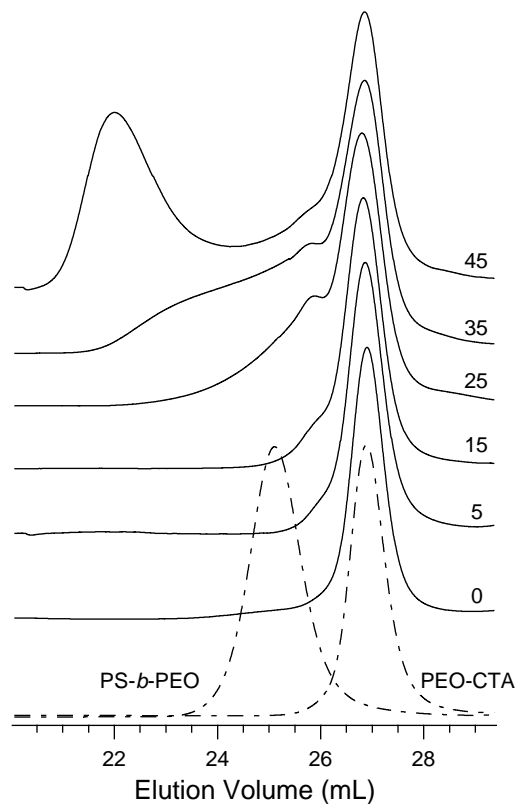
Figure 3.9: Size exclusion chromatography data of PIPS reaction aliquots. The labeled dash-dot lines are traces of a linear PS-*b*-PEO diblock prepared from the PEO-CTA during a separate experiment.

the PEO-CTA peak at an elution volume of *ca.* 27 mL would decrease as the P(S-*co*-DVB) block grows. To perform this analysis, however, the exact mass of ionic liquid carried through the filter paper during isolation of the solid would have to be known. In the future, NMR spectroscopy could potentially be used to determine the relative amount of ionic liquid and polymer in samples prepared for SEC.

Interestingly, it appears that even at $t = 45$ min, there remains a significant amount of unreacted PEO-CTA. It is possible that these chains are growing, but at $t = 45$ min, the shift to lower elution volume is within the limits of the instrument resolution. When growing diblocks couple to other diblocks, they have a higher probability of crosslinking, as the number of chemical crosslinking moieties (pendant

Table 3.3: Molar mass and dispersity for the SEC traces in Figure 3.9

	PEO-CTA	PS-b-PEO	reaction time, t (min)					
			0	5	15	25	35	45
M_n (kg/mol)	6.9	26.5	7.2	7.3	7.2	9.0	9.5	14.7
$Đ$	1.1	1.3	1.2	1.2	1.3	2.1	4.3	10.5

DVB vinyl groups) is higher than average. As a result, crosslinked diblocks tend to grow more rapidly than linear diblocks, perhaps explaining the presence of low elution volume peaks when the initial PEO-CTA peak is still present. Nonetheless, it is clear that as the reaction proceeds, aggregates with large hydrodynamic volume form before ultimately growing too large to dissolve in THF.

Ionic Conductivity

Figure 3.10 shows the measured conductivity as a function of time during the polymerization for three replicate P(S-co-DVB)-b-PEO PIPS PEM samples, all prepared with a nominal BMITFSI concentration of 21 overall vol%. All three experiments were performed in the custom-built conductivity cell shown in Figure 3.4, although for the sample in panel (a), the copper wires were immersed in the sample and used as the electrodes (the samples in (b) and (c) used platinum wire electrodes). Based on the qualitative similarities between the three samples, it does not appear that using copper wire electrodes had a significant effect on the measured conductivity. However, a small amount of green oxidized copper was observed when copper wire electrodes were used, so to avoid any possibility of a redox contribution to the measured signal, platinum wire electrodes were used thereafter.

After immersing the samples in the oil bath set to 120 °C, the conductivity quickly reaches a maximum between 6 and 7 mS/cm. In panel (c), it can be seen that the first frequency sweep was complete before the sample had thermally equilibrated, as the maximum conductivity was not reached until the second frequency sweep.
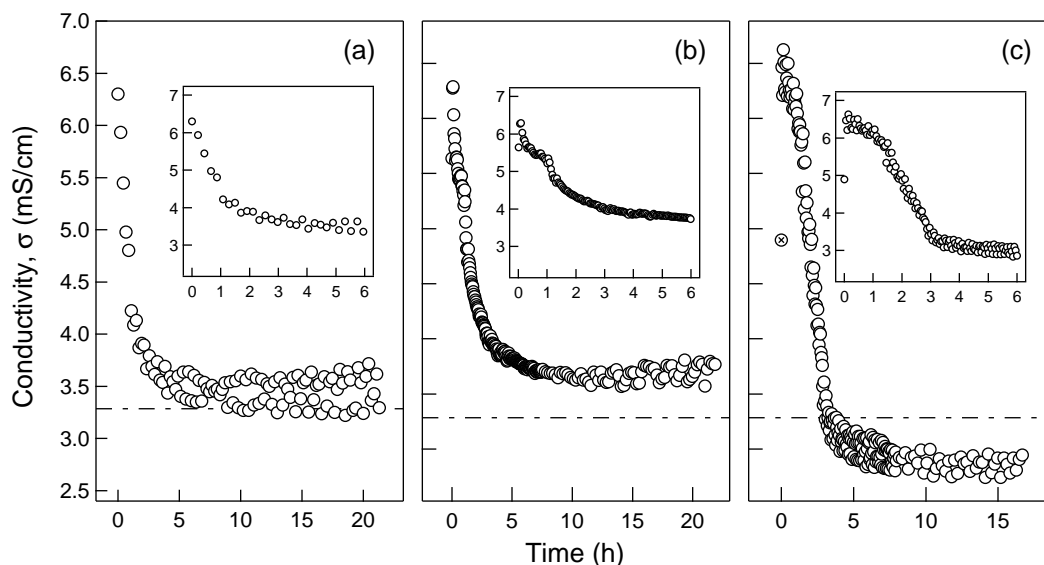
Figure 3.10: (a)–(c) Three replicate *in situ* conductivity experiments for PEO-*b*-P(S-*co*-DVB) samples prepared with 21 overall vol% BMITFSI. The dash-dot line is the conductivity of a solid membrane of equivalent composition. Crossed circle data points indicate that the sample had not yet thermally equilibrated at 120 °C before that frequency sweep was complete. The insets show an expanded view of the conductivity in the first 6 h.

The measured conductivity then decreases monotonically for several hours before plateauing between 3–4 h after the polymerization began. The conductivity drops by a factor of 2–3 over the course of the polymerization, with a plateau between 2.5 and 4 mS/cm. These values are close to the measured conductivity at 120 °C of a previously measured solid membrane of equivalent composition (see Figure 2.24 in Chapter 2 for the raw data, and the dash-dot line in Figure 3.10 for the conductivity at 120 °C), providing internal corroboration that the custom-built cell accurately measures the conductivity. Although the *in situ* samples were prepared with identical nominal BMITFSI concentration, the minor differences between plateau values of the *in situ* samples is likely due to small compositional differences among samples. The measurement error increases slightly as the polymerization proceeds, which might be a result of small bubbles that were kinetically trapped in the electrolyte as the samples solidified. The bubbles could be due to a combination of monomer evaporation (the
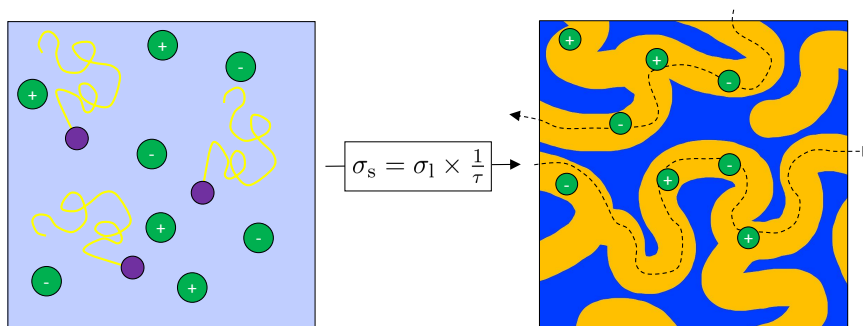
Figure 3.11: Relationship between conductivity of the initial liquid reaction mixture and the solid membrane after polymerization. Initially, PEO-CTA (yellow lines and purple circles, respectively) and ionic liquid (green circles) are dissolved in a mixture of S/DVB (light blue background). After polymerization, ions are confined to tortuous PEO conducting channels. σ_s and σ_l are the conductivity of the solid and liquid, respectively. The tortuosity, τ, quantifies the indirect pathway ions must traverse in the solid sample (denoted by dashed lines) relative to a straight path between electrodes.

reaction temperature, 120 °C, is close to the normal boiling point of styrene, 145 °C) or nitrogen gas that evolves upon dissociation of AIBN.

The following discussion will address the factor of 2–3 net decrease in measured conductivity observed during the PIPS reaction, after which the time dependence of measured conductivity will be discussed. As shown in Figure 3.11, the measured conductivity of the solid electrolyte, σ_s, can be related to the conductivity of the initial liquid mixture, σ_l, by

$$\sigma_s = \sigma_l \times \frac{1}{\tau} \tag{3.4}$$

Eq 3.4 differs slightly from the equation used in Chapter 2 (reproduced below as eq 3.5) to explain the reduction in conductivity of a nanostructured electrolyte relative to a homogeneous, homopolymer-based electrolyte.

$$\sigma = \sigma_c \frac{f_c}{\tau} \tag{3.5}$$

In particular, the volume fraction of conducting phase, f_c, is not needed in eq 3.4

because the number of ions does not change during the *in situ* conductivity experiment. f_c is used to predict the measured conductivity of a nanostructured electrolyte, because with a conducting phase with equivalent salt concentration as the bulk electrolyte, the total number of ions decreases when $f_c < 1$. A more subtle point that will be considered is that although the total number of ions does not change during the *in situ* experiment, the fraction of dissociated ions (*i.e.*, those that contribute to the measured current) might change.

Returning to eq 3.4, the intrinsic conductivity of the liquid mixture, σ_l, is a function of the number of dissociated ions, n, ion diffusivity, D, and the square of ion charge, z.

$$\sigma_l \sim D \times z^2 \times n \tag{3.6}$$

Combining eqs 3.4 and 3.6 should provide the physical parameters necessary to explain the reduction in conductivity as the polymerization progresses.

$$\sigma_s \sim D \times z^2 \times n \times \frac{1}{\tau} \tag{3.7}$$

The possible influence of each of the parameters will be discussed separately, although the observed reduction in conductivity is likely due to some combination of these factors.

(i) The charges of the constituent ions (*i.e.*, $z = +1$ and -1 for BMI^+ and $TFSI^-$, respectively) do not change during the polymerization.

(ii) Estimating a possible change in the fraction of dissociated ions, n, during the reaction is not straightforward. The Debye-Hückel-Onsager[28,33] theory provides physical insight into the factors that determine n in a strong electrolyte solution. At a fixed salt concentration and temperature, as is the case during the *in situ* conductivity experiment, n is related to the relative permittivity, ϵ_r, of the medium.[28] High ϵ_r media shield the attractive Coulombic potential between oppositely-charged ions over shorter length scales than low ϵ_r media, so n should increase with increasing ϵ_r. For

both styrene monomer and polystyrene, $\epsilon_r \approx 2.5$,[185] approximately half the value of
PEO, for which $\epsilon_r \approx 6$.[186] Assuming the local environment around an ion is equal to
the macroscopic concentration (*i.e.*, the mean field assumption), the ions in the sam-
ples in Figure 3.10 experience a local environment predominantly composed of styrene,
likely reducing the apparent ϵ_r closer to 2.5. When the sample microphase separates
during the polymerization, ions partition to the PEO-rich domains. It is therefore
possible that n increases during the reaction because the ionic liquid segregates to
an environment (PEO) that is more amenable to ion dissociation. Alternatively, if
the mean field assumption is not correct, and BMITFSI associates more closely with
PEO than with styrene and divinylbenzene in the liquid reaction mixture, the local
ϵ_r that the ions experience might not change substantially throughout the reaction.
PEO provides a relatively strong, long-range ion-dipole attractive interaction that the
BMI^+ cation does not experience with styrene, so the idea of close association be-
tween PEO and BMITFSI is plausible. Furthermore, there is experimental evidence
for the close association of ionic liquid and PEO in the liquid precursor: crystal-
lization of PEO was observed in mixtures of PEO-CTA + S/DVB sitting at room
temperature for several hours, whereas mixtures of PEO-CTA + S/DVB + BMITFSI
were macroscopically homogeneous at room temperature over the same time period.
This observation is consistent with DSC data presented in Chapter 2, where ionic
liquid was shown to inhibit crystallization of PEO chains. In any case, the preceding
arguments predict either no change or an increase in the measured conductivity as the
reaction proceeds, suggesting that they either do not capture the pertinent physics
or are overwhelmed by other factors.

(iii) The diffusivity, D, of ions in solution depends on the local friction of the
surrounding medium. For dilute electrolyte solutions in small molecule solvents, D
can be approximated by the Stokes-Einstein equation,

$$D = \frac{kT}{6\pi\eta R_{\text{h}}} \tag{3.8}$$

where k is the Boltzmann constant, T is temperature, η is the macroscopic viscosity of the continuum medium, and R_{h} is the hydrodynamic radius of the diffusing species. In a polymer melt, on the other hand, ion diffusion depends not on the macroscopic viscosity, but rather on the timescale of the local segmental chain relaxation, τ_{seg}. The PIPS liquid reaction mixture lies somewhere between these two limiting cases, as the ionic liquid is dissolved in a concentrated polymer solution (25 vol% PEO-CTA, in the case of the samples in Figure 3.10).

As the reaction proceeds, the local environment that governs the transport of BMITFSI transitions from a concentrated polymer solution (where S/DVB dilutes the PEO chains) to PEO-rich domains, eventually forming a conducting phase that is an approximately 50 vol% mixture of PEO and BMITFSI. Within the PEO/IL domains, the kinetics of ion transport are essentially identical to a bulk electrolyte of PEO homopolymer and ionic liquid. The local relaxation dynamics that determine BMITFSI migration are therefore expected to slow down over the course of the reaction, as τ_{seg} should increase in a polymer melt relative to a mixture of polymer chains and small molecule diluent. Measurements of conductivity should provide an estimate of the net decrease. In Figure 3.10, the maximum conductivity measured within the first few minutes (*ca.* 6.5 mS/cm) represents the conductivity of BMITFSI in a concentrated polymer solution of PEO and S/DVB, as the majority of the S/DVB monomers have not had sufficient time to polymerize.

Next, the conductivity of a bulk, homogeneous PEO homopolymer/IL electrolyte provides a measure of the intrinsic decrease in ion transport in the absence of geometric (*i.e.*, tortuosity) effects. A 50 vol% blend of PEO homopolymer and BMITFSI, for which $\sigma = 13.8$ mS/cm (see Figure B.6 in Appendix B.4), provides a comparable local environment to the conducting domains of the nanostructured electrolyte. However, to directly compare this value to the liquid reaction mixture, the conductivity must be reduced proportionally to the reduced number of ions (*ca.* 40%) in the nanostructured electrolyte, relative to the bulk electrolyte. The anticipated conductivity

of BMITFSI in the PEO conducting domains is therefore 5.7 mS/cm, slightly lower than the conductivity of the liquid reaction mixture. However, this estimate likely represents an upper limit, as the conductivity of polymer/IL blends drops off sharply when polymers are the majority component. The conclusion of this analysis is that diluting the PEO chains with S/DVB monomers provides the ions with a less viscous local environment than a polymer melt, and thus faster ion diffusion in the liquid precursor as compared to ions in the final PEO conducting domains. It is therefore plausible that the diffusivity term in eq 3.7 can at least partially explain the decrease in measured conductivity during the polymerization.

(iv) The final factor to consider is a geometric tortuosity parameter, τ, that attempts to account for the longer path ions must traverse between electrodes relative to a straight path. In the liquid precursor, there are no insulating barriers preventing direct ion migration between electrodes, so $\tau = 1$. In the final PEM, however, ions must migrate through tortuous conducting domains, decreasing the measured conductivity because $\tau > 1$. In Chapter 2, transmission and scanning electron micrographs provided direct visualization of the tortuous conducting channels in P(S-co-DVB)-b-PEO/BMITFSI PEMs. Furthermore, although the value of τ was not directly calculated, it was found that the decrease in measured conductivity of the nanostructured PIPS PEMs relative to bulk electrolytes could be rationalized by assuming values of τ between 1.5 and 3. This range is consistent with the work of Seo and Hillmyer,[124] who studied a similar nanoporous PIPS system prepared by etching polylactide (PLA) from a P(S-co-DVB)-b-PLA solid membrane. The authors used water and gas transport experiments to calculate values of τ of 1.4 and 1.7, respectively. More generally, Cussler[179] has noted that for transport of small molecules in one phase of a disordered, co-continuous composite, a physically reasonable range of τ is 1.5–3.

To summarize the preceding arguments, it appears D and τ in eq 3.7 play the largest role in the observed net decrease in measured conductivity during the PIPS
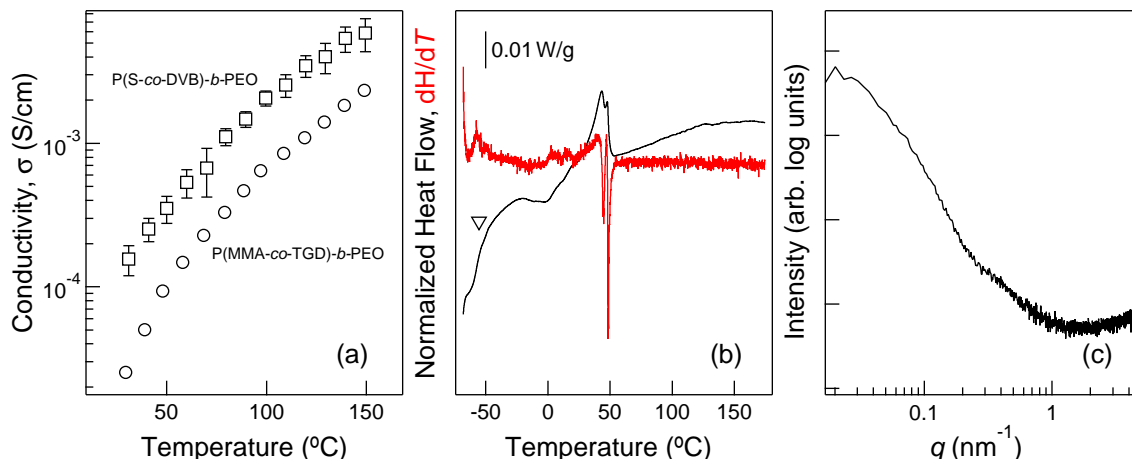
Figure 3.12: Characterization data for a P(MMA-*co*-TGD)-*b*-PEO sample. (a) Temperature-dependent conductivity of PMMA-based (circles) and PS-based (squares) preformed samples. (b) Black line: differential scanning calorimetry trace (endo up, second heating trace collected at 5 °C/min). Red line: first derivative of heat flow. The arrow points to a glass transition at −58 °C. (c) Small-angle X-ray scattering data with Kapton scattering subtracted, collected at room temperature.

reaction. However, the preceding analysis does not address the time dependence of the conductivity data. That is, why does conductivity drop sharply, then plateau at approximately 3–4 h? This question was explored by measuring the conductivity of a polymer electrolyte prepared with PEO-CTA in a monomer mixture of methyl methacrylate (MMA) and the crosslinking agent triethylene glycol dimethacrylate (TGD) (see Figure 3.3). The motivation was to replace the P(S-*co*-DVB) block with a poly(methyl methacrylate) (PMMA) block that is miscible with both PEO and BMITFSI, thus eliminating the drive for both microphase separation and for the ionic liquid to partition to one phase. The electrolytes prepared with PMMA were macroscopically homogeneous and solid at room temperature.

Figure 3.12 shows the results of three characterization experiments for a P(MMA-*co*-TGD)-*b*-PEO electrolyte prepared with 21 overall vol% BMITFSI. In panel (a), the conductivity of the PMMA-based electrolyte is approximately a factor of 3–4 lower than a PS-based electrolyte of equivalent ionic liquid concentration, over a wide

temperature range. Conductivity will be discussed more thoroughly shortly. In panel
(b), the DSC trace reveals only one glass transition temperature (T_g) at -58 °C, as
evidenced by a peak in the first derivative of heat flow. Interestingly, this temperature
is reasonably consistent with the T_g of PEO/BMITFSI blends. Furthermore, there
is a melting event with two peaks between 40–50 °C, which is only attributable to
melting PEO crystals. Assuming a heat of fusion of 200 J/g,[148] approximately 2 wt%
of the PEO melts during the heating ramp, although the presence of two melting
peaks suggests that there is not a single, well-defined population of PEO crystals.
Nonetheless, the fact that a small fraction of PEO crystallizes suggests some degree
of localized enrichment of PEO chains. PMMA homopolymer does not crystallize,
and it is not clear whether the T_g at –58 °C includes the influence of PMMA.

The fact that all three components (PEO + PMMA + BMITFSI) are nominally
miscible does not preclude the presence of multiple T_gs. Additionally, pairwise mis-
cibility does not guarantee three component miscibility. Mok et al.[187] studied the
thermal behavior of PMMA/EMITFSI blends across a wide range of concentration.
The authors found that although all of the blends were fully miscible, multiple glass
transitions were observed for blends containing between 30 and 55 wt% PMMA. These
results were consistent with a model developed by Lodge and McLeish,[188] in which the
observation of multiple glass transition temperatures is attributed to local enrichment
of like monomers due to chain connectivity. In the Lodge-McLeish model, the volume
of localized enrichment is defined by the Kuhn length of the homopolymer. Thus,
there exists the possibility of local regions of PEO/BMITFSI and PMMA/BMITFSI.
If this is the case, modulated DSC might be used to determine if the glass transition
associated with PMMA/BMITFSI is obscured by the melting peak of PEO. Finally,
in panel (c), the SAXS data do not exhibit a clear peak, indicating that there is not
a preferred length scale of segregation (this experiment probed length scales between
1.5 and 100 nm). Note that the X-ray scattering length density difference between
PMMA and PEO is identical to that between PS and PEO (see Table 3.5), so if the

electrolyte were nanostructured, a peak should be observed.

Returning to panel (a) of Figure 3.12, it is somewhat surprising that the conductivity of the PMMA-based electrolyte is only 3–4 times lower than the PS-based sample. A neat crosslinked PMMA network should exhibit a T_g at least as high as linear PMMA (*ca.* 120 °C), and conductivity strongly depends on the temperature interval above the T_g. Evidently, PEO and BMITFSI both serve to plasticize the PMMA network. Presumably, however, the homogeneous nature of the PMMA-based electrolyte compromises its mechanical robustness, and the plasticized PMMA network would likely soften substantially more than the PS-based electrolyte at high temperature. It might be of interest to prepare a PMMA-based tensile bar to compare the high temperature mechanical response to that of the PS-based samples. Furthermore, a PMMA-based homogeneous electrolyte would not be a viable option for Li-based salts, as Li^+ does not coordinate as effectively with PMMA as with PEO. One of the advantages of PS-based PIPS electrolytes is that they provide a nearly pure PEO phase suitable for Li^+ conduction.

Figure 3.13 shows the results of an *in situ* conductivity experiment for a PMMA-based electrolyte with equivalent ionic liquid concentration (21 overall vol%) as the PS-based electrolyte. Methyl methacrylate boils at 101 °C, so the reaction was carried out at 65 °C. To directly compare these results to those from the PS-based electrolytes, the measured conductivity, σ, was normalized to the maximum value, σ_m, to calculate normalized conductivity, σ_n, as

$$\sigma_n = \frac{\sigma}{\sigma_m} \tag{3.9}$$

The normalized conductivity for the PMMA-based electrolyte exhibits similar qualitative trends as the PS-based sample, namely a rapid monotonic drop before plateauing. However, the normalized conductivity for the PMMA-based sample plateaus at a lower value ($\sigma_n = 0.1$) than the PS-based sample ($\sigma_n = 0.45$), and at an earlier time (*ca.* 1 h versus 3 h for the PS sample). For both samples, the most likely explanation for the sharp drop in measured conductivity is the increase in local viscosity
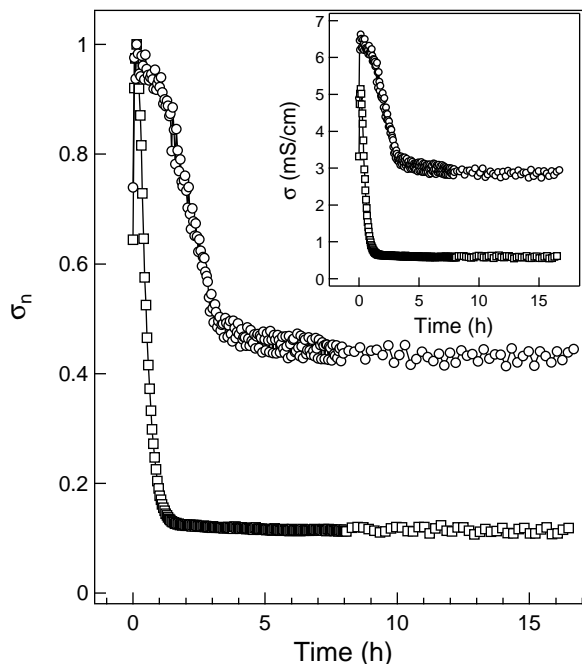
Figure 3.13: *In situ* conductivity data for PS- and PMMA-based electrolytes. Circles are P(S-*co*-DVB)-*b*-PEO/BMITFSI, squares are P(MMA-*co*-TGD)-*b*-PEO/BMITFSI. The concentration of BMITFSI is 21 overall vol% in both samples. $T_{\mathrm{rxn}} = 65$ and 120 °C for the PMMA- and PS-based samples, respectively. The inset shows measured conductivity data.

as the diblock grows linearly and begins to crosslink. Note that this local viscosity argument differs from the one presented earlier to describe the *net* decrease in conductivity. Here, the idea is that the ionic liquid remains miscible with the growing P(S-*co*-DVB) block early in the reaction, during which it experiences the increase in local viscosity because (i) the mobility of polystyrene is inherently lower than, for example, PEO, and (ii) crosslinking by DVB further slows relaxation dynamics.

The situation is similar in the PMMA-based electrolyte. The key difference is that in the case of the PS-based electrolyte, the ionic liquid partitions to the PEO phase when the PS block reaches some threshold molar mass. For example, He et al.[53,189] and Zhang et al.[23] prepared ions gels comprising poly(styrene-*b*-ethylene oxide-*b*-styrene) triblock copolymers in the ionic liquid 1-ethyl-3-methylimidazolium bis(trifluoromethylsulfonyl)imide (EMITFSI). The authors found that polystyrene

end blocks with $M \approx 3$ kg/mol were not miscible with EMITFSI and formed the physical crosslink nodes of the ion gel. Similarly, Susan et al.[79] attempted to prepare a homogeneous ion gel via direct polymerization of styrene and a crosslinking agent dissolved in EMITFSI. The initial reaction mixture was homogeneous, but the polystyrene network and ionic liquid phase separated during the course of the polymerization, although the authors did not investigate the details of the average molar mass at which phase separation occurred. Nevertheless, the conclusion to be drawn is that if the ionic liquid did not partition to the PEO phase, the conductivity would presumably continue to decrease before plateauing, as ion motion would be hindered by the decreasing relaxation rate of the crosslinked PS network.

This appears to be what happens in the PMMA electrolyte, where there is not a thermodynamic drive for the ionic liquid to partition to the PEO phase (in fact, there is likely not a well-defined PEO "phase" in the PMMA-based sample). Instead, ion motion slows as the PMMA block grows, resulting in a more rapid decrease of the PMMA-based electrolyte conductivity as compared to the PS-based electrolyte. The value at which the conductivity of the PMMA-based electrolyte plateaus simply reflects the net motion of ions through an aggregate matrix of PEO and crosslinked PMMA. The final factor to consider in the case of the PS-based sample is the development of tortuosity—which contributes to the net rate of decrease of measured conductivity—in the PEO conducting domains. Note that because the PMMA-based electrolyte is homogeneous, $\tau = 1$, so the observed decrease in conductivity is due entirely to the increase in local viscosity. Unfortunately, decoupling the contribution of microphase separation from tortuosity in the PS-based electrolyte is not possible from the *in situ* conductivity experiment alone, but this idea will be revisited after the scattering data have been discussed.
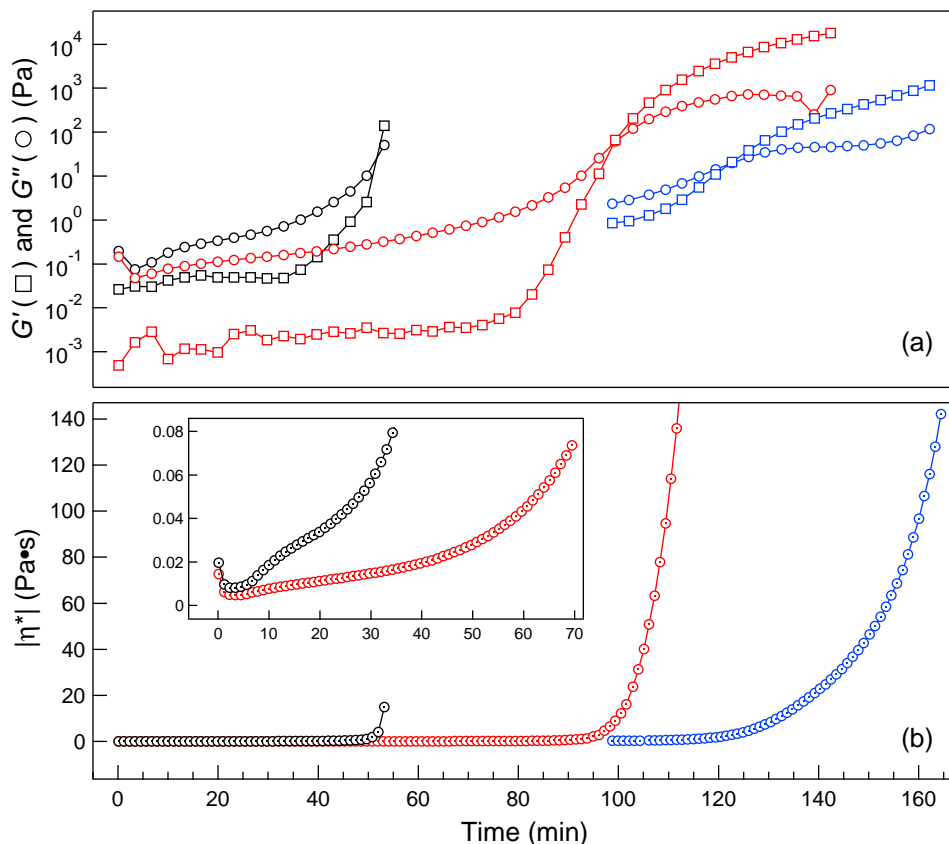
Figure 3.14: *In situ* shear rheology data measured at $T_{\mathrm{rxn}} = 120$ °C and an angular frequency, ω, of 10 rad/s. The concentration of BMITFSI was increased from 0 vol% (black), to 21 (red) and 30 (blue) vol%. (a) Dynamic elastic moduli. Squares are the elastic modulus, G', and circles are the viscous modulus, G''. (b) Magnitude of complex viscosity. The inset is an expanded view of the 0 and 21 vol% samples.

Rheology

Figure 3.14 shows *in situ* rheology data at $T_{\mathrm{rxn}} = 120$ °C for samples prepared with 21 and 30 overall vol% BMITFSI, as well as a neat sample. Note that for the 30 vol% sample, the strain amplitude was purposely set too low to obtain reliable data at early times ($t \lesssim 100$ min) to ensure that the sample remained inside the linear response regime as the gel point was approached.

The rheological response of the liquid reaction precursor was also fully characterized at room temperature. In general, the liquid reaction mixtures exhibit a liquid-like
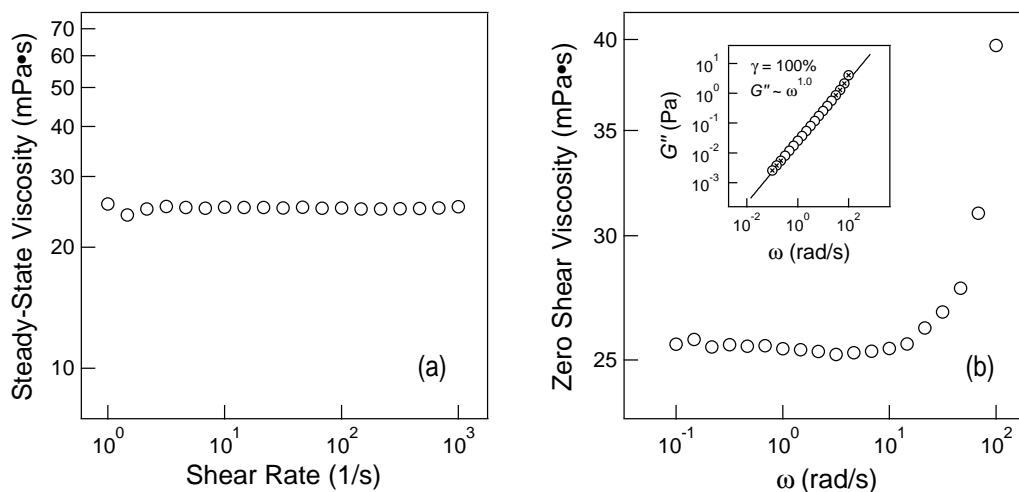
Figure 3.15: Room temperature viscosity of the liquid reaction mixture prepared with 21 vol% BMITFSI. Measurements were made using (a) steady-state viscosity as a function of shear rate, and (b) linear oscillatory shear, where the zero-shear viscosity, η_0, is calculated as G''/ω in the limit that $\omega \to 0$. Both experiments give $\eta \approx 25$ mPa·s.

response, with a shear rate-independent (over the range from 1–1000 1/s) viscosity of *ca.* 25 mPa·s (see Figure 3.15). This value is in excellent agreement with the zero-shear viscosity, η_0, obtained from a frequency sweep at room temperature, in which the reaction mixture exhibits terminal flow behavior (*i.e.*, $G'' \sim \omega^{1.0}$). To better understand the nature of the reaction mixture as a polymer solution, the experimentally-determined Mark-Houwink parameters, k and a, can be used to provide an estimate of the intrinsic viscosity, $[\eta]$.

$$[\eta] = kM^a \tag{3.10}$$

For PEO homopolymer in toluene (a reasonable proxy for the S/DVB mixture) at 35 °C, $k = 14.5 \times 10^{-3}$ (cm^3/g)(mol/g)$^{0.70}$ and $a = 0.70$,[40] from which one calculates $[\eta] = 5.6$ cm^3/g for 5 kg/mol PEO. The chain overlap concentration, c^*, can then be estimated as $1/[\eta] = 0.17$ g/cm^3. The reaction mixture therefore lies in the semidilute, coil overlap regime, for which $1 < c[\eta] < 10$. The increase in viscosity

over pure styrene monomer, for which $\eta_S = 0.7$ mPa·s at 25 °C, is then calculated as

$$\eta = \eta_S \left(1 + [\eta]c + k_h[\eta]^2c^2 + \cdots\right) \tag{3.11}$$

where k_h is the Huggins coefficient,[190,191] a dimensionless number ranging between 0.3 and 0.8 depending on solvent quality, and c is the concentration of PEO in g/cm³. Per eq 3.11 (assuming $k_h = 0.5$), the viscosity of a 0.3 g/cm³ PEO solution is expected to be *ca.* 4 mPa·s. The fact that the experimentally measured viscosity (25 mPa·s) is higher than eq 3.11 predicts means the bimolecular c^2 term is not sufficient to describe the interaction between polymer coils, and higher order terms are needed.

Although viscosity is the pertinent metric for a liquid, small amplitude oscillatory measurements—for which the dynamic moduli are reported—were used during the PIPS reaction in anticipation of the transition to a solid-like response. As shown in panel (a) of Figure 3.14, at early times the samples exhibit a predominantly liquid-like response, with $G'' > G'$. The dip in G'' within the first few minutes occurs because data collection was begun at room temperature, and the viscosity decreases by approximately a factor of 3 (from 25 to 8 mPa·s) as the sample is heated from room temperature to 120 °C. Note that the magnitude of G' at early times (specifically, before the sharp upturn) is likely not quantitatively accurate: the raw phase angle for early time data was > 150°, suggesting that instrument inertial effects dominated the response.[192]

After the samples thermally equilibrate at 120 °C, the viscosity monotonically increases, as evidenced by the increase in both G'' and the magnitude of the complex viscosity, $|\eta^*|$ (shown in panel (b) of Figure 3.14). The increase in viscosity is consistent with growth of the diblock before a significant degree of crosslinking has occurred. During this initial stage, G' exhibits only a modest increase, as the sample response is dominated by viscous dissipation. After the reaction has proceeded for some time, however, the elastic response quickly grows, beginning with a sharp upturn in G'. Accompanying the increase in G' is an asymptotic increase in $|\eta^*|$. The

Table 3.4: Apparent gel time and modulus at the gel point for samples in Figure 3.14

BMITFSI concentration (vol%)	time to gel (min)	modulus at gel point (Pa)
0	52	26
21	99	60
30	122	20

rate of increase in G' outpaces that of G'', and the crossover of G' and G'' indicates an apparent rheological transition from liquid-like to solid-like response. After the apparent gel point, G' continues to increase and will eventually plateau at a value of 0.1 GPa at 120 °C, as shown by the linear viscoelastic master curves of pre-formed samples in Chapter 2. However, the rheometer used for the *in situ* experiments could not measure the mechanical response throughout the remainder of the polymerization: the samples did not adhere to the rotating parallel plate after stiffening above 10^3–10^4 Pa, as evidenced by a drastic decrease in the instrument torque.

As shown in Figure 3.14 and summarized in Table 3.4, increasing the concentration of ionic liquid increases the time required to reach the apparent gel point, $t_{\text{gel}}^{\text{app}}$, where $G' = G''$. The increase in $t_{\text{gel}}^{\text{app}}$ is most likely simply a dilution effect, that is, a result of the decreasing concentration of macro chain-transfer agents. As the concentration of BMITFSI increases from 0 to 21 and 30 overall vol%, the concentration of PEO-CTA decreases from 30 to 25 and 22 vol%, respectively. In contrast to $t_{\text{gel}}^{\text{app}}$, the modulus at the crossover of G' and G'', $G_{\text{gel}}^{\text{app}}$, does not vary in a systematic manner with ionic liquid concentration. Nonetheless, in all three samples, $G_{\text{gel}}^{\text{app}}$ is quite low, ranging from 20–60 Pa. The ideal elastomer theory provides an estimate of the molar mass between chemical and transient (*i.e.*, entanglements that persist on the timescale of the experiment) crosslinks, M_x.[40]

$$M_x = \frac{\rho RT}{G_{\text{gel}}^{\text{app}}} \tag{3.12}$$

Taking $\rho = 1,000$ kg/m^3, the reaction temperature of 393 K, and using a representative $G_{\text{gel}}^{\text{app}}$ of 50 Pa, eq 3.12 predicts that $M_x \approx 65,000$ kg/mol. This value is unrealistically large, although it is important to remember that, in general, the ideal elastomer theory is not reliable near the gel point. Eq 3.12 assumes that the crosslink density is uniform throughout the gel, which is never the case at the gel point. Instead, some regions of the gel exhibit higher crosslink density than other regions, and the measured modulus is the average of high- and low-crosslink density regions throughout the entire sample. Nevertheless, the large predicted value of M_x and, perhaps more importantly, the fact that the rheological measurements were frequency-dependent, both suggest that the energy storage mechanism responsible for the solid-like $(G' > G'')$ response in the vicinity of $t_{\text{gel}}^{\text{app}}$ is not due entirely to crosslinking of the growing P(S-co-DVB) block.

As noted above, these experiments were performed at a frequency of 10 rad/s, so the possible role of entanglements should be considered. If the PEO block is entangled with neighboring PEO coils, the lifetime of entanglements is likely much shorter than the timescale at which the sample is being probed. At 120 °C, the entanglement plateau modulus, G_N, of a PEO melt is 1.7 MPa.[40] The longest relaxation time, τ_1, can then be estimated if the macroscopic viscosity at 120 °C is known.

$$\tau_1 \approx \frac{\eta}{G_N} \tag{3.13}$$

As shown in Figure B.10 in Appendix B.5, the measured viscosity of a 90 vol% blend of 4.6 kg/mol PEO homopolymer and EMITFSI is of order 0.1 Pa·s at 125 °C, providing a reasonable estimate for the viscosity of a 5 kg/mol PEO melt at 120 °C. Inserting this value into eq 3.13 gives $\tau_1 \approx 10^{-7}$ s, which can be considered an upper limit on the longest relaxation time, as a polymer solution will relax more quickly than a melt. That is, entanglements relax much more rapidly than the timescale of the experiment (10 rad/s corresponds to timescales of $\mathcal{O}(1)$ s). Similarly, it is not likely that transient entanglements exist in the PS block. The molar mass of a hypothetical

fully polymerized, linear (*i.e.*, no chemical crosslinking agent present) PS block for these samples is approximately 11 kg/mol, lower than $M_{\mathrm{e,PS}} = 13$ kg/mol. There could exist inter-chain entanglements in the growing P(S-*co*-DVB) block that are unable to relax due to chemical crosslinking; however, these trapped entanglement would contribute to the magnitude of $G_{\mathrm{gel}}^{\mathrm{app}}$, and so were accounted for in eq 3.12.

Alternatively, it is possible that the observed magnitude of $G_{\mathrm{gel}}^{\mathrm{app}}$ is partly due to the formation of a percolating network of jammed polymer flocs,[193] which happens to impart an elastic response at a frequency of 10 rad/s. The formation of a true, sample-spanning gel would then occur later in the reaction. This scenario would be internally consistent with the observation of insoluble particulates of crosslinked polymer at $t \geq 55$ min in the reaction kinetics experiment, as described earlier. One way to test this hypothesis would be to perform the *in situ* experiments at different frequencies, say 1 and 100 rad/s. The value of $t_{\mathrm{gel}}^{\mathrm{app}}$ would increase and decrease at 1 and 100 rad/s, respectively, if the flocculation argument is correct. Another potentially useful experiment would be to quench samples at various points during the reaction to "freeze" the gel at a moment in time. The sample could then be subjected to frequency sweeps to determine the point at which the sample exhibits a frequency-independent gel point. Finally, it might be of interest to track the modulus as the sample stiffens beyond the limits of the AR-G2 rheometer, as there might exist an additional rapid increase in modulus corresponding to the formation of a true, sample-spanning gel network.

Small-Angle X-ray Scattering

Figure 3.16 shows *in situ*, time-resolved small-angle X-ray scattering (SAXS) data for four different samples of P(S-*co*-DVB)-*b*-PEO electrolytes. The two samples in the left column were neat, and the two samples in the right column were prepared with 21 overall vol% BMITFSI. In general, the scattering data feature a broad peak with a local maximum at wave vectors between 0.3 and 0.5 nm^{-1} that grows in intensity
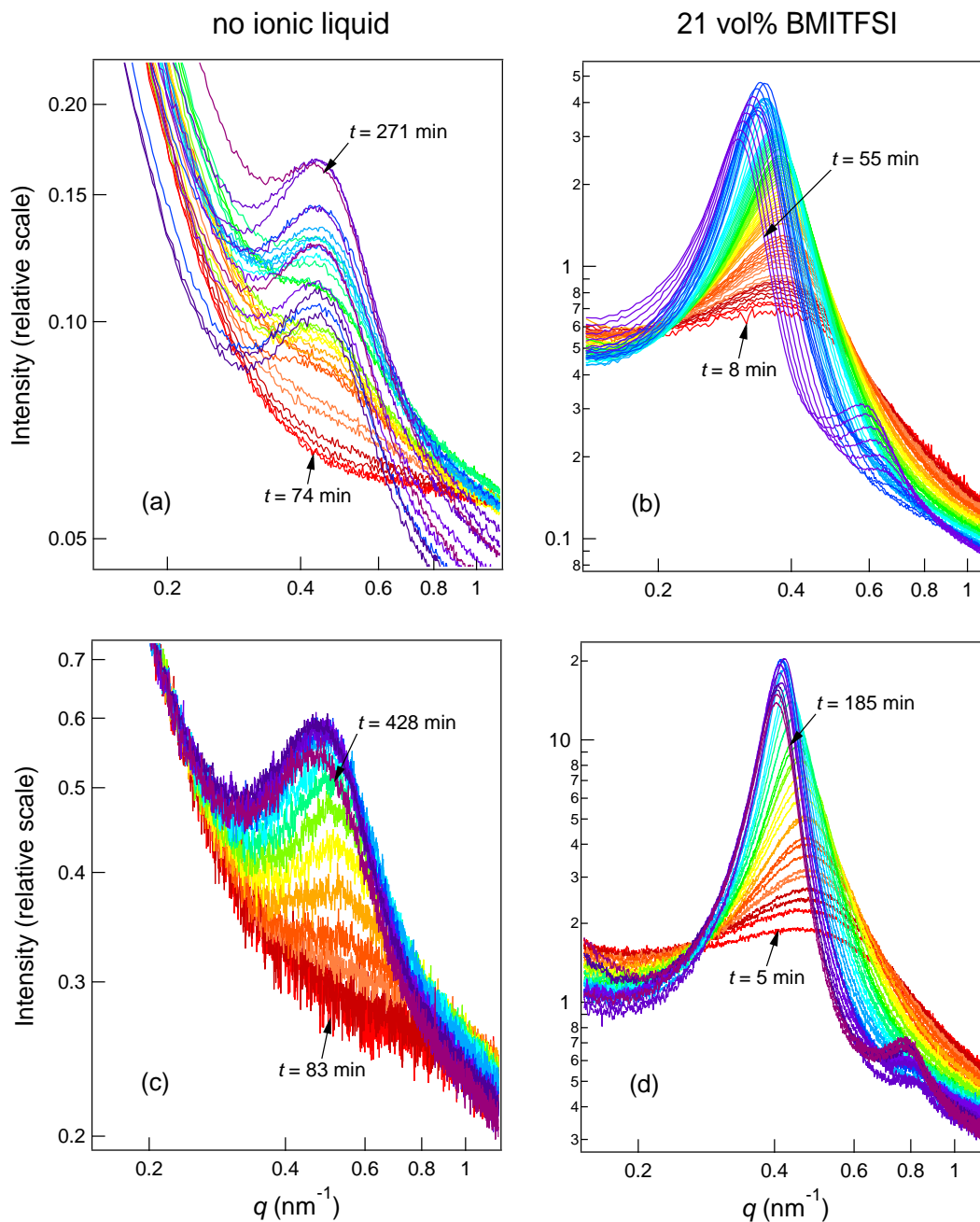
Figure 3.16: Replicate *in situ* time-resolved small angle X-ray scattering data for samples prepared with 0 (left column) and 21 (right column) overall vol% BMITFSI. The traces are color-coded according to ROYGBIV, where early time data are red and late time data are violet. The first and last collected traces are labeled with the time in minutes after the sample was heated to $T_{rxn} = 120\ °C$. The scattered intensity is on a common scale for all samples, but was not reduced to absolute units. That is, samples with ionic liquid scatter *ca.* 10–20 times stronger than neat samples. To show the relative change in intensity during the polymerization, traces were not shifted vertically.
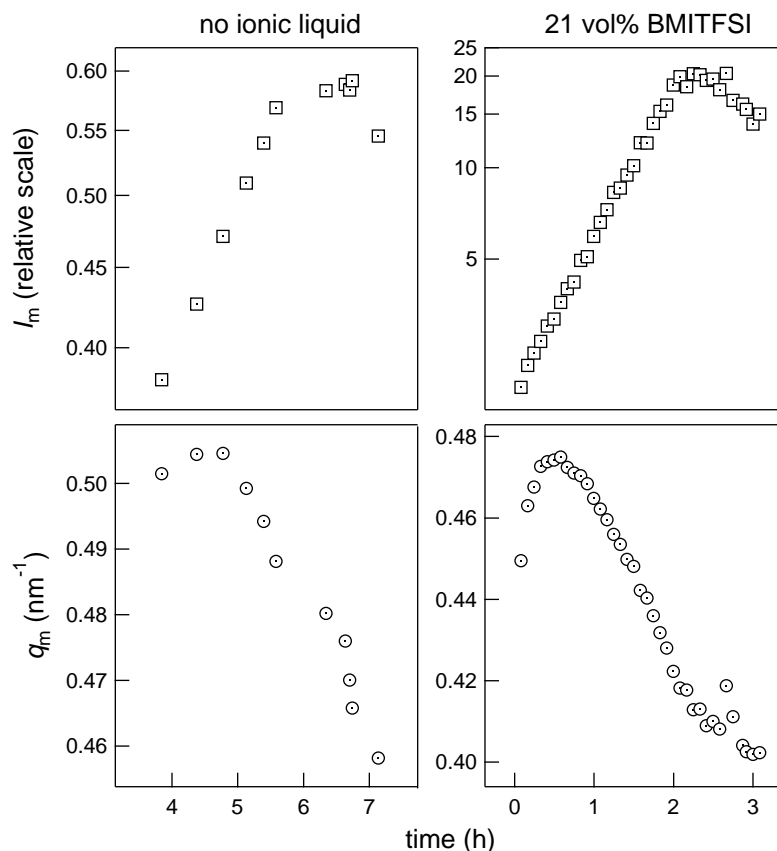
Figure 3.17: Time-resolved evolution of the maximum scattered intensity, I_{m}, of the primary structure factor peak located at wave vector q_{m}. The scattered intensity is on a common scale for all samples, but was not reduced to absolute units. That is, samples with ionic liquid scatter *ca.* 10–20 times stronger than neat samples. Samples in the left column are neat and correspond to panel (c) in Figure 3.16. Samples in the right column were prepared with 21 vol% BMITFSI and correspond to panel (d) in Figure 3.16.

as the reaction proceeds. In addition, samples prepared with ionic liquid develop a higher order peak late in the reaction. Both of these observations are consistent with SAXS data of pre-formed solid samples, as discussed in Chapter 2. Figure 3.17 shows the evolution of the maximum intensity, I_{m}, of the primary structure factor peak located at wave vector q_{m}. These values were extracted from fits of the peaks to a Lorentzian function (see Figures A.1 and A.2 in Appendix A.1).

Before proceeding, several comments on experimental details are in order. An unexpected result of these experiments was the decrease in intensity of the scattering

Table 3.5: X-ray scattering length density, ρ, of the constituent components in PIPS PEMs

species	ρ (10^{10} cm^{-2})
PS	8.8
PEO	9.8
PMMA	10.8
BMITFSI	11.5

peak late in the reaction. The most likely explanation for this observation is sample degradation by the high energy X-ray beam. For the sample in panel (a), in particular, the scattered intensity varied widely between exposures late in the reaction (note the spread between blue and violet-colored traces). Furthermore, frequent exposures to the X-ray beam might have accelerated the rate of polymerization. For example, comparing panels (b) and (d), the higher order peak emerges at approximately 52 min for sample (b) and 130 min for sample (d). Sample (b) was exposed to the X-ray beam more frequently than sample (d). Unfortunately, the decrease in intensity makes it difficult to interpret, for example, the time-resolved change in intensity of the scattering peak or calculated parameters such as the invariant. Small-angle neutron scattering (SANS) could be used to probe structural changes during the polymerization, as beam damage is not a concern in SANS. Additional advantages of SANS include (i) the ability to tailor the scattering contrast by deuterating different constituent components, and (ii) relative to SAXS, SANS is more amenable to reducing scattered intensity to absolute units, facilitating quantitative interpretation of scattering data. Although sample degradation and acceleration of the polymerization might have impacted the SAXS results late in the reaction, it appears that the early time points are internally consistent. That is, the peaks emerge at approximately the same time for replicate samples prepared without ionic liquid (74 and 83 min) and with ionic liquid (8 and 5 min). This suggests that, at the very least, the traces collected early in the reaction can provide some insight into the development of morphology.

Returning to the emergence of scattering peaks in Figure 3.16, in general, the scattered intensity is the square of the scattered amplitude, which is the three dimensional Fourier transform of the real space distribution of scattering length density. In particular, the two criteria necessary to observe a peak in scattering data are as follows: (i) there must exist a preferred length scale of spacing between scattering centers, which the Fourier transform returns as a peak in reciprocal space, and (ii) there must be sufficient contrast in scattering power between domains. In the case of SAXS experiments, scattering contrast is proportional to the square of the difference in X-ray scattering length density between domains. Table 3.5 summarizes the X-ray scattering length density of the constituent components in the PEMs studied in this chapter. In general, the scattering contrast is sufficient and should not limit the appearance of a peak in this system. For example, neat PS-*b*-PEO diblocks exhibit a relatively weak scattering peak, even at low degree of polymerization, and the addition of ionic liquid to the PEO phase substantially increases the contrast and the scattered intensity.

Interpretation of the scattering peaks in Figure 3.16 is still not necessarily straightforward, however, as the peaks could be a result of, *inter alia*, correlations in the disordered phase of the growing block polymer[154,194,195] or microphase separation between the P(S-*co*-DVB) and PEO or PEO/IL phases.[196] Both of these situations satisfy the criteria expressed above. One definite conclusion to be drawn from the scattering data in Figure 3.16 is that the lack of sharp, higher order Bragg peaks in PIPS samples rules out the existence of a well-defined, periodic structure with long-range order. This interpretation was corroborated in Chapter 2 by real space images, such as transmission and scanning electron micrographs, which provide direct visualization of the lack of long-range order of the microphase separated domains in pre-formed, solid PIPS PEMs. The question then becomes: at what point during the PIPS reaction does there exist a thermodynamic drive for microphase separation between the P(S-*co*-DVB) and the PEO or PEO/IL phases?
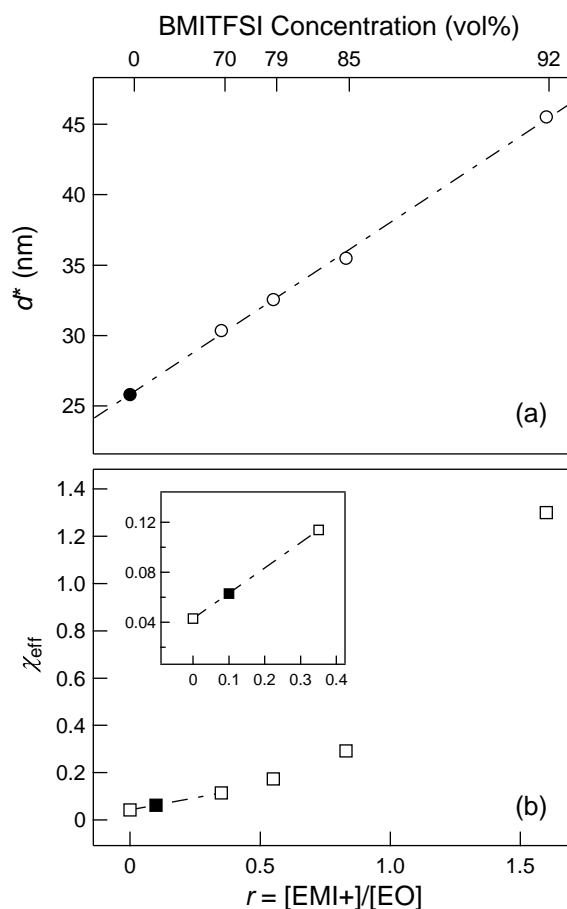
Figure 3.18: (a) Lamellar d-spacing at 150 °C for PS-b-PEO/EMITFSI blends (open circles, data from ref 56) and linear extrapolation to a hypothetical neat ($r = 0$) diblock (filled circle). (b) Estimation of the effective interaction parameter, $\chi_{\mathrm{salt}}^{\mathrm{eff}}$, at 150 °C for PS-$b$-PEO/EMITFSI as a function of salt loading, r. The filled square represents a PIPS PEM with 21 overall vol% BMITFSI. The inset shows an expanded view of the low-r data and the linear interpolation used to determine $\chi_{\mathrm{salt}}^{\mathrm{eff}}$ of the sample.

The effective interaction parameter, χ^{eff}, was not directly calculated for the P(S-*co*-DVB)-*b*-PEO/BMITFSI system studied here. However, Simone et al.[56] reported scattering data at 150 °C for lamellae-forming PS-*b*-PEO/EMITFSI blends that should provide a reasonable estimate for χ^{eff} in the PIPS system. As shown in Figure 3.18, Simone et al. measured the increase in *d*-spacing with increasing salt loading for four lamellae-forming PS-*b*-PEO/EMITFSI blends. Salt doping is analogous to blending diblocks with a selective solvent,[56,151] and increases the *d*-spacing both by simple volume addition to one phase and by increasing chain stretching at the interface. The concentration of EMITFSI is reported in terms of *r*—defined here as the molar ratio of cations to EO repeat units—to more readily compare these results to studies of diblock/salt interaction parameters in the literature.[85,155–159,197] The equivalent concentration in terms of volumetric units is also given in Figure 3.18.

In the work of Simone et al., the neat diblock formed cylinders, so a linear extrapolation of the four lamellae-forming data points was used in Figure 3.18(a) to estimate the *d*-spacing of a hypothetical neat diblock, for which $d^* \approx 25$ nm. Next, the relation between the *d*-spacing and χ^{eff} in the strong segregation limit (defined as $\chi N >> 10$) due to Semenov[160] can be used to determine the increase in the interaction parameter upon salt doping, $\chi^{\text{eff}}_{\text{salt}}$, relative to that for a neat diblock, $\chi^{\text{eff}}_{\text{neat}}$.

$$\chi^{\text{eff}}_{\text{salt}} = \chi^{\text{eff}}_{\text{neat}} \left(\frac{d^*_{\text{salt}}}{d^*_{\text{neat}}} \right)^6 \tag{3.14}$$

The interaction parameter of a neat PS-*b*-PEO diblock was calculated by Zhu et al.,[153] who fit scattering data of the disordered diblock to Leibler's[154] RPA structure factor. Well above the order-disorder transition temperature (T_{ODT}), the calculated interaction parameter was linear in inverse temperature, and it exhibited the expected deviation due to fluctuations near the T_{ODT}. In the linear regime, the temperature dependence of $\chi^{\text{eff}}_{\text{SO}}$ (SO refers to PS-*b*-PEO) is

$$\chi^{\text{eff}}_{\text{SO}}(T) = \frac{21.3}{T} - 7.05 \times 10^{-3} \tag{3.15}$$

using a reference volume of 100 Å^3.

Figure 3.18(b) shows the results of applying eq 3.14 to the data in panel (a), after using eq 3.15 to calculate $\chi_{\text{neat}}^{\text{eff}} = 0.043$ at 150 °C. The concentration of BMITFSI in PIPS electrolytes prepared with 21 overall vol% corresponds to $r = 0.1$, so linear interpolation was used to estimate an increase in χ^{eff} of 1.5 relative to the neat diblock, or $\chi_{\text{salt}}^{\text{eff}} = 0.065$. Strictly speaking, this value of $\chi_{\text{salt}}^{\text{eff}}$ is valid at 150 °C, but salt doping has a much stronger effect on the interaction parameter than temperature, so the factor of 1.5 increase in χ^{eff} for $r = 0.1$ should be valid at 120 °C, as well.

Figure 3.19 uses the values of $\chi_{\text{neat}}^{\text{eff}}$ and $\chi_{\text{salt}}^{\text{eff}}$ calculated above to compare the segregation strength, χN, for a linear PS-b-PEO diblock to the mean field prediction for the segregation strength at the ODT, $(\chi N)_{\text{ODT}}$. For a neat diblock, the combination of χN and the volume fraction, f, of one of the blocks defines the morphological equilibrium on the classic phase portrait.[198] One of the challenges in modeling the PIPS system is that the values of both χN and f change as the reaction progresses. Figure 3.19 therefore makes several important simplifying assumptions about the PIPS system. (i) The growth of the P(S-co-DVB) block off a 5 kg/mol PEO-CTA is modeled by calculating the value of χN assuming a neat, linear diblock at discrete values of M_{PS}.[iii] In reality, the P(S-co-DVB)-b-PEO diblock is growing in a monomer mixture of S/DVB. At 120 °C, the S/DVB mixture is effectively a neutral solvent and screens some of the net repulsive interactions between P(S-co-DVB) and PEO. (ii) The addition of ionic liquid is modeled by simply increasing the magnitude of χ^{eff} by a factor of 1.5. That is, the volume addition of the ionic liquid to the PEO phase is not accounted for. (iii) $(\chi N)_{\text{ODT}}$ was calculated from the mean field prediction, which ignores spontaneous concentration fluctuations that exist in the disordered melt in the vicinity of the T_{ODT}. As in the case of growing the diblock in a neutral solvent, fluctuations will screen net unfavorable interactions. The values of χN in Figure 3.19 therefore

---

[iii]Note that χN was calculated with respect to a reference volume of 100 Å^3, but the horizontal axis of Figure 3.19 is reported in terms of the molar mass of the polystyrene block, M_{PS}, which is proportional to the chemical degree of polymerization.
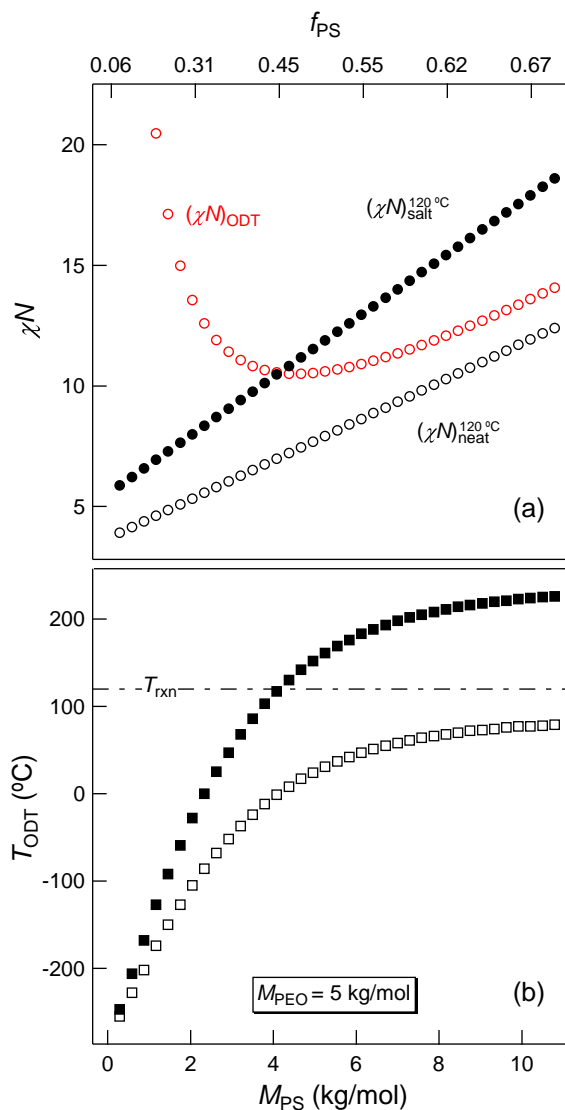
Figure 3.19: (a) Segregation strength, χN, as a function of the molar mass of the growing polystyrene block. The top axis give the equivalent volume fraction of the PS block, calculated on a 100 Å^3 basis. $(\chi N)_{\text{ODT}}$ is the mean field prediction for segregation strength at the order-disorder transition temperature. $(\chi N)_{\text{neat}}^{120\,°C}$ is the calculated segregation strength of a neat PS-b-PEO diblock at 120 °C, calculated using data from ref 153. $(\chi N)_{\text{salt}}^{120\,°C}$ is the segregation strength with the addition of 21 overall vol% BMITFSI, calculated assuming $\chi_{\text{salt}}^{\text{eff}} = 1.5\chi_{\text{neat}}^{\text{eff}}$, based on an analogous system of PS-b-PEO/EMITFSI. (b) Mean field prediction for the T_{ODT} as a function of PS molar mass for a neat PS-b-PEO diblock (open squares) and PS-b-PEO/BMITFSI (filled squares).

represent an upper limit, as both the neutral solvent and fluctuations will stabilize the disordered phase, pushing $(\chi N)_{ODT}$ higher than the mean field prediction.

Despite the simplifications discussed above, Figure 3.19 provides valuable insight into the PIPS reaction. In a sense, the time variable in the PIPS experiments is analogous to inverse temperature for a diblock melt. Early in the reaction (or equivalently, high temperature for a linear diblock) the diblock is disordered, and the local composition can be described by the mean field. In Figure 3.19, this corresponds to low M_{PS}, where the value of χN for both the neat and salt-doped diblock is much lower than $(\chi N)_{ODT}$. As the reaction progresses and M_{PS} increases (the temperature of a neat diblock is lowered toward the T_{ODT}), a thermodynamic drive emerges to first develop concentration fluctuations and ultimately to order.

The segregation strength of the neat sample is always much lower than that of the sample with ionic liquid, possibly explaining why scattering peaks emerge much later in the reaction for the neat sample relative to the electrolyte. For $M_{PS} \geq 4$ kg/mol, the segregation strength for the sample with ionic liquid is larger than $(\chi N)_{ODT}$, indicating a thermodynamic drive to order. If the system were at equilibrium, the volume fraction of PS at the crossover would place the diblock in the lamellae-forming region of the diblock phase portrait. Interestingly, the segregation strength of the neat diblock at 120 °C is always lower than $(\chi N)_{ODT}$, even for a fully polymerized diblock. That is, even if all the styrene monomer were incorporated into the neat PS-b-PEO diblock—for which $M_{tot} \approx 16$ kg/mol and $f_{PS} \approx 0.7$—the system would be disordered. This is perhaps not surprising, as χ_{SO}^{eff} is rather low (0.046 at 120 °C), requiring a relatively high chemical degree of polymerization (> 300) to place PS-b-PEO inside the ordered window at 120 °C.

Figure 3.19(b) re-casts the segregation strength data in terms of the mean field prediction for the T_{ODT}, using the temperature dependence for χ_{neat}^{eff} reported by Zhu et al.[153] and the estimated increase in χ_{salt}^{eff} found in Figure 3.18(b). As the PS block grows off the PEO-CTA, T_{ODT} increases. When the T_{ODT} is higher than the reaction
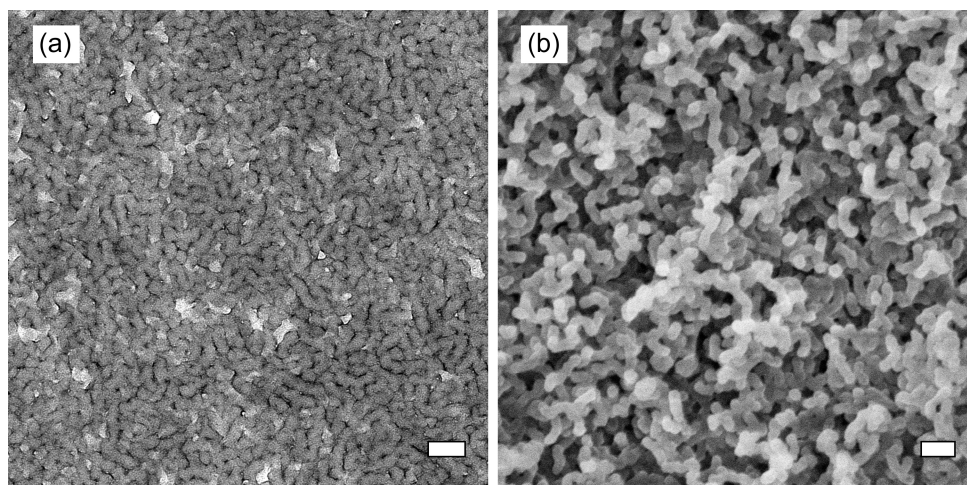
Figure 3.20: Real space images of pre-formed PIPS PEMs prepared with 28 kg/mol PEO-CTA and 21 vol% BMITFSI. (a) Transmission electron micrograph. The PEO/IL domains appear dark after staining with RuO_4. The crosslinked polystyrene domain appears bright. (b) Scanning electron micrograph. The voids/pores are regions where PEO/IL domains were etched with hydroiodic acid. Bright regions are crosslinked polystyrene. The scale bar equals 100 nm in both images.

temperature (120 °C), there is a thermodynamic drive to order. As in the case of χN, the diblock with ionic liquid first enters the ordered window when $M_{PS} \approx 4$ kg/mol, whereas the neat diblock is disordered during the entire reaction.

The segregation strength arguments summarized in Figure 3.19 concern the ordering transition of the growing diblock, but to reiterate, the observed morphology of fully polymerized PIPS PEMs has been shown to be microphase separated *without* long-range order. Representative TEM and SEM images from Chapter 2 are reproduced in Figure 3.20 to illustrate this point. The morphology observed in the electron micrographs is reminiscent of the fluctuation-induced, disordered bicontinuous structure known to exist in neat diblock melts in the vicinity of the T_{ODT}.[129,199,200] This disordered network morphology is a direct result of the "frustrated" state of the diblock: the two blocks experience net unfavorable enthalpic interactions, but the temperature is not yet low enough to induce the chain stretching associated with the ordering process. The connectivity of the diblock restricts the compositional heterogeneity to

length scales of $\mathcal{O}(R_\mathrm{g})$. It is likely that the long-range domain continuity observed in PIPS PEMs is a direct result of kinetically trapping (via chemical crosslinking) this disordered network structure prior to ordering of the growing diblock.

There is literature precedence for this interpretation. For example, Sakamoto et al.[130,131] studied the ordering kinetics of nearly symmetric poly(styrene-b-isoprene) diblocks when quenched from a disordered melt to below the T_ODT. The authors provided direct visualization (via TEM) of samples quenched from the disordered state, which revealed an isotropic network morphology similar to that shown in Figure 3.20. The disordered network structure persisted for a period of time slightly below the T_ODT, until the equilibrium lamellar morphology had sufficent time to nucleate and grow. Bates et al.[129] studied a nearly symmetric poly[(ethylene-propylene)-b-ethylethylene] diblock with small-angle neutron scattering and noted qualitative similarities between the structure factor of the disordered diblock melt and the transient morphology observed during macrophase separation of binary blends via spinodal decomposition. In particular, the structures of the disordered diblock and the binary blend are characterized by isotropically-oriented sinusoidal composition fluctuations.

There are important differences, however. The disordered diblock melt represents an equilibrium morphology, and the position of the structure factor peak is restricted by the size of the diblock. The peak observed during spinodal decomposition is non-equilibrium, with a length scale that represents a compromise between the rate of mutual diffusion and interfacial tension between the species undergoing phase separation. Furthermore, the length scale of heterogeneity observed during spinodal decomposition ultimately diverges to infinity. Interestingly, Bates et al. argued that the similarities between the scattered intensity of the diblock and the binary blend should break down, because the late stages of spinodal decomposition are characterized by a square-wave composition profile, whereas disordered diblock melts had previously been associated with small amplitude composition fluctuations characteristic of the weak segregation regime ($10 < \chi N < 100$). More recently, however,

Lee et al.[161] showed that the ODT of a nearly symmetric poly(isoprene-b-lactide) diblock was consistent with a "pattern transition", in which the amplitude of fluctuations does not change through the T_{ODT}. Instead, the physical interpretation of the ODT is that domain purity is both high and constant through the transition, and the ordering process simply corresponds to a rearrangement of the interface between domains.

As mentioned above, there is a large difference in the time it takes for the scattering peaks to emerge in neat samples as compared to IL-containing samples. Despite the difference in timescales, however, the scattering data for both neat and IL-containing samples exhibit similar qualitative trends, namely an exponential increase in scattered intensity (before the drop-off, which is most likely due to sample degradation), and an increase, then decrease in the position of the scattering peak, q_m. If the scattered intensity is primarily due to the amplitude of the concentration profile, the exponential increase would be consistent with the amplitude growing at a rate limited by the effective mutual diffusion coefficient of the growing diblock.[201–203] Previously, Seo et al.[124] and Yamamoto et al.[137] studied systems similar to that presented here. These authors also observed an exponential increase in intensity while growing a diblock in a monomer mixture, and interpreted this observation as evidence that the system was undergoing macrophase separation via spinodal decomposition. Although it is true that models for spinodal decomposition[127,204] predict scattering signatures such as an exponential increase in intensity and a preferred wavelength of composition fluctuations, observation of these phenomena does not necessarily imply that spinodal decomposition is the operative mechanism.

In this work, the preferred length scale of compositional heterogeneity appears to be closely tied to the size of the diblock. The characteristic center-to-center distance for the samples in Figures 3.6 and 3.7 is between 13–16 nm. The unperturbed R_g of a linear PS-b-PEO diblock—taking $N \approx 200$ and $b \approx 0.6$ nm—is $ca.$ 4 nm, which would result in $d^* \approx 8$ nm. However, chains will be stretched relative to a random coil

at the interface, so locally, the d-spacing should approximate an equilibrium lamellar morphology. The relation developed by Semenov[160] for the d-spacing in the strong segregation limit (SSL) can therefore be used to estimate d^*.

$$d^* \approx 4 \left(\frac{3}{\pi^2} \right)^{\frac{1}{3}} b N^{\frac{2}{3}} \chi^{\frac{1}{6}} \tag{3.16}$$

Inserting the same values used above to estimate R_{g} and the measured value of $\chi_{\mathrm{SO}}^{\mathrm{eff}} = 0.047$ at 120 °C, eq 3.16 predicts $d^* \approx 34$ nm, in reasonably close agreement with the measured d-spacing. The factor of two difference likely stems from the fact that eq 3.14 is intended for diblocks in the SSL. It is not surprising that chains in this hypothetical PS-b-PEO (for which $\chi N \approx 10$) are not as stretched as the SSL predicts, as the N dependence will be weaker than the 2/3 power. Nonetheless, this rough calculation suggests that the 13–16 nm size scale can be rationalized by a molecular picture of two layers of stretched blocks in each domain. In contrast, the preferred wavelength of fluctuations during spinodal decomposition is much larger than the characteristic size of the constituent molecules, ultimately diverging to infinity upon macrophase separation. The decrease in q_{m} during the course of the reaction might reflect an increase in chain stretching as the segregation strength increases during the reaction. The Δq_{m} corresponds to an increase of approximately 2 nm, which could easily be accommodated by chain stretching. Presumably, the SAXS experiments were terminated too early to observe a clear plateau in the value of q_{m}.

Two experiments were performed to test the hypothesis that the PIPS strategy relies on kinetically trapping a disordered, bicontinuous morphology prior to ordering. First, samples were prepared by varying the mole fraction of divinylbenzene in the monomer mixture from 0 (pure styrene) to 100% (pure DVB). The concentration of the PEO-CTA was fixed at 32 wt%. Note that the radical initiator AIBN was not used for the DVB-variation samples.

Figure 3.21 shows SAXS results of the resulting electrolytes prepared with 21 overall vol% BMITFSI. For context, the DVB concentration typically used in this
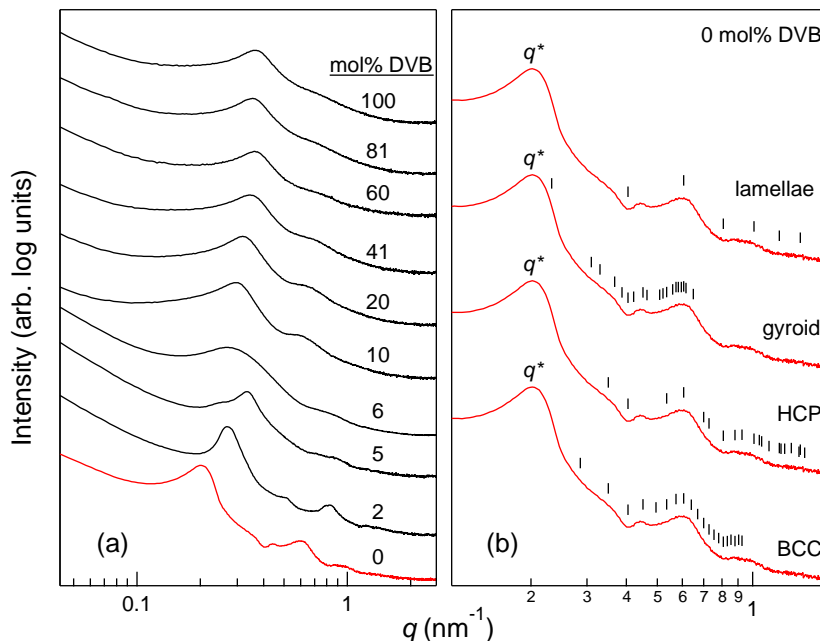
Figure 3.21: (a) SAXS data for samples prepared with 5 kg/mol PEO-CTA (32 wt%), 21 overall vol% BMITFSI, and S/DVB, with varying concentration of DVB. (b) SAXS data for the sample in (a) with 0 mol% DVB, referenced to four common diblock copolymer equilibrium morphologies. The tick marks give the locations of allowed reflections for lamellae, gyroid, hexagonally close-packed (HCP) cylinders, and body-centered cubic (BCC) spheres. Allowed reflections are given as ratios of q/q^*. Lamellar: $1 : 2 : 3 : 4 \ldots$; gyroid (Ia$\bar{3}$d): $\sqrt{6} : \sqrt{8} : \sqrt{14} : \sqrt{16} : \sqrt{20} \ldots$; HCP: $1 : \sqrt{3} : \sqrt{4} : \sqrt{7} : \sqrt{9} : \sqrt{12} \ldots$; BCC: $1 : \sqrt{2} : \sqrt{3} : \sqrt{4} : \sqrt{5} : \sqrt{6} \ldots$

work is 20 mol% (*i.e.*, a 4/1 molar ratio of S/DVB). Samples prepared with DVB concentrations between 6 and 100 mol% exhibit a broad primary peak and, in some cases, a relatively weak higher order correlation peak. Although these samples were not imaged in real space, these scattering signatures are consistent with other PIPS PEM samples that have been shown to exhibit long-range continuity of domains that lack periodic order.

In contrast, samples prepared with 5 mol% DVB or less exhibit relatively sharp Bragg peaks, suggesting some degree of long-range, periodic order. As shown in panel (b), the higher order reflections do not appear to correspond to any of the common equilibrium morphologies for neat diblocks. However, with the exception of
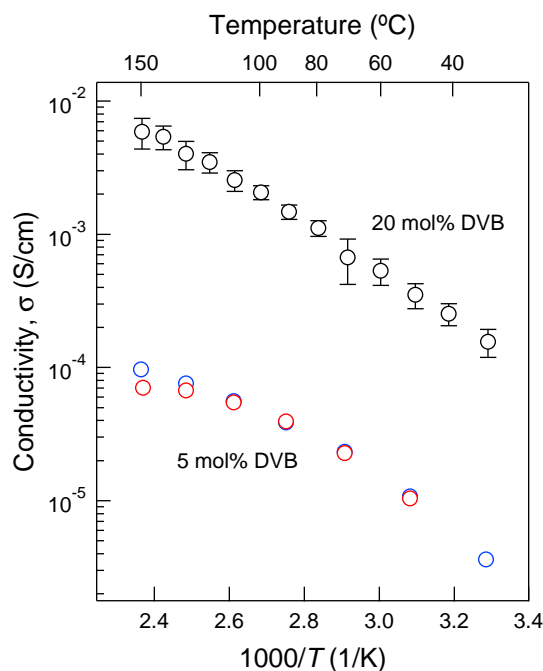
Figure 3.22: Temperature-dependent conductivity as a function of DVB concentration. Both samples were prepared with 5 kg/mol PEO-CTA and 21 overall vol% BMITFSI. The 5 mol% DVB sample was dried and annealed at 150 °C for several hours prior to beginning the impedance sweeps. Data were then collected upon cooling (blue circles), then heating (red circles). Error bars for the 20 mol% DVB sample represent one standard deviation based on three samples.

the linear diblock (*i.e.*, the 0 mol% DVB sample), chemical crosslinking likely prevents relaxation to morphological equilibrium. Even in the case of the linear diblock, the close proximity of the reaction temperature to the T_g of linear PS (*ca.* 100 °C) might slow relaxation to equilibrium, and the sample was not annealed at a temperature higher than 120 °C after the reaction was complete. Nevertheless, Figure 3.21 suggests that the PIPS reaction mixture is *en route* to microphase separation with long-range order, and some threshold concentration of crosslinking agent is required to prevent the growing diblock from undergoing a transition from the disordered network to an ordered morphology.

From the viewpoint of the resulting membrane performance, trapping the bicontinuous network structure prior to ordering appears to be critically important, as

illustrated in Figure 3.22. At equal concentration of ionic liquid (21 overall vol%), the conductivity of a sample prepared with only 5 mol% DVB is approximately a factor of 60 lower than a sample prepared with 20 mol% DVB. As previously discussed, the conductivity of the sample prepared with 20 mol% DVB is consistent with the reduction in conductivity relative to a homogeneous, homopolymer-based electrolyte, based on volume fraction and geometric arguments.

$$\sigma = \sigma_c \frac{f_c}{\tau} \tag{3.17}$$

In particular, the conductivity of the sample prepared with 20 mol% DVB suggests that the conducting domains exhibit long-range continuity. There are two primary reasons why the measured conductivity would be lower than eq 3.17 predicts: (i) the conducting domains are not continuous, and instead exhibit network defects such as dead ends and isolated domains, and (ii) the conducting domains do not behave like the bulk electrolyte, due to, for example, a wide interfacial thickness. It is unlikely that interfacial effects could account for the factor of 60 reduction in measured conductivity observed in the sample prepared with 5 mol% DVB. Instead, it is plausible that when the system undergoes a transition to an ordered state (which should be verified by real space images), the conductivity is reduced by network defects, such as grain boundaries and dead ends. The detrimental effects of network defects on the conductivity of ordered block polymer electrolytes are well documented in the literature.[84,86,90]

In addition to the low conductivity of the sample prepared with 5 mol% DVB, the mechanical properties were poor. 5 mol% DVB is evidently not sufficient to gel the system, as the sample was found to flow at high temperature. Even at room temperature, the sample was a soft solid and could be easily manipulated with a spatula. The PIPS strategy therefore represents a unique opportunity to simultaneously increase both the mechanical properties and conductivity of a PEM. In the future, it might of interest to study a series of samples with increasing DVB concentration. As
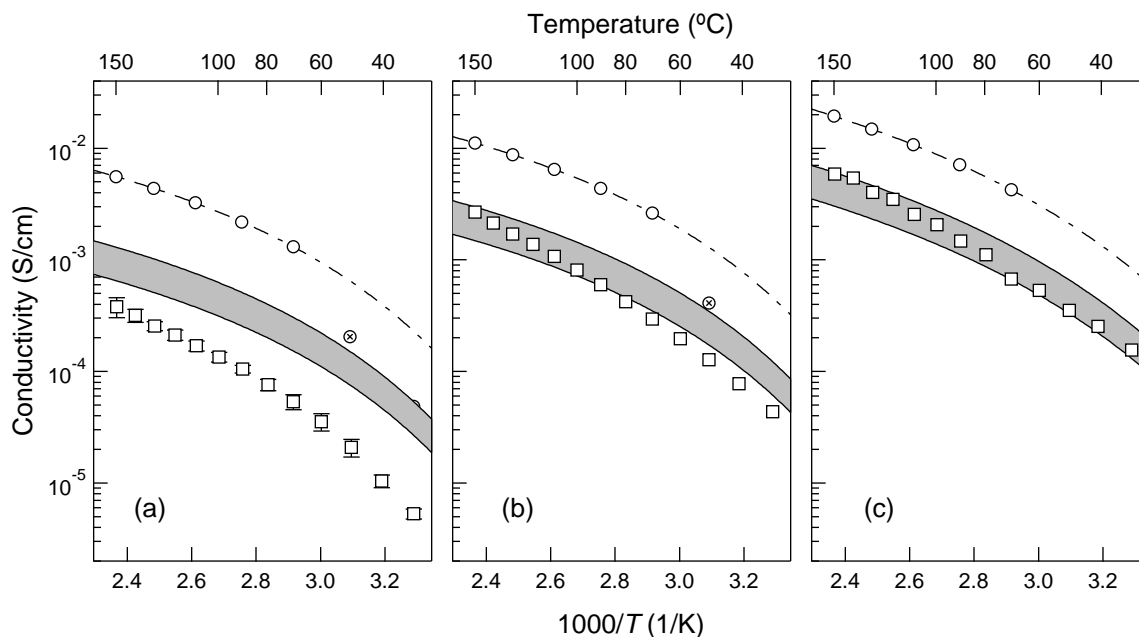
Figure 3.23: Comparison of measured conductivity, σ, to that anticipated by $\sigma = \sigma_c \left(f_c / \tau \right)$. The PIPS PEM sample (squares) was prepared with 5 kg/mol PEO-CTA with (a) 5, (b) 12, and (c) 21 overall vol% BMITFSI. The circles and dash-dot line are the measured conductivity and VFT fit of 8 kg/mol PEO homopolymer/BMITFSI electrolytes with equivalent concentration as the conducting phase in the nanostructured electrolyte. The concentration of the homogeneous electrolytes is (a) 15, (b) 30, and (c) 45 vol% BMITFSI. Crossed circles were at temperatures below $T_{m,PEO}$ and were omitted from the fit. The gray region was calculated assuming a range of tortuosity, $1.5 \leq \tau \leq 3$.

the concentration of DVB is increased from 0 to 20 mol%, there might be a drastic increase in conductivity at some threshold DVB concentration, corresponding to the formation of a bicontinuous network structure. Increasing the concentration of DVB above 20 mol% should not have a significant impact on the conductivity, *if* the network structure is retained. This series of experiments would also directly demonstrate that the mechanical and ion transport properties are largely decoupled, as increasing the crosslink density in the P(S-*co*-DVB) domain should not affect ion transport in the PEO domain.

The results of the second experiment are summarized in Figure 3.23. As discussed in Chapter 2, the conductivity of the nanostructured PIPS PEMs is consistent with

the tortuosity model (assuming $1.5 \leq \tau \leq 3$), suggesting both long-range continuity of the conducting domains, as well as a relatively narrow interface between domains. That is, the close proximity of the crosslinked polystyrene network does not appear to impede ion motion, as the interface comprises a small fraction of the PEO domain, and the conducting domain effectively behaves like the bulk electrolyte. This interpretation is consistent with the pattern transition discussed above, namely that the composition profile is a square-wave in the vicinity of the ODT. However, there is evidence that this is not always the case. As shown in panel (a), the conductivity of a PIPS sample prepared with only 5 overall vol% BMITFSI is lower than anticipated based on volume fraction and geometric arguments. Increasing the concentration to 12 and 21 vol% (panels (b) and (c), respectively) increases the measured conductivity to inside the bounds of anticipated conductivity. One possible explanation for this result is that the lower concentration of BMITFSI results in lower segregation strength (see Figure 3.18) and, thus, a smaller amplitude composition profile. The resulting wider interface would lower ionic conductivity by retarding PEO chain relaxation due to infiltration of the glassy, crosslinked PS network.[114] Some threshold segregation strength is therefore required to ensure narrow interfacial thickness or, equivalently, pure domains. An alternative explanation for the conductivity in panel (a) is that the degree of connectivity of the conducting domains is lower in panel (a) relative to panels (b) and (c), as dead ends in the conducting pathway would also reduce the measured conductivity.

3.4   Conclusions

The goal of this chapter is to understand the mechanism by which the PIPS reaction mixture transitions from a liquid to a high modulus solid. Having discussed the details of each *in situ* experiment, the composite data in Figures 3.6 and 3.7 will now be reanalyzed in aggregate. In general, the data support a molecular picture of the growing

P(S-*co*-DVB)-*b*-PEO diblock forming an isotropic, bicontinuous network as a result of concentration fluctuations. This morphology is then kinetically trapped before the ordering transition occurs. The calculated values of χN during the reaction indicate that the system does not even reach the order-disorder transition, although this could simply reflect uncertainty in the value of χ^{eff}. This scenario would be consistent with the "pattern transition" recently reported by Lee et al.[161] Alternatively, the system could pass through the ODT, yet still be unable to relax toward long-range order due to chemical crosslinking.

The rheology and scattering data for the IL-containing samples are consistent with the above hypothesis. The presence of ionic liquid induces microphase separation early in the reaction, as evidenced by the emergence of the structure factor peak. Microphase separation is then followed by the apparent rheological gel point, $G_{\text{gel}}^{\text{app}}$. As mentioned earlier, one of the key differences between neat and IL-containing samples is the inversion of the characteristic times observed in rheology and scattering experiments. The scattering peaks appear earlier for the sample with ionic liquid than the neat sample, likely because of the substantial increase in segregation strength upon salt-doping. For the neat sample, $G_{\text{gel}}^{\text{app}}$ occurs well before the emergence of scattering peaks. If the sample formed a homogeneous, crosslinked gel network prior to microphase separation, the chains would not be able to rearrange into the observed network morphology. However, $G_{\text{gel}}^{\text{app}}$ does not appear to represent true macroscopic gelation, so the fact that $G_{\text{gel}}^{\text{app}}$ precedes the emergence of SAXS peaks in the neat sample might not contradict the proposed model. More careful rheological experiments should place the true gel point after the emergence of the scattering peak.

The conductivity and mass yield experiments in Figure 3.7 provide additional insight into the proposed molecular picture of the PIPS reaction. Earlier, the sharp increase in mass yield at $t \approx 60$ min was attributed to the formation of discrete flocs of crosslinked polymer. This result also correlates well with the upturn in G', indicating an increase in the elastic contribution to the mechanical response. The

conductivity results, on the other hand, exhibit a gradual decrease from the value in the liquid precursor at 120 °C to the final value in the solid PEM. As discussed previously, the decrease in conductivity at early times is most likely a result of the increase in local viscosity. The ionic liquid remains soluble in the growing P(S-*co*-DVB) block for some amount of time, before eventually segregating to the PEO domains. The final value of conductivity reflects a combination of the local viscosity of the PEO environment and the tortuosity of the conducting pathways. In this sense, conductivity is perhaps the most informative experiment to probe formation of the network structure. The conductivity reaches its plateau value of 3 mS/cm at a reaction time of 3–4 h, suggesting that the PEO/IL domains are fully developed at that point. If scattering experiments of the ionic liquid-containing sample were extended to later in the reaction (while avoiding degradation issues), the values of I_m and q_m would likely plateau in the vicinity of 3–4 h, as well.

Chapter 4

Morphology, Modulus, and Conductivity of a Triblock Terpolymer/Ionic Liquid Electrolyte Membrane[i]

4.1 Introduction

The previous chapters detailed the study of polymer electrolyte membranes (PEMs) exhibiting outstanding combinations of mechanical properties and conductivity owing to the long-range continuity of high-modulus and ion transport domains. The bicontinuous stucture in those PEMs was generated via polymerization-induced phase separation (PIPS), a strategy that exploits kinetic control over morphology. Alternatively, block polymers provide a rich offering of thermodynamically stable morphologies suitable for PEMs. The focus of the work described in this chapter was the synthesis and characterization of a PEM prepared from a triblock terpolymer known

---

[i]Adapted with permission from McIntosh, L. D.; Kubo, T.; Lodge, T. P. *Macromolecules* **2014**, *47*, 1090-1098. Copyright 2014 American Chemical Society.

to exhibit several equilibrium network morphologies. The goal, of course, remains the same, namely to develop PEMs exhibiting high conductivity and superior mechanical properties.

Relative to diblock copolymers, ABC triblock terpolymers add minimal synthetic difficulty, but offer the design flexibility of a third block and a substantially larger phase window for isotropically-connected network morphologies.[94,96,98–101,105] Furthermore, although diblock copolymers can be designed to exhibit high modulus at low strain, they cannot achieve the elasticity and fracture toughness possible in multiblock polymers.[115] However, relatively little work has been done on triblock terpolymer-based electrolytes beyond fundamental morphological studies. The focus in this chapter is on the well-studied triblock terpolymer poly(isoprene-b-styrene-b-ethylene oxide) (ISO), whose phase diagram exhibits three distinct equilibrium network morphologies in which each phase is continuous throughout the sample.[96,98,100] ISO is well-suited as a polymer electrolyte because the glassy polystyrene (S) block provides mechanical integrity and mobile charges can be incorporated into the poly(ethylene oxide) (PEO) phase. The polyisoprene (I) block serves to induce self-assembly into the network morphology, but essentially wastes volume in the final electrolyte membrane. Ultimately, one could envision replacing the I block with a polar block that is immiscible with PEO (*e.g.*, poly(ethyl acrylate)),[205] and effectively doubling the volume fraction of conductive phase.

The target morphology here is the O^{70} orthorhombic network, as it occupies the largest phase window of the three network phases. Furthermore, there is no *a priori* reason to expect that minor differences in geometry—for example, cubic versus orthorhombic unit cell or even long-range periodic order versus microphase-separated but disordered—affect conductivity, so long as domains are well-connected. An important issue to consider is that blending ISO with salts such as $LiClO_4$ can
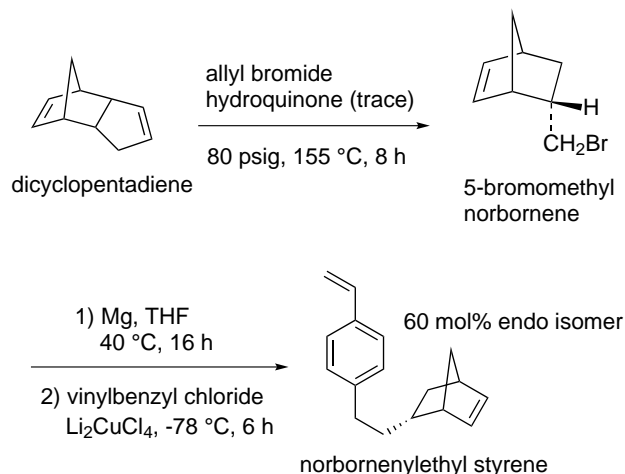
Figure 4.1: Synthetic scheme for norbornenylethyl styrene.

induce phase transitions away from the desired network morphology.[103,104] There-fore, chemical crosslinking functionality was included in the form of a norbornene-functionalized styrene monomer, with the goal of retaining the known phase behav-ior of ISO and adding the ability to lock in the desired network structure before incorporating mobile charges into the PEO domain. As an added benefit, chemical crosslinking substantially increases the overall toughness of the membrane and enables high-temperature operation (above the T_g of linear polystyrene). In this study, the salt is a room-temperature ionic liquid that exhibits high conductivity when blended with PEO.[23,24,56] This chapter focuses on the morphology, modulus, and ionic con-ductivity of a triblock terpolymer/ionic liquid polymer electrolyte membrane, with an emphasis on how crosslinking impacts each of these key properties.

4.2   Experimental Section

Synthesis and Characterization

All materials were purchased from Sigma-Aldrich unless noted otherwise and were used as received unless otherwise indicated. As shown in Figure 4.1, norbornenylethyl
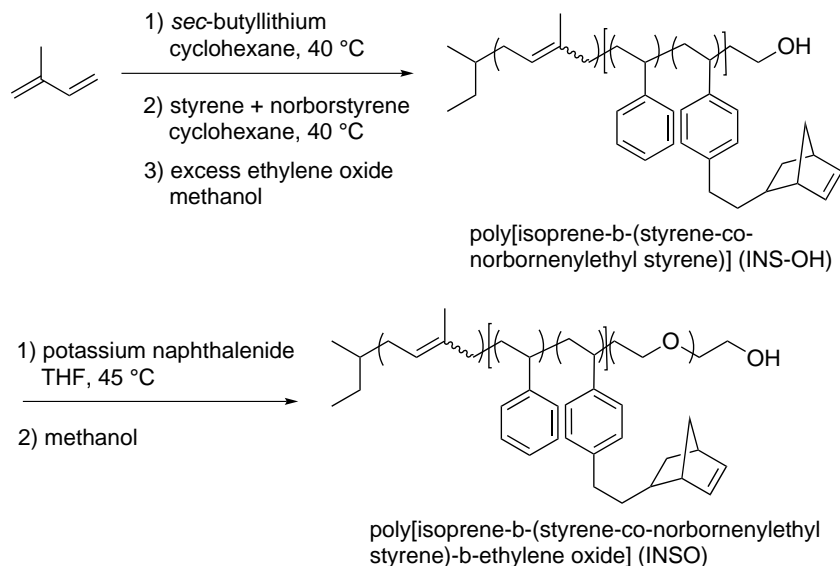
Figure 4.2: Reaction scheme for poly[isoprene-*b*-(styrene-*co*-norbornenylethyl styrene)-*b*-ethylene oxide] (INSO).

styrene (N) was synthesized following a procedure reported by Chen and Hillmyer.[206] Dicyclopentadiene, allyl bromide, and trace hydroquinone were heated to 155 °C in a high pressure reactor for 8 h. The product 5-bromomethyl norbornene was isolated via fractional distillation. Next, 5-bromomethyl norbornene was added dropwise to a suspension of magnesium powder in anhydrous THF. The as-formed Grignard reagent was transferred via cannulation to a solution of vinylbenzyl chloride with Li_2CuCl_4 in anhydrous THF under argon at –78 °C. After 6 h, NH_4Cl was used to quench the reaction, and the product was extracted with diethyl ether. Norbornenylethyl styrene was isolated via silica column using hexanes as the mobile phase. Purity (96 mol%) and chemical structure were confirmed with ^{1}H-NMR spectroscopy. Chemical shifts agreed well with previously reported values.[206]

The triblock terpolymer poly[isoprene-*b*-(styrene-*co*-norbornenylethyl styrene)-*b*-ethylene oxide] (INSO) was synthesized using well-established anionic polymerization techniques.[144,145] As shown in Figure 4.2, hydroxyl-terminated poly[isoprene-*b*-(styrene-*co*-norbornenylethyl styrene)]-OH (INS-OH) was prepared in cyclohexane
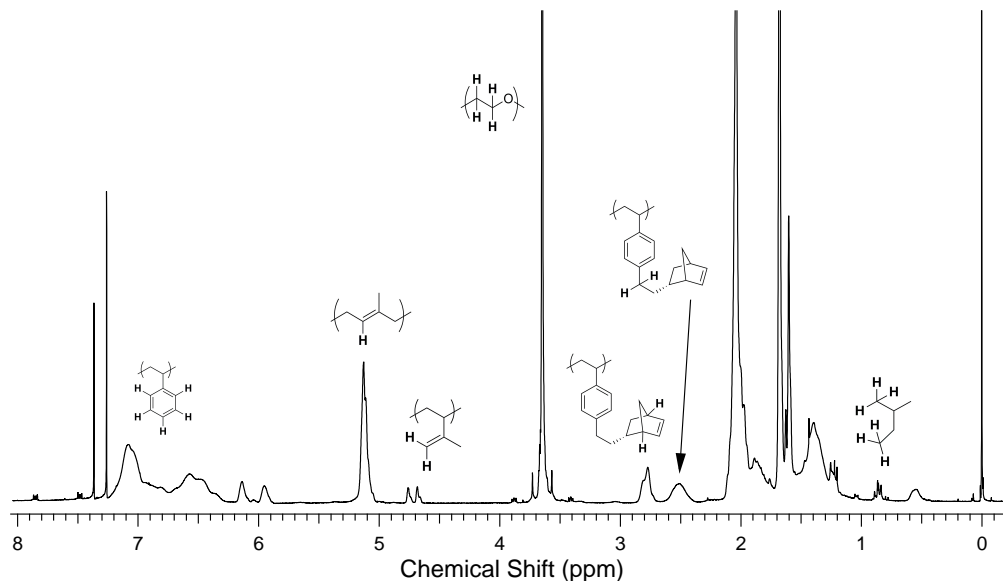
Figure 4.3: ^{1}H-NMR spectroscopy data for poly[isoprene-*b*-(styrene-*co*-norbornenylethyl styrene)-*b*-ethylene oxide] (INSO).

using *sec*-butyllithium initiator and the sequential addition of isoprene, then styrene + norbornenylethyl styrene. The living blocks were end-capped with hydroxyl functionality by the addition of excess ethylene oxide and were terminated with acidic methanol. INS-OH was isolated and purified by repeated precipitations in a mixture of isopropanol and methanol. The ethylene oxide block was added by reinitiating INS-OH via titration with potassium naphthalenide. The reaction was terminated with acidic methanol. The chemical composition of INSO was verified with ^{1}H-NMR spectroscopy and the SEC trace showed a single narrow peak (Figures 4.3 and 4.4, respectively). INSO was purified by repeated dialysis against pure THF because the addition of the ethylene oxide block to the INS-OH intermediate leaves potassium salt in the final product, which could interfere with conductivity experiments. Per atomic emission spectroscopy, dialysis decreased the concentration of potassium salt from 56 to less than 0.3 ppm (the detection limit of the instrument).

The room-temperature ionic liquid 1-ethyl-3-methylimidazolium bis(trifluoromethyl-sulfonyl)imide (EMITFSI) was synthesized following established procedures.[44,58,59]
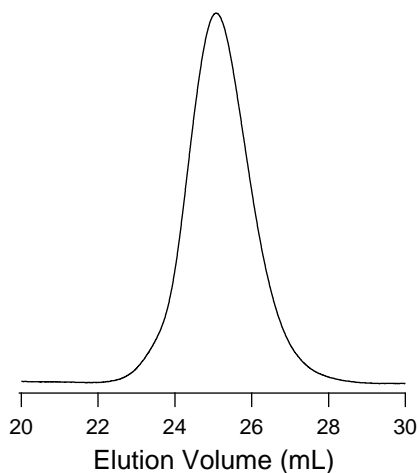
Figure 4.4: Size exclusion chromatography trace for INSO. The sample was run in a mixture of THF + amine.

EMIBr (Ionic Liquid Technologies) and LiTFSI (3M) were mixed in distilled water and stirred at 70 °C for 24 h. After the anion exchange reaction was complete, the product was diluted in chloroform, and LiBr was extracted by repeated washes with distilled water. EMITFSI was passed through an alumina column to remove impurities. After drying under dynamic vacuum at elevated temperature, purity (> 99 mol%) was verified with ^{1}H-NMR spectroscopy in deuterated DMSO and differential scanning calorimetry (DSC). Chemical shifts and thermal transitions observed in DSC ($T_g = -92$ °C, $T_m = -12$ °C) agreed well with previously reported values.[44,58,59] EMITFSI was stored in an argon-filled glovebox and was dried under dynamic vacuum at elevated temperature prior to each use.

Differential scanning calorimetry (DSC) experiments were performed on a TA Instruments Discovery DSC. Samples were prepared by sealing a known mass of sample in a standard aluminum pan. Samples were annealed at 150 °C (above any suspected thermal transitions) for 10 min, followed by cooling to –70 °C at 10 °C/min. The temperature was then immediately ramped back to 150 °C at 10 °C/min. All data shown were recorded during the second heating ramp.

Morphological Characterization

Small angle X-ray scattering (SAXS) experiments were performed at the 5-ID-D line at the Argonne National Laboratory Advanced Photon Source. Samples intended for equilibrium morphological experiments were annealed at 150 °C under dynamic vacuum for at least 24 h prior to SAXS experiments. Samples were then sealed in aluminum pans and were heated on the SAXS line and thermally equilibrated before exposure. The sample-to-detector distance was typically 5000 mm, and the nominal vacuum X-ray wavelength, λ, was 0.729 Å. Scattered intensity was recorded by a 2D MAR CCD, and the corrected 2D data were azimuthally integrated to obtain 1D plots of scattered intensity versus wave vector $q = 4\pi \sin(\theta/2)/\lambda$, where θ is the angle of scattered photons relative to the transmitted beam.

Samples for transmission electron microscopy (TEM) experiments were prepared by cryo-microtoming (Leica UC6 Ultramicrotome) bulk samples to obtain sections with a nominal thickness of 80 nm. Sections were collected on a 400 mesh copper grid and were stained with the vapor of a 2 wt% aqueous solution of OsO_4 for 5 min to enhance contrast between phases. TEM experiments were performed on an FEI Tecnai G2 Spirit Bio-TWIN using an accelerating voltage of 120 kV. Fourier transform (FT) analysis of TEM images was done using ImageJ software, which was used to generate FTs of raw TEM images and azimuthally integrate pixel intensity to generate plots of intensity versus wave vector q.

Samples for scanning electron microscopy (SEM) experiments were prepared by etching PEO with a 57 wt% aqueous solution of hydroiodic acid.[207] Samples were then dried and coated with *ca.* 1 nm of platinum to reduce charging. Imaging was done on a Hitachi S-900 at an accelerating voltage of 5 kV.

Mechanical Response

Rheological experiments were performed using a variety of deformation modes, geometries, and instruments (TA Instruments Rheometric Series ARES and RSA-G2),

depending on the mechanical response of the sample. In general, the frequency-dependent response was obtained as follows. Samples were thermally equilibrated for at least 10 min at a given temperature under a nitrogen purge. Samples were then subjected to an isochronal strain sweep to determine the limit of linear response, followed by a frequency sweep at fixed strain. For dynamic mechanical analysis (*i.e.*, temperature sweeps), the temperature was lowered at a rate of 1 °C/min at a fixed frequency, and strain amplitude was adjusted to remain within the linear viscoelastic response regime.

Ionic Conductivity

Ionic conductivity was measured using 2-point probe impedance spectroscopy on a Solartron 1255B frequency response analyzer connected to a Solartron SI 1287 electrochemical interface. Samples were stored in an argon-filled glovebox and were dried under dynamic vacuum at elevated temperature prior to measurements. Samples were then sandwiched between stainless steel electrodes and measurements were performed in open atmosphere. Water absorption is often a concern with polymer electrolytes containing Li-based salt. However, EMITFSI is relatively hydrophobic, and measurements were repeated after allowing the sample to sit in open air for 24 h to ensure that water absorption did not significantly affect the results. The sample temperature was controlled during experiments with a custom-built sample heating stage with a temperature feedback loop and was monitored with an independent thermocouple placed next to the sample. Ionic conductivity, σ, was calculated as $\sigma = l/(Ra)$, where l is the sample thickness, a is the superficial area, and R is the bulk resistance as determined from the high-frequency plateau in the real part of impedance, Z'.
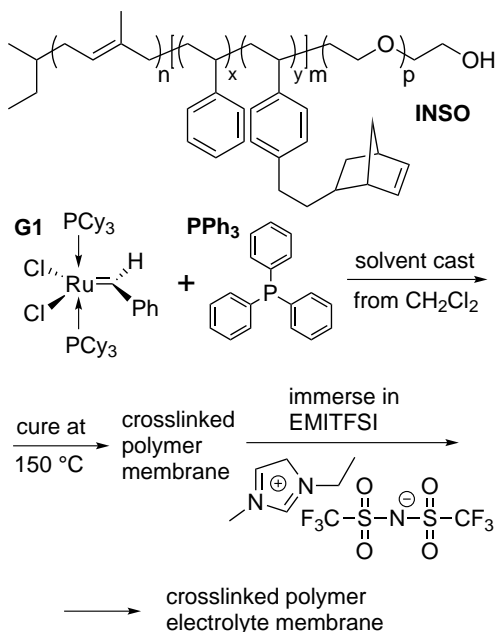
Figure 4.5: Reaction scheme used to generate crosslinked polymer electrolyte membranes.

4.3 Results and Discussion

Table 4.1 summarizes properties of the triblock terpolymer used in this study, poly[isoprene-b-(styrene-co-norbornenylethyl styrene)-b-ethylene oxide] (INSO). The volume fractions, f, of the blocks placed INSO inside the phase window for the O^{70} network morphology.[96] ^{1}H-NMR spectroscopy was used to calculate the number of norbornenylethyl styrene (N) repeat units in an average chain ($y/(x + y)$ in Figure 4.5), which was found to be 25 mol% (*ca.* 20 repeat units). The critical crosslink density is inversely proportional to the number of repeat units in an average chain, so for a polymer of this degree of polymerization (*ca.* 200 repeat units), fewer than 5–6 crosslinkable groups per chain should be sufficient to gel the system. This was demonstrated experimentally for a similar poly(N-co-S)-containing polymer reported by Price et al.[208] However, higher crosslink density was targeted with the goal of substantially increasing the modulus and high-temperature stability. The distribution of N repeat units in the middle block was not directly measured, but several previous

Table 4.1: Properties of INSO

M_n^i (kg/mol)	$Đ$	block volume fraction, f^{ii}			mol% N in N-*co*-S block[ii]
		f_I	$f_{N\text{-}co\text{-}S}$	f_{PEO}	
16.5	1.08	0.40	0.43	0.17	25

[i] Measured by size exclusion chromatography in series with a multi-angle light
    scattering detector
[ii] Calculated from ^{1}H-NMR spectroscopy peak integration

reports have suggested that N adds randomly to the growing N-*co*-S block.[206,208,209]

Figure 4.5 summarizes the strategy used to prepare crosslinked polymer electrolyte membranes. A known mass of INSO was dissolved in dichloromethane with the 1st generation Grubbs catalyst (G1, 0.25 overall wt%) and triphenylphosphine (PPh$_3$, 0.75 overall wt%), which was necessary to prevent gelation while the sample was still in solution at room temperature. The solution was cast into a custom-built stainless steel mold with a diameter of 50 mm, which resulted in films of order 100 μm thick. After the dichloromethane evaporated at room temperature over the course of *ca.* 20 min, the sample was placed in a vacuum oven set to 150 °C, which ensured all dichloromethane was removed and effected crosslinking via the ring-opening metathesis polymerization of norbornene moieties. Samples were typically allowed to react overnight, after which the INSO films could be peeled off the mold and were optically transparent with a brownish tint (due to the presence of G1). After this procedure, INSO could not be dissolved in good solvents such as THF and dichloromethane, indicating successful crosslinking.

To incorporate mobile charges into the PEO domain, INSO films were immersed in an excess volume of the ionic 1-ethyl-3-methylimidazolium bis(trifluoromethylsulfonyl)imide (EMITFSI) for several days at elevated temperature. The resulting volume fraction of EMITFSI was determined by massing the dry and ionic liquid-swollen membrane and converting to volume with known densities at 140 °C.[73] It is reasonable to expect that the ionic liquid resides exclusively in the PEO domain,[56,85,91] which is corroborated by DSC data (Figure 4.6), where the incorporation of EMITFSI into an
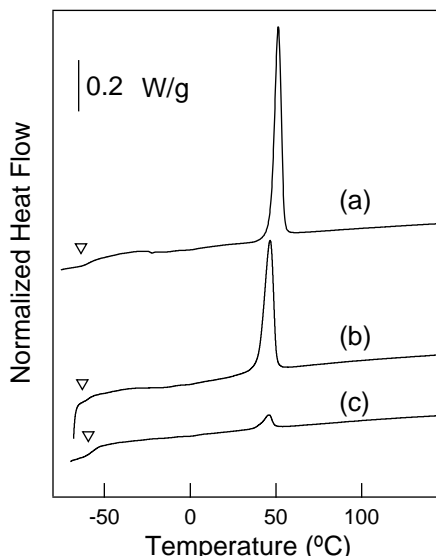
Figure 4.6: Differential scanning calorimetry data (exo down) for INSO (a) before crosslinking, (b) after crosslinking, and (c) after crosslinking and swelling the PEO domain with ionic liquid. Traces shown were collected upon the second heating cycle at 10 °C/min. The arrows point to the T_g of the polyisoprene domain. The peaks correspond to melting PEO crystals. Crystalline weight fractions, assuming 200 J/g for bulk PEO crystal,[148] are (a) 0.12, (b) 0.10, (c) 0.01.

INSO sample results in a factor of 10 decrease in the PEO crystalline weight fraction but has no influence on the T_g of the polyisoprene domain. The T_g of the N-*co*-S domain was not observed in DSC, as will be discussed later.

Morphological Characterization

The morphology of INSO electrolytes was characterized using a combination of SAXS, TEM, and SEM both before and after crosslinking and the incorporation of ionic liquid into the PEO domain. Figure 4.7 summarizes SAXS data of INSO at each step of the crosslinking procedure. Figure 4.7(a) shows SAXS data after annealing the sample at 150 °C for 24 h to promote rearrangement of chains prior to the SAXS experiment. No Grubbs catalyst was present, which precluded the crosslinking reaction. The T_{ODT} of INSO was not observed in this study, even up to 220 °C (the highest T used in this study). However, it is plausible that the observed morphology
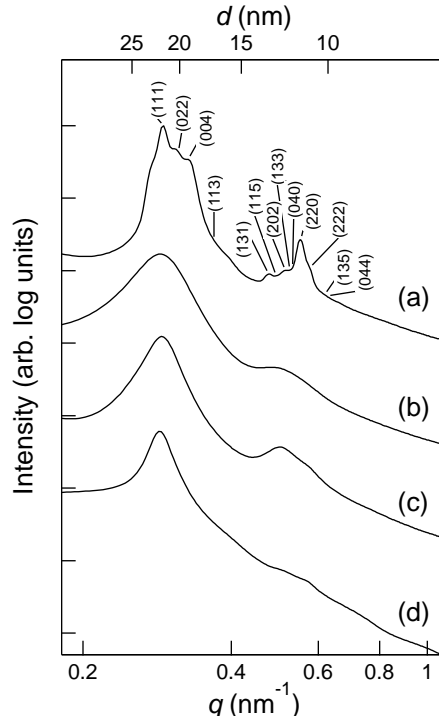
Figure 4.7: Small angle X-ray scattering of INSO samples at 30 °C. (a) INSO without the Grubbs catalyst, annealed at 150 °C for 24 h prior to the SAXS experiment. The numbers in parentheses are Miller lattice indices and point to the q values of allowed reflections for the O^{70} morphology. The best-fit lattice parameters (in nm) are $a = 25.8$, $b = 47.2$, and $c = 77.0$. (b) INSO with catalyst, solvent-cast from dichloromethane at room temperature. The sample was maintained at room temperature prior to and during SAXS exposure. (c) INSO after crosslinking. (d) INSO after crosslinking and swelling the PEO domain with ionic liquid.

represents thermodynamic equilibrium, as it was independent of the solvent used for casting (THF was used in addition to dichloromethane). The SAXS profile exhibits sharp Bragg peaks indicative of a well-defined periodic structure. The peak locations were referenced to allowed reflections for the O^{70} network morphology, a well-studied morphology observed in an analogous ISO triblock terpolymer without crosslinking functionality,[96,98,100] by fitting experimental peaks to the following equation:

$$q_{hkl} = 2\pi \left[\left(\frac{h}{a} \right)^2 + \left(\frac{k}{b} \right)^2 + \left(\frac{l}{c} \right)^2 \right]^{\frac{1}{2}} \tag{4.1}$$
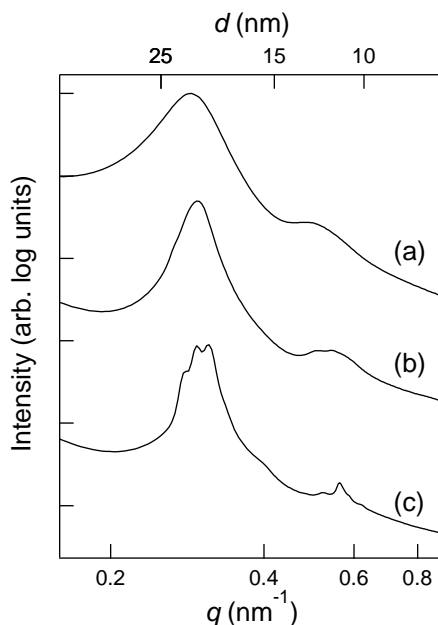
Figure 4.8: Small angle X-ray scattering (SAXS) data for INSO without catalyst, solvent-cast from dichloromethane at room temperature (RT). The sample was maintained at RT until the SAXS experiment and was then heated on the SAXS line and exposed at (a) 25 °C (as-cast), (b) 150 °C after a 2 min anneal, and (c) 200 °C after a 2 min anneal.

In eq 4.1, h, k, and l are Miller lattice indices and a, b, and c are the lattice parameters. The Matlab code used to calculate the best-fit lattice parameters is shown in Appendix C.1. To reiterate, the block volume fractions in INSO were chosen to target O^{70} because it occupies the largest phase window in the ISO phase diagram and, more importantly, because all three domains are continuous in space.

The SAXS data after the solvent-casting procedure (Figure 4.7(b)) are notably different than the equilibrium morphology observed in the sample without Grubbs catalyst. The sharp Bragg peaks of the equilibrium morphology are replaced by a relatively broad single peak at low q and a higher-order shoulder. The solvent-casting procedure results in a non-equilibrium structure, which is then kinetically trapped when INSO is heated to effect chemical crosslinking, as shown in Figure 4.7(c). This hypothesis was confirmed by a control experiment in which INSO was solvent-cast from dichloromethane without the Grubbs catalyst and was then heated

Table 4.2: Miller lattice indices for SAXS data of INSO/EMITFSI blends in Figure 4.9

concentration of EMITFSI (vol%)	T (°C)	a (nm)	b (nm)	c (nm)
1	150	26.8	50.5	79.7
1	220	25.4	47.6	75.4
10	150	28.5	56.8	78.2
10	220	28.4	54.1	83.7

on the SAXS line. As shown in Figure 4.8, four minutes at elevated temperature provides enough time for INSO to begin relaxing to morphological equilibrium, as evidenced by re-emergence of the Bragg peaks. This experiment also provides insight into the timescale of the crosslinking kinetics. When INSO is solvent-cast with catalyst and heated, the polystyrene chains gel within a few minutes, more rapidly than the polymer can relax to morphological equilibrium. Interestingly, the ratio of peaks in Figure 4.8(c) is approximately $q/q^* = \sqrt{3}$, suggesting some degree of local hexagonally close-packed character. However, the lack of refined higher order peaks suggests the correlation length does not extend further than a few domains. As shown in Figure 4.8(d), swelling a crosslinked INSO film with EMTIFSI has minimal effect on the overall morphology.

Figure 4.9 shows SAXS data of INSO/EMITFSI blends prepared without the Grubbs catalyst to allow morphological equilibration at elevated temperature. All samples were annealed at 150 °C for 24 h prior to the SAXS experiments, and the data shown were collected upon heating from room temperature. The concentration of EMITFSI is given as the volume fraction of the PEO/IL domain (PEO is 17 vol% of the triblock), as well as in terms of r, which is defined as the molar ratio of ethylene oxide repeat units to cations. For context, lithium salt-doped amorphous PEO electrolytes exhibit a maximum in conductivity in the vicinity of $r \approx 10$–25.[67,111,210] In general, blending INSO with EMITFSI shifts the equilibrium phase behavior away from the well-defined O^{70} network morphology toward hexagonally-packed cylinders.
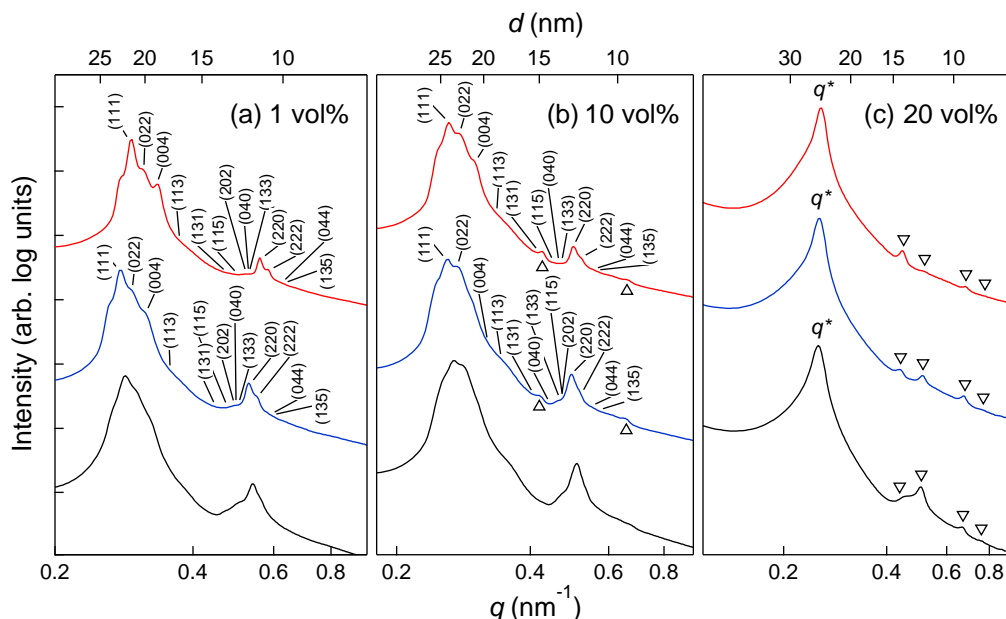
Figure 4.9: Small angle X-ray scattering data of blends of uncrosslinked INSO and the ionic liquid EMITFSI. Samples were annealed at 150 °C for 24 h prior to SAXS experiments and were then thermally equilibrated and exposed at three temperatures: 50 (black), 150 (blue), and 220 °C (red). Blends were prepared at three ionic liquid concentrations: (a) 1 vol%, $r = 667$; (b) 10 vol%, $r = 61$; (c) 20 vol%, $r = 27$. Reflections in (a) and (b) at 150 and 220 °C were referenced to the O^{70} morphology. The numbers are Miller lattice indices and point the locations of allowed reflections. Best-fit lattice parameters are given in Table 4.2. Open triangles (∇) in (c) indicate the locations of allowed reflections for hexagonally-packed cylinders ($q/q^* = 1 : \sqrt{3} : \sqrt{4} : \sqrt{7} : \sqrt{9}...$). Open triangles ($\triangle$) in (b) indicate possible reflections for hexagonally-packed cylinders.

Even at a concentration of 1 vol% (Figure 4.9(a)), the Bragg peaks are not as sharp at low temperature (50 °C) relative to high temperature (220 °C). This likely reflects minor distortions in the long-range periodic order of the network due to the increase in interfacial energy between PEO/IL and N-*co*-S, relative to neat PEO and N-*co*-S.

The shift in phase behavior becomes more pronounced at EMITFSI concentrations of 10 and 20 vol% (Figures 4.9(b) and (c)). At all temperatures, the Bragg peaks at 10 vol% are smeared relative to neat INSO. In addition, there is possible coexistence of the network morphology and hexagonally-packed cylinders at 150 and 220 °C (the open triangles point to peaks that cannot be accounted for by the O^{70} morphology). If
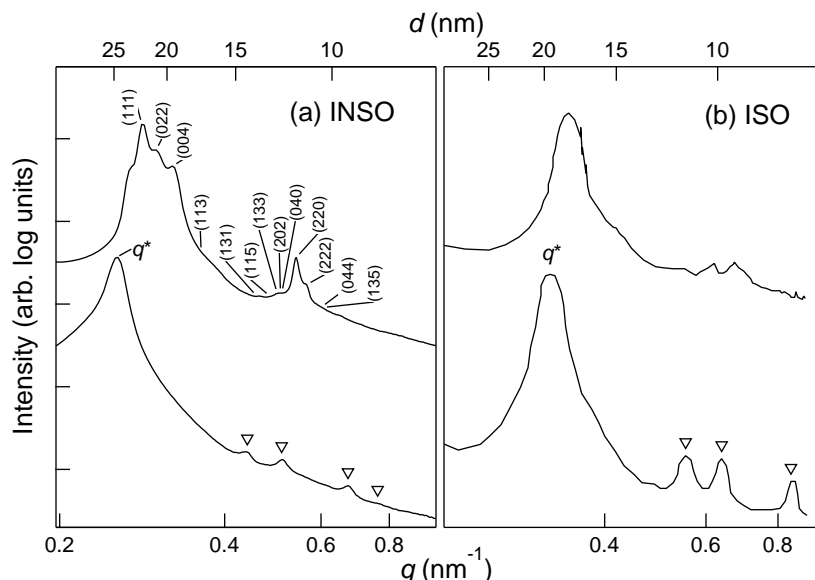
Figure 4.10: Small angle X-ray scattering data showing the effect on morphology of blending salt with (a) INSO and (b) an analogous ISO triblock without crosslinking functionality. (a, upper) Neat INSO at 140 °C. (a, lower) INSO mixed with EMITFSI at 20 vol% of the PEO domain ($r = 27$) at 150 °C. Numbers in (a) are Miller lattice indices and point to the locations of allowed reflections for the O^{70} morphology. Best-fit lattice parameters (in nm) are $a = 26.3$, $b = 49.5$, $c = 78.3$. (b, upper) Neat poly(isoprene-b-styrene-b-ethylene oxide) (ISO) at 140 °C. (b, lower) ISO blended with $LiClO_4$ at a concentration of $r = [EO]/[Li^+]$ = 24. Open triangles ($\triangledown$) in the lower curves point to locations of allowed reflections for hexagonally-packed cylinders ($q/q* = 1 : \sqrt{3} : \sqrt{4} : \sqrt{7} : \sqrt{9}$...). Data in (b) are from ref 104.

the extraneous peaks are assumed to be the $\sqrt{3}$ and $\sqrt{4}$ peaks of hexagonally-packed cylinders, it is found that the low q shoulder relative to the (111) peak appears where one expects the primary HCP peak. The data at 20 vol% corroborate this assignment, as the INSO/EMITFSI blend exhibits a fully developed lyotropic phase transition from the O^{70} network phase to well-defined hexagonally-packed cylinders. In a similar study, Epps et al. [103,104] showed that blending ISO with $LiClO_4$ shifted the equilibrium phase behavior away from network morphologies in favor of hexagonally-packed core-shell cylinders (CSC), where PEO is confined to the core and is surrounded by a shell and matrix of S and I, respectively. Figure 4.10 shows the similarities in SAXS data of INSO/EMITFSI and ISO/$LiClO_4$ blends at similar values of r. In both cases,
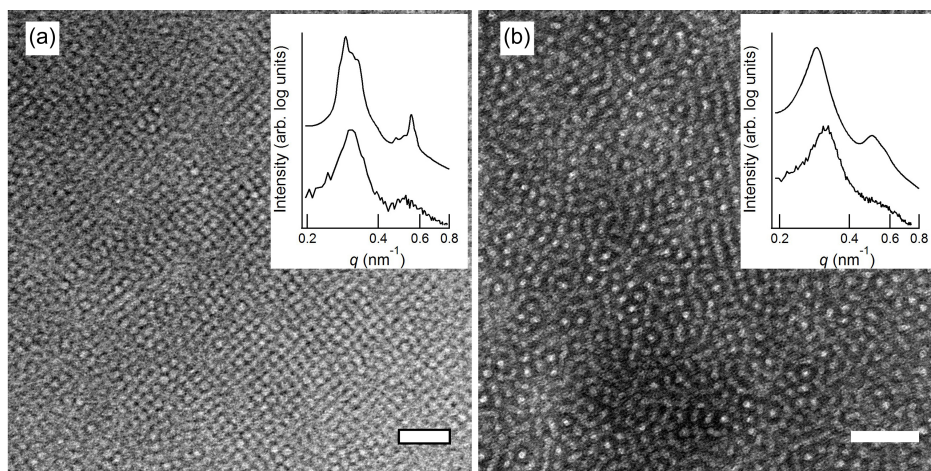
Figure 4.11: Transmission electron micrographs of INSO (a) without catalyst, annealed at 150 °C prior to sectioning, and (b) after solvent-casting and crosslinking. Polyisoprene domains appear dark as a result of OsO_4 staining prior to imaging. The inset plots compare SAXS data of bulk samples (upper curves) to pixel intensity versus wave vector data (lower curves) generated from Fourier transforms of the corresponding TEM image.

the result of salt-doping is a pronounced shift from the O^{70} network morphology to hexagonally-packed cylinders, a result of the increase in the experimental interaction parameter, χ, between PEO/salt and S/N-*co*-S.[104]

The real-space images in Figures 4.11 and 4.14 corroborate the scattering data discussed above. Figure 4.11 compares TEM micrographs of neat INSO before and after crosslinking. Before crosslinking, INSO exhibits long-range, periodic order, consistent with the sharp Bragg peaks seen in the SAXS data. Using a level set model developed by Cochran et al.,[95,96] simulated TEM images were generated and assigned the (202) projection of the O^{70} unit cell to the experimental micrograph (Figure 4.13). Furthermore, the integrated pixel intensity versus wave vector plot of a Fourier transform of the TEM image agrees remarkably well with SAXS data of the bulk sample (see Figure 4.12 for additional details), corroborating that the structure observed in TEM accurately represents the bulk. After solvent-casting and subsequent crosslinking, INSO loses long-range periodic order but retains domain heterogeneity on length scales of order 10 nm. Figure 4.14 shows two additional TEM micrographs of neat,
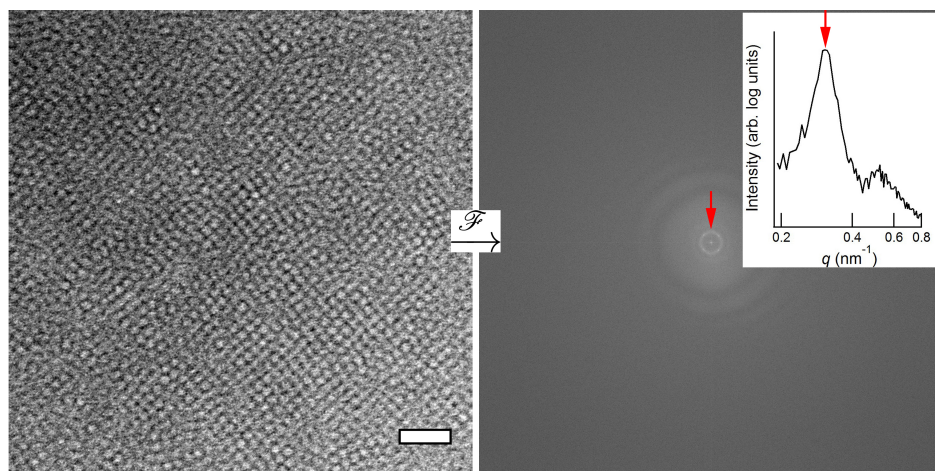
Figure 4.12: Example of Fourier transform (FT) analysis of TEM images. (a) Original TEM image of uncrosslinked INSO. Polyisoprene domains appear dark as a result of OsO_4 staining prior to imaging. The scale bar represents 100 nm. (b) The corresponding FT of the TEM image. Pixel intensity in the FT was azimuthally integrated and plotted versus wave vector q in the inset. The red arrows point to the isotropic feature in the FT that appears as a peak in the 1D plot.

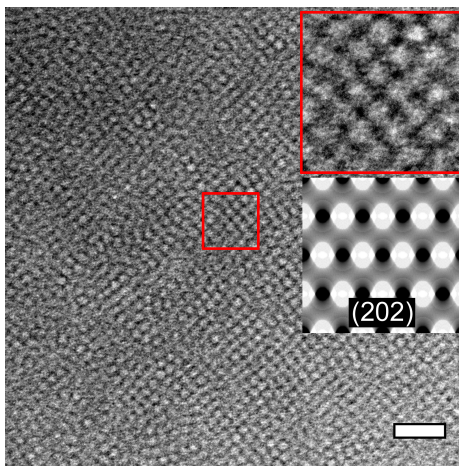**Figure 4.13:** Comparison of an experimental TEM micrograph of neat INSO to a simulated image generated by level-set modeling. The sample was prepared without the Grubbs catalyst and was annealed at 150 °C prior to imaging. The area inside the red box was magnified to allow comparison of the spatial arrangement of light and dark regions to the simulated image of the (202) projection of the O^{70} morphology.

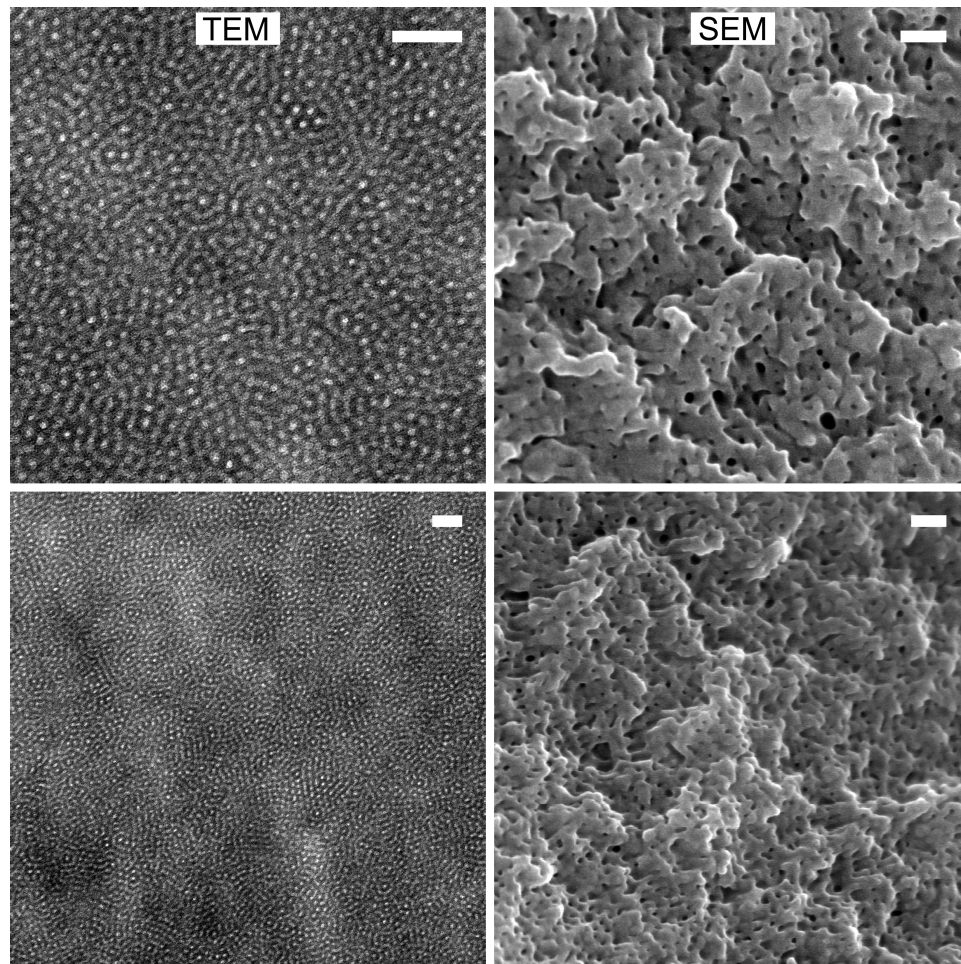**Figure 4.14:** Real-space images of INSO after crosslinking. Left column: transmission electron micrographs. Polyisoprene domains appear dark as a result of OsO4 staining prior to imaging. Right column: scanning electron micrographs of crosslinked INSO after etching PEO with a 57 wt% aqueous solution of hydroiodic acid. The remaining structure is polyisoprene and crosslinked polystyrene. All scale bars represent 100 nm.
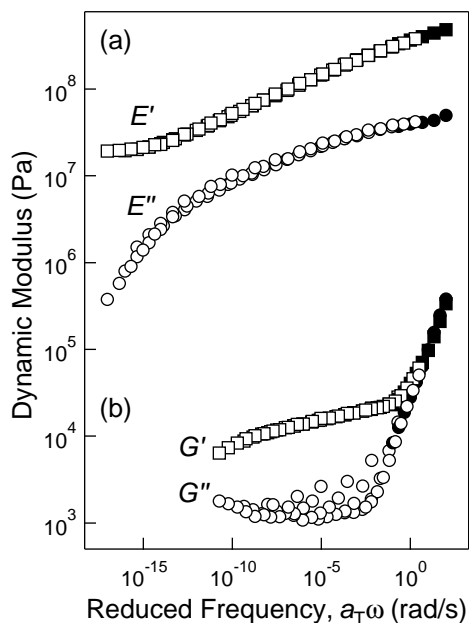
Figure 4.15: Time-temperature superposition master curves showing the linear mechanical response of INSO. G and E refer to shear and tensile deformation, and single and double prime denote the elastic and viscous moduli. (a) Shifted frequency sweeps measured from 35–165 °C ($T_{ref} = 35$ °C) after crosslinking and swelling the PEO domain with ionic liquid. The concentration of ionic liquid in the PEO domain is 26 vol%. (b) Shifted frequency sweeps measured from 40–180 °C ($T_{ref} = 40$ °C) before crosslinking. In both (a) and (b), filled symbols are the reference frequency sweeps. Shift factors are plotted in Figure 4.17

crosslinked INSO, as well as SEM images of INSO after the PEO domain was etched with hydroioidic acid. The resulting porous structure echoes the TEM structure in both size scale and the non-equilibrium spatial arrangement of the domains, and confirms that at least on the length scale of 100s of nm, the PEO domains are continuous.

Mechanical Response

Figure 4.15 shows viscoelastic master curves comparing the linear mechanical response of INSO before and after the crosslinking procedure and incorporation of ionic liquid into the PEO domain (shift factors are shown in Figure 4.17). Before crosslinking, INSO is a soft solid exhibiting a nearly frequency-independent elastic modulus, G', of order 10^4 Pa that spans almost 10 decades of reduced frequency. Over most of the
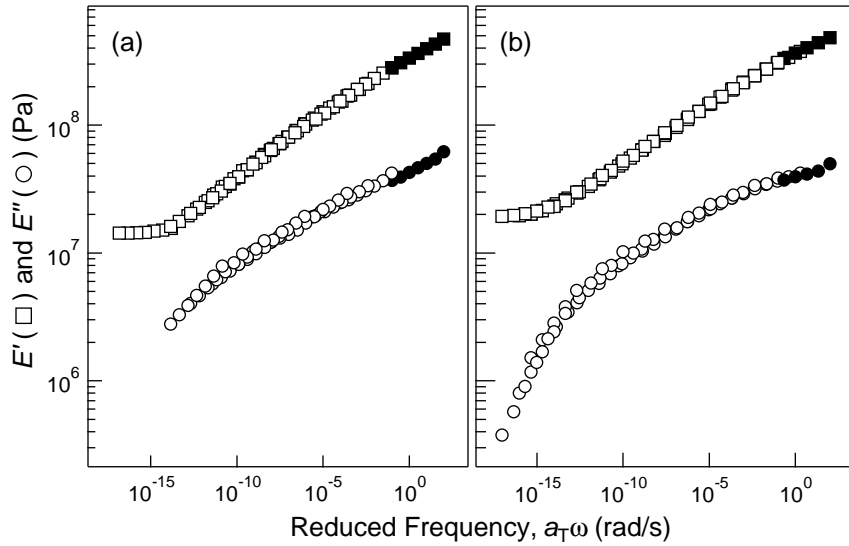
Figure 4.16: Time-temperature superposition master curves of crosslinked INSO (a) before and (b) after swelling the PEO domain with the ionic liquid EMITFSI. Symbols denote the elastic, E', and viscous, E'', moduli. In panel (b), the concentration of ionic liquid in the PEO domain is 26 vol%. Frequency sweeps in (a) were collected from 35–175 °C ($T_{\mathrm{ref}} = 35$ °C), in (b) from 35–165 °C ($T_{\mathrm{ref}} = 35$ °C). Filled symbols are the reference frequency sweeps. The temperature-dependent shift factors, a_{T}, are shown in Figure 4.17.

Figure 4.17: Temperature-dependent shift factors a_{T}, for the tTS master curves shown in Figures 4.15 and 4.16. Symbols correspond to INSO before crosslinking ($\square$), after crosslinking ($\bigcirc$), and after crosslinking and swelling the PEO domain with ionic liquid ($\triangle$).

Figure 4.18: Isochronal temperature sweeps for INSO (a) before and (b) after crosslinking. The elastic and viscous dynamic moduli, E' and E'', were measured upon cooling at 1 °C/min. The sample in (a) was annealed at 100 °C for 20 min prior to the controlled cooling ramp. No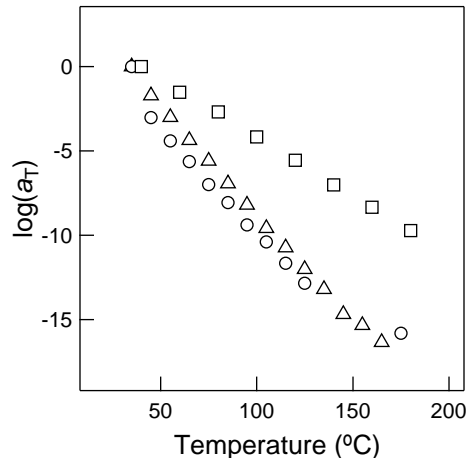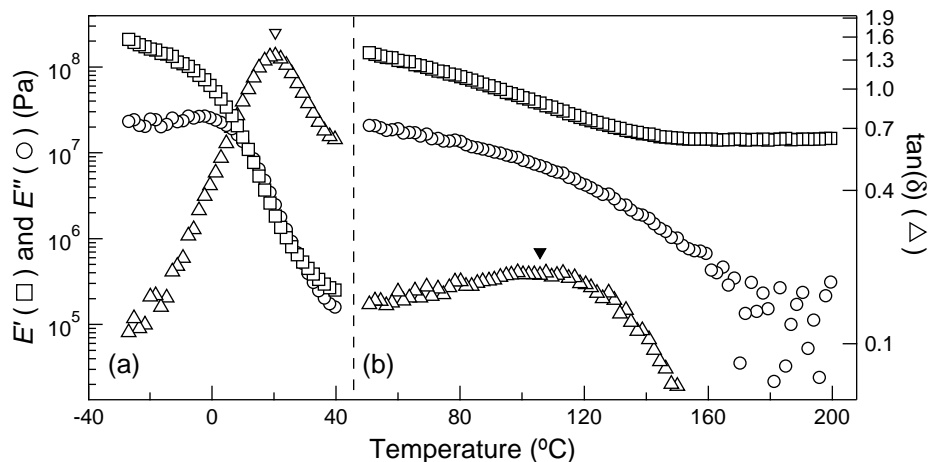 Grubbs catalyst was present to avoid crosslinking at the annealing temperature. The T_g was taken to be the peak of tan(δ). The T_g before crosslinking is 20 °C (open triangle). After crosslinking, the T_g increases to 105 °C (filled triangle).

temperature range studied, the elastic response is a product of the network morphology, as the temperatures probed were higher than the thermal transitions of all three blocks (per DSC, $T_{m,PEO} \approx 43$ °C).[96,211] Interestingly, the transition to the glassy response of the N-*co*-S block is only observed at the lowest temperatures studied (close to room temperature). The T_g of the N-*co*-S block was not observed using DSC, so dynamic mechanical analysis was used to locate the T_g at *ca.* 20 °C (Figure 4.18). The molar mass of polystyrene in INSO is 7 kg/mol, so it is reasonable to expect a slight reduction in T_g relative to bulk polystyrene. For example, Santangelo and Roland[212] reported the Kanig-Ueberreiter parameters for the molar mass dependence of polystyrene homopolymer, from which one calculates $T_g \approx 83$ °C for 7 kg/mol PS. Similarly, Zhang et al.[23] found that polystyrene of $M = 3$ kg/mol exhibited $T_g = 72$ °C. Chen et al.[206] reported the T_g of bulk poly(norbornenylethyl styrene) homopolymer ($M_n = 6.7$ kg/mol, $Đ = 1.04$) to be 81 °C. Evidently, incorporating N at 25 mol% in the N-*co*-S random copolymer block results in an interesting non-Fox or Gordon-Taylor reduction in the T_g from *ca.* 75 °C to lower than room temperature.
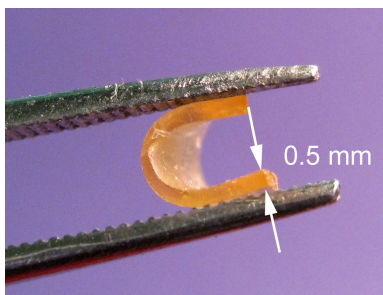
Figure 4.19: Photograph of a crosslinked INSO membrane qualitatively demonstrating the nonlinear mechanical properties.

As shown in Figure 4.15, crosslinking the polystyrene block increases the elastic modulus by almost four orders of magnitude, from 10^4 to 10^8 Pa. Furthermore, although the nonlinear mechanical response was not quantified, a crosslinked INSO membrane 0.5 mm thick and 1 cm in diameter could be bent in half without breaking (Figure 4.19).

After crosslinking, the elastic response is dominated by the glassy N-*co*-S block. Incorporating ionic liquid into the PEO domain results in minimal decrease of the modulus, as shown in Figure 4.16. The modulus approaches 1 GPa at low temperature because $T_{g,\text{N-}co\text{-S}}$ increases from 20 to 105 °C upon crosslinking (Figure 4.18), and crucially, INSO remains a highly elastic solid at elevated temperature (> 100 °C). Chemical crosslinking therefore enables high temperature operation, which may offer an advantage over block polymer-based electrolytes that are stiff solids only below the T_g of the glassy block and soften at elevated temperature.[76]

Ionic Conductivity

Figure 4.20 shows the measured conductivity, σ, of an INSO electrolyte with 50 vol% EMITFSI in the PEO domains. The conductivity data exhibit the expected curvature for polymer/ionic liquid blends on an Arrhenius plot,[3] and were fit with
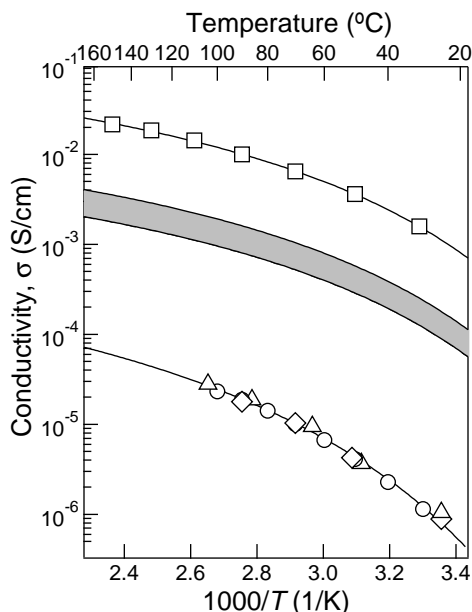
Figure 4.20: Ionic conductivity of EMITFSI in a crosslinked INSO membrane. Symbols correspond to ($\square$) a 50 vol% PEO homopolymer/EMITFSI mixture and ($\bigcirc$, $\triangle$, and $\diamondsuit$) three replicate samples of crosslinked INSO with 50 vol% EMITFSI in the PEO phase (12 vol% overall). Solid lines are fits of the data to the Vogel-Fulcher-Tammann equation (fitting parameters are given in Table 4.3). The gray region is the expected reduction in conductivity for tortuous conducting pathways in a nanostructured electrolyte (given by eq 4.3, where $f_c = 0.25$ and $1.5 \leq \tau \leq 3$).

excellent agreement to the Vogel-Fulcher-Tammann (VFT) equation,

$$\sigma = \sigma_0 \exp\left(\frac{-B}{T - T_0}\right) \tag{4.2}$$

In eq 4.2, σ_0 is related to the concentration of mobile charges, B reflects the local, primarily entropic barrier to free volume creation, and T_0 is the finite temperature at which conductivity drops to zero. The fitting parameters for the samples shown in Figure 7 are given in Table 4.3.

One expects a reduction in the nanostructured INSO electrolyte measured conductivity relative to the bulk, homopolymer control sample conductivity, σ_c, because (i) there are fewer mobile charges and (ii) ions must diffuse through tortuous conducting

Table 4.3: VFT parameters for INSO conductivity data in Figure 4.20

sample	σ_0 (S/cm)	B (K)	T_0 (K)
PEO/IL	0.15 ± 0.081	390 ± 140	218 ± 22
INSO/IL	$8.9 \times 10^{-4} \pm 7.8 \times 10^{-5}$	552 ± 230	219 ± 6

pathways.

$$\sigma = \sigma_{\mathrm{c}} \frac{f_{\mathrm{c}}}{\tau} \tag{4.3}$$

In eq 4.3, f_{c} is the volume fraction of the conducting phase and τ is the tortuosity. To generate the gray region of expected conductivity in Figure 4.20, a range of tortuosity between 1.5 and 3 was assumed, which is based on previously reported values for diffusion of small molecules in one phase of disordered, co-continuous network morphologies.[179–182] However, the INSO conductivity data are a factor of 40 lower than the reduction expected from eq 4.3. Possible explanations for the low conductivity include dead ends in the conducting phase or diffusion barriers at grain boundaries, both of which are commonly-cited problems for block polymer-based electrolytes.[83,84,86,90,119] These network defects likely stem from the solvent-casting procedure, which limits the number of continuous conducting pathways.

Much of the block polymer-based electrolyte literature has focused on ion transport in equilibrium morphologies such as cylinders or lamellae. To more directly compare INSO to these systems, INSO was blended with 50 vol% EMITFSI in the PEO domain, but without the Grubbs catalyst to allow morphological equilibration at the annealing temperature (150 °C). Recall that blending INSO with 20 vol% EMITFSI in the conducting phase induces a phase transition from the O^{70} network morphology to a core-shell cylinder (CSC) morphology, and it is conceivable that the CSC phase window extends to this concentration. The impedance of this uncrosslinked sample was too high to accurately measure the ionic conductivity. There are a number of possible explanations for the immeasurably low conductivity. During the thermal anneal, an insulating layer could form between the electrode and electrolyte due to

preferential wetting by the I or N-*co*-S block. Alternatively, the conducting domains could be isolated, which is reasonable if PEO/EMITFSI cylinders are surrounded by a shell of N-*co*-S within a matrix of I.

The above result contrasts with many studies of diblock copolymer-based electrolytes, where ions migrate through isotropically-oriented grains of conducting lamellae or cylinders.[56,76,88–90,111,117] In INSO, the low volume fraction of the conducting phase (*ca.* 24 vol%) and the presence of the third block make difficult a direct comparison to diblock-based systems. In addition, previous studies of LiClO$_4$-doped ISO did not report conductivity, so there is not a direct analogue for this result. Nevertheless, the low conductivity of the CSC morphology demonstrates the importance of trapping the desired network morphology prior to doping the polymer membrane with ionic liquid.

The rich phase behavior of triblock terpolymers warrants further work in the field of polymer electrolytes. An inherent limitation of the polymer studied here is the low volume fraction of PEO, and increasing f_{PEO} would likely result in a higher fraction of continuous conducting domains. Long-range connectivity of the conducting phase is required for high conductivity, as demonstrated in diblock-based electrolytes in which PEO is the majority phase.[90] In the context of triblocks, the network morphologies originally studied in the ISO system, and more recently in analogous triblock terpolymers using a poly(methyl methacrylate) polar block, exhibit continuous networks even when the volume fraction of the polar block is close to 0.50.[99,101,213,214] It should be emphasized, though, that (i) long-range periodic order of domains is not a prerequisite for high performance electrolytes, and (ii) the volume fraction of the conducting phase cannot be increased at the expense of the mechanically robust phase if high modulus is required. Defect-free continuity of both the mechanically robust and ion transport domains is critical. Finally, in terms of improving the processing conditions, solvent-casting and vapor annealing are known to be versatile techniques.[215–217] It is possible that refinements in the solvent-casting procedure would enable long-range

continuity of the conductive domain prior to crosslinking, substantially enhancing the conductivity. Alternatively, a photo-initiated crosslinking reaction could be employed to allow morphological equilibration at high temperature prior to crosslinking.

4.4 Conclusions

In this chapter, a polymer electrolyte comprising the triblock terpolymer poly[isoprene-b-(styrene-co-norbornenylethyl styrene)-b-ethylene oxide] (INSO) and the ionic liquid 1-ethyl-3-methylimidazolium bis(trifluoromethylsulfonyl)imide (EMITFSI) is investigated, with the goal of taking advantage of an equilibrium network morphology in which both the conductive and high modulus domains are continuous throughout the sample. Co-continuous morphologies optimize the decoupling of mechanical and ion transport properties. Although neat INSO exhibits the expected O^{70} network morphology, the solvent-casting procedure results in a non-equilibrium—but predominantly co-continuous—structure, which is trapped by chemically crosslinking the styrene block via the ring-opening metathesis polymerization of norbornene moieties. Crosslinking the polystyrene domain substantially enhances the mechanical properties, increasing the elastic modulus from 10^4 Pa to close to 1 GPa. In addition, INSO retains a high modulus at elevated temperature (> 100 °C), where devices such as ionic liquid-based fuel cells could hypothetically operate. The conductivity of EMITFSI in the PEO domains is found to be limited. This may be due to dead ends in the conducting pathways or isolated conducting domains resulting from the solvent-casting procedure, but it is plausible that refinements in the solvent-casting/annealing procedure would allow relaxation to the desired network morphologies prior to crosslinking.

Chapter 5

Concluding Remarks

5.1 Summary

The goal of this thesis is to design polymer electrolytes that exhibit high ionic con-
ductivity while simultaneously addressing an orthogonal mechanical property, such
as modulus, fracture toughness, or high temperature creep resistance. Mechanically
robust polymer electrolyte membranes (PEMs) will play a vital role in the next gen-
eration of energy storage and conversion devices (*e.g.*, lithium metal batteries or
anhydrous fuel cells), where an all-solid-state design promises to enhance key metrics
such as safety and energy density.

The general strategy adopted in this work is to employ nanostructured electrolytes,
in which ion-conducting and mechanically robust domains are microphase separated,
effectively decoupling the macroscopic properties. One of the key results in this the-
sis is a unique synthetic approach to generating nanostructured PEMs. A simple,
yet versatile polymerization route—termed polymerization-induced phase separation,
or PIPS—is used to prepare PEMs that exhibit an unprecedented combination of
high modulus and high conductivity. One of the advantages of the PIPS strategy
is that the reaction precursor can be easily processed as a liquid, followed by *in*

situ solidification to obtain a solid membrane. The outstanding macroscopic performance is enabled by a network morphology comprising co-continuous domains of ion-conducting poly(ethylene oxide)/ionic liquid (PEO/IL) and highly crosslinked polystyrene (P(S-*co*-DVB)). This critically important morphology appears to be the product of kinetically trapping (via chemical crosslinking) the fluctuation-induced, disordered network in the growing P(S-*co*-DVB)-*b*-PEO/IL diblock. These fluctuations are universal in disordered diblock polymer melts and solutions, suggesting that the PIPS strategy can be readily tuned to address the requirements of particular applications.

In terms of bulk properties of the solid PEMs, the ionic conductivity exceeds the 1 mS/cm benchmark cited for lithium metal batteries. More importantly, however, the conductivity is as high as volume fraction and geometric constraints allow in structured electrolytes. That is, the conductivity of PIPS PEMs is not limited by network defects, which have limited the commercial viability of diblock polymer-based electrolytes to specific markets (*e.g.*, vehicle batteries) that allow for operation at relatively high temperature (*ca.* 80 °C). PIPS PEMs are glassy solids near room temperature, and soften only moderately at temperatures as high as 200 °C, enabling a much wider operational temperature window than PEMs that rely only on, for example, a glassy block for mechanical integrity. Additionally, this inherent mechanical robustness should allow for thinner membranes, lowering the resistance of the electrolyte layer in electrochemical devices.

This thesis also explores PEMs prepared by accessing a thermodynamically stable network morphology exhibited by the triblock terpolymer poly[isoprene-*b*-(styrene-*co*-norbornenylethyl styrene)-*b*-ethylene oxide] (INSO). Norbornene moieties in the polystyrene block are used to chemically crosslink the membrane, imparting a glassy response at low temperature, as well as significant high temperature stability. The conductivity of the INSO system presents one of the characteristic challenges of diblock polymer-based electrolyte, namely that the solvent-casting procedure used to

prepare thin films resulted in network defects that ultimately limits the conductivity. However, it is possible that refinements to the solvent casting procedure could eliminate these network defects.

5.2   Proposed Future Directions

Given the outstanding combination of superior mechanical properties and high ionic conductivity exhibited by PIPS PEMs, the natural progression is to implement these PEMs in an electrochemical device. This is not necessarily straightforward, however, as even the simplest electrochemical device comprises a multitude of components, each optimized to address the requirements of a particular application. To highlight one example, a recent review on lithium-ion batteries by Bryner et al.[20] provides an excellent discussion of the inherent trade-offs that must be made when designing batteries. Once certain criteria are set (*e.g.*, long overall battery lifetime versus high capacity per charge), the choice of materials is essentially fixed by the existing production infrastructure. Even if PIPS PEMs offer significant improvements over existing polymer or liquid-based electrolytes, their commercial viability will ultimately be a function of many factors. For example, if batteries prepared with PIPS PEMs outperform existing batteries, does this enhanced performance justify the cost of modifying the existing production infrastructure? These questions are, of course, well outside the scope of this thesis, but ultimately they deserve attention, in light of the promising performance of PIPS PEMs.

One strategy to increase the conductivity of PIPS PEMs would be to etch PEO, rendering the membranes nanoporous. The pores could then be backfilled with either pure ionic liquid or ionic liquid/Li-salt mixtures. The conductivity would increase because the conductivity of neat ionic liquids is intrinsically higher than polymer/ionic liquid mixtures. This strategy was not pursued thus far primarily because it eliminates the one-pot aspect of the PIPS strategy. Instead of transitioning directly from the
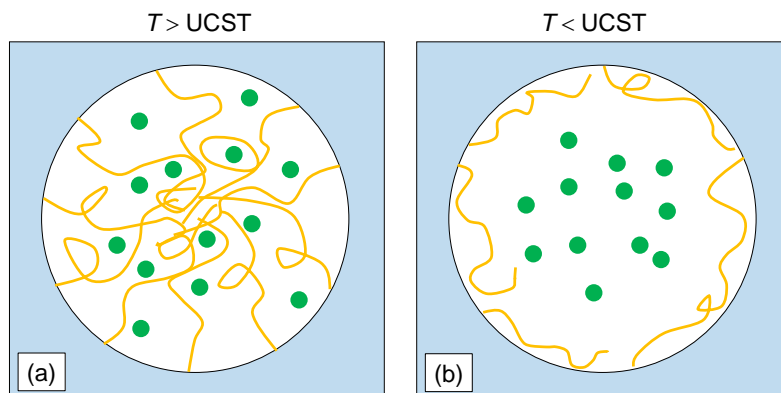
Figure 5.1: Schematic of phase separation between polymer (yellow lines) and ionic liquid (green dots) within the conducting phase of a PIPS PEM. The blue matrix represents the crosslinked polystyrene domain. The view is down the z-axis of a conducting channel. (a) The PEM is reacted at a temperature above the upper critical solution temperature (UCST), where the polymer and ionic liquid are miscible. (b) When T is below the UCST, the polymer and ionic liquid phase separate. Polymer chains collapse onto the domain wall because they are anchored, whereas the ionic liquid is free to migrate in the middle of the domain.

liquid precursor to a high modulus electrolyte, backfilling a nanoporous membranes would require a multi-step procedure. If this strategy were pursued, the polylactide (PLA)-based system reported by Seo and Hillmyer[124] would be more amenable than the PEO-based electrolytes studied in this thesis, as PLA is more easily etched than PEO. Alternatively, one could exploit the known phase behavior of polymer/ionic liquid mixtures[54] to induce phase separation within the conducting channels after the desired bicontinuous morphology has been formed during the PIPS reaction.

Figure 5.1 shows a schematic of how this proposed system might work. The PEM would have to be prepared at a temperature at which the polymer and ionic liquid are one phase, so the PIPS reaction can generate the desired co-continuous networks of polymer/ionic liquid and crosslinked polystyrene. At sufficiently high temperature, then, the solid PEM would behave identically to those studied in this thesis, in which the conducting phase is a one phase mixture of polymer and ionic liquid. However, the system would be chosen such that the polymer and ionic liquid exhibit an upper
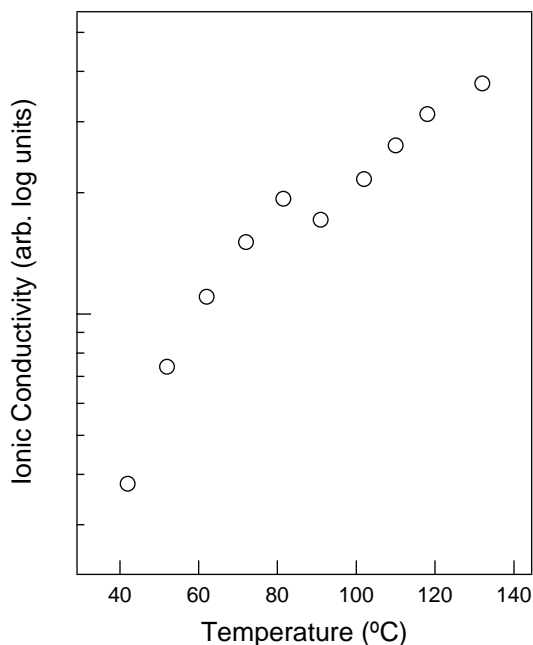
Figure 5.2: Relative conductivity of a PIPS PEM prepared with PNIPAm and BMITFSI. Each data point was collected after a 1 h thermal anneal.

critical solution temperature (UCST) and phase separate upon cooling. Because the polymer chains are anchored to the domain walls, they should collapse against the walls, leaving the ionic liquid free to migrate in the middle of the domain. The ions would therefore experience a decrease in local viscosity, increasing the conductivity of the PEM relative to a hypothetical mixture of the polymer and ionic liquid at that temperature. In this way, the one-pot nature of the PIPS strategy could be retained while enhancing the low temperature conductivity.

Figure 5.2 shows the results of a proof-of-concept test of the UCST idea. The PEM was prepared via the RAFT polymerization of S/DVB off a poly(*N*-isopropylacryl-amide) macro chain-transfer agent (PNIPAm-CTA), and 21 vol% BMITFSI. PNI-PAm and EMITFSI exhibit a UCST between 20 and 40 °C, depending on the molar mass and concentration of the PNIPAm.[218,219] It was hypothesized that mixtures of PNIPAm and BMITFSI should exhibit a UCST at higher temperature than PNI-PAm/EMITFSI due to the increased hydrophobic character of BMITFSI relative to

EMITFSI. Due to difficulties in sanding down membranes of PNIPAm-based samples, the sample shown in Figure 5.2 was prepared in an *in situ* conductivity cell, such as those used in Chapter 3. Unfortunately, the cell was not calibrated with the KCl standard, so the absolute magnitude of conductivity is not known. Instead, the conductivity, σ, in Figure 5.2 was simply calculated as $\sigma = 1/R$, where R is the bulk resistance. However, it is the relative change in conductivity that is of interest.

As the temperature is lowered from 140 °C, the conductivity decreases, as expected, and exhibits curvature that is typical of polymer/ionic liquid mixtures. Cooling from 90 to 80 °C, however, results in a 13% increase in conductivity. This increase is admittedly modest, although the fact conductivity *increases* as temperature is *lowered* is worth attention. Furthermore, this strategy might allow increased flexibility in the choice of macro-CTA used. For example, a high T_g macro-CTA could be used— perhaps out of synthetic necessity—while retaining the intrinsically high conductivity of a neat ionic liquid in the PEM. Below 80 °C, the conductivity decreases again as expected, although the temperature scaling appears to be different than the data above 90 °C. It is plausible that the increase in conductivity between 90 and 80 °C corresponds to phase separation of PNIPAm and BMITFSI. If this is the case, the conductivity above 90 °C reflects a PNIPAm/BMITFSI mixture, whereas the conductivity below 80 °C is that of effectively neat BMITFSI. This would place the UCST of PNIPAm/BMITFSI approximately 40–50 °C above the UCST of PNIPAm/EMITFSI, which is physically reasonable. This is a single preliminary experiment, so the results should be reproduced, as well as corroborated by a suite of complementary experiments, including DSC, cloud point measurements of the bulk PNIPAm/BMITFSI mixtures, scattering, and real space images. Nevertheless, this is an exciting result that warrants further investigation.

References

[1] Cowie, J. M. G.; Cree, S. H. *Annu. Rev. Phys. Chem.* **1989**, *40*, 85–113.

[2] Chandrasekhar, V. *Adv. Polym. Sci.* **1998**, *135*, 139–205.

[3] Ogata, N. *J. Macromol. Sci. Part C Polym. Rev.* **2002**, *42*, 399–439.

[4] Maranas, J. K. *Polymers for Energy Storage and Delivery: Polyelectrolytes for Batteries and Fuel Cells*; American Chemical Society: Washington, DC, 2012; Vol. 1096.

[5] Hallinan, D. T.; Mullin, S. A.; Stone, G. M.; Balsara, N. P. *J. Electrochem. Soc.* **2013**, *160*, A464–A470.

[6] Young, W.-S.; Kuan, W.-F.; Epps, T. H. *J. Polym. Sci. Part B Polym. Phys.* **2014**, *52*, 1–16.

[7] Zhang, S. S. *J. Power Sources* **2007**, *164*, 351–364.

[8] Steele, B. C.; Heinzel, A. *Nature* **2001**, *414*, 345–52.

[9] Selim, R.; Bro, P. *J. Electrochem. Soc.* **1974**, *121*, 1457.

[10] Epelboin, I.; Froment, M.; Garreau, M.; Thevenin, J.; Warin, D. *J. Electrochem. Soc.* **1980**, *127*, 2100.

[11] Monroe, C.; Newman, J. *J. Electrochem. Soc.* **2003**, *150*, A1377.

[12] Monroe, C.; Newman, J. *J. Electrochem. Soc.* **2004**, *151*, A880.

[13] Monroe, C.; Newman, J. *J. Electrochem. Soc.* **2005**, *152*, A396.

[14] Stone, G. M.; Mullin, S. A.; Teran, A. A.; Hallinan, D. T.; Minor, A. M.; Hexemer, A.; Balsara, N. P. *J. Electrochem. Soc.* **2012**, *159*, A222–A227.

[15] Steiger, J.; Kramer, D.; Mönig, R. *J. Power Sources* **2014**, *261*, 112–119.

[16] Wright, P. V. *MRS Bull.* **2002**, *27*, 597–602.

[17] Aricò, A. S.; Bruce, P.; Scrosati, B.; Tarascon, J.-M.; van Schalkwijk, W. *Nat. Mater.* **2005**, *4*, 366–77.

[18] Meyer, W. H. *Adv. Mater.* **1998**, *10*, 439–448.

[19] Tarascon, J. M.; Armand, M. *Nature* **2001**, *414*, 359–67.

[20] Bryner, M.; Clarke, G. M.; Jansen, A. N.; Patel, A.; Spotnitz, R. *Chem. Eng. Prog.* **2013**.

[21] Mathias, M. F.; Makharia, R.; Gasteiger, H. A.; Conley, J. J.; Fuller, T. J.; Gittleman, C. J.; Kocha, S. S.; Miller, D. P.; Mittelsteadt, C. K.; Xie, T.; Yan, S. G.; Yu, P. T. *Electrochem. Soc. Interface* **2005**, *14*, 24–35.

[22] Yang, X.; Loos, J. *Macromolecules* **2007**, *40*, 1353–1362.

[23] Zhang, S.; Lee, K. H.; Frisbie, C. D.; Lodge, T. P. *Macromolecules* **2011**, *44*, 940–949.

[24] Zhang, S.; Lee, K. H.; Sun, J.; Frisbie, C. D.; Lodge, T. P. *Macromolecules* **2011**, *44*, 8981–8989.

[25] Lee, K. H.; Kang, M. S.; Zhang, S.; Gu, Y.; Lodge, T. P.; Frisbie, C. D. *Adv. Mater.* **2012**, *24*, 4457–62.

[26] Gu, Y.; Zhang, S.; Martinetti, L.; Lee, K. H.; McIntosh, L. D.; Frisbie, C. D.; Lodge, T. P. *J. Am. Chem. Soc.* **2013**, *135*, 9652–9655.

[27] Newman, J. *Electrochemical Systems*, 2nd ed.; Wiley, 1991.

[28] Atkins, P. W. *Physical Chemistry*, 3rd ed.; Oxford University Press, 1986.

[29] Klein, R. J.; Zhang, S.; Dou, S.; Jones, B. H.; Colby, R. H.; Runt, J. *J. Chem. Phys.* **2006**, *124*, 144903.

[30] Wong, D. H. C.; Thelen, J. L.; Fu, Y.; Devaux, D.; Pandya, A. A.; Battaglia, V. S.; Balsara, N. P.; DeSimone, J. M. *Proc. Natl. Acad. Sci.* **2014**, *2*, 2–6.

[31] Fuoss, R. M. *Proc. Natl. Acad. Sci.* **1978**, *75*, 16–20.

[32] Seo, D. M.; Borodin, O.; Balogh, D.; O'Connell, M.; Ly, Q.; Han, S.-D.; Passerini, S.; Henderson, W. A. *J. Electrochem. Soc.* **2013**, *160*, A1061–A1070.

[33] Debye, P. J. W. *The Collected Papers of Peter J. W. Debye*; Interscience: New York, 1954.

[34] Berg, J. C. *An Introduction to Interfaces & Colloids: The Bridge to Nanoscience*, 1st ed.; World Scientific Publishing: Hackensack, NJ, 2010; p 465.

[35] Gebbie, M. A.; Valtiner, M.; Banquy, X.; Fox, E. T.; Henderson, W. A.; Israelachvili, J. N. *Proc. Natl. Acad. Sci. U. S. A.* **2013**, *110*, 9674–9.

[36] Hunt, P. A.; Gould, I. R.; Kirchner, B. *Aust. J. Chem.* **2007**, *60*, 9.

[37] Sangoro, J. R.; Serghei, A.; Naumov, S.; Galvosas, P.; Karger, J.; Wespe, C.; Bordusa, F.; Kremer, F. *Phys. Rev. E* **2008**, *77*, 051202.

[38] Sangoro, J.; Iacob, C.; Serghei, A.; Naumov, S.; Galvosas, P.; Karger, J.; Wespe, C.; Bordusa, F.; Stoppa, A.; Hunger, J.; Buchner, R.; Kremer, F. *J. Chem. Phys.* **2008**, *128*, 214509–5.

[39] Tokuda, H.; Tsuzuki, S.; Susan, M. A. B. H.; Hayamizu, K.; Watanabe, M. *J. Phys. Chem. B* **2006**, *110*, 19593–600.

[40] Hiemenz, P. C.; Lodge, T. P. *Polymer Chemistry*, 2nd ed.; CRC Press: Boca Raton, FL, 2007.

[41] *Broadband Dielectric Spectroscopy*; Kremer, F., Schönhals, A., Eds.; Springer Berlin Heidelberg: Berlin, Heidelberg, 2003.

[42] Adam, G.; Gibbs, J. H. *J. Chem. Phys.* **1965**, *43*, 139.

[43] Chambers, J. F.; Stokes, J. M.; Stokes, R. H. *J. Phys. Chem.* **1956**, *60*, 985–986.

[44] Tokuda, H.; Hayamizu, K.; Ishii, K.; Susan, M. A. B. H.; Watanabe, M. *J. Phys. Chem. B* **2005**, *109*, 6103–10.

[45] Korson, L.; Drost-Hansen, W.; Millero, F. J. *J. Phys. Chem.* **1969**, *73*, 34–39.

[46] Ryu, S.-W.; Trapa, P. E.; Olugebefola, S. C.; Gonzalez-Leon, J. A.; Sadoway, D. R.; Mayes, A. M. *J. Electrochem. Soc.* **2005**, *152*, A158.

[47] Bouchet, R.; Maria, S.; Meziane, R.; Aboulaich, A.; Lienafa, L.; Bonnet, J.-P.; Phan, T. N. T.; Bertin, D.; Gigmes, D.; Devaux, D.; Denoyel, R.; Armand, M. *Nat. Mater.* **2013**, *12*, 452–7.

[48] Cho, J. H.; Lee, J.; Xia, Y.; Kim, B.; He, Y.; Renn, M. J.; Lodge, T. P.; Frisbie, C. D. *Nat. Mater.* **2008**, *7*, 900–6.

[49] Fenton, D.; Parker, J.; Wright, P. *Polymer* **1973**, *14*, 589.

[50] Wright, P. V. *Br. Polym. J.* **1975**, *7*, 319–327.

[51] Armand, M. B.; Chabagno, J.-M.; Duclot, M. J. Poly-Ethers as Solid Electrolytes. *Fast Ion Transport in Solids*, New York, 1979; pp 131–136.

[52] Armand, M. *Solid State Ionics* **1983**, *9-10*, 745–754.

[53] He, Y.; Boswell, P. G.; Bühlmann, P.; Lodge, T. P. *J. Phys. Chem. B* **2007**, *111*, 4645–52.

[54] Ueki, T.; Watanabe, M. *Macromolecules* **2008**, *41*, 3739–3749.

[55] Lodge, T. P. *Science* **2008**, *321*, 50–1.

[56] Simone, P. M.; Lodge, T. P. *ACS Appl. Mater. Interfaces* **2009**, *1*, 2812–20.

[57] Wilkes, J. S. *Green Chem.* **2002**, *4*, 73–80.

[58] Tokuda, H.; Hayamizu, K.; Ishii, K.; Susan, M. A. B. H.; Watanabe, M. *J. Phys. Chem. B* **2004**, *108*, 16593–16600.

[59] Tokuda, H.; Ishii, K.; Susan, M. A. B. H.; Tsuzuki, S.; Hayamizu, K.; Watanabe, M. *J. Phys. Chem. B* **2006**, *110*, 2833–9.

[60] *Electrochemical Aspects of Ionic Liquids*; Ohno, H., Ed.; John Wiley & Sons.

[61] Garcia, B.; Lavallée, S.; Perron, G.; Michot, C.; Armand, M. *Electrochim. Acta* **2004**, *49*, 4583–4588.

[62] Seki, S.; Kobayashi, Y.; Miyashiro, H.; Ohno, Y.; Usami, A.; Mita, Y.; Kihira, N.; Watanabe, M.; Terada, N. *J. Phys. Chem. B* **2006**, *110*, 10228–30.

[63] Seki, S.; Ohno, Y.; Kobayashi, Y.; Miyashiro, H.; Usami, A.; Mita, Y.; Tokuda, H.; Watanabe, M.; Hayamizu, K.; Tsuzuki, S.; Hattori, M.; Terada, N. *J. Electrochem. Soc.* **2007**, *154*, A173.

[64] Armand, M.; Endres, F.; MacFarlane, D. R.; Ohno, H.; Scrosati, B. *Nat. Mater.* **2009**, *8*, 621–9.

[65] Gin, D. L.; Noble, R. D. *Science* **2011**, *332*, 674–6.

[66] Gu, Y.; Lodge, T. P. *Macromolecules* **2011**, *44*, 1732–1736.

[67] Robitaille, C. D.; Fauteux, D. *J. Electrochem. Soc.* **1986**, *133*, 315.

[68] MacGlashan, G. S.; Andreev, Y. G.; Bruce, P. G. *Nature* **1999**, *398*, 792–794.

[69] Bruce, P. G. *Solid State Electrochemistry*; Cambridge University Press: Cambridge, 1994; Vol. 8.

[70] Seki, S.; Susan, M. A. B. H.; Kaneko, T.; Tokuda, H.; Noda, A.; Watanabe, M. *J. Phys. Chem. B* **2005**, *109*, 3886–92.

[71] Gray, F. M. *Solid State Ionics* **1990**, *40*, 637–640.

[72] Albinsson, I.; Mellander, B.-E.; Stevens, J. R. *J. Chem. Phys.* **1992**, *96*, 681.

[73] Fetters, L. J.; Lohse, D. J.; Richter, D.; Witten, T. A.; Zirkel, A. *Macromolecules* **1994**, *27*, 4639–4647.

[74] Orwoll, R. A. Densities, Coefficients of Thermal Expansion, and Compressibilities of Amorphous Polymers. In *Physical Properties of Polymers Handbook*; Mark, J. E., Ed., 2nd ed.; Springer, 2007; Chapter 7, pp 93–101.

[75] Kolbeck, C.; Lehmann, J.; Lovelock, K. R. J.; Cremer, T.; Paape, N.; Wasserscheid, P.; Fröba, A. P.; Maier, F.; Steinrück, H.-P. *J. Phys. Chem. B* **2010**, *114*, 17025–36.

[76] Singh, M.; Odusanya, O.; Wilmes, G. M.; Eitouni, H. B.; Gomez, E. D.; Patel, A. J.; Chen, V. L.; Park, M. J.; Fragouli, P.; Iatrou, H.; Hadjichristidis, N.; Cookson, D.; Balsara, N. P. *Macromolecules* **2007**, *40*, 4578–4585.

[77] Watanabe, M.; Sanui, K.; Ogata, N.; Inoue, F.; Kobayashi, T.; Ohtaki, Z. *Polym. J.* **1984**, *16*, 711–716.

[78] Noda, A.; Watanabe, M. *Electrochim. Acta* **2000**, *45*, 1265–1270.

[79] Susan, M. A. B. H.; Kaneko, T.; Noda, A.; Watanabe, M. *J. Am. Chem. Soc.* **2005**, *127*, 4976–83.

[80] Soo, P. P.; Huang, B.; Jang, Y.-I.; Chiang, Y.-M.; Sadoway, D. R.; Mayes, A. M. *J. Electrochem. Soc.* **1999**, *146*, 32.

[81] Watanabe, M.; Oohashi, S.; Sanui, K.; Ogata, N.; Kobayashi, T.; Ohtaki, Z. *Macromolecules* **1985**, *18*, 1945–1950.

[82] Wang, C. B.; Cooper, S. L. *Macromolecules* **1983**, *16*, 775–786.

[83] Ye, Y.; Choi, J.-H.; Winey, K. I.; Elabd, Y. A. *Macromolecules* **2012**, *45*, 7027–7035.

[84] Choi, J.-H.; Ye, Y.; Elabd, Y. A.; Winey, K. I. *Macromolecules* **2013**, *46*, 5290–5300.

[85] Wanakule, N. S.; Virgili, J. M.; Teran, A. A.; Wang, Z.-G.; Balsara, N. P. *Macromolecules* **2010**, *43*, 8282–8289.

[86] Weber, R. L.; Ye, Y.; Schmitt, A. L.; Banik, S. M.; Elabd, Y. A.; Mahanthappa, M. K. *Macromolecules* **2011**, *44*, 5727–5735.

[87] Weber, R. L.; Ye, Y.; Banik, S. M.; Elabd, Y. A.; Hickner, M. A.; Mahanthappa, M. K. *J. Polym. Sci. Part B Polym. Phys.* **2011**, *49*, 1287–1296.

[88] Hoarfrost, M. L.; Tyagi, M. S.; Segalman, R. A.; Reimer, J. A. *Macromolecules* **2012**, *45*, 3112–3120.

[89] Virgili, J. M.; Hoarfrost, M. L.; Segalman, R. A. *Macromolecules* **2010**, *43*, 5417–5423.

[90] Young, W.-S.; Epps, T. H. *Macromolecules* **2012**, *45*, 4689–4697.

[91] Virgili, J. M.; Hexemer, A.; Pople, J. A.; Balsara, N. P.; Segalman, R. A. *Macromolecules* **2009**, *42*, 4604–4613.

[92] Bates, F. S.; Fredrickson, G. H. *Phys. Today* **1999**, 32–38.

[93] Lodge, T. P. *Macromol. Chem. Phys.* **2003**, 265–273.

[94] Bates, F. S.; Hillmyer, M. A.; Lodge, T. P.; Bates, C. M.; Delaney, K. T.; Fredrickson, G. H. *Science* **2012**, *336*, 434–40.

[95] Cochran, E. W. Ph.D. thesis, University of Minnesota, 2004.

[96] Epps, T. H.; Cochran, E. W.; Bailey, T. S.; Waletzko, R. S.; Hardy, C. M.; Bates, F. S. *Macromolecules* **2004**, *37*, 8325–8341.

[97] Torquato, S. *Annu. Rev. Mater. Res.* **2010**, *40*, 101–129.

[98] Epps, T. H.; Cochran, E. W.; Hardy, C. M.; Bailey, T. S.; Waletzko, R. S.; Bates, F. S. *Macromolecules* **2004**, *37*, 7085–7088.

[99] Tureau, M. S.; Kuan, W.-F.; Rong, L.; Hsiao, B. S.; Epps, T. H. *Macromolecules* **2012**, *45*, 4599–4605.

[100] Bailey, T. S.; Hardy, C. M.; Epps, T. H.; Bates, F. S. *Macromolecules* **2002**, *35*, 7007–7017.

[101] Tureau, M. S.; Epps, T. H. *Macromol. Rapid Commun.* **2009**, *30*, 1751–5.

[102] Epps, T. H.; Bates, F. S. *Macromolecules* **2006**, *39*, 2676–2682.

[103] Epps, T. H.; Bailey, T. S.; Pham, H. D.; Bates, F. S. *Chem. Mater.* **2002**, *14*, 1706–1714.

[104] Epps, T. H.; Bailey, T. S.; Waletzko, R.; Bates, F. S. *Macromolecules* **2003**, *36*, 2873–2881.

[105] Kuan, W.-F.; Roy, R.; Rong, L.; Hsiao, B. S.; Epps, T. H. *ACS Macro Lett.* **2012**, *1*, 519–523.

[106] Ruzette, A.-V. G.; Soo, P. P.; Sadoway, D. R.; Mayes, A. M. *J. Electrochem. Soc.* **2001**, *148*, A537.

[107] Sadoway, D. R. *J. Power Sources* **2004**, *129*, 1–3.

[108] Trapa, P. E.; Won, Y.-Y.; Mui, S. C.; Olivetti, E. A.; Huang, B.; Sadoway, D. R.; Mayes, A. M.; Dallek, S. *J. Electrochem. Soc.* **2005**, *27*, A1.

[109] Wanakule, N. S.; Panday, A.; Mullin, S. A.; Gann, E.; Hexemer, A.; Balsara, N. P. *Macromolecules* **2009**, *42*, 5642–5651.

[110] Gomez, E. D.; Panday, A.; Feng, E. H.; Chen, V.; Stone, G. M.; Minor, A. M.; Kisielowski, C.; Downing, K. H.; Borodin, O.; Smith, G. D.; Balsara, N. P. *Nano Lett.* **2009**, *9*, 1212–6.

[111] Panday, A.; Mullin, S.; Gomez, E. D.; Wanakule, N.; Chen, V. L.; Hexemer, A.; Pople, J.; Balsara, N. P. *Macromolecules* **2009**, *42*, 4632–4637.

[112] Mullin, S. A.; Stone, G. M.; Panday, A.; Balsara, N. P. *J. Electrochem. Soc.* **2011**, *158*, A619.

[113] Teran, A. A.; Tang, M. H.; Mullin, S. A.; Balsara, N. P. *Solid State Ionics* **2011**, *203*, 18–21.

[114] Yuan, R.; Teran, A. A.; Gurevitch, I.; Mullin, S. A.; Wanakule, N. S.; Balsara, N. P. *Macromolecules* **2013**, *46*, 914–921.

[115] Hermel, T. J.; Hahn, S. F.; Chaffin, K. A.; Gerberich, W. W.; Bates, F. S. *Macromolecules* **2003**, *36*, 2190–2193.

[116] Hermel, T. J.; Wu, L.; Hahn, S. F.; Lodge, T. P.; Bates, F. S. *Macromolecules* **2002**, *35*, 4685–4689.

[117] Hoarfrost, M. L.; Segalman, R. A. *Macromolecules* **2011**, *44*, 5281–5288.

[118] Noda, A.; Susan, M. A. B. H.; Kudo, K.; Mitsushima, S.; Hayamizu, K.; Watanabe, M. *J. Phys. Chem. B* **2003**, *107*, 4024–4033.

[119] Chen, H.; Choi, J.-H.; Salas-de La Cruz, D.; Winey, K. I.; Elabd, Y. A. *Macromolecules* **2009**, *42*, 4809–4816.

[120] Scalfani, V. F.; Wiesenauer, E. F.; Ekblad, J. R.; Edwards, J. P.; Gin, D. L.; Bailey, T. S. *Macromolecules* **2012**, *45*, 4262–4276.

[121] Choi, U. H.; Liang, S.; O'Reilly, M. V.; Winey, K. I.; Runt, J.; Colby, R. H. *Macromolecules* **2014**, 140428135834006.

[122] Majewski, P. W.; Gopinadhan, M.; Jang, W.-S.; Lutkenhaus, J. L.; Osuji, C. O. *J. Am. Chem. Soc.* **2010**, *132*, 17516–22.

[123] Jackson, E. A.; Lee, Y.; Hillmyer, M. A. *Macromolecules* **2013**, *46*, 1484–1491.

[124] Seo, M.; Hillmyer, M. A. *Science* **2012**, *336*, 1422–1425.

[125] Bates, F. S. *Science* **1991**, *251*, 898–905.

[126] Bates, F. S.; Wiltzius, P. *J. Chem. Phys.* **1989**, *91*, 3258.

[127] Cahn, J. W. *J. Chem. Phys.* **1965**, *42*, 93.

[128] Jinnai, H.; Nishikawa, Y.; Koga, T.; Hashimoto, T. *Macromolecules* **1995**, *28*, 4782–4784.

[129] Bates, F. S.; Rosedale, J. H.; Fredrickson, G. H. *J. Chem. Phys.* **1990**, *92*, 6255.

[130] Sakamoto, N.; Hashimoto, T. *Macromolecules* **1998**, *31*, 3292–3302.

[131] Sakamoto, N.; Hashimoto, T. *Macromolecules* **1998**, *31*, 3815–3823.

[132] Wiltzius, P.; Bates, F.; Dierker, S.; Wignall, G. *Phys. Rev. A* **1987**, *36*, 2991–2994.

[133] Yamanaka, K.; Inoue, T. *J. Mater. Sci.* **1990**, *25*, 241–245.

[134] Yamanaka, K.; Takagi, Y.; Inoue, T. *Polymer* **1989**, *60*, 1839–1844.

[135] Ohnaga, T.; Chent, W.; Inoue, T. *Polymer* **1994**, *35*, 3774–3781.

[136] Trifkovic, M.; Hedegaard, A.; Huston, K.; Sheikhzadeh, M.; Macosko, C. W. *Macromolecules* **2012**, *45*, 6036–6044.

[137] Yamamoto, K.; Ito, E.; Fukaya, S.; Takagi, H. *Macromolecules* **2009**, *42*, 9561–9567.

[138] Jones, B. H.; Lodge, T. P. *Chem. Mater.* **2010**, *22*, 1279–1281.

[139] Jones, B. H.; Lodge, T. P. *J. Am. Chem. Soc.* **2009**, *131*, 1676–7.

[140] Zhou, N.; Lodge, T. P.; Bates, F. S. *J. Phys. Chem. B* **2006**, *110*, 3979–89.

[141] Fredrickson, G. H.; Bates, F. S. *J. Polym. Sci. Part B Polym. Phys.* **1997**, *35*, 2775–2786.

[142] Bates, F.; Maurer, W.; Lipic, P.; Hillmyer, M.; Almdal, K.; Mortensen, K.; Fredrickson, G.; Lodge, T. *Phys. Rev. Lett.* **1997**, *79*, 849–852.

[143] Hillmyer, M. A.; Maurer, W. W.; Lodge, T. P.; Bates, F. S.; Almdal, K. *J. Phys. Chem. B* **1999**, *103*, 4814–4824.

[144] Ndoni, S.; Papadakis, C. M.; Bates, F. S.; Almdal, K. *Rev. Sci. Instrum.* **1995**, *66*, 1090.

[145] Pangborn, A. B.; Giardello, M. A.; Grubbs, R. H.; Rosen, R. K.; Timmers, F. J. *Organometallics* **1996**, *15*, 1518–1520.

[146] Lai, J. T.; Filla, D.; Shea, R. *Macromolecules* **2002**, *35*, 6754–6756.

[147] Kong, Y.; Hay, J. *Eur. Polym. J.* **2003**, *39*, 1721–1727.

[148] Beaumont, R.; Clegg, B.; Gee, G.; Herbert, J.; Marks, D.; Roberts, R.; Sims, D. *Polymer* **1966**, *7*, 401–417.

[149] Powell, M. *Phys. Rev. B* **1979**, *20*, 4194–4198.

[150] Roe, R.-J. *Methods of X-ray and Neutron Scattering in Polymer Science*, 1st ed.; Oxford University Press: New York, 2000; p 331.

[151] Lodge, T. P.; Pudil, B.; Hanley, K. J. *Macromolecules* **2002**, *35*, 4707–4717.

[152] Fredrickson, G. H.; Bates, F. S. *Annu. Rev. Mater. Sci.* **1996**, *26*, 501–550.

[153] Zhu, L.; Cheng, S. Z. D.; Calhoun, B. H.; Ge, Q.; Quirk, R. P.; Thomas, E. L.; Hsiao, B. S.; Yeh, F.; Lotz, B. *Polymer* **2001**, *42*, 5829–5839.

[154] Leibler, L. *Macromolecules* **1980**, *13*, 1602–1617.

[155] Knychała, P.; Banaszak, M.; Balsara, N. P. *Macromolecules* **2014**, *47*, 2529–2535.

[156] Nakamura, I.; Balsara, N. P.; Wang, Z.-G. *ACS Macro Lett.* **2013**, *2*, 478–481.

[157] Teran, A. A.; Balsara, N. P. *J. Phys. Chem. B* **2014**, *118*, 4–17.

[158] Thelen, J. L.; Teran, A. A.; Wang, X.; Garetz, B. A.; Nakamura, I.; Wang, Z.-G.; Balsara, N. P. *Macromolecules* **2014**, *47*, 2666–2673.

[159] Young, W.-S.; Epps, T. H. *Macromolecules* **2009**, *42*, 2672–2678.

[160] Semenov, A. N. *Macromolecules* **1993**, *26*, 6617–6621.

[161] Lee, S.; Gillard, T. M.; Bates, F. S. *AIChE J.* **2013**, *59*, 3502–3513.

[162] Maurer, W. W.; Bates, F. S.; Lodge, T. P.; Almdal, K.; Mortensen, K.; Fredrickson, G. H. *J. Chem. Phys.* **1998**, *108*, 2989.

[163] Bishop, C.; Teeters, D. *Electrochim. Acta* **2009**, *54*, 4084–4088.

[164] Godovsky, Y. K.; Slonimsky, G. L.; Garbar, N. M. *J. Polym. Sci. Part C* **1972**, *38*, 1–21.

[165] Lee, W.; Chen, H.-L.; Lin, T.-L. *J. Polym. Sci. Part B Polym. Phys.* **2002**, *40*, 519–529.

[166] Loo, Y.-L.; Register, R. A.; Ryan, A. J.; Dee, G. T. *Macromolecules* **2001**, *34*, 8968–8977.

[167] Müller, A. J.; María, B.; Arnal, L. *Adv. Polym. Sci.* **2005**, *190*, 1–63.

[168] Schmalz, H.; Knoll, A.; Müller, A. J.; Abetz, V. *Macromolecules* **2002**, *35*, 10004–10013.

[169] Weimann, P. A.; Hajduk, D. A.; Chu, C.; Chaffin, K. A.; Brodil, J. C.; Bates, F. S. *J. Polym. Sci. Part B Polym. Phys.* **1999**, *37*, 2053–2068.

[170] Nakamura, I.; Balsara, N.; Wang, Z.-G. *Phys. Rev. Lett.* **2011**, *107*, 1–5.

[171] Singh, M.; Odusanya, O.; Balsara, N. P. *Polym. Mater. Sci. Eng.* **2006**, *95*, 846.

[172] Williams, M. L.; Landel, R. F.; Ferry, J. D. *J. Am. Chem. Soc.* **1955**, *77*, 3701–3707.

[173] Berriot, J.; Montes, H.; Lequeux, F.; Long, D.; Sotta, P. *Macromolecules* **2002**, *35*, 9756–9762.

[174] Lin, P.-H.; Khare, R. *Macromolecules* **2010**, *43*, 6505–6510.

[175] Ediger, M. D. *Annu. Rev. Phys. Chem.* **2000**, *51*, 99–128.

[176] Torquato, S.; Hyun, S.; Donev, A. *Phys. Rev. Lett.* **2002**, *89*, 266601.

[177] Gibiansky, L.; Torquato, S. *Phys. Rev. Lett.* **1993**, *71*, 2927–2930.

[178] Torquato, S.; Hyun, S.; Donev, A. *J. Appl. Phys.* **2003**, *94*, 5748.

[179] Cussler, E. L. *Diffusion: Mass Transfer in Fluid Systems*, 3rd ed.; Cambridge University Press: Cambridge, UK, 2009; Vol. 31.

[180] Milhaupt, J. M.; Lodge, T. P. *J. Polym. Sci. Part B Polym. Phys.* **2001**, *39*, 843–859.

[181] Chen, L.; Phillip, W. A.; Cussler, E. L.; Hillmyer, M. A. *J. Am. Chem. Soc.* **2007**, *129*, 13786–7.

[182] Phillip, W. A.; Amendt, M.; O'Neill, B.; Chen, L.; Hillmyer, M. A.; Cussler, E. L. *ACS Appl. Mater. Interfaces* **2009**, *1*, 472–80.

[183] Barteau, K. P.; Wolffs, M.; Lynd, N. A.; Fredrickson, G. H.; Kramer, E. J.; Hawker, C. J. *Macromolecules* **2013**, *46*, 8988–8994.

[184] Sax, J.; Ottino, J. M. *Polym. Eng. Sci.* **1983**, *23*, 165–176.

[185] *CRC Handbook of Chemistry and Physics*; Haynes, W. M., Ed.; CRC Press, 2014.

[186] Fanggao, C.; Saunders, G. A.; Lambson, E. F.; Hampton, R. N.; Carini, G.; Di Marco, G.; Lanza, M. *J. Polym. Sci. Part B Polym. Phys.* **1996**, *34*, 425–433.

[187] Mok, M. M.; Liu, X.; Bai, Z.; Lei, Y.; Lodge, T. P. *Macromolecules* **2011**, *44*, 1016–1025.

[188] Lodge, T. P.; McLeish, T. C. B. *Macromolecules* **2000**, *33*, 5278–5284.

[189] He, Y.; Lodge, T. P. *Macromolecules* **2008**, *41*, 167–174.

[190] Muthukumar, M.; Freed, K. F. *Macromolecules* **1977**, *10*, 899–906.

[191] Freed, K. F. *J. Chem. Phys.* **1975**, *62*, 4032.

[192] Arvidson, S. A.; Lott, J. R.; McAllister, J. W.; Zhang, J.; Bates, F. S.; Lodge, T. P.; Sammler, R. L.; Li, Y.; Brackhagen, M. *Macromolecules* **2013**, *46*, 300–309.

[193] Macosko, C. W. *Rheology: Principles, Measurements, and Applications*; Wiley-VCH, 1994.

[194] Bates, F. S. *Macromolecules* **1985**, *18*, 525–528.

[195] Bates, F. S. *Macromolecules* **1987**, *20*, 2221–2225.

[196] Lodge, T. P. *Microchim. Acta* **1994**, *31*, 1– 31.

[197] Eitouni, H. B.; Balsara, N. P. Thermodynamics of Polymer Blends. In *Physical Properties of Polymers Handbook*; Mark, J. E., Ed., 2nd ed.; Springer, 2007; Chapter 19.

[198] Matsen, M. W.; Bates, F. S. *Macromolecules* **1996**, *29*, 1091–1098.

[199] Bates, F. S. *Macromolecules* **1984**, *17*, 2607–2613.

[200] Fredrickson, G. H.; Helfand, E. *J. Chem. Phys.* **1987**, *87*, 697.

[201] Hashimoto, T.; Kowsaka, K.; Shibayama, M.; Kawai, H. *Macromolecules* **1986**, *19*, 754–762.

[202] Hashimoto, T.; Kowsaka, K.; Shibayama, M.; Suehiro, S. *Macromolecules* **1986**, *19*, 750–754.

[203] Hashimoto, T. *Macromolecules* **1987**, *20*, 465–468.

[204] Cahn, J. W. *Acta Metall.* **1961**, *9*, 795–801.

[205] Noro, A.; Matsushita, Y.; Lodge, T. P. *Macromolecules* **2008**, *41*, 5839–5844.

[206] Chen, L.; Hillmyer, M. A. *Macromolecules* **2009**, *42*, 4237–4243.

[207] Mao, H.; Hillmyer, M. A. *Macromolecules* **2005**, *38*, 4038–4039.

[208] Price, S. C.; Ren, X.; Jackson, A. C.; Ye, Y.; Elabd, Y. A.; Beyer, F. L. *Macromolecules* **2013**, *46*, 7332–7340.

[209] Amendt, M. A.; Chen, L.; Hillmyer, M. A. *Macromolecules* **2010**, *43*, 3924–3934.

[210] Lascaud, S.; Perrier, M.; Vallee, A.; Besner, S.; Prud'homme, J.; Armand, M. *Macromolecules* **1994**, *27*, 7469–7477.

[211] Kossuth, M. B.; Morse, D. C.; Bates, F. S. *J. Rheol.* **1999**, *43*, 167.

[212] Santangelo, P. G.; Roland, C. M. *Macromolecules* **1998**, *31*, 4581–4585.

[213] Chatterjee, J.; Jain, S.; Bates, F. *Macromolecules* **2007**, *40*, 2882–2896.

[214] Meuler, A. J.; Hillmyer, M. A.; Bates, F. S. *Macromolecules* **2009**, *42*, 7221–7250.

[215] Bates, F. S.; Berney, C. V.; Cohen, R. E. *Macromolecules* **1983**, *16*, 1101–1108.

[216] Benetatos, N. M.; Winey, K. I. *Macromolecules* **2007**, *40*, 3223–3228.

[217] Sinturel, C.; Vayer, M.; Morris, M.; Hillmyer, M. A. *Macromolecules* **2013**, *46*, 5399–5415.

[218] Ueki, T.; Watanabe, M. *Chem. Lett.* **2006**, *35*, 964–965.

[219] Asai, H.; Fujii, K.; Ueki, T.; Sawamura, S.; Nakamura, Y.; Kitazawa, Y.; Watanabe, M.; Han, Y.-S.; Kim, T.-H.; Shibayama, M. *Macromolecules* **2013**, *46*, 1101–1106.

[220] Kinning, D. J.; Thomas, E. L. *Macromolecules* **1984**, *17*, 1712–1718.

[221] Lee, I.; Panthani, T. R.; Bates, F. S. *Macromolecules* **2013**, *46*, 7387–7398.

Appendices

Appendix A

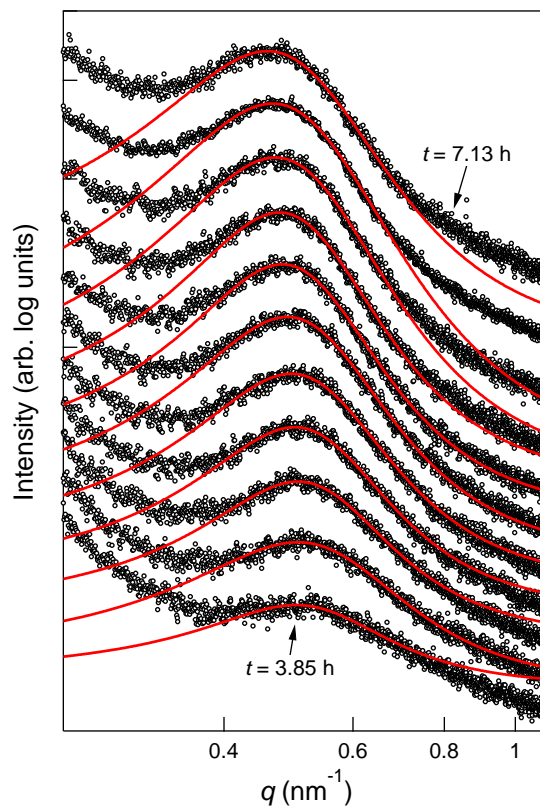# Chapter 3 Appendix

A.1 SAXS Data Peak Fitting

Figure A.1: *In situ* SAXS data for a PEM prepared without ionic liquid. Black circles are data, red lines are fits to a Lorentzian function. Values of q_{m} and I_{m} were extracted from the fits and are summarized graphically in Figure 3.6. Traces were vertically shifted.
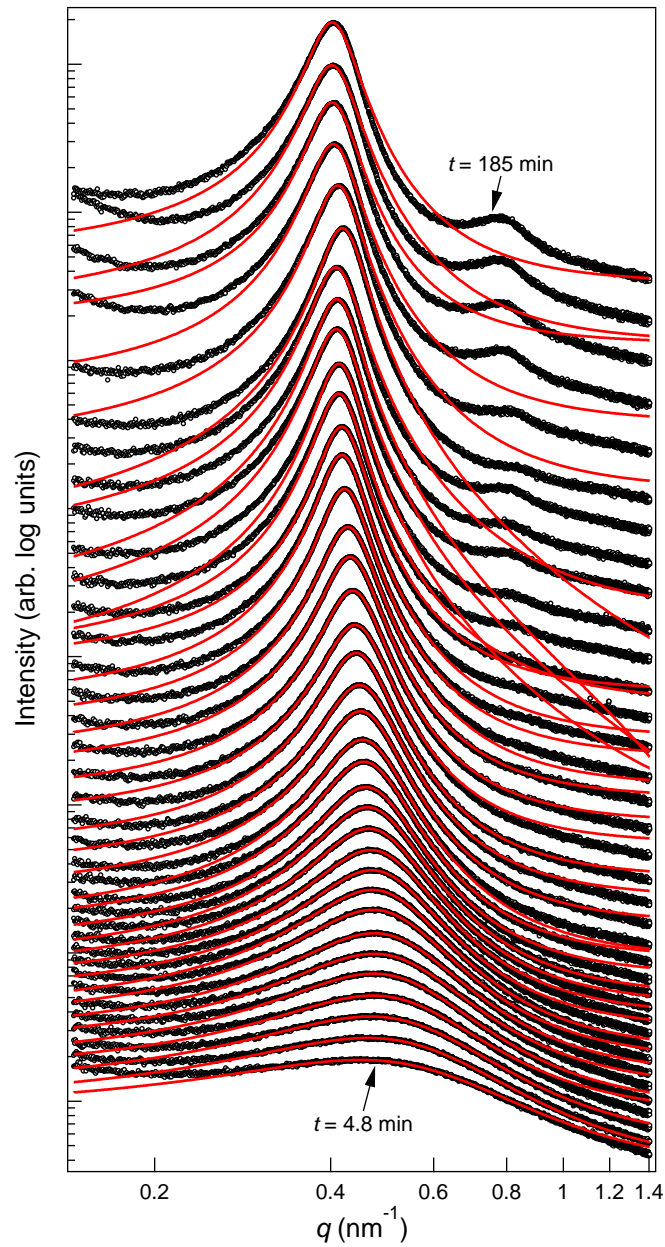
Figure A.2: *In situ* SAXS data for a PEM prepared with 21 overall vol% BMITFSI. Black circles are data, red lines are fits to a Lorentzian function. Values of q_m and I_m were extracted from the fits and are summarized graphically in Figure 3.7. Traces were vertically shifted.

A.2 Dynamic Light Scattering Study of the PIPS PEM Reaction Precursor

Dynamic light scattering (DLS) was used in an attempt to track the growth of the P(S-*co*-DVB)-*b*-PEO diblock during polymerization-induced phase separation, with the goal of correlating DLS data with gelation. The results are summarized below. The experiment did not work as expected, as the primary relaxation event in the experimentally-relevant time scale (1 μs to 1 s) was that of the poly(ethylene oxide) "mesh", rather than translational diffusion of growing "blobs" of crosslinked polymer. In all of the figures in this section, the sample was styrene (S)/divinylbenzene (DVB) (4/1 molar ratio S/DVB), 5 kg/mol PEO-CTA at 32 wt%, and 21 vol% BMITFSI.
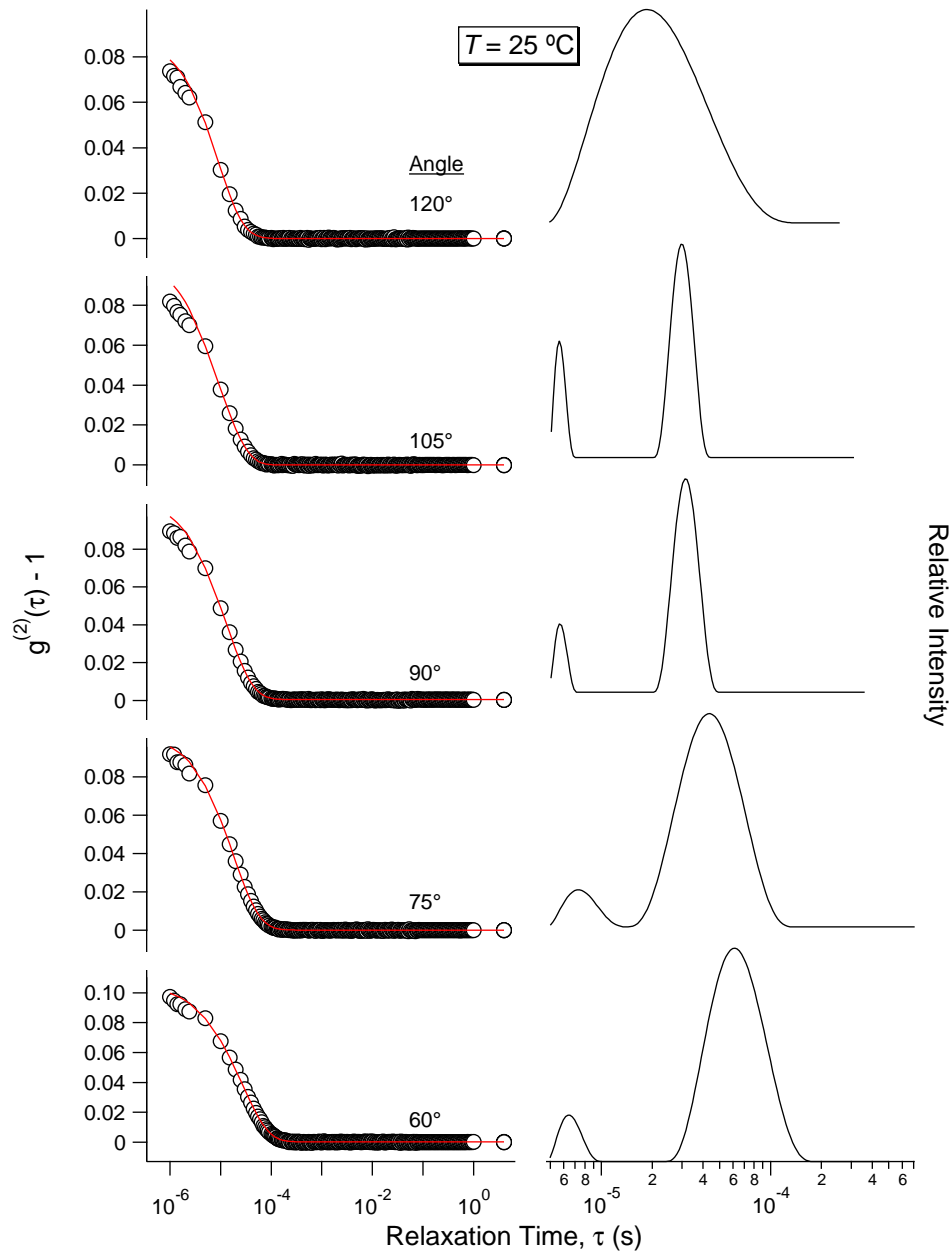
Figure A.3: Left: normalized intensity autocorrelation data ($\bigcirc$) and REPES fit (red line). Right: Relaxation time distribution from a Laplace inversion of the intensity autocorrelation function.
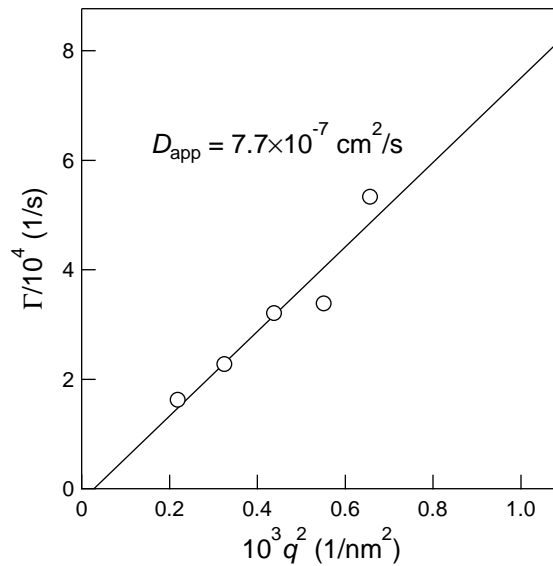
Figure A.4: Relaxation rate, Γ, versus q^2. Values of Γ were extracted from the maximum intensity of the largest peak at each angle in Figure A.3. The near-zero intercept suggests the concentration fluctuations are relaxing via Fickian diffusion. The slope gives an apparent diffusion coefficient, D_{app}, of 7.7×10^{-7} cm^2/s.
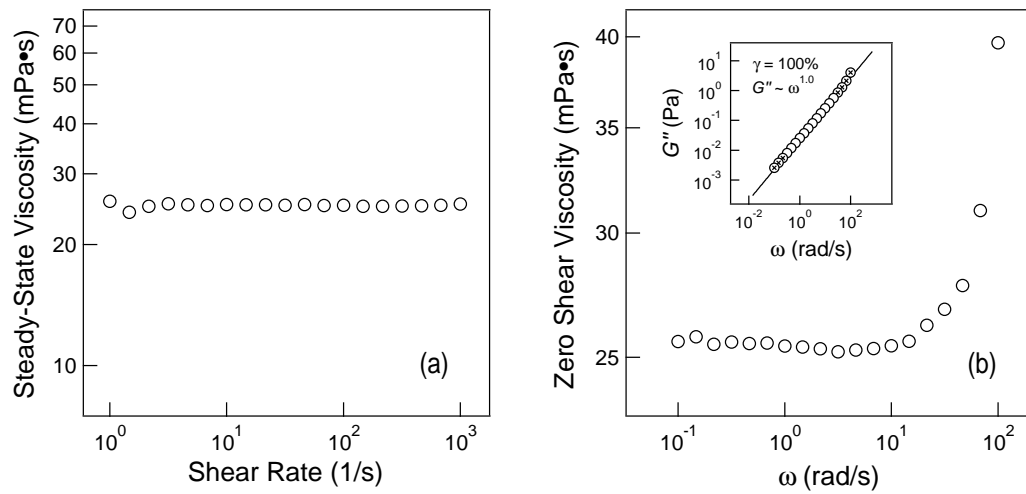
Figure A.5: Viscosity of the PIPS PEM reaction precursor at 25 °C. Measurements were made using (a) steady-state viscosity as a function of shear rate, and (b) linear oscillatory shear, where the zero-shear viscosity, η_0, is calculated as G''/ω as $\omega \to 0$. In both cases, η is *ca.* 25 mPa·s.
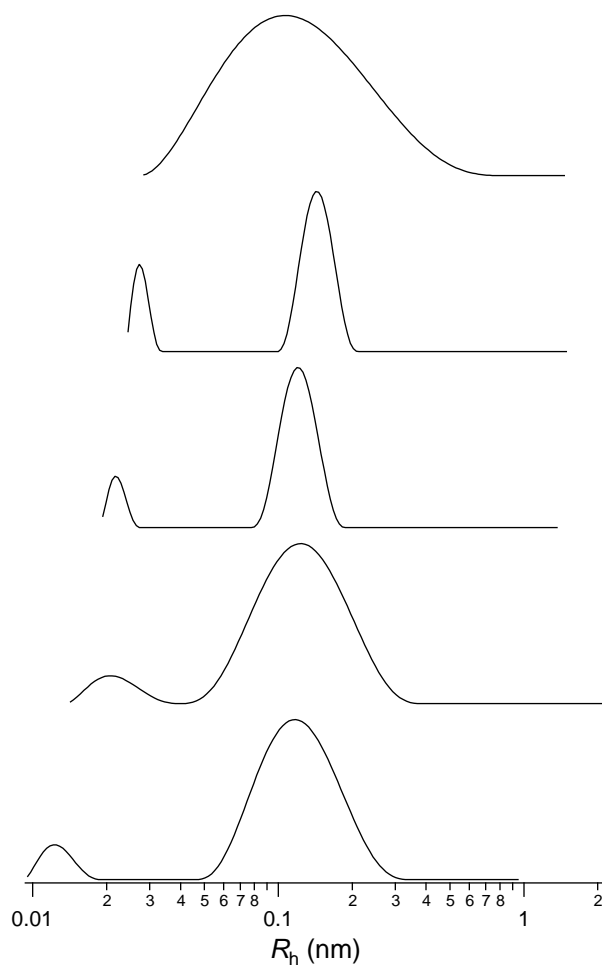
Figure A.6: Apparent hydrodynamic radius, R_h, of the PIPS PEM reaction precursor, at 25 °C. R_h was calculated as $kT/(6\pi\eta D_\mathrm{app})$, where D_app is the apparent diffusion coefficient calculated in Figure A.4 and η is the viscosity shown in Figure A.5. The traces correspond to angles of 60°, 75°, 90°, 105°, and 120° (lowest to highest trace). The unreasonably small magnitude of R_h suggests that the measured relaxation is of the PEO "mesh", as opposed to translational diffusion of crosslinked diblock flocs.
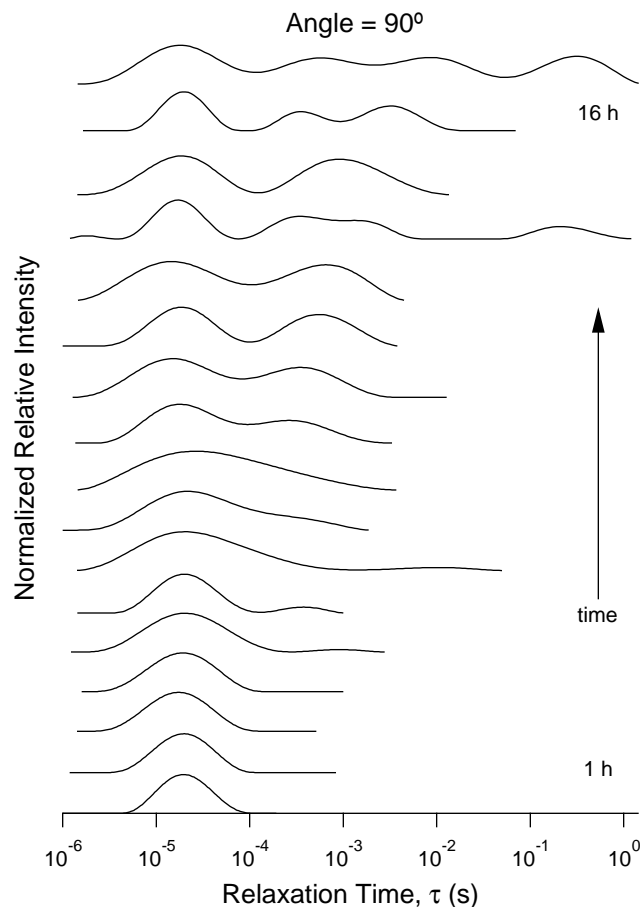
Figure A.7: Distribution of relaxation time during the course of a PIPS PEM reaction. Due to instrument limitations, the reaction was run at 60 °C, whereas T_{rxn} is typically 120 °C. After 18 h at 60 °C, the sample still flowed (albeit slower than before the heat treatment), suggesting that gelation had not yet occurred. Nonetheless, the wide distribution and multiple modes of relaxation suggest that the crosslinking reaction was proceeding.

Appendix B

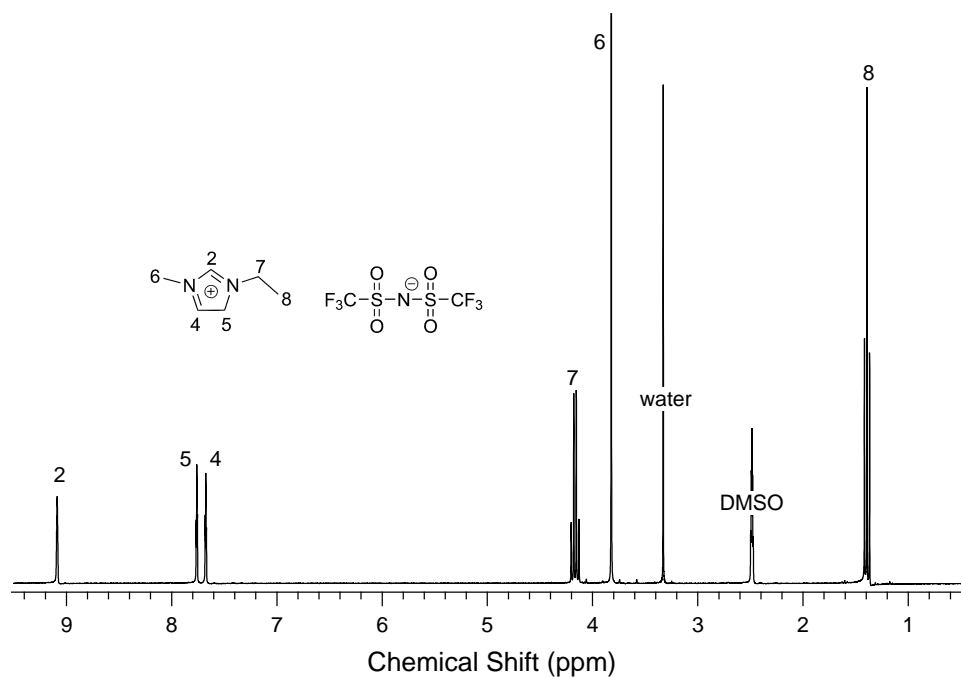# Miscellaneous Characterization Data

B.1 EMITFSI

Figure B.1: ¹H-NMR spectrum of the ionic liquid 1-ethyl-3-methylimidazolium bis(tri-fluoromethylsulfonyl)imide (EMITFSI). The sample was run in deuterated DMSO on a 300 MHz Varian Inova (VI-300).
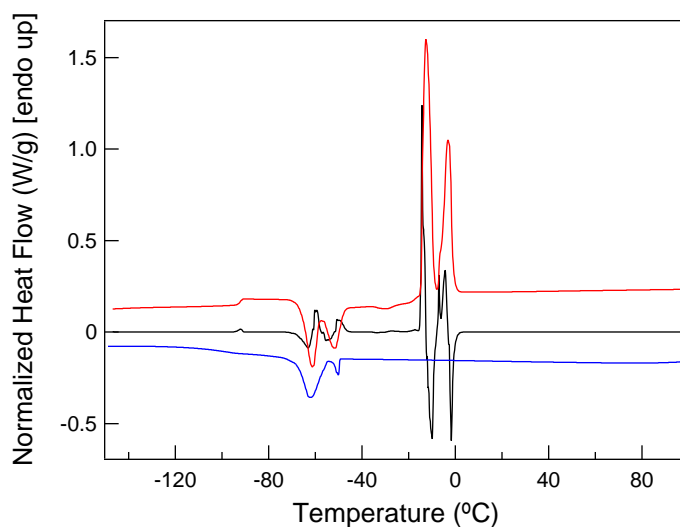
Figure B.2: Differential scanning calorimetry data (TA Instruments Q1000) of the ionic liquid EMITFSI. Red and blue traces are heating and cooling ramps, respectively, at 10 °C/min. The sample was annealed at 100 °C (above any suspected thermal transitions) for 5 min. After cooling to −150 °C, the sample was annealed for 5 min before heating. The black line is the first derivative of heat flow during the heating ramp. $T_{\mathrm{g}} = -92$ °C, taken to be the inflection point in the heating trace. $T_{\mathrm{m}} = -13$ °C, corresponding to be the maximum in the melting peak. The melting peak centered at 0 °C is likely due to water contamination.
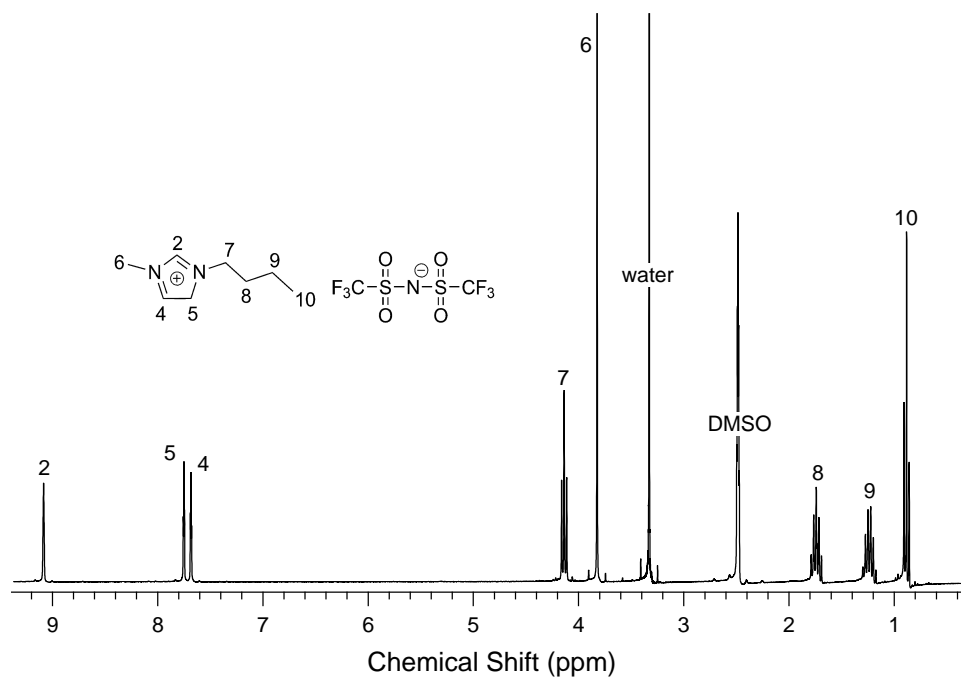
B.2   BMITFSI

Figure B.3: ^{1}H-NMR spectrum of the ionic liquid 1-butyl-3-methylimidazolium bis(tri-fluoromethylsulfonyl)imide (BMITFSI). The sample was run in deuterated DMSO on a 300 MHz Varian Inova (VI-300).

B.3   PEO Homopolymer
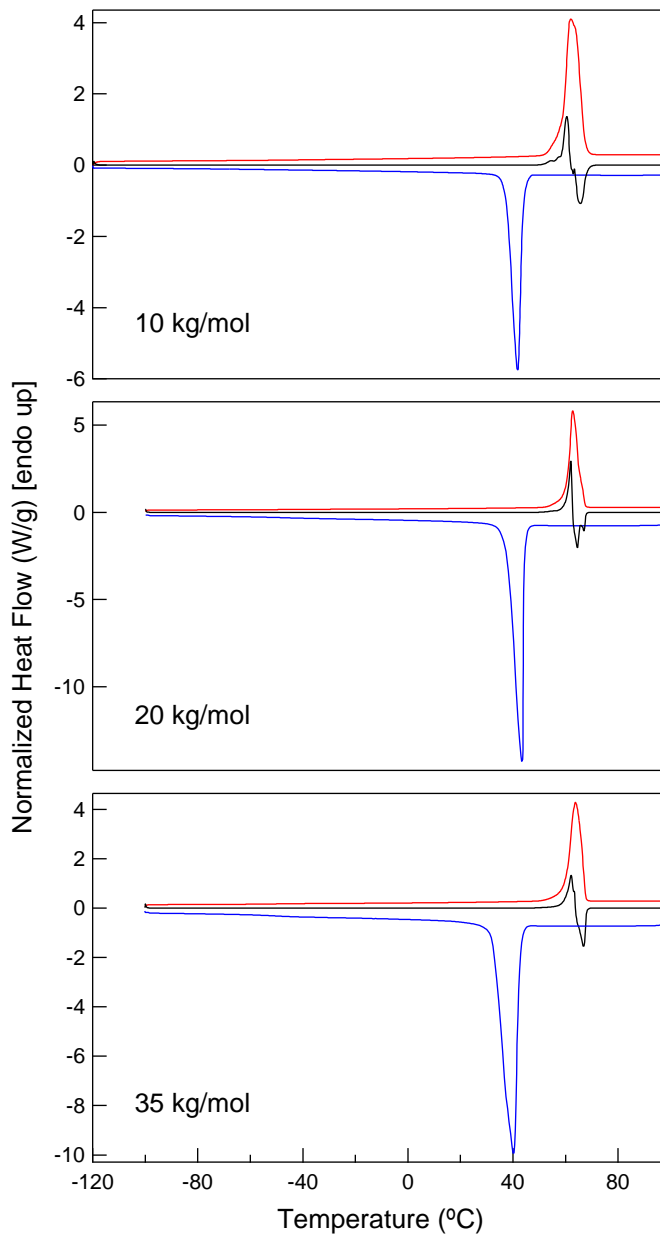
Figure B.4:   Differential scanning calorimetry data (TA Instruments Q1000) of poly(ethylene oxide) homopolymer (M indicated in each plot). Red and blue traces are heating and cooling ramps, respectively, at 10 °C/min. The sample was annealed at 100 °C (above any suspected thermal transitions) for 5 min. After cooling to -100 or -120 °C, the sample was annealed for 5 min before heating. The black line is the first derivative of heat flow during the heating ramp.

Table B.1: Melting transitions[i] of PEO homopolymers shown in Figure B.4

M_{PEO} (kg/mol)	T_{m}[ii] (°C)	degree of crystallinity[iii] (wt%)
10	62	80
20	63	77
35	64	68

[i] The T_{g} was not detected for these samples

[ii] Taken to be the maximum of the melting peak

[iii] Crystalline weight fraction was calculated by dividing the measured enthalpy of melting by the heat of fusion for a pure PEO crystal (200 J/g)

B.4 PEO/BMITFSI Blends
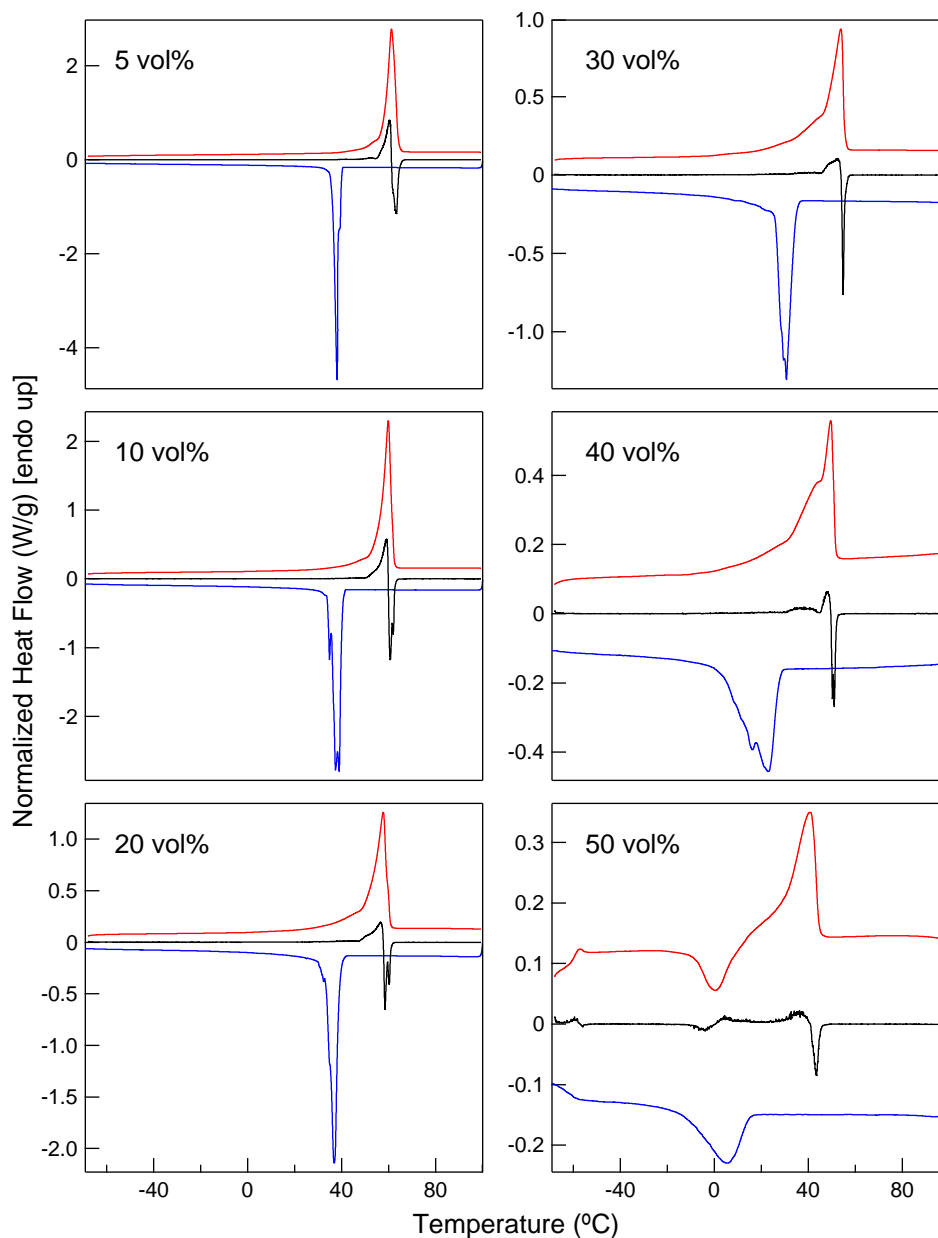
Figure B.5: Differential scanning calorimetry data (TA Instruments Discovery DSC) of blends of PEO homopolymer ($M = 8$ kg/mol) and the ionic liquid BMITFSI. The numbers in the plots give the volume fraction of BMITFSI. Red and blue traces are heating and cooling ramps, respectively, at 5 °C/min. The sample was annealed at 100 °C (above any suspected thermal transitions) for 5 min. After cooling to −60 °C, the sample was heated without annealing. The black line is the first derivative of heat flow during the heating ramp.

Table B.2: Thermal transitions of PEO/BMITFSI blends shown in Figure B.5

BMITFSI concentration (vol%)	T_{g}[i] (°C)	T_{m}[ii] (°C)	degree of crystallinity[iii] (wt%)
5	nd	61	75
10	nd	60	60
20	nd	58	53
30	nd	54	43
40	nd	50	30
50	−60	40	15

[i] nd means the T_{g} was not detected

[ii] Taken to be the maximum of the melting peak

[iii] Crystalline weight fraction was calculated by dividing the measured enthalpy of melting by the heat of fusion for a pure PEO crystal (200 J/g)
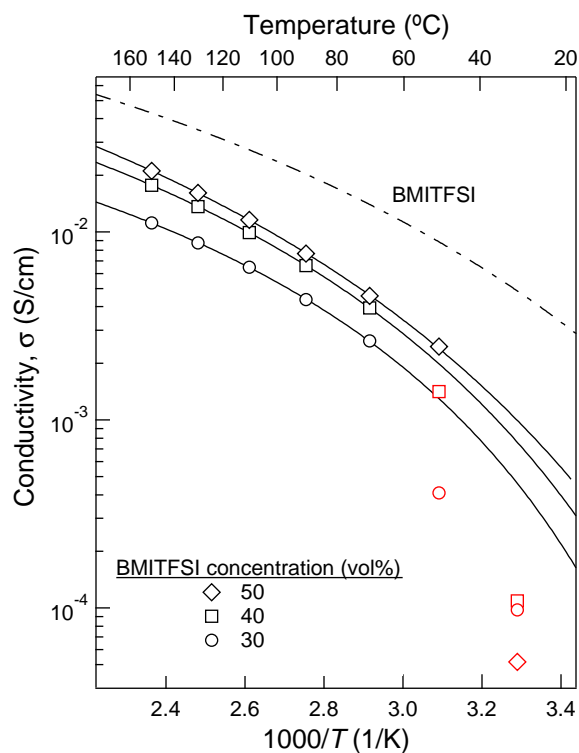
Figure B.6: Ionic conductivity of blends of 8 kg/mol PEO homopolymer and the ionic liquid BMITFSI. Solid black lines are fits of the data to the VFT equation. Red symbols are at temperatures less than $T_{m,PEO}$ and were omitted from the fit. The dash-dot line is the conductivity of pure BMITFSI and was generated using parameters from Tokuda et al.[44]

Table B.3: VFT parameters for PEO/BMITFSI blend
conductivity data in Figure B.6

concentration of BMITFSI (vol%)	σ_0 (mS/cm)	B (K)	T_0 (K)
30	99 ± 6.0	437 ± 20	223 ± 3.6
40	223 ± 6.0	554 ± 9.2	208 ± 1.5
50	371 ± 35	661 ± 37	192 ± 5.1
100[i]	430 ± 20	565 ± 140	178 ± 2

[i] VFT parameters for neat BMITFSI taken from Tokuda et al.[44]

B.5   PEO/EMITFSI Blends

Figure B.7: Differential scanning calorimetry data (TA Instruments Q1000) of polymer-rich blends of PEO homopolymer (M = 10 kg/mol) and the ionic liquid EMITFSI. The numbers in the plots give the volume fraction of EMITFSI. Red and blue traces are heating and cooling ramps, respectively, at 10 °C/min. The sample was annealed at 100 °C (above any suspected thermal transitions) for 5 min. After cooling to −120 °C, the sample was heated after a 5 min anneal. The black line is the first derivative of heat flow during the heating ramp. The inset is an expanded view of the first derivative trace showing the peak used to identify the T_g.
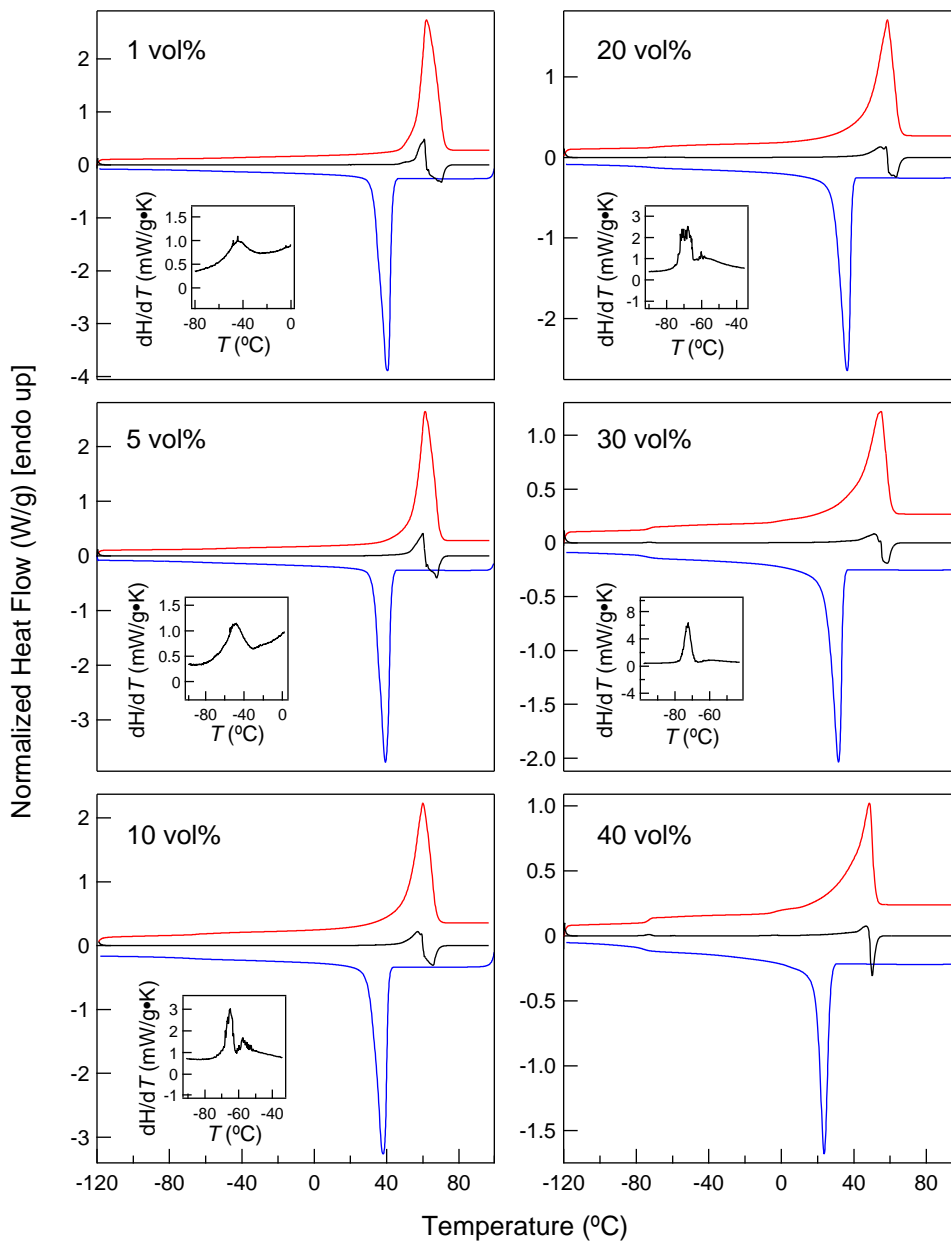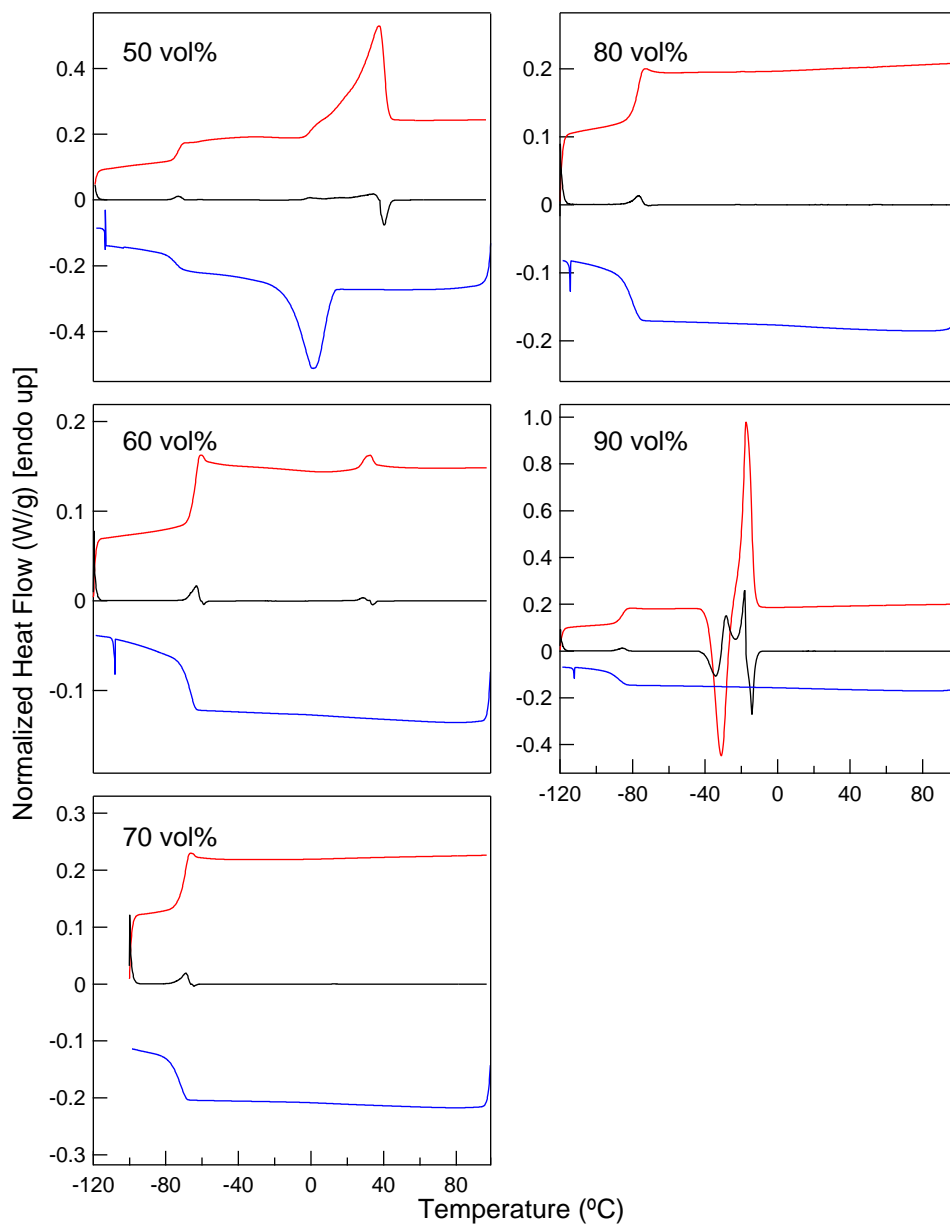
Figure B.8: Differential scanning calorimetry data (TA Instruments Q1000) of ionic liquid-rich blends of PEO homopolymer ($M = 10$ kg/mol) and the ionic liquid EMITFSI. The numbers in the plots give the volume fraction of EMITFSI. Red and blue traces are heating and cooling ramps, respectively, at 10 °C/min. The sample was annealed at 100 °C (above any suspected thermal transitions) for 5 min. After cooling to -100 or -120 °C, the sample was heated after a 5 min anneal. The black line is the first derivative of heat flow during the heating ramp.

Table B.4: Thermal transitions of PEO[i]/EMITFSI blends shown in Figures B.7 and B.8

EMITFSI concentration (vol%)	T_g (°C)	T_m[ii,iii] (°C)	degree of crystallinity[iii] (wt%)
1	−44	62	81
5	−49	61	80
10	−65	60	75
15	−68	58	61
24	−73	55	49
33	−73	48	36
50	−73	37	18
60	−64	33	< 1
70	−69	np	np
80	−76	np	np
90	−85	−18[v]	-

[i] M_{PEO} = 10 kg/mol
[ii] Taken to be the maximum of the melting peak
[iii] np means a melting transition was not present
[iv] Crystalline weight fraction was calculated by dividing the measured enthalpy of melting by the heat of fusion for a pure PEO crystal (200 J/g)
[v] Melting transition of EMITFSI
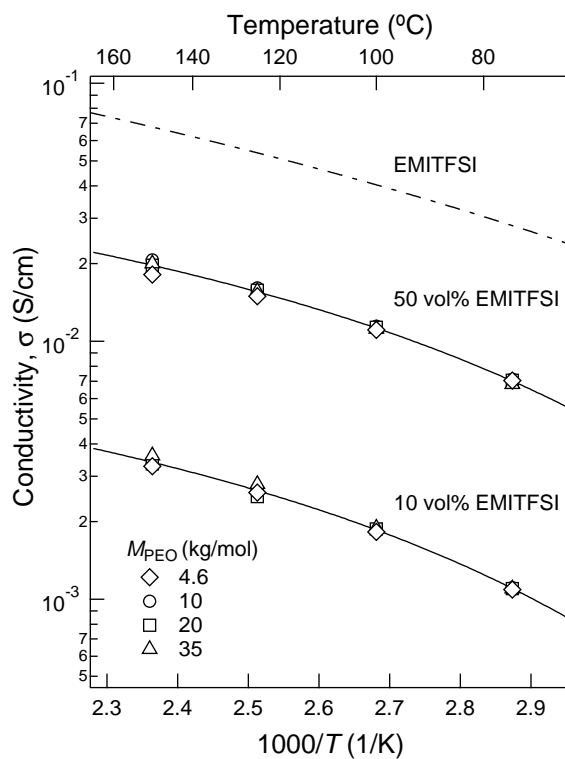
Figure B.9: Ionic conductivity of blends of PEO homopolymer (4.6, 10, 20, and 35 kg/mol) and the ionic liquid EMITFSI (10 and 50 vol%). Conductivity data were measured using the Agilent 4980A LCR dielectric accessory for the TA Instruments ARES rheometer, with 25 mm stainless steel parallel plates.

Table B.5: VFT parameters for PEO/EMITFSI blend conductivity data in Figure B.9

concentration of EMITFSI (vol%)	σ_0 (mS/cm)	B (K)	T_0 (K)
10	16 ± 6.5	274 ± 101	245 ± 22
50	89 ± 45	276 ± 132	239 ± 31
100[i]	580 ± 20	554 ± 130	165 ± 2

[i] VFT parameters for neat EMITFSI taken from Tokuda et al.[44]

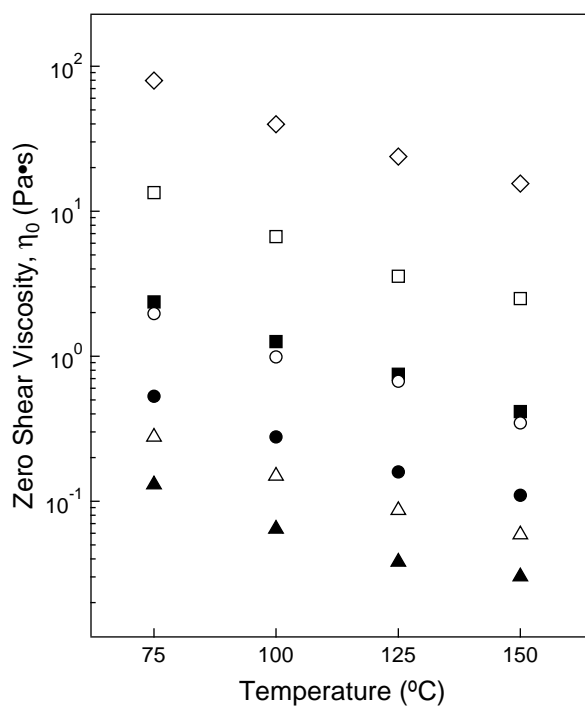**Figure B.10:** Zero shear viscosity, η_0, of PEO homopolymer/EMITFSI blends. Open and closed symbols correspond to 10 and 50 vol% EMITFSI, respectively. $M_{\mathrm{PEO}} = 4.6$ (triangles), 10 (circles), 20 (squares), and 35 (diamond) kg/mol. η_0 was calculated from frequency sweeps in the terminal regime as G''/ω in the limit that $\omega \to 0$.

Appendix C

Code

C.1   O^{70} Network Morphology Lattice Parameters

The higher order peaks for the O^{70} network morphology do not reduce to simple multiples of the primary peak. Referencing experimental small-angle scattering peaks to O^{70} instead requires calculating the best-fit lattice parameters a, b, and c, which can be done with the following Matlab code.[i] The q_{hkl} values of allowed reflections are then calculated with eq C.1 and compared to the experimentally-observed peaks. h, k, and l are the Miller lattice indices.

$$q_{hkl} = 2\pi \left[\left(\frac{h}{a}\right)^2 + \left(\frac{k}{b}\right)^2 + \left(\frac{l}{c}\right)^2 \right]^{\frac{1}{2}} \tag{C.1}$$

C.1.1   Matlab Code

```
%% Best-Fit Lattice Parameters for the O70 Morphology
% This code calculates best-fit lattice parameters for the O70
% network morphology.
```

---
[i]Thanks to Dr. Douglas R. Tree for writing the Matlab code.

```matlab
clear;
clc;


% The inputs are the peak positions of experimentally observed SAXS
% Bragg peaks. Fill the q_expt vector with peaks from high to low q.
% Units are 1/nm.
q_expt = [0.66604,0.64226,0.52035,0.37465,0.35978];


% h, k, and l are the Miller lattice indices of the allowed reflections.
% This code will calculate the location of 13 allowed Bragg peaks, which
% in my experience, is sufficient. However, more can be added by the user.
h = [1,0,0,1,1,1,0,1,2,2,2,0,1];
k = [1,2,0,1,3,1,4,3,0,2,2,4,3];
l = [1,2,4,3,1,5,0,3,2,0,2,4,5];


% Guess physically reasonable lattice parameters (a, b, and c) in units
% of nm. The latpar vector is [a,b,c].
latpar = [20,30,70];


index = 1;
bindex = 1;
latind = zeros(5, 3, 1287);
bf_latpar = zeros(3, 1287);
SSE = zeros(1287, 1);


for i=1:13
    for j=1:i-1
        for m=1:j-1
            for n=1:m-1
                for u=1:n-1

                    latind(:, :, index) = ...
                            [h(u), k(u), l(u); ...
                             h(i), k(i), l(i); ...
```

```matlab
                        h(j), k(j), l(j); ...
                        h(m), k(m), l(m); ...
                        h(n), k(n), l(n)];


            options = optimset('Display','off');


            [bf_latpar(:, index), SSE(index)] = fminsearch( ...
            @(opt_latpar) calc_SSE(opt_latpar, latind(:, :, index), ...
            q_expt), latpar, options);


            %disp(latind);
            %disp(index);
            %disp([i-1, j-1, m-1, n-1]);
            index = index + 1;


            end
        end
    end
  end
end


%% Display results
% Matlab will calculate the 10 best fits, in order of the least to most
% SSE. It is up to the user to decide which fit is physically reasonable,
% both on the basis of literature precedence and knowledge of the Fddd
% space group. For example, the lowest q peak is typically associated
% with the (111) plane. If the best fit reports that the "primary" peak
% is a reflection from the (135) plane, that fit is likely incorrect.


% Once the best-fit lattice parameters are known, the 13 allowed
% reflections should be compared to the experimental SAXS data. I have
% written an Igor procedure to tag a plotted trace of experimental '
% SAXS data with the locations of allowed reflections.
```

```matlab
clc;

[sort_SSE, sort_index] = sort(SSE);
top_ten_index = sort_index(1:10);
top_ten_SSE = sort_SSE(1:10);


top_ten_latpar = bf_latpar(:, top_ten_index);
top_ten_latind = latind(:, :, top_ten_index);


for i = 1:10

    disp('------------------');
    disp('rank: ');
    disp(i)
    disp('The optimal lattice indices are:');
    disp(top_ten_latind(:, :, i));
    disp('The optimal lattice parameters are: ');
    disp(top_ten_latpar(:, i));
    disp('With a squared error of: ');
    disp(top_ten_SSE(i));

end
```

The following function takes the three vectors defined in the above Matlab file and calculates the sum of squares error (SSE).

```matlab
function [ SSE ] = calc_SSE( latpar, latind, q_expt )

% calculate q_theo
a = latpar(1);
b = latpar(2);
c = latpar(3);


h = latind(:, 1);
```

```
k = latind(:, 2);
l = latind(:, 3);


q_theo = 2*pi*((h/a).^2 + (k/b).^2 + (l/c).^2).^0.5;


SSE = dot(q_theo-q_expt',q_theo-q_expt');


end
```

C.1.2   Igor Pro Procedure

The following procedure requires an active plot of scattering data.

```
Function PlotO70AllowedReflections()

Variable a,b,c
Variable q_theo1,q_theo2,q_theo3,q_theo4,q_theo5
Variable q_theo6,q_theo7,q_theo8,q_theo9,q_theo10
Variable q_theo11,q_theo12,q_theo13

Prompt a, "Enter a: " // Set prompt for a param
Prompt b, "Enter b: " // Set prompt for b param
Prompt c, "Enter c: " // Set prompt for b param

DoPrompt "Enter Lattice Parameters", a, b, c
if (V_Flag)
return -1 // User canceled
endif

Make/O/N=3 mli1, mli2, mli3, mli4, mli5, mli6
Make/O/N=3 mli7, mli8, mli9, mli10, mli11, mli12, mli13

mli1 = {0,0,4}
mli2 = {0,2,2}
mli3 = {1,1,1}
mli4 = {1,1,3}
mli5 = {1,1,5}
mli6 = {1,3,1}
mli7 = {1,3,3}
mli8 = {0,4,0}
mli9 = {2,0,2}
mli10 = {2,2,0}
mli11 = {1,3,5}
mli12 = {0,4,4}
mli13 = {2,2,2}
```

```
q_theo1=2*pi*((mli1[0]/a)^2+(mli1[1]/b)^2+(mli1[2]/c)^2)^0.5
q_theo2=2*pi*((mli2[0]/a)^2+(mli2[1]/b)^2+(mli2[2]/c)^2)^0.5
q_theo3=2*pi*((mli3[0]/a)^2+(mli3[1]/b)^2+(mli3[2]/c)^2)^0.5
q_theo4=2*pi*((mli4[0]/a)^2+(mli4[1]/b)^2+(mli4[2]/c)^2)^0.5
q_theo5=2*pi*((mli5[0]/a)^2+(mli5[1]/b)^2+(mli5[2]/c)^2)^0.5
q_theo6=2*pi*((mli6[0]/a)^2+(mli6[1]/b)^2+(mli6[2]/c)^2)^0.5
q_theo7=2*pi*((mli7[0]/a)^2+(mli7[1]/b)^2+(mli7[2]/c)^2)^0.5
q_theo8=2*pi*((mli8[0]/a)^2+(mli8[1]/b)^2+(mli8[2]/c)^2)^0.5
q_theo9=2*pi*((mli9[0]/a)^2+(mli9[1]/b)^2+(mli9[2]/c)^2)^0.5
q_theo10=2*pi*((mli10[0]/a)^2+(mli10[1]/b)^2+(mli10[2]/c)^2)^0.5
q_theo11=2*pi*((mli11[0]/a)^2+(mli11[1]/b)^2+(mli11[2]/c)^2)^0.5
q_theo12=2*pi*((mli12[0]/a)^2+(mli12[1]/b)^2+(mli12[2]/c)^2)^0.5
q_theo13=2*pi*((mli13[0]/a)^2+(mli13[1]/b)^2+(mli13[2]/c)^2)^0.5

Tag/C/I=1/N=mli1/F=0/O=90/L=1 Bottom, q_theo1, "\Z10(004)"
Tag/C/I=1/N=mli2/F=0/O=90/L=1 Bottom, q_theo2, "\Z10(022)"
Tag/C/I=1/N=mli3/F=0/O=90/L=1 Bottom, q_theo3, "\Z10(111)"
Tag/C/I=1/N=mli4/F=0/O=90/L=1 Bottom, q_theo4, "\Z10(113)"
Tag/C/I=1/N=mli5/F=0/O=90/L=1 Bottom, q_theo5, "\Z10(115)"
Tag/C/I=1/N=mli6/F=0/O=90/L=1 Bottom, q_theo6, "\Z10(131)"
Tag/C/I=1/N=mli7/F=0/O=90/L=1 Bottom, q_theo7, "\Z10(133)"
Tag/C/I=1/N=mli8/F=0/O=90/L=1 Bottom, q_theo8, "\Z10(040)"
Tag/C/I=1/N=mli9/F=0/O=90/L=1 Bottom, q_theo9, "\Z10(202)"
Tag/C/I=1/N=mli10/F=0/O=90/L=1 Bottom, q_theo10, "\Z10(220)"
Tag/C/I=1/N=mli11/F=0/O=90/L=1 Bottom, q_theo11, "\Z10(135)"
Tag/C/I=1/N=mli12/F=0/O=90/L=1 Bottom, q_theo12, "\Z10(044)"
Tag/C/I=1/N=mli13/F=0/O=90/L=1 Bottom, q_theo13, "\Z10(222)"

KillWaves mli1, mli2, mli3, mli4, mli5, mli6, mli7, mli8
KillWaves mli9, mli10, mli11, mli12, mli13

End
```

C.2   Modified Hard Sphere Structure Factor

The following code is used in Igor Pro to fit experimental scattering data to a modified hard sphere model, sometimes referred to in the literature as the Kinning-Thomas model.[220] The code was not directly used for the work described in this thesis, but was written during the course of a collaboration on triblock terpolymer ion gels. The model, although simplistic, has found great utility in fitting a variety of systems, including micelles in solution, ion gels with cores exhibiting liquid-like packing, and thermoplastic elastomers with sphere-in-matrix microstructure.[221] Figure C.1 is an
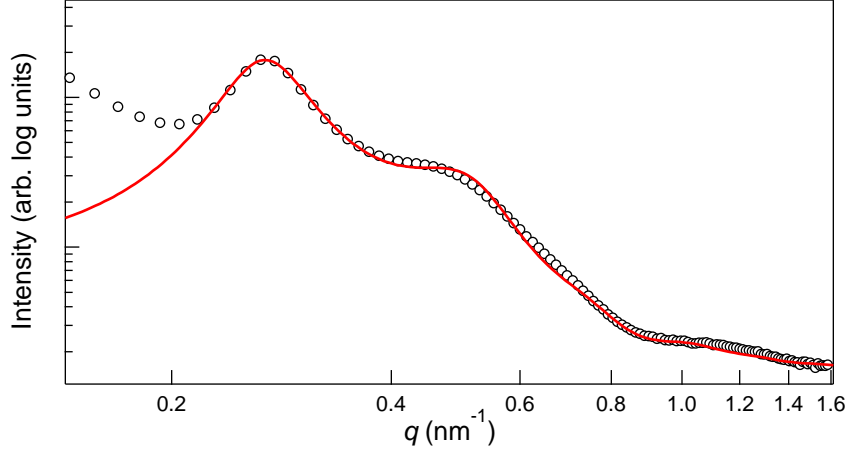
Figure C.1: Example of fitting experimental scattering data to the modified hard sphere model. Circles are data, the red line is the fit. The best-fit parameters (described in the text) are $R_c = 5.6 \pm 0.009$ nm, $\sigma_R = 0.89 \pm 0.02$ nm, $R_{hs} = 12 \pm 0.007$ nm, and $\phi = 0.40 \pm 0.0007$.

example of a fit to small-angle X-ray scattering data from a poly(styrene-*b*-ethylene oxide-*b*-styrene)/EMITFSI ion gel. The microstructure of this particular sample consists of 6 nm spheres of polystyrene (giving rise to the peak centered around 1.1 nm^{-1}), which exhibit liquid-like packing, as evidenced by the broad peaks at low q.

C.2.1 Model Description

Scattering data are fit to a modified hard sphere model, which includes terms for self-correlation of the spheres (physically, the spheres are, for example, cores of micelles or nodes of the gel) and cross-correlation between different spheres. The form factor, P, describing the self-correlation of a hard sphere with radius R_c is given by

$$P_c(q) = N_{agg}^2 \beta^2 A_c^2(q) \tag{C.2}$$

A_c is the scattered field amplitude from a uniform hard sphere (core) and is given by

$$A_c = \left(\frac{3}{qR_c} \right) [\sin(qR_c) - qR_c \cos(qR_c)] \tag{C.3}$$

N_{agg} is the aggregation number of chains in a core, β is the excess scattering length density of the core relative to the corona/matrix, and $q = |\mathbf{q}| = 4\pi \sin(\theta/2)/\lambda$ is the magnitude of the scattering wave vector, where θ is the angle of scattered intensity and λ is the vacuum wavelength of incident radiation. In practice, this code has only been used to model SAXS data, which are typically not reduced to absolute intensity. The prefactor $N_{\text{agg}}^2 \beta^2$ is therefore ignored and is replaced by an arbitrary multiplicative fitting parameter.

The structure factor for low-q scattering is described using the Percus-Yevick (PY) closure relation, which gives the direct correlation function, $c(r)$, as a function of inter-particle spacing, r, for particles with excluded volume interaction potential. That is, scattering centers experience infinite interaction potential at a center-to-center distance less than or equal to $2R_{\text{hs}}$ (hs = hard sphere) and have zero interaction potential with particles further than $2R_{\text{hs}}$ away. Note that the PY closure relation only allows for one primary scattering peak at low q; that is, it can only account for one preferred length scale of packing. If two low-q peaks of commensurate intensity are observed in the scattering data, it is likely that two distinct packing length scales exist, and the PY form should not be used. The direct correlation function is

$$
\begin{aligned}
c(r) &= 0 \text{ for } r > 2R_{\text{c}} \\
c(r) &= -\lambda_1 - 6\phi\lambda_2 \frac{r}{2R_{\text{c}}} - \frac{\phi}{2}\lambda_1 \frac{r^3}{(2R_{\text{c}})^3} \text{ for } r \le 2R_{\text{c}}
\end{aligned}
\tag{C.4}
$$

where ϕ is the volume fraction of "equivalent" hard spheres and is calculated as

$$
\phi = \frac{4}{3}\pi \bar{N} R_{\text{c}}^3
\tag{C.5}
$$

$\bar{N}$ is the number volume density of scattering particles. R_{hs} is typically larger than R_{c} because the coronas of micelles in close proximity exert a net repulsive interaction potential well before the cores physically touch. The parameters λ_1 and λ_2 in eq C.4

are defined as

$$\lambda_1 = \frac{(1 + 2\phi)^2}{(1 - \phi)^4} \tag{C.6}$$

and

$$\lambda_2 = \frac{-(1 + \phi/2)^2}{(1 - \phi)^4} \tag{C.7}$$

In Fourier space, the direct correlation function is denoted $C(q)$, and is given by

$$\begin{aligned}
\bar{N}C(q) = -24\phi \left\{ \lambda_1 \left[\frac{\sin(x) - x\cos(x)}{x^3} \right] - \right. \\
6\phi\lambda_2 \left[\frac{x^2\cos(x) - 2x\sin(x) - 2\cos(x) + 2}{x^4} \right] \\
\left. -\phi\frac{\lambda_1}{2} \left[\frac{x^4\cos(x) - 4x^3\sin(x) - 12x^2\cos(x) + 24x\sin(x) + 24\cos(x) - 24}{x^6} \right] \right\}
\end{aligned} \tag{C.8}$$

where $x = 2qR_{\text{hs}}$. The structure factor, $S(q)$, is

$$S(q) = \frac{1}{1 - \bar{N}C(q)} \tag{C.9}$$

The total scattered intensity from a solution of uniform spheres is

$$I_{\text{u}}(q) \sim P_{\text{c}}(q)S(q) \tag{C.10}$$

To account for dispersity of core radii, a Gaussian distribution is assumed, given by

$$Đ(R_{\text{c}}) = \frac{1}{\sqrt{2\pi}\sigma_{\text{R}}} \exp\left[\frac{-(R_{\text{c}} - \langle R_{\text{c}} \rangle)^2}{2\sigma_{\text{R}}^2} \right] \quad \text{for } R_{\text{c}} \geq 0 \tag{C.11}$$

where σ_{R} is the standard deviation of core radii about a mean of $\langle R_{\text{c}} \rangle$. The scattered intensity from a solution of disperse spheres is then given by

$$I(q) \sim \int Đ(R_{\text{c}})I_{\text{u}}(q)dR_{\text{c}} \tag{C.12}$$

$$I(q) \sim S(q) \int Đ(R_{\text{c}})P_{\text{c}}(q)dR_{\text{c}} \tag{C.13}$$

$$I(q) = C_1 \left[S(q) \int Đ(R_c) P_c(q) dR_c \right] + C_2 \tag{C.14}$$

where C_1 and C_2 are arbitrary scaling parameters.

C.2.2 Igor Pro Procedure

```
#pragma rtGlobals=1 // Use modern global access method

Function HardSphereModel(w,inx) : FitFunc

// Fits data to a model including terms for the hard
// sphere form factor and a structure factor
// approximated by the Percus-Yevick closure relation

Wave w
Variable inx

// Average core radius
Variable/G aveR = w[0]

// Standard deviation in core radius
Variable/G sigR = w[1]

// Equivalent hard sphere radius
Variable/G Rhs = w[2]

// Equivalent hard sphere volume fraction
// Set to 0 and hold constant to ignore
// the structure factor terms
Variable/G phi = w[3]

// Thickness of the interface between the
// core and the surrounding matrix
// Set to 0 and hold constant to ignore this term
Variable/G t_int = w[4]

// Arbitrary multiplicative scaling constant
Variable/G c1 = w[5]

// Arbitrary additive scaling constant
Variable/G c2 = w[6]

Variable/G xx = inx

// Zero out integration over core radii
Variable integration = 0
```

```
// Total scattered intensity to be compared to experimental data
Variable model = 0

// Lower limit of core radius integration = 0 nm
Variable a = 0

// Upper limit of core radius integration = 100 nm
Variable b = 100

// Integrate over core radii from 0 to 100 nm
// using trapezoidal integration (option 0) with 100 sub-intervals
integration = Integrate1D(HardSphereFFwithGaussDist, a, b, 0, 100)

model = c1*(integration*PY_HardSphere(inx, Rhs, phi)) + c2

Return model

End


//// Form Factor ////

// Form factor of dilute hard spheres with Gaussian distribution
// of radii. Pass current value of core radius, current_R, during
// integration
Function HardSphereFFwithGaussDist(current_R)

Variable current_R

NVAR xx, t_int, aveR, sigR

Return (HardSphereAmp(xx, current_R))^2 *
Gauss_Dist(current_R, aveR, sigR) *
exp(-xx^2*t_int^2)

End

// Amplitude of scatter from dilute uniform hard spheres
Function HardSphereAmp(current_q, current_R)

// Current q that is evaluating and R value in the
// current slice of integral
Variable current_q, current_R

// Dummy variable
Variable qR = current_q*current_R

Return (3/qR^3) * (sin(qR) - qR*cos(qR))

End

// Gaussian distribution of the sphere core radii
```

```
Function Gauss_Dist(current_R, aveRc, sigRc)

// R value in the current slice of integral,
// average and std dev
Variable current_R, aveRc, sigRc

Return 1/( sigRc*sqrt(2*pi) )*exp(-(current_R-aveRc)^2/(2*sigRc^2))

End

//// Structure Factor ////

// Structure factor for uniform hard spheres using Percus-Yevick
// closure relation
Function PY_HardSphere(current_q, Rhs, phi)

// Rhs is the equivalent hard sphere radius
// phi is the volume fraction of equivalent hard spheres
Variable current_q, Rhs, phi
// Parameters/prefactors using phi
Variable lambda1, lambda2

// A = argument of the sine and cosine functions
//    = 2*current_q*Rhs
Variable A

// The 3 terms in the long structure factor equation
Variable First, Second, Third

// NbarC(q) = the long equation that goes into the
// structure factor as S = 1/(1-NbarC(q))
Variable NbarC

lambda1 = ((1+2*phi)^2) / ((1-phi)^4)
lambda2 = (-(1+phi/2)^2) / ((1-phi)^4)
A = 2*current_q*Rhs

First = lambda1*((sin(A)-A*cos(A))/A^3)
Second = -6*phi*lambda2*((A^2*cos(A)-2*A*sin(A)-2*cos(A)+2)/A^4)
Third = -phi*lambda1/2*((A^4*cos(A)-4*A^3*
sin(A)-12*A^2*cos(A)+24*A*sin(A)+24*cos(A)-24)/A^6)

NbarC = First + Second + Third

Return 1/(1 + 24*phi*NbarC)

End
```